Durham University

Durham E-Theses

Percolative Current Flow through Anisotropic High-Field Superconductors under Strain

JACK RICHARD GREENWOOD

How to cite:

GREENWOOD, JACK RICHARD (2023) Percolative Current Flow through Anisotropic High-Field Superconductors under Strain. Doctoral thesis, Durham University.

Use policy

This work is licensed under a Creative Commons Attribution Non-commercial Share Alike 3.0 (CC BY-NC-SA)

Academic Support Office, The Palatine Centre, Durham University, Stockton Road, Durham, DH1 3LE
e-mail: e-theses.admin@durham.ac.uk Tel: +44 0191 334 6107
https://etheses.durham.ac.uk

Percolative Current Flow through Anisotropic High-Field Superconductors under Strain

Jack Greenwood

A thesis presented for the degree of

Doctor of Philosophy

Department of Physics

Durham University

United Kingdom

13th April 2023

For Laura

Percolative Current Flow through Anisotropic High-Field Superconductors under Strain

Jack Greenwood

Abstract

For decades, flux pinning scaling laws based upon unimodal, infinitesimally narrow, averaged distributions of critical superconducting parameters have been used to explain what limits the critical currents of practical superconducting materials in high fields. These scaling laws have enabled superconducting technologies ranging from MRI scanners, to high field research magnets, to magnets for particle accelerators and fusion energy. However in this work, we progress beyond these approximations and provide:

(i) The first comprehensive analysis of critical current density data showing that in high magnetic fields, technological low and high temperature superconducting materials can be treated as a percolative network of Josephson junctions. We then extract the size and normal state properties of the grain boundaries, the underlying T_C distribution within the grains, and the dimensionality of the current flow within the material

(ii) The first reported measurements of the in-plane, biaxial strain dependence of J_C for (RE)BCO tapes. This provides a description and understanding of the effects of the two most important strain components on J_C and

(iii) The first comprehensive framework for percolative current flow in LTS and HTS superconductors under strain. It explicitly includes the factors suppressing J_C and describes percolative flow within an anisotropic material containing a distribution of critical superconducting parameters.

Our results show that large improvements to J_C are available from further optimisation of the grains and grain boundaries in (RE)BCO and Nb_3Sn which will help enable the successful delivery of commercial fusion tokamaks.

Supervisors: Prof. Damian Hampshire and Prof. Ray Sharples

Acknowledgements

I would like to start by thanking my wife Laura for her love and her infinite patience through the many long days and various existential crises that occurred while getting this thesis finished. I would next like to thank my Mum, Dad, Chloe, and my grandparents for their love and encouragement throughout my life. I would also like to thank Q. and A. Masoum for their friendship over many years.
My next thanks must go to my supervisor, Professor D. Hampshire, for his support, guidance, and scientific wisdom throughout this long journey. I would also like to say a special thank you to M. Raine for his support, and for inspiring me to pursue a PhD in applied superconductivity after teaching me how to perform high-field measurements in the ITER lab back in 2015. I would like to thank all the other members of Durham University Superconductivity Group that I have known - Y. Tsui, G. Wang, P. Branch, F. Ridgeon, C. Robson, A. Blair, A. Smith, S. Chislett-McDonald, A. Nader, C. Gurnham, B. Din, and C. Haddon. I shall miss the office chats around life and politics, (and occasionally superconductivity) tremendously. The experiments in this thesis simply would not have been possible without the expertise of Durham's Mechanical Workshop - special thanks here must go to A. Crosby and S. Lishman. They were always on hand to offer expert advice and sarcastic remarks that left me with a sense of great accomplishment in my designs. I would like to thank M. Lakrimi, A. Thomas, and M. Wozniak for making me feel welcome during my time at Siemens and for introducing me to superconductivity on an industrial scale. I would also like to say thanks to M. Lloyd, T. Davis, and D. Celis-Garza at Oxford University for graciously hosting me during that time. I would finally like to thank my colleagues at UKAEA for making me feel welcome and from whom I continue to learn a lot - special thanks here must go to E. Surrey, P. Goodwin, and S. Allen.

This work is funded by EPSRC grant EP/L01663X/1 that supports the EPSRC Centre for Doctoral Training in the Science and Technology of Fusion Energy. This work has also been carried out within the framework of the EUROfusion Consortium and has received funding from the Euratom research and training programme.

Contents

Declaration

The work in this thesis is based on research carried out at Durham University Superconductivity Group, Department of Physics, University of Durham, England. No part of this thesis has been submitted elsewhere for any other degree or qualification, and it is the sole work of the author unless referenced to the contrary in the text.

Some of the work presented in this thesis has been previously published in journals and presented at conferences - the relevant publications and conferences are listed below.

Publications

J. R. Greenwood and D. P. Hampshire; The Effects of Strain on Percolative Current Flow through a (RE)BCO Coated Conductor in High Magnetic Fields, *In progress for Superconductor Science and Technology*)

J. R. Greenwood, E. Surrey, and D. P. Hampshire; The Biaxial Strain Dependence of J_C of a (RE)BCO Coated Conductor at 77 K in Low Fields, *IEEE Transactions on Applied Superconductivity* **29**(5) (2019)

J. R. Greenwood, E. Surrey, and D. P. Hampshire; Biaxial Strain Measurements of J_C on a (RE)BCO Coated Conductor, *IEEE Transactions on Applied Superconductivity* **28**(4) (2018)

Conference Presentations

J. R. Greenwood, E. Surrey, and D. P. Hampshire; The Effects of Percolation and Distributions on $J_C(B, T, \varepsilon)$ of (RE)BCO in High Fields for Fusion (Oral), Applied Superconductivity Conference, Florida, USA (2020)

J. R. Greenwood, E. Surrey, and D. P. Hampshire; Electro-Mechanical Properties of Superconductors in High Magnetic Fields for Fusion Applications (Oral), Culham PhD Showcase, Oxford, UK (2020)

J. R. Greenwood, E. Surrey, and D. P. Hampshire; The Effects of Percolation and Distributions of Critical Parameters on $J_C(B, T, \varepsilon)$ (Oral), European Conference on Applied Superconductivity, Glasgow, UK (2019)

J. R. Greenwood, E. Surrey, and D. P. Hampshire; 2D Strain Dependent Critical Current Density of High Temperature Superconductors for Fusion Applications (Oral), Fusion Frontiers and Interfaces Workshop, York, UK (2019)

J. R. Greenwood, E. Surrey, and D. P. Hampshire; The Biaxial Strain Dependence of the Critical Current Density of a (RE)BCO Coated Conductor at 77 K (Poster), Applied Superconductivity Conference, Washington, USA (2018)

J. R. Greenwood, E. Surrey, and D. P. Hampshire; Biaxial Strain Measurements of J_C on a (RE)BCO Coated Conductor (Poster), European Conference on Applied Superconductivity, Geneva, Switzerland (2017)

J. R. Greenwood, E. Surrey, and D. P. Hampshire; Biaxial Strain Measurements of J_C on a (RE)BCO Coated Conductor (Poster), Culham PhD Showcase, Oxford, UK (2017)

J. R. Greenwood, E. Surrey, and D. P. Hampshire; The Strain Dependence of the Critical Current Density of High Temperature Superconductors for Fusion (Poster), Fusion Frontiers and Interfaces Workshop, York, UK (2017)

13th April 2023

Jack Greenwood

Copyright © 2023 by Jack Greenwood.

"The copyright of this thesis rests with the author. No quotation from it should be published without the author's prior written consent and information derived from it should be acknowledged"

Courses

The Fusion CDT is a partnership between the Universities of Oxford, Durham, York, Manchester, Liverpool, and the Culham Centre for Fusion Energy. Students on the CDT course attend a number of lecture courses and hands-on laboratory experience delivered by world experts in particular aspects of fusion-related science. The aim of the courses is to give enrolled PhD students a firm and broad grounding in the physics, materials science, and engineering considerations for fusion energy, from which they can produce fruitful and contextual research. The programme is split into 'materials science' and 'plasma physics' strands. The author is a member of the former. The first 9 months of the PhD course are spent between the various partner institutions and require full-time study from students. Table 1 lists the courses attended.

Industrial Placement

In the second year of the Fusion CDT PhD programme, students complete a collaboratory project of up to 12 weeks in an area of research that may or may not be fully aligned with their thesis topic. Students have the choice of doing this project in industry or in an academic organisation. In this PhD, an industrial placement was completed at Siemens Healthineers Magnet Technology, Eynsham, Oxfordshire, UK, from June to August 2018. Siemens are the world's largest man-

Table 1: First year courses attended as part of the Fusion CDT. The Frontiers of Fusion course is not assigned a grade.

Course Name	**Location and Date**	**Grade**
Introduction to Plasma Physics	York, UK, 2016	Distinction
Introduction to Computer Techniques	York, UK, 2016	Distinction
Introduction to Materials	York, UK, 2016	Distinction
Materials Applications in Fusion	Oxford, UK, 2016	Distinction
Radiation Damage	Oxford, UK, 2016	Distinction
Fusion Technology	Oxford, UK, 2017	Distinction
Materials Applications in Fusion	Oxford, UK, 2016	Distinction
Plasma Materials Interactions Lab	Liverpool, UK, 2017	Distinction
Characterisation/Analytical Tools	Oxford, UK, 2017	Pass
Finite Element Method and Design Codes	Manchester, UK, 2017	Distinction
Integrated Systems and Project Management	Durham, UK,2017	Pass
Frontiers of Fusion	York, UK, 2017	N/A

ufacturer of superconducting magnets for MRI scanners. The exact details of the project cannot be disclosed due to IP restrictions.

Chapter 1

Introduction

The inherent issues with fossil fuels mean that renewable, low carbon sources of energy must be developed and adapted at a rapid scale in the 21st Century. This will likely be the defining challenge for this century. Several forms of renewable, low carbon energy generation already exist, such as wind and solar power. However, these technologies are intermittent as they depend upon favourable weather conditions, which cannot be controlled. Large scale energy storage is often thought of as a potential solution, however, there are doubts that storage solutions of sufficient energy density and efficiency can be deployed at scale in time. Nuclear fission is another potential solution. However, it has potentially very severe safety issues [1, 2, 3, 4], it is very costly to dispose and monitor the long-lived radioactive waste [5], and it can proliferate the development of weapons of mass destruction. There is one technology that has the potential to completely transform global power generation, with none of the drawbacks listed above - fusion energy.

Fusion is the process that powers the stars, in which lighter nuclei are fused into heavier nuclei, and energy is released as a by-product. In the 21st Century, Fusion is rapidly moving from the realms of science fiction into reality, with many projects underway, both publicly and privately funded. Arguably, the most well-studied approach to power generation from fusion is using a magnetically confined plasma in a toroidal shape, using a tokamak. Since the early works of Tamm, Sakharov, and other pioneers in the 1950's, [6], the fusion community has moved

ever closer to achieving net power output from a fusion tokamak. The ITER fusion reactor, that is currently under construction in France, will demonstrate that it is possible to generate enough fusion power within a plasma for the plasma to sustain itself at its operating conditions [7]. Looking beyond ITER, concepts for large prototype/demonstration fusion power plants are currently being studied by several states and superstates such as Japan [8], the UK [9], China [10], and the EU [11]. Several private start-ups/spin-offs have also been created that are investigating faster ways to achieve commercial fusion power by using compact tokamaks [12, 13].

The fusion power generated by the plasma scales very strongly with the plasma's magnetic field. The only way for magnetic confinement fusion power plants to generate the large amounts of power needed for commercially viable fusion is if they use superconducting magnets. Only superconducting magnets can generate these very high fields for long durations, as the superconductors have zero dc electrical resistance. It is this unique property of superconducting materials, along with their perfect diamagnetism, that has allowed technologies ranging from Magnetic Resonance Imaging (MRI) scanners [14], to particle accelerators such as the Large Hadron Collider (LHC) [15], to high-field, dc research magnets [16], to levitating trains [17]. Superconductors continue to play prominent roles in other emerging technologies as well, such as electric aircraft propulsion [18].

While Low Temperature Superconductors (LTS) such as Nb-Ti and Nb_3Sn have been used for decades in technologies such as MRI and high-field magnets, it is likely that High Temperature Superconductors (HTS) will become the workhorse of future superconducting technologies, including commercial fusion power plants. This is because of their much higher critical temperatures (T_C's), upper critical fields (B_{c2}'s), and critical current densities (J_C's). The HTS 'grain boundary problem' [19, 20], that was identified after the discovery of HTS in the 1980's [21], has largely been solved by the development of coated conductor technologies, enabling high J_C 'tapes'. Nevertheless, the J_C's of technological HTS (and LTS) remain

orders of magnitude below the theoretical depairing current density limit [22]. For decades, flux pinning scaling laws, that consider the forces on the fluxons within the flux lattice in the superconducting material, have been used to inform magnet designers of the critical currents of superconducting materials (see Ekin's excellent review [23, 24, 25] and the voluminous number of references therein). These scaling laws are perhaps less useful for HTS due to the many pinning mechanisms that occur within the material.

All technological superconductors, with the exception of Nb-Ti, are brittle. This is a key issue for the adoption of superconductors in fusion magnet systems, as the Lorentz forces on the magnets are large. This issue is often exacerbated in HTS fusion magnets, in which the high B_{c2} and J_C values are exploited to generate very high fields using very high currents [26]. Traditionally, the flux pinning scaling laws used to parameterise the strain dependent J_C's of technological superconductors have assumed that the material under analysis has a singular, strain dependent value of T_C and B_{c2}, and therefore J_C. This analysis approach has recently been shown to not be viable for the HTS (Rare Earth)$Ba_2Cu_3O_{7-\delta}$ (i.e., '(RE)BCO'), and has also called into question the validity of analyses for the strain dependence of Nb_3Sn [27, 28, 29]. A 1D chain model has been developed to better describe the strain dependence of J_C of a superconducting material that contains 2 competing domains with different strain dependencies [27, 28, 29, 30, 31, 32]. The source of the competition between the domains for (RE)BCO is demonstrated by the intrinsic anisotropic strain dependent superconducting properties of single crystals [33, 34]. The fact that the superconducting properties of (RE)BCO single crystals depend upon the direction along which the strain is applied has implications for HTS cable and conductor designs for fusion, too. The (RE)BCO tapes within the cables are often twisted and/or transposed to reduce ac losses, which means that the strains within the tapes in the cables are multi-directional. Of the experiments performed on (RE)BCO tapes to investigate their strain dependent properties, the vast majority have focused upon tensile strains along the length of the tape. Fewer have

investigated compressive strains along the length, even fewer have investigated the effects of strain applied along tapes' other axes [35, 36, 37, 38], and with the notable exception of the work by Ilin et. al. that considered the complex combination of uniaxial, torsional and transverse strains, there are no reports of work that has investigated the effects of multiaxial strains applied in-plane (along the important *a*- and *b*-axes) simultaneously [35].

The aim of the work in this thesis is to better understand the factors that limit the critical currents of (RE)BCO coated conductors, namely multiaxial strains, the material properties and dimensions of non-superconducting regions within tapes such as grain boundaries, imperfections within the superconducting regions that manifest as distributions of critical superconducting parameters, and current percolation. A better understanding of these effects on J_C will lead to improved HTS fusion magnet designs and improved J_C's within the tapes themselves, moving the fusion community one step closer to commercial fusion energy and other exciting applications.

Chapter 2 gives an overview of the basic properties and theories of superconductors and an overview of fusion energy. Chapter 3 discusses the literature on the key factors that can limit J_C in technological HTS - strain, grain boundaries, and current percolation. Chapter 4 presents (to our knowledge) the first reported measurements for the in-plane, biaxial strain dependence of J_C for (RE)BCO tapes. It also extends the 1D chain model by incorporating the biaxial strain dependence of the superconducting properties of (RE)BCO single crystals, to enable the experimental data to be analysed. The design of a 1 kA probe that will be capable of measuring the biaxial strain dependence of J_C at 4.2 K in high fields with in-situ strain control is also presented. Chapter 5 presents in-depth measurements for the field, temperature, strain and angular dependence of J_C for a (RE)BCO tape containing Artificial Pinning Centres (APC's). We will show that global flux pinning analyses [23, 24, 25] for this sample break down at low temperatures due to the unphysically high values of B_{c2} that are required to fit the data. The chapter

then presents a new scaling law for J_C that is based upon the current flow across Superconductor Normal Superconductor (SNS) Josephson junctions with thick normal barriers that contain fluxons. With the analysis, we extract the dimensions and normal state properties of the superconducting electrodes and normal barriers (likely grain or twin boundaries) for APC and Non-APC (RE)BCO tapes, and a Nb_3Sn strand. Chapter 6 begins by re-analysing the J_C data presented in Chapter 4 using the 1D chain model. We show that the 1D chain model cannot explain the strain dependence of J_C across the entire strain range. We therefore present a percolation model for J_C that contains distributions of critical superconducting parameters. By using this model, not only can we obtain better fits to the data, but we can also extract the T_C distribution characteristics and the dimensionality of the current flow within (RE)BCO tapes and Nb_3Sn strands from J_C data for the first time. We finish the thesis with some concluding remarks and avenues for future work in Chapter 7.

Chapter 2

Applied Superconductivity and Fusion

2.1 Introduction

Superconductivity was first discovered by Kamerlingh Onnes in 1911, during his experiments on the properties of mercury at low temperatures [39]. He found that the dc electrical resistance of mercury dropped to zero below a certain temperature known today as a critical temperature, T_C. Since 1911, many materials have been found to exhibit the phenomenon of superconductivity, such as the ductile alloy Nb-Ti [40] and the brittle intermetallic Nb_3Sn [41]. These two Nb-based compounds have enabled technologies such as high-field research magnets and MRI scanners [14], as well as contributing significantly to more experimental technologies such as particle accelerators [15] and Magnetic Confinement Fusion (MCF) reactors [42].

In 1986, superconductivity in the cuprate La-Ba-Cu-O with a T_C of $\approx$30 K was reported by Bednorz and Müller [21], which caused the field of superconductivity to undergo a renaissance. Cuprates with even higher T_C's such as $YBa_2Cu_3O_{7-\delta}$ (commonly known as 'YBCO', with a T_C of $\approx$93 K) were quickly discovered [43], which allowed the development of superconductor technologies that use liquid ni-

trogen as a coolant rather than liquid helium. The quest to discover T_C's on the order of room temperature or greater continues, with the highest known T_C to date ($\approx$288 K) being found in a carbonaceous sulphur hydride under a pressure of 270 GPa [44]. However, superconductivity in this material has recently been called into question by Hirsch [45].

This chapter provides an overview of the fundamentals of superconductivity and how superconductors are used in fusion reactors. Section 2.2 discusses the characteristic properties of superconductors and outlines London theory. Section 2.3 gives an overview of Bardeen-Cooper-Schrieffer (BCS) theory, Section 2.4 gives an overview of Ginzburg-Landau (G-L) theory, Section 2.5 discusses critical currents and flux pinning, Section 2.6 gives an overview of the crucial role that superconductors play in magnetic confinement fusion reactors and Section 2.7 gives some concluding comments.

2.2 Characteristic Properties of Superconductors

All materials that are in the superconducting state share two key physical properties- zero dc electrical resistance, and the ability to expel magnetic fields when they are placed in a background magnetic field and then cooled below their transition temperature. Kamerlingh Onnes was the first to observe zero dc electrical resistance as discussed in the previous section and it was originally thought that superconductors were in fact *perfect conductors* due to their zero electrical resistance and their ability to exclude a magnetic field that was applied after cooling. However, in 1933 Meissner and Oschenfeld showed that if a magnetic field is applied to a superconductor *before* it is cooled below its transition temperature, the applied magnetic field is expelled when it is then cooled [46]. A perfect conductor would not behave like this- it would retain its magnetic field upon its transition into the 'perfectly conducting' state. Figure 2.1 shows the differences expected between

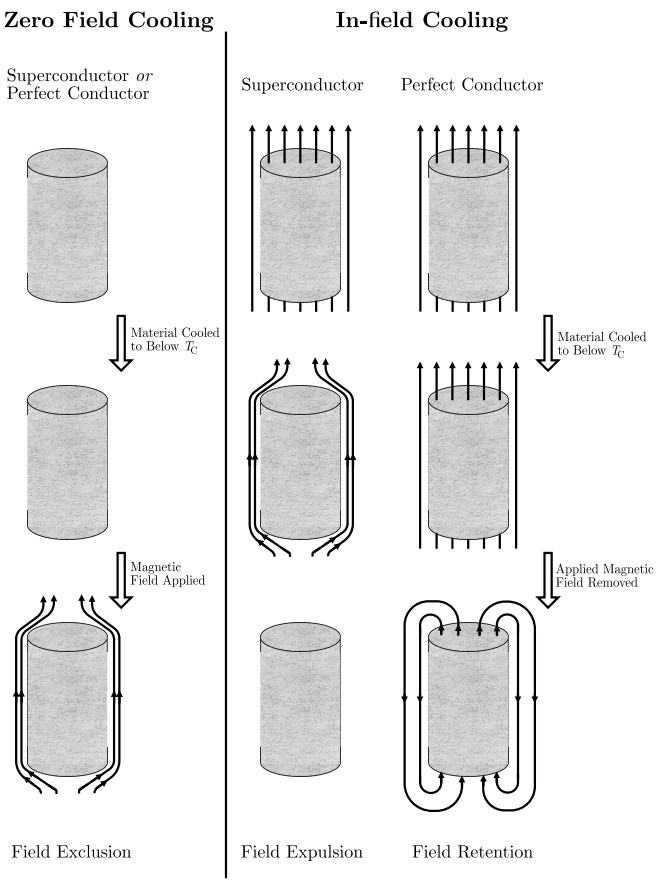

Figure 2.1: The transient behaviours of superconductors and perfect conductors during zero-field cooling and in-field cooling. Adapted from [28].

perfect conductors and superconductors undergoing in-field cooling and zero-field cooling. The brothers Heinz and Fritz London devised two equations, which combine the phenomena of zero dc electrical resistance and field expulsion during field cooling (i.e. superconductors behaving as *perfect diamagnets*), which are [47]:

$$\frac{\partial \boldsymbol{J}_s}{\partial t} = \frac{n_s e^2}{m_e} \boldsymbol{E} \tag{2.2.1}$$

and

$$\nabla \times \boldsymbol{J}_s = -\frac{n_s e^2}{m_e} \boldsymbol{B}, \tag{2.2.2}$$

where $\boldsymbol{J}_s$ is the supercurrent density, n_s is the number density of superconducting electrons, e is the elementary charge and m_e is the free electron mass. Equation 2.2.1 describes the phenomenon of zero electrical resistance. If a static current is

maintained in a superconductor, there is no electric field, so there is no potential difference and no dc electrical resistance. The second equation describes the perfect diamagnetism and when it is combined with Maxwell's equations it yields

$$\nabla^2 \boldsymbol{B} = \frac{\boldsymbol{B}}{\lambda_L^2}, \tag{2.2.3}$$

where λ_L is the London penetration depth

$$\lambda_L = \left(\frac{m_e}{\mu_0 e^2 n_s}\right)^{1/2} \tag{2.2.4}$$

and μ_0 is the vacuum permeability. For an infinitely thick superconducting slab that spans from $x = 0$ to $x = \infty$, the magnetic field has the form of an exponential decay function. As one moves from $x = 0$ into the slab, the magnetic field decays over a characteristic length λ_L, known as the penetration depth. The penetration depth is one of the two important length scales for superconductivity, the other being the coherence length which is introduced in Section 2.4.

2.3 BCS Theory

BCS theory states that superconductivity occurs in a material due to an attractive interaction between pairs of electrons, that is mediated by phonons. The origins of the theory can be traced back to Fröhlich [48], who suggested that an electron with momentum $\boldsymbol{k}$ can become coupled to another electron with momentum $\boldsymbol{k'}$ via a phonon of crystal momentum $\boldsymbol{q}$. The phonon arises through the interaction between the electrons and the positive ions in a metallic lattice. A simplified potential for this interaction, proposed by Bardeen, Cooper and Schrieffer [49], is

$$V_{\boldsymbol{k}\boldsymbol{k'}} = \begin{cases} -V_{\mathrm{BCS}} & \text{if } |E_{\boldsymbol{k}}| < \hbar\omega_D \text{ and } |E_{\boldsymbol{k'}}| < \hbar\omega_D \\ 0 & \text{otherwise} \end{cases}, \tag{2.3.1}$$

where $E_{\boldsymbol{k}}$ and $E_{\boldsymbol{k'}}$ are the energies of the electron states with wave numbers $\boldsymbol{k}$ and $\boldsymbol{k'}$ respectively, ω_D is the Debye frequency of the phonons in the metallic lattice and V_{BCS} is a constant. Solving Schrödinger's equation for a system of many electrons

that interact according to 2.3.1 leads to the possibility of an energy state (the superconducting state) existing below the normal ground state. The energy gap Δ_s between the normal ground state and the superconducting state has the form [49]

$$\Delta_s = 2\hbar\omega_D \exp\left(-\frac{1}{g(E_{F,s})V_{\mathrm{BCS}}}\right) \tag{2.3.2}$$

at zero temperature, where $g(E_{F,s})$ is the density of energy states at the Fermi surface at zero temperature. This equation is valid in the 'weak coupling' limit, where $|\Delta_s| \ll \hbar\omega_D \ll E_{F,s}$ and $E_{F,s}$ is the Fermi energy.

One of the strongest pieces of experimental evidence that supports the phonon coupling as described in BCS theory is the so-called 'isotope effect' [50, 51], where T_{C} depends on the masses of the ions in the lattice. BCS theory predicts

$$3.52 k_B T_{\mathrm{C}} = 2\Delta_s(0) \tag{2.3.3}$$

where $\Delta_s(0)$ is the energy gap at absolute zero temperature. Comparing 2.3.2 and 2.3.3, we see that $T_{\mathrm{C}} \propto \hbar\omega_D$ and in turn, $\omega_D \propto M^{-0.5}$ where M is the mass of an ion in the lattice.

2.4 Ginzburg-Landau Theory

2.4.1 The Ginzburg-Landau Free Energy

Ginzburg-Landau (G-L) theory examines superconductivity near the superconductor-normal phase transition temperature [52]. In G-L theory, the phase of a system is characterised by a complex order parameter ψ. If the system is in the superconducting phase, $\psi \neq 0$ and if the system is in the normal phase, $\psi = 0$. In the superconducting phase, in the presence of a magnetic field, close to T_{C} (where ψ is small), the time-independent G-L free energy density functional of the superconductor g_s is [53]:

$$g_s = f_n + \alpha_s |\psi|^2 + \frac{\beta_s}{2}|\psi|^4 + \frac{\Upsilon_s}{2m}|(-i\hbar\boldsymbol{\nabla} + 2e\boldsymbol{A})\,\psi|^2 + \frac{\boldsymbol{B}^2}{2\mu_0} - \boldsymbol{H_0}\cdot\boldsymbol{B} + \frac{\mu_0 \boldsymbol{H_0}^2}{2}, \tag{2.4.1}$$

where f_n is the free energy density of the superconductor's normal phase in the absence of a magnetic field, α_s, β_s and Υ_s are temperature dependent coefficients that are different for each superconducting material, $\boldsymbol{\nabla} \times \boldsymbol{A} = \boldsymbol{B}$ is the magnetic flux density, $\boldsymbol{H_0}$ is the applied magnetic field and m is the effective boson (Cooper pair) mass. Writing the G-L functional in this way ensures that the magnetic energy associated with the coils that produce the field $\boldsymbol{H_0}$ is accounted for, and it also ensures that the correct expressions for the critical fields of thin film superconductors are derived, if they are required in subsequent work [53]. In standard analysis, Υ_s is usually set to be unity.

2.4.2 Ginzburg-Landau Equations

Minimising Equation 2.4.1 with respect to variations in the complex conjugate of the order parameter ψ^* using variational methods leads to the G-L equation

$$\frac{\Upsilon_s}{2m}\left|(-i\hbar\boldsymbol{\nabla} + 2e\boldsymbol{A})^2\,\psi\right| + \alpha_s\psi + \beta_s\left|\psi\right|^2\psi = 0. \tag{2.4.2}$$

By considering a one-dimensional superconducting system in zero applied magnetic field (i.e., $\boldsymbol{A} = \boldsymbol{0}$), we obtain

$$\frac{\hbar^2\Upsilon_s}{2m}\frac{\mathrm{d}^2\psi}{\mathrm{d}x^2} + \alpha_s\psi + \beta_s\left|\psi\right|^2\psi = 0, \tag{2.4.3}$$

where x corresponds to the single spatial dimension. By further considering that the superconductor spans from $x = 0$ to $x = \infty$ with the boundary condition $\lim_{x\to\infty}\left(\frac{\mathrm{d}\psi}{\mathrm{d}x}\right) = 0$ (so that ψ is spatially invariant deep in the superconductor), we obtain

$$\psi = \psi_\infty \tanh\left(\frac{x}{\xi_s\sqrt{2}}\right) \tag{2.4.4}$$

where $\psi_\infty = \frac{|\alpha_s|}{\beta_s}$ is the order parameter deep inside the superconductor and

$$\xi_s = \left(\frac{\hbar^2\Upsilon_s}{2m\left|\alpha_s\right|}\right)^{1/2} \tag{2.4.5}$$

is the G-L coherence length. The coherence length can be thought of as the characteristic length over which the order parameter decays from the value found in the bulk of the superconductor. The coherence length is the other key length scale for superconductivity, along with the penetration depth discussed earlier.

If we minimise the G-L free energy (Eqn. 2.4.1) with respect to variations in the magnetic vector potential, then we obtain the second G-L equation:

$$\boldsymbol{J}_s = -\frac{2ie\hbar}{m}\left(\psi^*\boldsymbol{\nabla}\psi - \psi\boldsymbol{\nabla}\psi^*\right) - \frac{2e^2}{m}\left|\psi\right|^2\boldsymbol{A} \tag{2.4.6}$$

This equation can be used to derive an expression for the G-L penetration depth λ_s.

2.4.3 Type I and Type II Superconductors and Critical Fields

The Ginzburg-Landau parameter $\kappa_s = \lambda_s/\xi_s$ can be used to classify superconductors into two types:

$$\kappa_s \begin{cases} \leq \frac{1}{\sqrt{2}}, \text{ Type I} \\ > \frac{1}{\sqrt{2}}, \text{ Type II.} \end{cases} \tag{2.4.7}$$

Type I and Type II superconductors have different magnetic properties, which are summarised in Figure 2.2.

In the presence of an applied magnetic field, bulk Type I superconductors behave as perfect diamagnets (i.e. they are in the *Meissner state*) until the thermodynamic critical magnetic field B_{C} is reached. B_{C} is the field at which the diamagnetic energy (associated with the currents that screen the applied magnetic field) is equal to the superconductor's condensation energy. In other words:

$$B_{\mathrm{C}} = \left(\frac{\mu_0\left|\alpha_s\right|^2}{\beta_s}\right)^{1/2}. \tag{2.4.8}$$

A bulk Type II superconductor also behaves as a perfect diamagnet, but only until the lower critical magnetic field B_{c1} is reached. At this point, the applied magnetic field begins to penetrate the superconductor as an array of magnetic flux vortices ('fluxons'). This is known as the mixed state for Type II superconductors.

Abrikosov was the first to derive a solution to the G-L equations for the mixed state, in the limit that ψ is small, and he showed that the fluxons form a periodic lattice structure [54].

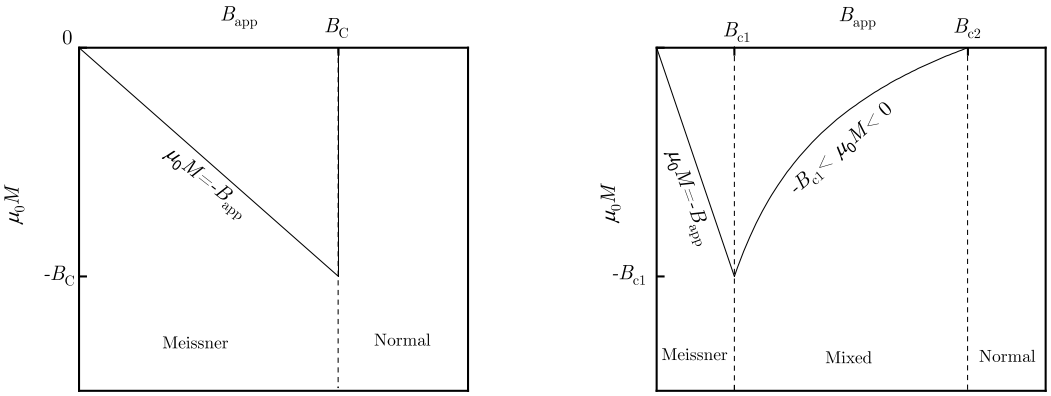

Type I **Type II**

Figure 2.2: The magnetisation of Type I and Type II superconductors as a function of applied magnetic field.

In the fluxon lattice, each fluxon has a magnetic flux equal to the flux quantum Φ_0, has a radius of ξ_s, and supercurrents circulate the fluxon up to a distance λ_s from the fluxon's core. The core of each fluxon is in the normal state. As the applied magnetic field increases from B_{c1}, the spacing between fluxons gets smaller, until the spacing is equal to ξ_s. The applied magnetic field associated with this vortex spacing is the upper critical magnetic field B_{c2} and at this field, the bulk material is no longer superconducting. Close to B_{c2}, the coherence length can be related to B_{c2} using

$$\xi_s = \left(\frac{\Phi_0}{2\pi B_{c2}}\right)^{1/2}. \tag{2.4.9}$$

2.5 Critical Currents and Flux Pinning

Arguably, the most important superconducting material property for technological applications such as high-field superconducting magnets, is the critical current density J_C. It is the maximum supercurrent density that a superconductor can carry without dissipation. It is essential that high-field superconducting magnets

operate well below $J = J_C$, to reduce the risk of magnet quenches.

In the best technological Type II superconductors today, the critical current density is orders of magnitude lower than the *depairing* current density J_D, which is the theoretical maximum current density (at which the kinetic energy associated with the supercurrent is equal to the superconductor's condensation energy). The depairing current density calculated from G-L theory is [55]:

$$J_D = \frac{\Phi_0}{3\sqrt{3}\pi\mu_0\lambda_s^2\xi_s}. \tag{2.5.1}$$

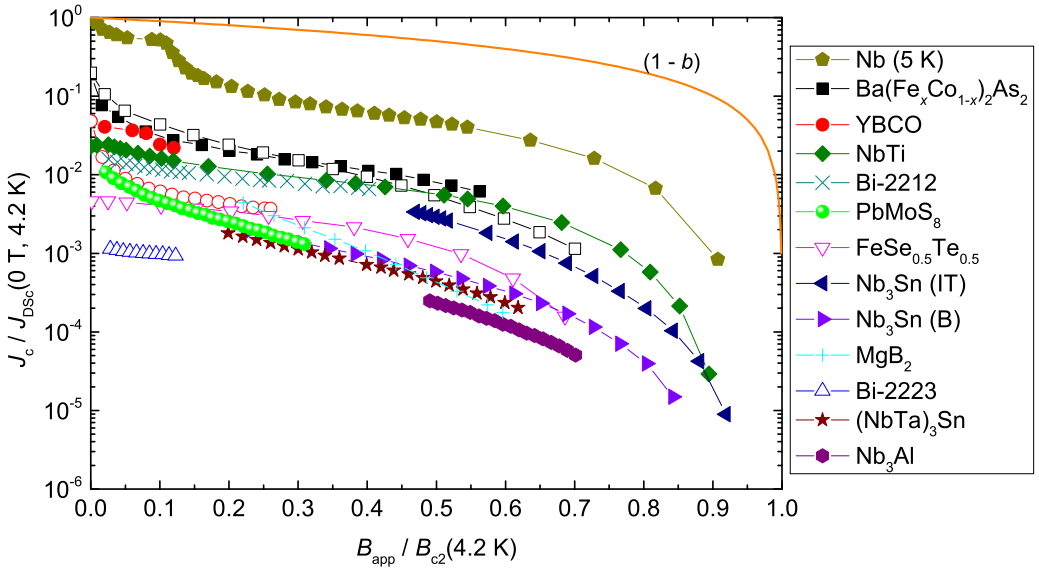

Figure 2.3: The ratio $\frac{J_C}{J_D}$ as a function of reduced magnetic field $\frac{B_{app}}{B_{c2}}$ for different technological superconductors [22].

Figure 2.3 shows the ratio of $\frac{J_C}{J_D}$ for different technological superconductors.

In technological type II superconductors, it is energetically favourable for the fluxons to be pinned in place on defects such as grain boundaries or dislocations, which are non-superconducting. It is also thought that fluxons are pinned in superconducting regions that have different values of κ_s from the bulk [56]. These defects exert a pinning force F_P on the fluxons. Flux pinning models attribute J_C to being the current density at which the Lorentz force on the fluxons is equal to the pinning force. In other words, if $J \perp B$, then

$$F_P = J_C \times B. \tag{2.5.2}$$

Above J_C, the fluxons become unpinned in the material and begin to move, which in turn generates an electric field (and therefore dissipation occurs). In general, the magnetic field dependence of the pinning force can be parameterised using [23, 24, 25, 56, 57, 58, 59, 60]

$$F_P = Cb^p(1-b)^q, \tag{2.5.3}$$

where C is a field independent prefactor and b is the reduced magnetic field B/B^*_{c2}, where B^*_{c2} is the irreversibility field. The irreversibility field is the field at which the vortex lattice melts or J_C hits the noise floor of the measurement, and it is always lower than B_{c2}. We will return to consider Equation 2.5.3 in detail later in this thesis. The two indices p and q have different half-integer values depending on the type of defect upon which a vortex is pinned [56]. For example, grain boundary pinning, which dominates in polycrystalline Nb_3Sn wires, has $p \approx 0.5$ and $q \approx 2$ [60, 61], whereas in Nb-Ti wires, α-Ti precipitates in the form of ribbons lead to $p \approx 0.5$ and $q \approx 0.5 - 1$. In real type II superconductors, fluxons are pinned on many different types of defects, so in practice, p and q rarely take exact half-integer values. It is well-accepted that current percolation and distributions of critical superconducting parameters can also distort the shape of $F_P(b)$ curves near $b = 1$ [62, 63, 64], which led Ekin to remark that the "*the tail does not scale*" [23].

The beauty of parameterising J_C data using 2.5.3 is that the equation is *separable*, with all of the reduced field dependence contained in $b^p(1-b)^q$ factor and the remaining temperature and strain dependence contained in the C factor. Over the last several decades, flux pinning scaling laws have developed to a point where they can now accurately parameterise the magnetic field, temperature and mechanical strain dependence of J_C [60, 65, 66, 67, 68]. An excellent review of the flux pinning scaling laws has been published by Ekin [23, 24, 25].

2.6 The Role of Superconductors in Fusion

2.6.1 Magnetic Confinement Fusion - the Power Source of the Future

The International Energy Authority (IEA) predicts that the world's total annual electrical energy demand will nearly double from its 2017 value of ~25 PW h to ~40 PW h by 2040 [69]. Other long-term models predict that this figure will increase to ~100 000 TW h by the end of the century [70, 71, 72, 73]. This huge increase in demand, combined with global climate change caused by CO_2 emissions, mean that alternative ways of generating cheap, clean energy must be sought quickly. One of the most promising options is nuclear fusion power- the energy generation process of the Sun.

In stars, fusion is a process in which nuclei that are lighter than ^{56}Fe fuse together to form heavier nuclei. The Sun's fusion reaction chain begins with two protons, but fusion reactors on Earth usually use a mixture of deuterium and tritium (D-T) nuclei as fuel because these nuclei have a significantly higher fusion reaction cross-section at temperatures that are achievable in reactors [74]. Deuterium has an isotopic abundance of ~0.015% in water [75] and tritium can be bred from the 17.5 billion tons of ^{6}Li that is available in, for example, seawater, [75, 76] using neutrons. This means that there is enough D-T fuel on Earth to power it for ~6 million years [77].

In any fusion reaction, the parent nuclei need sufficient energy to overcome the Coulomb repulsion barrier, which means that very high temperatures are required. The cores of stars have these very high temperatures (~2 keV in the Sun [78]) because of the gravitational force acting on their huge masses (~2×10^{30} kg for the Sun [79]). It is impossible to create such large gravitational forces on Earth, so other techniques have emerged to create the high temperatures. The two main techniques today are known as magnetic confinement fusion (MCF) and inertial

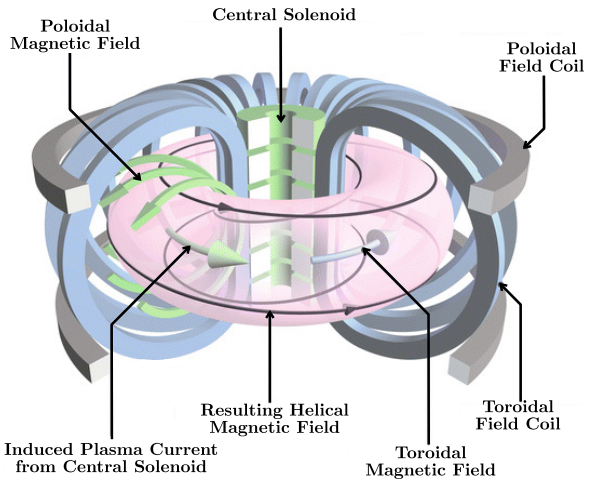

Figure 2.4: A schematic of the TF, PF and CS coils used in MCF and how they confine the plasma. Adopted from [80].

confinement fusion (ICF). The rest of this section will focus on MCF, as superconductors are generally not used for confinement in ICF.

2.6.2 Technological Superconductors for Fusion

In MCF, a high temperature, low density plasma (with a free electron density of ~10^{18}m^{-3} [81]) undergoing fusion is confined using high magnetic fields. The conventional tokamak is the most developed MCF reactor design, in which a plasma is confined to a toroid shape using toroidal field (TF) and poloidal field (PF) coils. A central solenoid (CS) is used to induce a current in the plasma, which shapes and ohmically heats the plasma. Figure 2.4 shows an overview of the magnet systems in an MCF reactor.

In an MCF plasma, the volumetric fusion power density P_{fus} is

$$P_{fus} \propto \beta_{fus}^2 B^4, \tag{2.6.1}$$

for fixed β_{fus}, where β_{fus} is the ratio of the plasma pressure to the magnetic field pressure [82, 83]. This is the driving factor for using superconducting magnets with high J_C and B_{c2} values in MCF. Superconducting magnets can generate high

magnetic fields for relatively low cooling costs compared to water or cryogenically cooled conductors [26, 84]. Superconductors can be used in either the TF, PF or CS coils. Even high residual resistivity ratio (RRR) copper and aluminium are of limited use because they suffer from magnetoresistive effects in high magnetic fields at cryogenic temperatures [85].

Table 2.1: A summary of some of the best commercially available superconductors today, and some of their key properties. $B^*_{c2}(0)$ is the irreversibility field at absolute zero and $J_{C,e}$ is the engineering critical current density (the critical current density of the whole conductor architecture).

Compound	T_C (K)	$B^*_{c2}(0)$ (T)	$J_{C,e}$(5 T, 4.2 K) (GAm^{-2})	Comments
Nb-Ti	10 [86]	16 [87, 88]	1.2 [89]	Ductile. Cheap due to mass adoption by MRI industry
Nb_3Sn	18 [90]	30 [90]	0.77 [91]	Part of the A15 class of superconducting materials. Off the shelf wires must be heat treated to form Nb_3Sn
MgB_2	39 [92]	25 [92]	0.57 [93]	Cheap to manufacture, but the anisotropic in-field properties of single crystals limit the performance of polycrystalline filaments in strands [94].
$Bi_2Sr_2Ca_1Cu_2O_8$ (Bi-2212)	95 [95]	$\lesssim 100$ (B||c-axis) [96]	0.98 [97]	The only cuprate that is currently fabricated as a round wire. The in-field superconducting properties of the round wires are isotropic.
$Bi_2Sr_2Ca_2Cu_3O_{10}$ (Bi-2223)	109 [98]	$\lesssim 85$ ($B \perp$ tape) [99]	0.51 ($B \perp$ tape) [100]	Its irreversibility field is relatively low at higher temperatures such as 77 K, limiting its use there.
(RE)$Ba_2Cu_3O_{7-\delta}$ ((RE)BCO)	93 [101]	$\lesssim 90$ ($B \perp$ tape) [29]	0.87 ($B \perp$ tape) [97]	Best performance at 77 K (< 2 T [99]). In general J_C is limited by weak links in polycrystalline material. Expensive to manufacture. Tapes have anisotropic in-field properties.

Table 2.1 provides an overview of some of the key technological superconductors that are available for use in fusion magnets today. The three key superconducting parameters which determine a superconductor's applicability for fusion magnets

(and form the superconductor's *critical surface*) are T_{C}, the irreversibility field $B^*_{\mathrm{c2}}(T)$ and the engineering critical current density, $J_{\mathrm{C},e}$. Technological superconductors usually have normal material such as copper in parallel with the superconducting component of the wire to improve thermal, electrical and mechanical stability. By convention, $J_{\mathrm{C},e}$ is taken to be the J_{C} of the whole wire.

2.6.3 The Path to Commercial Fusion Energy

The most important figure of merit for the performance of any fusion reactor is the fusion energy gain factor Q. It is the ratio of the power produced by the plasma and the heating power required to sustain it. A Q of 1 is known as *breakeven* and has not yet been reached in any MCF reactor. Another important milestone for fusion is *ignition*, at which point the heating produced by the fusion reactions themselves is enough to completely sustain the plasma and $Q \to \infty$. The Lawson criterion is a triple product of plasma properties that represents a minimum plasma performance needed for this to occur. For a D-T plasma [102]:

$$n_{i+e} T \tau_E > 3 \times 10^{21} \mathrm{keV\ s\ m^{-3}}, \tag{2.6.2}$$

where n_{i+e} is the combined number density of ions and electrons and τ_E is the energy confinement time- the average time that a particle remains confined in the plasma.

The ITER fusion reactor, a collaborative project between the United Kingdom, European Union, United States, Japan, China, South Korea and India has been designed to yield a Q of 10. Commissioning using a D-D plasma is due to begin in 2025 and D-T experiments yielding $Q \geq 10$ are due to begin in 2035. ITER uses Nb_3Sn for the TF coils and CS coils and it uses Nb-Ti for the PF coils [7]. The surplus energy generated by ITER will not be used to generate electricity and a Q of 10 may not be enough for commercial fusion. Some of the states involved in ITER are already planning separate demonstration ('DEMO') reactors that will prove the commercial viability of fusion [9, 10, 11].

There are several ways to reach higher Q's. One is to reduce the 'aspect ratio' by reducing the major radius and increasing the minor radius, which makes the reactor more spherical. This allows the plasma to experience a greater magnetic field as it sits closer to the field coils. However, these so-called spherical tokamaks have much smaller central columns, which makes it difficult to fit in and adequately shield the CS coils and TF coil sections in the centre column. Another way to improve Q, motivated by Equation 2.6.1, is to use superconducting magnets that use high temperature superconductors with high B_{c2}'s and $J_{\mathrm{C},e}$'s, although this will result in higher reactor capital costs because these superconductors are still relatively expensive. One possible way to circumvent this, that is being pursued by private enterprises Tokamak Energy in the UK [12] and Commonwealth Fusion in the US [13, 26], is to build compact reactors whose production cycles are easier to upscale.

2.7 Concluding Comments

BCS theory explains the fundamental origins of superconductivity on a microscopic scale, but it struggles to explain some of the properties of more recently discovered superconductors such as the cuprates, that have high T_{C}'s. On the the other hand, the phenomenological Ginzburg-Landau theory describes the behaviour of superconductors in magnetic fields well. Flux pinning theories take the flux lattice in a superconductor and use it to explain how the pinning force on the fluxons determines the practical current carrying capacity of technological superconductors, known as the critical current. The critical current is arguably one of a superconductor's most important properties when deciding if it can be used in an application such as MCF. A deeper understanding of what limits the critical current will lead to significant improvements in fusion power output in MCF reactors, due to the strong scaling between the critical current and fusion power density. Future chapters will explore in more detail what limits the critical current.

Chapter 3

Factors that Limit J_C in Technological HTS

3.1 Introduction

As was seen in Chapter 2, the critical current densities of state-of-the-art inhomogeneous technological superconductors, including HTS, are much lower than the theoretical limit, the depairing current density J_D. This Chapter reviews three key mechanisms through which the J_C's of HTS can be suppressed - strain, grain boundaries in the superconductor, and current percolation caused by distributions of critical superconducting parameters in the superconductor. Section 3.2 reviews the effects of strain on J_C. Section 3.3 reviews the effects that grain boundaries have on J_C in technological HTS, and it also introduces Josephson Junctions, as Josephson Junction models of grain boundaries can be used to understand how the grain boundaries limit current flow. Section 3.4 reviews percolation theory, and how it has been used to understand current flow in superconducting materials. Finally, Section 3.5 gives some concluding comments.

3.2 The Effect of Strain on J_C

3.2.1 Overview

During operation, the superconductors in superconducting magnet systems are subjected to stresses and strains due to, for example, thermal contraction or hoop stresses from the interaction between the magnetic field and current. With the exception of Nb–Ti, technological superconductors are generally brittle compounds, so it is essential that the effects of strain on J_C are well understood.

When a superconductor is strained, J_C is generally *reversible* up to some value that is known as the irreversible strain limit, ε_{irr}. If a strain less than ε_{irr} is applied to a superconductor and then removed, J_C is unchanged. The same is not true when a strain greater than ε_{irr} is applied and removed. There is a permanent change (and usually a degradation) in J_C due to, for example, plastic deformation of the superconductor or surrounding materials such as copper [103, 104], or cracking or breaking of the superconductor [105, 106, 107]. There are various ways of defining ε_{irr}. Two common definitions for (RE)BCO tapes include retention criteria (the maximum strain at which I_C stays above a certain value) and recovery criteria (the maximum strain at which I_C recovers to a certain value when the strain is removed) [108, 109]. For (RE)BCO tapes, the exact values of ε_{irr} depend on the tape's manufacturer, as different manufacturers use different substrate materials and thicknesses [108, 109].

For (RE)BCO tapes in the reversible region, $J_C(\varepsilon_{app})$ can usually be parameterised using a simple parabolic relationship (see, e.g., [31]):

$$\frac{J_C(\varepsilon_{app})}{J_C(0)} = 1 - \beta_\varepsilon(\varepsilon_{app} - \varepsilon_{peak})^2 + \beta_\varepsilon\varepsilon_{peak}^2 \tag{3.2.1}$$

where β_ε is a field and temperature dependent constant and ε_{peak} is the strain at which $J_C(\varepsilon_{app})$ is maximised and it is also field and temperature dependent. Figure 3.1 shows a parabolic fit to $J_C(\varepsilon_{app})$ data using Equation 3.2.1 [110].

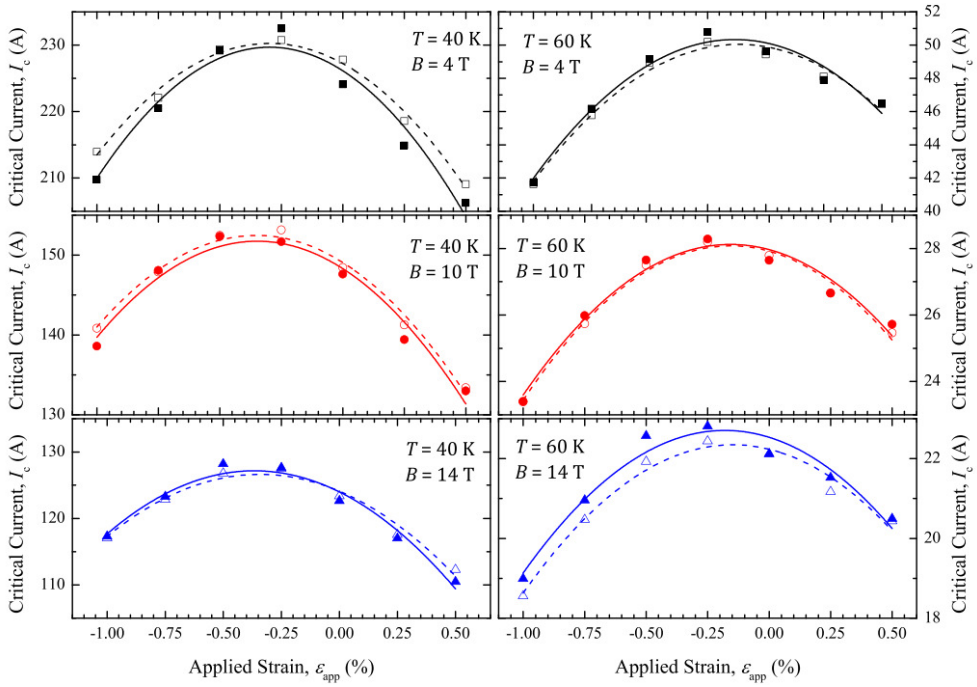

Figure 3.1: Experimental $I_C(\varepsilon_{app})$ data for a SuperPower Non-APC (Artificial Pinning Centres) tape, for different fields and temperatures. In all cases, the magnetic field was applied parallel to the *ab*-planes in the tape. The fits shown were obtained by fitting the data using Equation 3.2.1, [29]. The open data points (and dashed lines) were taken first, after which the field orientation was fully cycled. The closed data points (and solid lines) were then taken.

The flux pinning scaling laws outlined in Section 2.5 can also be used to parameterise the strain dependence of J_C for LTS and HTS. Polynomial [66] or exponential [111] expressions for the strain dependencies of T_C and B^*_{c2} are incorporated into Equation 2.5.3. This type of analysis has been used for decades for LTS such as Nb_3Sn (see Ekin's review [23, 24, 25]), but it does not explain why ε_{peak} strongly varies with magnetic field and temperature in (RE)BCO tapes [27, 29, 112]. A 1D Chain Model for J_C has been developed in the last few years to explain the field and temperature dependence of J_C [27, 29, 30, 31, 32], and is now outlined.

3.2.2 The 1D Chain Model for J_C

It is well known that for the (RE)BCO single crystals, the strain dependence of T_C is anisotropic [33, 113, 114, 115]. This anisotropy, combined with the fact that the

(RE)BCO layers of tapes have a twinned microstructure [116] with two distinct orientations for the domains, has been used to construct a 1D Chain Model for the strain dependence of J_C.

In the 1D Chain Model, a tape's (RE)BCO layer is treated as a 1D chain of domains. Given in the SuperPower tapes (investigated in this thesis and previously), the crystallographic axes of the microtwins are aligned either parallel or perpendicular to the tape's overall length direction, the domains are designated as type 'A' or type 'B'. A-domains have their crystallographic a-axis aligned with the overall tape length direction and B-domains have their b-axis aligned with the overall tape length direction, as shown in Figure 3.2. The broad approach in the Chain Model is to assume the strain dependence of T_C for each of the domains determines the strain dependence of the system.

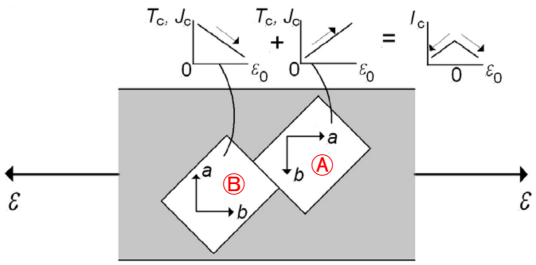

Figure 3.2: A and B domains in a (RE)BCO layer of a (RE)BCO tape, showing how opposite strain dependencies for A and B domains leads to competing behaviour and a peak in the strain dependence of I_C. Adapted from [30].

Given that that the strain dependence of T_C in a single crystal along its a-axis is approximately equal and opposite to that along its b-axis [33, 34], then the strain dependencies of the T_C's of the domains are given by:

$$T_{C,k}(\varepsilon_{JD}) = \begin{cases} T_{C,k}(0) + \left|\frac{dT_{C,k}}{d\varepsilon_{JD}}\right|_{\varepsilon_{JD}=0\%} \varepsilon_{JD}, & i = A \\ T_{C,i}(0) - \left|\frac{dT_{C,k}}{d\varepsilon_{JD}}\right|_{\varepsilon_{JD}=0\%} \varepsilon_{JD}, & i = B. \end{cases} \tag{3.2.2}$$

Here, $T_{C,k}$ corresponds to the critical temperature of the kth domain, $\left|\frac{dT_{C,k}}{d\varepsilon_{JD}}\right|_{\varepsilon_{JD}=0\%}$ is a constant, and ε_{JD} is the strain on a domain, defined as $\varepsilon_{JD} = \varepsilon_{app} - \varepsilon_{J_{C,A}=J_{C,B}}$ where ε_{app} is the applied strain and $\varepsilon_{J_{C,A}=J_{C,B}}$ is the strain at which the J_C's (and

T_C's) of the A- and B-domains are equal. To calculate the J_C of the 1D chain of domains, one must first use the $E - J$ power law [117]

$$\frac{E}{E_C} = \left(\frac{J}{J_C}\right)^N \tag{3.2.3}$$

where E_C is an electric field criterion, E is the electric field and N is a temperature, magnetic field and strain dependent constant, often referred to as the N-value or transition index in the literature. As the domains are in series, then

$$\left(\frac{J}{J_{C,1DC}}\right)^{N_{1DC}} = f\left(\frac{J}{J_{C,A}}\right)^{N_A} + (1-f)\left(\frac{J}{J_{C,B}}\right)^{N_B} \tag{3.2.4}$$

where $J_{C,1DC}$ and N_{1DC} are the J_C and transition index of the 1D chain of domains as a whole, f is the fraction of A-domains in the chain (so that $1 - f$ gives the fraction of B-domains), $J_{C,A}$ and $J_{C,B}$ are the J_C's of the A- and B-domains respectively and N_A and N_B are the transition indices of the A- and B-domains respectively.

The Chain Model has been used to parameterise $\varepsilon_{peak}(B,T)$. Branch *et al.* [27, 29] outlined a method to find an approximate analytic expression for $\varepsilon_{peak}(B,T)$ by assuming a linear, equal and opposite strain dependence for $J_{C,A}$ and $J_{C,B}$, assuming N_A and N_B are equal to each other (and N_{1DC}) at all strains, and taking a second order Taylor expansion of Equation 3.2.4 around ε_{JD}. The resultant expression for $\varepsilon_{peak}(B,T)$ is:

$$\varepsilon_{peak} = \varepsilon_{J_{C,A}=J_{C,B}} + \frac{2f-1}{f\,(1-f)}\frac{N_0}{g(B,T)\left[N_0\,(N_0+1) - 2S_N\,(N_0-1)\right]}. \tag{3.2.5}$$

Here, N_0 is the transition index of the whole chain (or tape) at zero strain and it is field and temperature dependent, $g(B,T)$ is an analytic expression that depends upon the chosen temperature and strain parameterisation of B^*_{c2}. Figure 3.3 shows a fit to experimental $\varepsilon_{peak}(B,T)$ data for a SuperPower SCS4050 Non-APC tape.

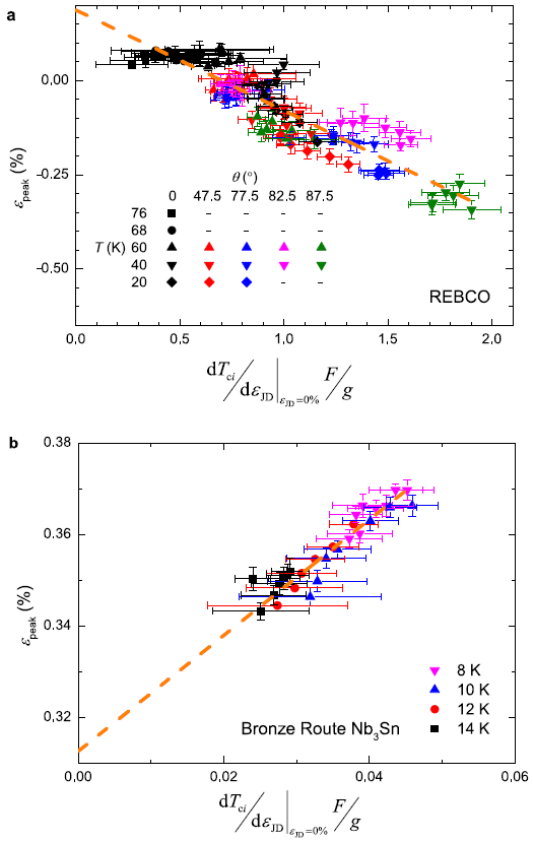

Figure 3.3: Fits for $\varepsilon(B,T)$ using Equation 3.2.5 for a SuperPower Non-APC tape and Nb_3Sn [27].

Although the chain model broadly fits the experimental $\varepsilon_{\text{peak}}(B,T)$ data well, it predicts that as $B \to 0$, $\varepsilon_{\text{peak}}(B,T) \to 0$ because $J_C \to 0$ for $p > 1$, which is an artefact of using Equation 2.5.3. The Chain Model also predicts that there is a discontinuity in the gradient of the strain dependence of T_C and B_{c2} for the tape at $\varepsilon_{JD} = 0$, because the probability density function for T_C and B_{c2} in the chain is a bimodal delta-function.

The Chain Model also fits $\varepsilon_{\text{peak}}(B,T)$ for Nb_3Sn and challenges the idea that Nb_3Sn can be thought of as unimodal material, with the peak in J_C occurring at some optimal strain where the Nb_3Sn lattice spacing leads to the highest values for some superconducting parameters such as T_C [27, 118, 119].

3.3 Effects of Grain Boundaries on J_C

3.3.1 Grain Boundaries in Technological HTS

Shortly after the cuprate HTS compounds were discovered, it was realised that polycrystalline cuprate samples had very low J_C values, due to poor current flow across the grain boundaries. Over the last 30 or so years, a huge amount of experimental work and theoretical work has been done to understand why high-angle grain boundaries limit J_C. A few key results of this work are presented here.
Figure 3.4 shows three simple examples of different grain boundaries.

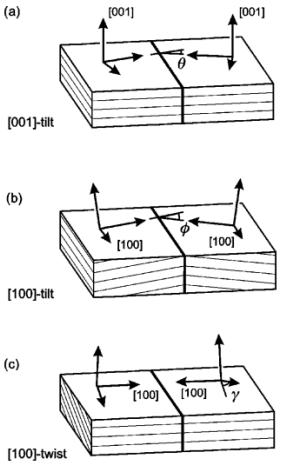

Figure 3.4: Three types of grain boundaries in a cubic material - two tilt and one twist boundary [20].

In tilt boundaries, the misorientation occurs around an axis that is parallel to the plane of the grain boundary. In the twist boundaries, the misorientations occur around one of the two orthogonal axes that are perpendicular to the plane of the grain boundary. Fabrication techniques have been developed that allow very long lengths of (RE)BCO tape to be made, in which the misorientation angles in the (RE)BCO layer are very small (typically less than 5°). At such grain boundaries, rather than a strained, continuous grain boundary being present, a chain of dislocations is present instead. Figure 3.5 shows a TEM micrograph of a low-angle

grain boundary [20, 120].

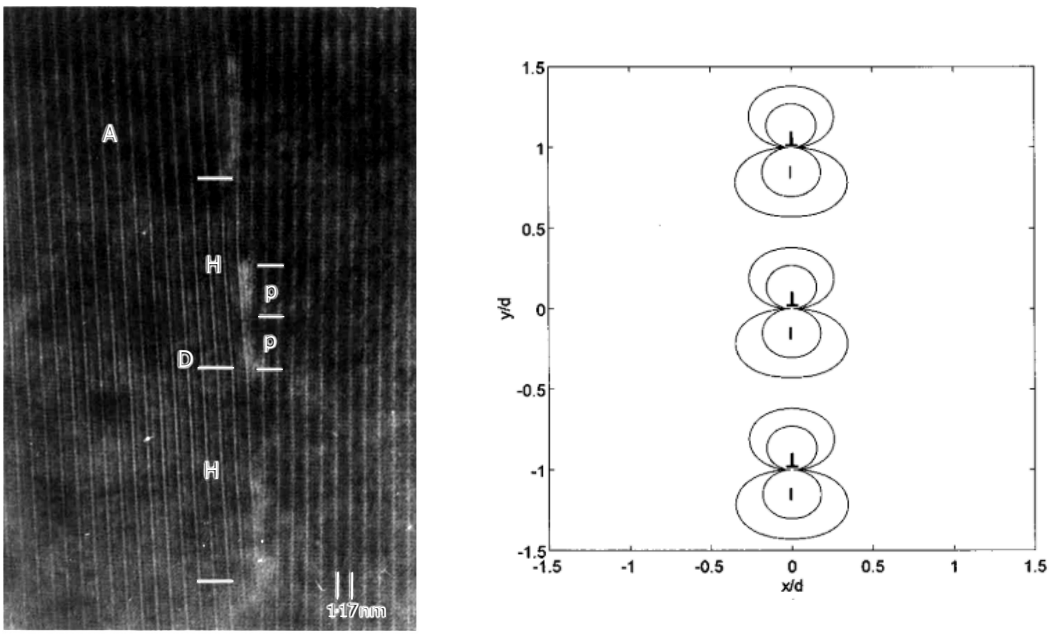

Figure 3.5: Left: TEM image of a 5° tilt boundary in bulk-processed $YBa_2Cu_3O_{7-\delta}$ [20, 120]. The boundary contains an array of dislocations (e.g., D) separated by a distance H. The length of 1.17 nm is the magnitude of the Burgers vector of the defect D. D has seperated into partial dislocations of characteristic dimension p. Right: predicted insulating and normal regions (denoted by inner and outer contours respectively), for Bi-2212, resulting from a 1D chain of dislocations along the boundary [121]. The boundary has a misorientation angle of 15°. d here corresponds to the distance between the centres of the equally spaced dislocations along the boundary.

Various models have been proposed to explain the effects these grain boundaries have on J_C and a comprehensive review has been published by Hilgenkamp [20]. J_C can be suppressed by mechanisms such as strain-field induced reductions of the superconducting order parameter (and Figure 3.5 shows an example of predicted strain-induced normal and insulating regions at a low angle grain boundary for Bi-2212) [19, 20, 121, 122, 123], distributions in critical superconducting parameters resulting from sub-optimal stoichiometry in the grain boundary [20, 124, 125], and reductions due to the $d_{x^2-y^2}$ symmetry of the order parameter [20, 126].

3.3.2 SNS Josephson Junctions

Josephson junction models can be used to explain how supercurrents tunnel through a barrier such as a grain boundary. By considering the wave functions on either side of the barrier, and solving the Schrödinger equations for the wave functions, one can derive the Josephson equations [127, 128]:

$$I = I_{\mathrm{C}} \sin(\phi_J) \tag{3.3.1}$$

$$\frac{\partial \phi_J}{\partial t} = \frac{2eV}{\hbar} \tag{3.3.2}$$

where ϕ_J is the phase difference of the order parameter across the barrier and V is the voltage across the barrier. These equations describe the evolution of the current and phase difference across the junction with time. More complicated Josephson Junction models have been developed to describe the current flow characteristics of junctions when they contain no fluxons, in both low and high fields [129, 130, 131]. These models offer fairly low utility for parameterising $J_{\mathrm{C}}(B, T, \varepsilon)$ in the parameter space relevant for high-field applications such as fusion, where there are likely to be many fluxons in the junction. To address this, a new high-field expression for J_{C} has been developed for arbitrarily wide junctions where there are many fluxons in the junction [132, 133]. This model is discussed in more detail in Chapter 5.

3.4 Current Percolation

Percolation theory is used to explain how the properties of a network change when nodes and/or links between nodes are added or removed. It is a mathematical theory and concept that has been adopted in a huge range of disciplines. Applications of percolation theory include: modelling the spread of disease [134], the spread of opinions through communities [135], forest fires [136], and mass bankruptcies in a financial crisis [137], as well as more 'physical' phenomena such as the spread of

liquids through porous media [138] and electrical current flow through a material [139].

3.4.1 Basic Theory

The two common types of percolation model are 'bond percolation' and 'site percolation'. Bond models contain a fixed number of sites (nodes) and the properties of the network are investigated when bonds are added or removed between sites. Likewise, site models contain a fixed number of bonds (links) and sites are added or removed. Figure 3.6 shows the effects of removing a bond and site from a bond and a site percolation model respectively. As shown in the Figure, removing a site can have a greater impact on the overall connectivity of the network compared to removing a bond, which is why site models tend to have higher *percolation thresholds*. The percolation threshold p_c is the minimum fraction of bonds or sites that must be present in order for a network spanning cluster of bonds or sites to exist, when bonds are added or removed at random. Its value heavily depends on the coordination number z of the network. The coordination number characterises the number of adjacent sites or bonds to a particular site or bond when all possible sites or bonds are present. Table 3.1 gives the value of the bond p_c for several network types found in the literature.

3.4.2 Percolation in Resistor-Insulator Networks

One of the first applications of percolation theory was the treatment of electrical current flow in resistor networks when resistors (i.e. bonds) were added or removed. In these models, a missing resistor can be treated as an insulating bond. Early experimental results on sheets of conducting colloidal graphite paper indicated that just above the percolation threshold, when the fraction of resistive bonds p_r is just enough to cause a system spanning network of resistive bonds to form, the effective

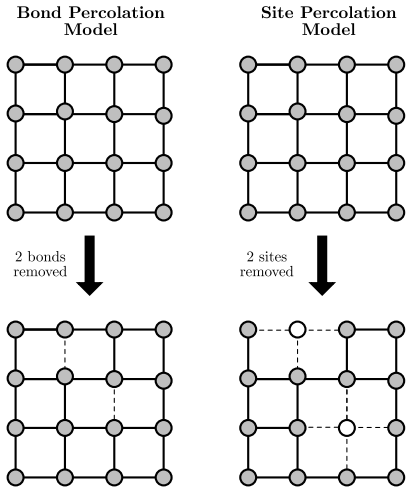

Figure 3.6: Left: the effect of removing 2 bonds in a bond percolation model. Right: the effect of removing 2 sites in a site percolation model

Table 3.1: Percolation thresholds for different networks

Network Type	Representation	Bond Percolation Threshold p_c
1D chain		1
2D honeycomb	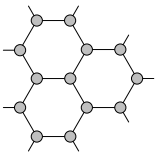	$1 - 2\sin\left(\frac{\pi}{18}\right) = 0.653$ [140]
2D square	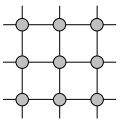	$\frac{1}{2}$ [140]
2D triangular	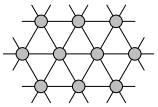	$2\sin\left(\frac{\pi}{18}\right) = 0.347$ [140]
3D simple cube	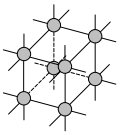	~0.247 [141]
Bethe ($z = 3$)	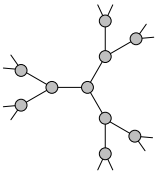	$\frac{1}{2}$ ($\frac{1}{z-1}$ in general) [142, 143]

conductivity of the network σ^{Net} remains limited as p_r increases, as the network spanning cluster is a tortuous path with many dead-ends and weak-links. Around the same time, the first computational results for $\sigma^{Net}(p_r)$ were produced and similar phenomena were found, regardless of the coordination number and dimensions of the network [139]. Figure 3.7 shows some of these early computational results from Kirkpatrick [139].

In general, there are no exact analytic treatments of percolation in resistor-insulator networks that lead to an accurate description of $\sigma^{Net}(p_r)$ in the range $p_c \leq p_r \leq 1$, except for very simple networks such as a 1D chain of resistors. However, Effective Medium Theory (EMT) describes the behaviour close to $p_r = 1$ very well [139]. By considering the change in the local and external electric field when a resistor is removed from a network that has a voltage applied to it, one is able to derive [139, 144]:

$$\sigma^{Net} = \sigma^{Net}(p_r = 1)\frac{p_r - p_c}{1 - p_c} \tag{3.4.1}$$

Similarly, close to $p_r = p_c$, the effective conductivity of the network σ^{Net} can be described using

$$\sigma^{Net} = \sigma^{Net}(p_r = 1)\left(\frac{p_r - p_c}{1 - p_c}\right)^{t_p} \tag{3.4.2}$$

where t_p is a constant with a typical value of $\frac{3}{2}$ for both 2D and 3D networks.

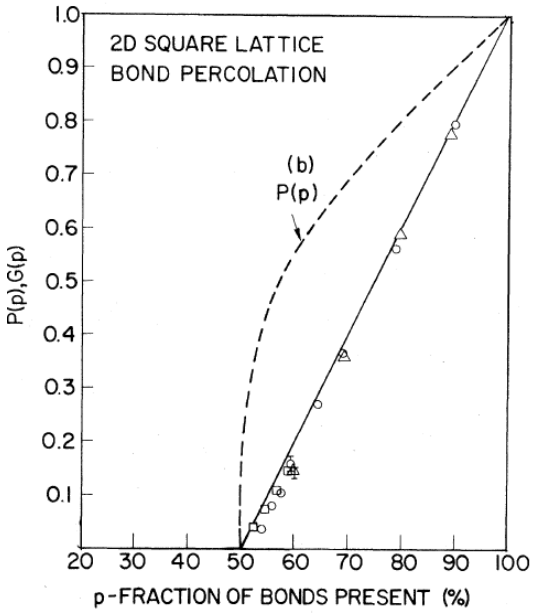

Figure 3.7: The probability that a resistive bond will belong to the system spanning cluster ($P(p_r)$) and the effective conductivity of the network $G(p_r)$ (i.e., $\sigma^{Net}/\sigma^{Net}(p_r = 1)$) for a 2D square lattice. The solid line is an EMT fit to the computational scatter data for $G(p_r)$ [139].

3.4.3 Percolation in Superconducting Materials

Percolation theory has been used to explain a variety of phenomena in superconducting materials. Two examples from the literature are discussed here.

Markiewicz and Tóth modelled the resistive transition to the normal state in polycrystalline Nb_3Sn using a finite element analysis (FEA) based percolation model, in which the fraction of superconducting material is gradually increased from 0 upwards [145]. Their model results suggested that $\approx 15\% - 35\%$ of the material needed to be superconducting in order for the effective resistivity of the material to reach zero, which is common for 3D networks, as shown in Table 3.1. They then modelled the resistive transition of the material from $p_{sc} = p_c$ to $p_{sc} = 1$ using an empirical form $\sigma^{Net} = C_1 \exp\left(-C_2/\left(p_{sc} - C_3\right)\right)$ where p_{sc} is the superconductor fraction and the C's are constants, along with a normal distribution of T_C, for four superconductors with different compositions investigated in the FEA model. Figure 3.8 shows the results from their empirical model.

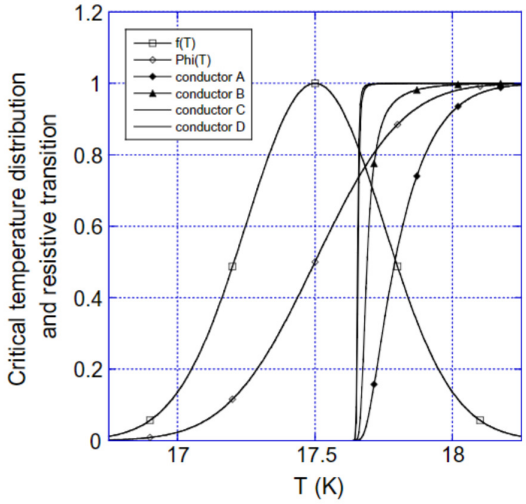

Figure 3.8: The probability density function Phi(T) and cumulative distribution function f(T) for a normal distribution of T_C, for 4 different conductors [145].

The resistive transition broadens as more normal components such as copper are added to the model. Although this model may be useful in analysing the resistive transition of a Nb_3Sn strand, it cannot be used to model J_C and it does include the possible bimodal nature of $T_C(\varepsilon)$ for Nb_3Sn [27].

Eisterer *et al.* have also created a percolation model to calculate the J_C of polycrystalline MgB_2 superconductors [94, 146]. They argued that because grain boundaries do not limit the current flow in MgB_2, a distribution of grain orientations and anisotropic B^*_{c2} is responsible instead. To calculate J_C, they used

$$J_C(B) = \int_0^{J_C^{Max}(B)} \left(\frac{p_{sc}(J) - p_c}{1 - p_c} \right)^t \mathrm{d}J \tag{3.4.3}$$

where J_C^{Max} is the J_C of the element that completes the system spanning superconducting cluster at $p_{sc} = p_c$, and t is a constant that is $\approx 1 - 2$. In this model, J is ramped from 0 until J exceeds the J_C of an element. The excess current density is then shared between the other elements. This process continues as J is ramped further until all elements carry currents at their J_C values. The overall J_C of the material is the value of J at which this occurs. Figure 3.9 shows fits to different MgB_2 samples using the model and Figure 3.10 shows how the fit parameters p_c and the B^*_{c2} anisotropy factors vary with temperature. The fact that these para-

meters vary with temperature suggests that a distribution of T_C is also limiting J_C. The model also assumes that the $E - J$ transition index N for each element is infinite. This may not be appropriate for (RE)BCO at higher temperatures and fields.

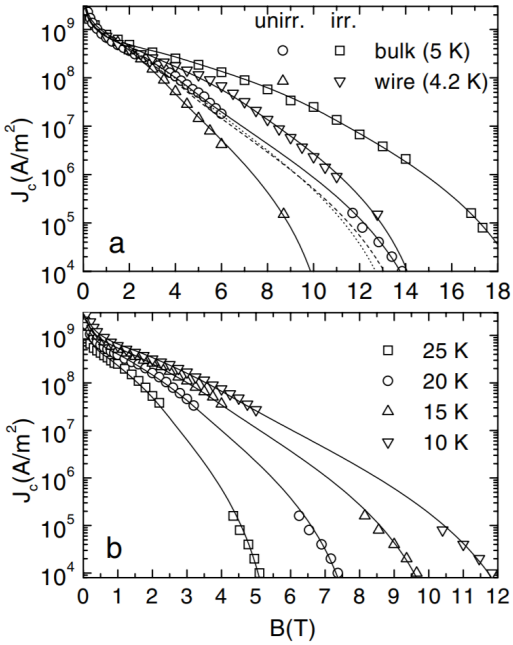

Figure 3.9: Fits to J_C data using Equation 3.4.3 for unirradiated and neutron irradiated MgB_2 samples. The top panel shows fits at low temperatures for bulk and wire samples and the bottom panel shows fits at higher temperatures for bulk samples [94].

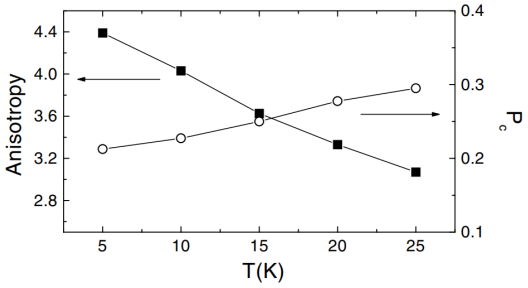

Figure 3.10: The temperature dependence of the anisotropy factor of B^*_{c2} and percolation threshold for a bulk MgB_2 sample [94].

3.5 Conclusion

A comprehensive model of J_C that takes into account the effects of strain, competing domains, grain boundaries and percolation is needed to understand properly what is limiting the performance of state-of-the-art HTS. On the whole, the rest of this thesis is dedicated to the development of such a model, along with the necessary experimental validation.

Chapter 4

The In-plane, Biaxial Strain Dependence of J_C of a (RE)BCO Coated Conductor at 77 K in Low Fields

4.1 Introduction

For quite a few years, it has been possible to measure the uniaxial strain dependence of J_C for (RE)BCO tapes, in both tension and compression, when the strain is applied along the tape [147, 148]. However in practice, tapes are subjected to three-dimensional strains (i.e. from multiple directions) during cable fabrication and operation. For example, CORC® (Conductor-On-Round-Core) cables [149, 150], which consist of HTS tapes helically wound onto a copper core, are subjected to axial, transverse and shear strains in fusion magnet systems [151]. HTS Roebel cables are also subjected to multiaxial strains, due to the discontinuties across the width of the cable [36].

Multiphysics models are used to predict the electrical performance of HTS magnets during operation. If the multiaxial strain dependence of J_C is known, then the

designs of magnets and the cables and tapes they are wound from can be optimised. Therefore, there is a need to develop experimental techniques and mathematical models to measure and explain the multiaxial strain dependence of J_C.

The strain dependence of J_C is well understood when the strain is applied along the length of the tape [27, 29, 31, 30, 112, 152, 99, 153, 154], and for strains less than the irreversible strain limit ε_{irr} this can be described quite well using the 1D Chain Model as outlined in Section 3.1. However, there have not been many studies on the effect of strain on J_C when the strain is applied along another direction [35, 36, 37, 38], and even fewer studies on the effect of strain when it is applied along multiple directions *simultaneously* [35]. In this chapter, we describe a new 2D sample holder, known as a 'Crossboard', that is capable of applying biaxial strains to a HTS tape in the plane of the tape, along with some experimental results and analysis for $J_C(B, \varepsilon_{xx}, \varepsilon_{yy})$, where ε_{xx} is the applied strain along the tape length and ε_{yy} is the applied strain orthogonal to the tape length, in the plane of the tape. This work has been published in two recent papers by the author of this thesis [155, 156]. This chapter also outlines another 2D sample holder known as a 'Strutted Springboard' that is capable of varying the 2D strain state of a tape *in-situ*, and an accompanying probe that is capable of supplying currents on the order of 10^3 A to a tape. This sample holder and probe will be used in future work in Durham.

Section 4.2 details the design of the Crossboard and some mechanical finite element simulations for its strain distribution under applied loads. Section 4.3 details the experimental setup used to measure $J_C(B, \varepsilon_{xx}, \varepsilon_{yy})$ in low fields at 77 K. Section 4.4 outlines the experimental results and extends the 1D Chain Model analysis for the $J_C(B, \varepsilon_{xx}, \varepsilon_{yy})$ data to consider samples strained with independent control of strain in two directions in the plane of the tape. Section 4.5 outlines the Strutted Springboard, associated high current probe and some preliminary results. Section 4.6 gives a discussion of all the results in the chapter and Section 4.7 gives some conclusions.

4.2 Crossboard Design

The Crossboard is a biaxial, cruciform shaped sample holder onto which (RE)BCO tapes can be soldered. Cu-Be alloy Berylco 25 was chosen as the Crossboard material due to its high elastic strain range and good solderability [157]. Figure 4.1 shows the design of the Crossboard and the equipment used to apply strain to it. Stainless steel grippers with teeth are used to hold the Crossboard in place. M2 nuts and bolts are used to bend the wings of the Crossboard up or down around the teeth, which strains the Crossboard. By bending the wings of the Crossboard in this way, arbitrary combinations of x-strain and y-strain can be generated at the centre of the board. In other words, the possible combinations of x- and y-strain are not constrained by the Poisson ratio of the Berylco. The strain homogeneity at the centre of the Crossboard was optimised iteratively using mechanical Finite Element Analysis (FEA) software within Autodesk Inventor [158]. Figure 4.2 shows the results of an FEA simulation when forces of 1800 N were applied to the four points shown by the arrows. The values of ε_{xx} and ε_{yy} at the centre of the board were 0.48% and -0.48% respectively. The effective Poisson ratio of the board when only 2 opposite wings are bent in the same direction was $\nu_{\varepsilon,eff} \approx -0.42$.

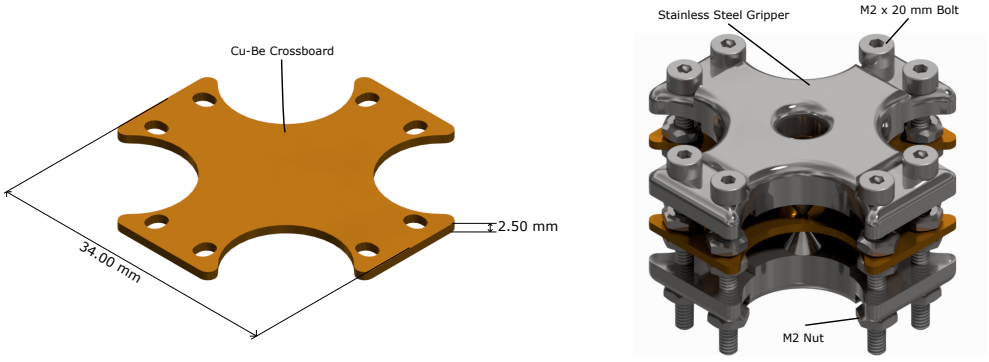

Figure 4.1: Left: a 3D Model of the Crossboard. Right: a 3D Model of the Crossboard, along with the stainless steel grippers, nuts and bolts used to apply strain to the Crossboard.

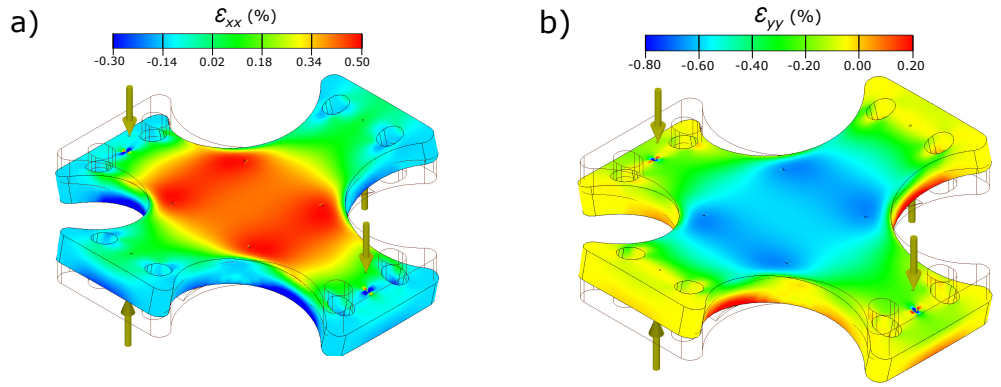

Figure 4.2: FEA results for a) the applied x-strain distribution and b) the applied y-strain distribution when the wings are bent.

4.3 Experimental Setup

Current transport measurements of $J_C(B, \varepsilon_{xx}, \varepsilon_{yy})$ have been performed on multiple SuperPower APC SCS4050 tape samples [159] in low fields at 77 K. The experimental setup is shown in Figure 4.3 and summarised below:

A 24 mm long and 4 mm wide (RE)BCO tape was soldered substrate side-down onto the centre of the Crossboard using Pb-Sn solder. Voltage taps and current leads were soldered onto the top surface of the tape. A HBM 1-XY91-1.5/120 2D T-rosette strain-gauge [160] was then glued on top of the tape, in between the voltage taps, at the centre of the Crossboard. The Crossboard was then placed within the grippers and strained at ambient temperature using the nuts and bolts. A Lakeshore Model 121 low-noise current source supplied current to the strain gauge, and the voltages were recorded and converted into ε_{xx} and ε_{yy} values. The Crossboard was then attached to the end of a probe and placed in an open liquid nitrogen bath that was surrounded by a water cooled electromagnet that provided a static, homogeneous magnetic field of up to 0.7 T. After the sample had reached 77 K (which was verified by monitoring the voltages from the strain gauge), the strain gauge voltages were recorded (with the magnetic field switched off) and the voltages converted into ε_{xx} and ε_{yy} values.

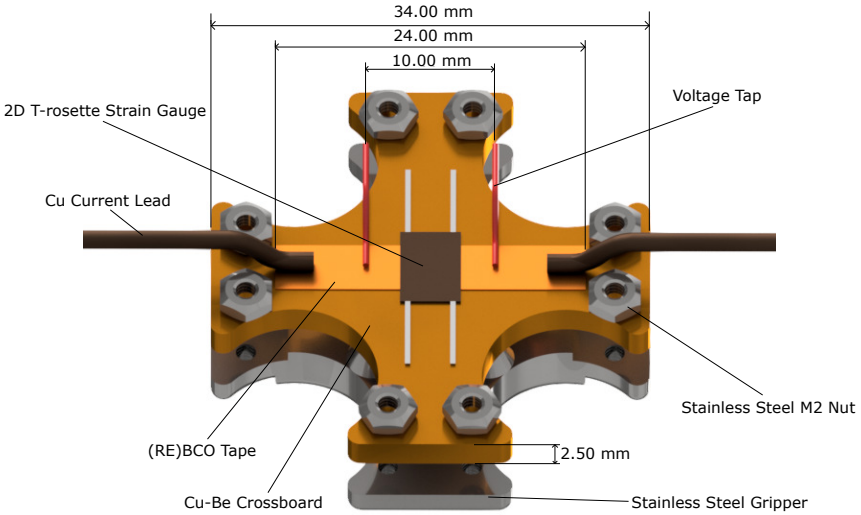

Figure 4.3: The experimental setup used to measure $J_C(B, \varepsilon_{xx}, \varepsilon_{yy})$. The liquid nitrogen bath, electromagnet, M2 bolts, some of the M2 nuts and one of the stainless steel grippers are not shown.

Before each sample was cooled to 77 K for the very first time, no strain was applied at ambient temperature. This was done by ensuring that the M2 nuts and bolts were loose. That way, the strain gauge voltages corresponding to zero applied strain at both ambient temperature and 77 K could be recorded.

The background magnetic field was applied perpendicular to the direction of current flow in the tape. The J_C measurements were performed with the field aligned parallel to the tape plane (0°) and perpendicular to the tape plane (90°).

After the $J_C(B, \varepsilon_{xx}, \varepsilon_{yy})$ measurements were taken for a single combination of x- and y-strain, the Crossboard was warmed back to room temperature and a new combination of x- and y-strains were then applied.

4.4 Results and 1D Chain Model Analysis

Table 4.1 summarises the 3 samples measured in this work, and the types of strain that were applied to each sample. All three samples were taken from the same spool of SuperPower APC SCS4050 APC tape. In total, 6 datasets were collected across the 3 samples. The datasets are labelled in chronological order. For example

Dataset VI was taken after Dataset V, which was taken after Dataset IV, and so on.

Table 4.1: The datasets collected for each sample.

Sample	Year Measured	Datasets Collected
A	2017	I
B	2017	II, III
C	2018	IV, V, VI

Figure 4.4 shows the strains that were applied to the tape for each of the 6 datasets. A linear fit of the form $\varepsilon_{yy}(\varepsilon_{xx}) = \frac{\mathrm{d}\varepsilon_{yy}}{\mathrm{d}\varepsilon_{xx}}\varepsilon_{xx} + \varepsilon_{yy}(\varepsilon_{xx} = 0\%)$ was performed for each dataset and Table 4.2 contains the resultant fit parameters.

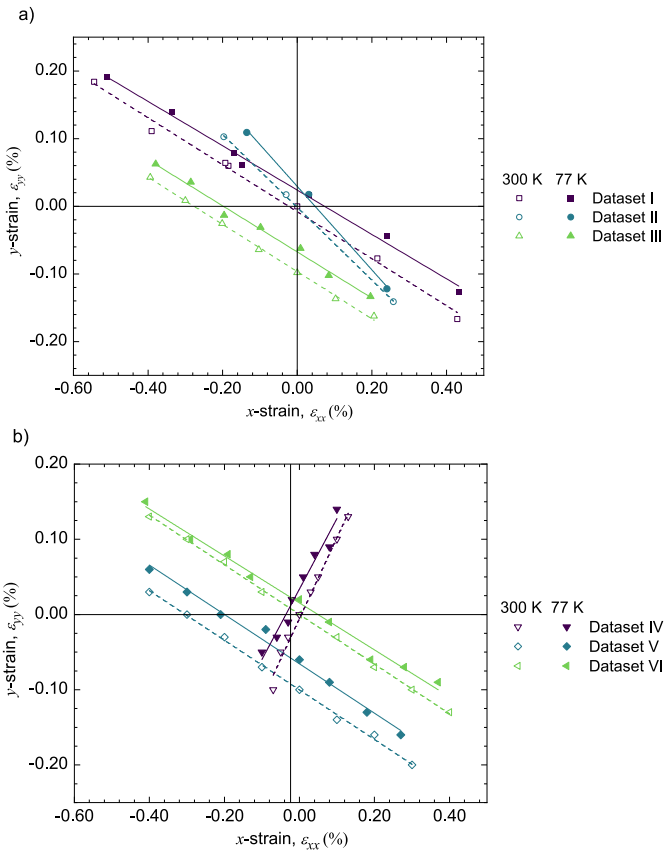

Figure 4.4: a) The strains that were applied to (RE)BCO tape samples A and B (Datasets I-III). b) The strains that were applied to (RE)BCO tape sample C (Datasets IV-VI).

Table 4.2: The fit parameters for the linear fits of $\varepsilon_{yy}(\varepsilon_{xx})$ in Figure 4.4.

Dataset	Temperature (K)	$\frac{d\varepsilon_{yy}}{d\varepsilon_{xx}}$	$\varepsilon_{yy}(\varepsilon_{xx}=0\%)$ (%)
I	300	-0.35 ± 0.01	-0.008 ± 0.004
	77	-0.33 ± 0.01	0.024 ± 0.003
II	300	-0.54 ± 0.01	-0.002 ± 0.002
	77	-0.62 ± 0.03	0.029 ± 0.005
III	300	-0.349 ± 0.007	-0.097 ± 0.002
	77	-0.34 ± 0.01	-0.068 ± 0.003
IV	300	1.03 ± 0.02	-0.002 ± 0.001
	77	0.94 ± 0.01	0.034 ± 0.006
V	300	-0.330 ± 0.007	-0.100 ± 0.002
	77	-0.33 ± 0.02	-0.066 ± 0.004
VI	300	-0.330 ± 0.007	0.000 ± 0.001
	77	-0.31 ± 0.01	0.015 ± 0.003

Figure 4.5 shows $E-J$ plots for different strains taken from Dataset III. To calculate the values of J (and J_C) from the raw current data, it was assumed that the (RE)BCO layer had a thickness of 1 µm. J_C was extracted from fits to the $E-J$ data that used Equation 3.2.3, with the criterion of E_C =100 µV m^{-1}.

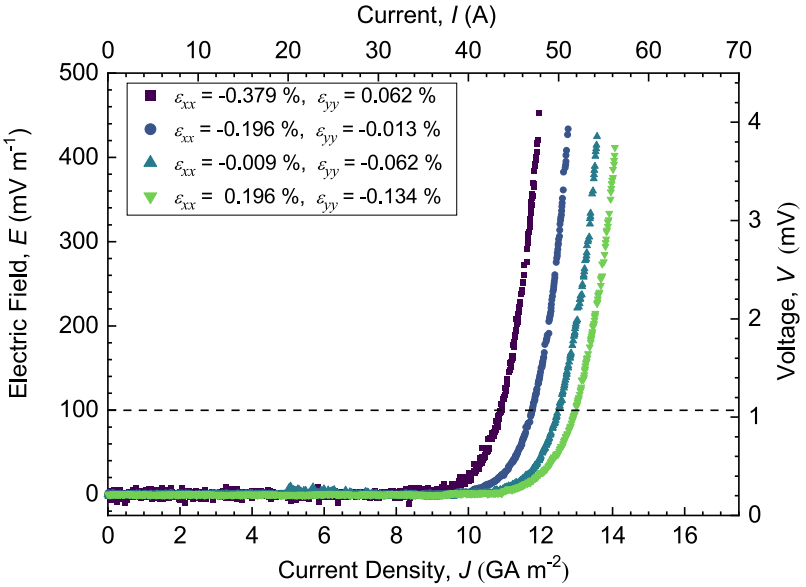

Figure 4.5: $E-J$ plots for four different strains from Dataset III. The applied magnetic field was 0.2 T and was parallel to the tape normal.

Figure 4.6 shows plots for J_C as a function of strain for Datasets I-III. In Dataset I, strain was applied along the x-axis of the tape (i.e. its length direction). In

Dataset II strain was applied along the y-axis of the tape (i.e. its width direction). In Dataset III a strain was first applied along the y-direction and then x-strain was applied. Although data have only been plotted for 3 different magnetic fields and a single field orientation, data were obtained for 0.1 T, 0.2 T, 0.4 T, and 0.6 T and other field orientations too. The values of J_C for Dataset III were reduced by 7% because the in-field, zero strain values for J_C were 7% higher for this tape (sample B) compared to the tape measured for Datasets I and II (sample A).

The J_C data were fit using Equation 3.2.1 with ε_{app} set to ε_{xx} and ε_{peak} set to $\varepsilon_{xx,peak}$. The results of these fits are shown in Table 4.3.

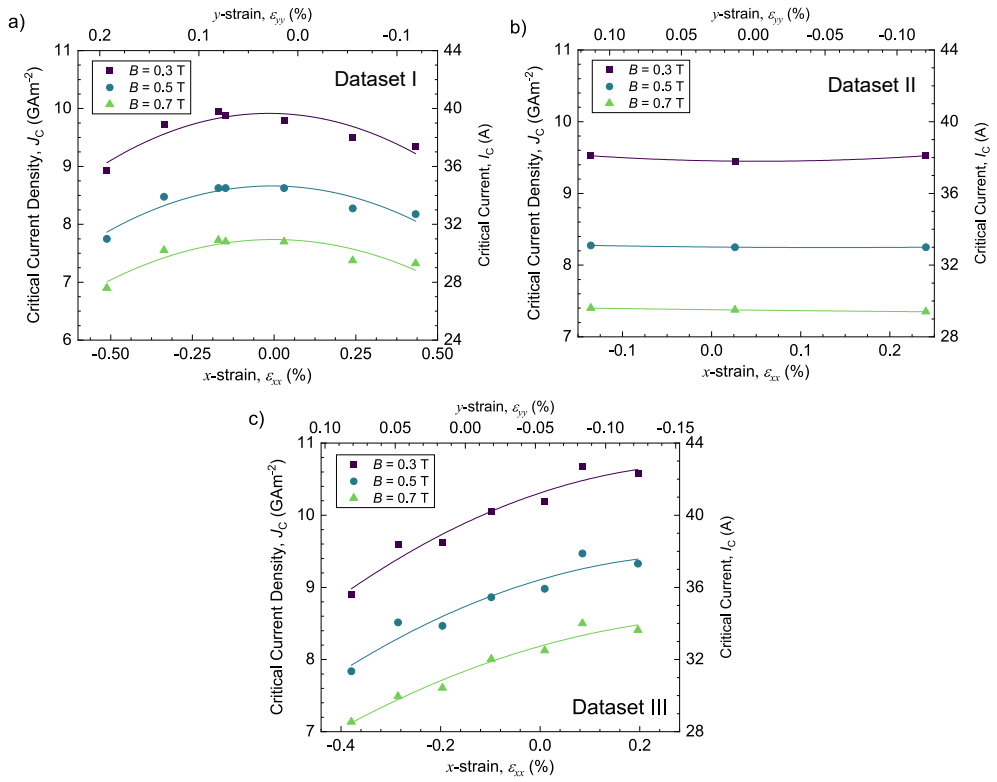

Figure 4.6: a) The strain dependence of J_C for Dataset I. b) The strain dependence of J_C for Dataset II. c) The strain dependence of J_C for Dataset III. For all data in this Figure, the magnetic field was applied parallel to the tape normal. The ε_{yy} coordinates were calculated using the linear fits shown in Figure 4.4 and listed in Table 4.2.

Table 4.3: Fit parameters associated with the parabolic fits for the J_C data in Figure 4.6 for $B = 0.5$ T. The values of $\varepsilon_{yy,\text{peak}}$ were calculated using the linear fits shown in Figure 4.4 and listed in Table 4.2.

Dataset	$\varepsilon_{xx,\text{peak}}$ (%)	$\varepsilon_{yy,\text{peak}}$ (%)	$J_C(\varepsilon_{xx,\text{peak}})$ GAm^{-2}
I	−0.01	0.03	8.65
II	0.1	−0.03	8.3
III	0.4	−0.2	9.61

Figure 4.7 shows J_C as a function of strain for Datasets IV-VI, which were all taken on sample C. In Dataset IV, both x- and y- strains were applied so that the strain data lay approximately on the $\varepsilon_{yy} = \varepsilon_{xx}$ line. In Dataset V, strain was applied along the x-axis of the tape, and in Dataset VI a strain was first applied along the y-direction and then x-strain was applied. Although the data presented here are only for four different magnetic fields and a single field orientation, data were obtained for 0.2 T, 0.4 T, and 0.6 T and other field orientations too (not shown).

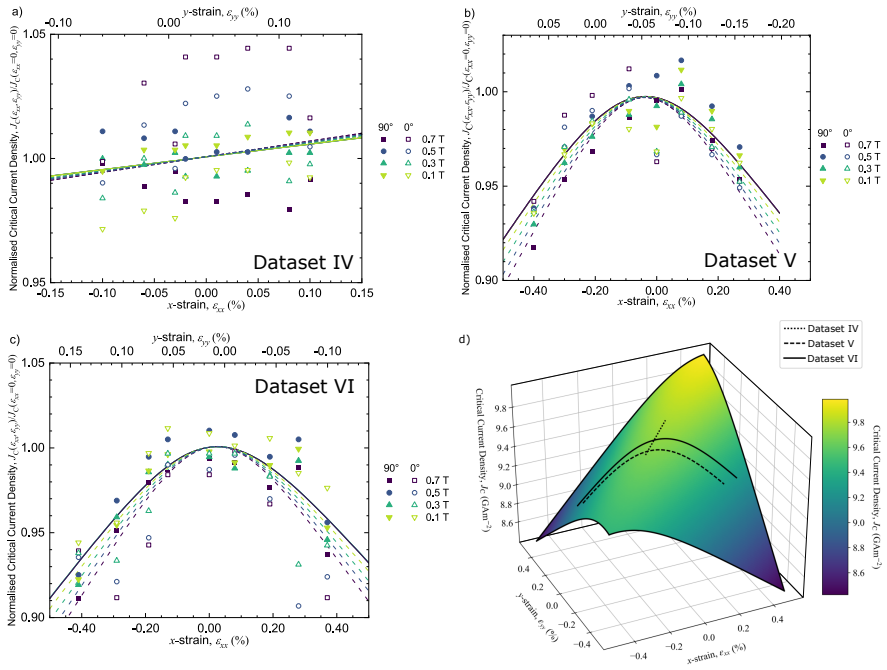

Figure 4.7: a) The strain dependence of J_C for Dataset IV. b) The strain dependence of J_C for Dataset V. c) The strain dependence of J_C for Dataset VI and d) a surface plot for the Chain Model fit for the $B = 0.5$ T data. For all data in this Figure, the magnetic field was applied parallel to the tape normal. The ε_{yy} coordinates in a)-c) and the values of $\varepsilon_{yy,\text{peak}}$ were calculated using the linear fits shown in Figure 4.4 and listed in Table 4.2.

The 1D Chain Model outlined in Chapter 3 has been extended to incorporate biaxial strains (with independent control of strain in two directions), so that the J_C data for Datasets IV-VI can be analysed. As with the standard Chain Model, it is assumed that the (RE)BCO layer can be represented by a 1D chain of A- and B-domains that have their crystallographic a- and b-axes aligned with the length direction of the tape respectively. The J_C of the chain can be calculated by rearranging Equation 3.2.4 to give

$$J_C = \left[f J_{C,A}^{-N} + (1-f) J_{C,B}^{-N} \right]^{-\frac{1}{N}} . \tag{4.4.1}$$

To arrive at this expression, it was assumed that $N_{1DC} = N_A = N_B$. This is a reasonable assumption for this work because the experimental values of N extracted from the $E-J$ data for this work were broadly independent of field and strain and had a value of ≈ 18. The J_C's of the A- and B-domains are calculated using the engineering scaling law [27, 29, 91, 161, 162]

$$J_{C,k} = A \left[B^*_{c2,k} \right]^{n-3} b_k^{*p-1} (1-b_k^*)^q \, T^{*2}_{C,k} \left(1 - t_k^{*2} \right)^2 , \tag{4.4.2}$$

where k is either A or B, A, p, q and n are constants, $B^*_{c2,k}$ is the effective upper critical magnetic field of domain type k, b_k^* is the reduced magnetic field $B/B^*_{c2,k}$, $T^*_{C,k}$ is the effective critical temperature of domain type k, and t_k^* is the reduced temperature $T/T^*_{C,k}$. For this work, n was fixed at 2.5 [60, 163]. The temperature and strain dependence of $B^*_{c2,k}$ is parameterised using [27, 29, 91, 161]

$$B^*_{c2,k}(T, \varepsilon_{xx}, \varepsilon_{yy}) = B^*_{c2}(0,0,0) \left(\frac{T^*_{C,k}(\varepsilon_{xx}, \varepsilon_{yy})}{T^*_C(0,0)} \right)^w (1-t^*)^s . \tag{4.4.3}$$

$B^*_{c2,k}(0,0,0)$ is fixed at 98.7 T for measurements where the magnetic field is parallel to the tape normal and 185 T for measurements where the magnetic field is parallel to the tape plane [27, 29, 164]. $T^*_C(0,0)$ is fixed at 90.1 K [164, 113], w is fixed at 2.2 [27, 29, 91] and s is fixed at 1.26 [27, 29]. Single crystal measurements show that the strain dependencies of the critical temperatures of the domains along any of the

principle axes are linear [33, 34, 113]. Therefore their biaxial strain dependencies can be given by

$$T^*_{\mathrm{C,A}}(\varepsilon_{xx},\varepsilon_{yy}) = T^*_{\mathrm{C}}(0,0)\left[1 + g_{\mathrm{A}}\left(\varepsilon_{xx} - \varepsilon_{xx0}\right) + g_{\mathrm{B}}\left(\varepsilon_{yy} - \varepsilon_{yy0}\right)\right] \tag{4.4.4}$$

and

$$T^*_{\mathrm{C,B}}(\varepsilon_{xx},\varepsilon_{yy}) = T^*_{\mathrm{C}}(0,0)\left[1 + g_{\mathrm{B}}\left(\varepsilon_{xx} - \varepsilon_{xx0}\right) + g_{\mathrm{A}}\left(\varepsilon_{yy} - \varepsilon_{yy0}\right)\right], \tag{4.4.5}$$

where $g_{\mathrm{A}} = \left(\partial T^*_{\mathrm{C,A}}/\partial\varepsilon_{xx}\right)_{\varepsilon_{yy}=0} = \left(\partial T^*_{\mathrm{C,B}}/\partial\varepsilon_{yy}\right)_{\varepsilon_{xx}=0}$ and $g_{\mathrm{B}} = \left(\partial T^*_{\mathrm{C,B}}/\partial\varepsilon_{xx}\right)_{\varepsilon_{yy}=0} = \left(\partial T^*_{\mathrm{C,A}}/\partial\varepsilon_{yy}\right)_{\varepsilon_{xx}=0}$ are the sensitivities of a domain's T^*_{C} when there are only strains along the a- or b-axes respectively (i.e., when strains resulting from Poisson's ratio are not included). The strains ε_{xx0} and ε_{yy0} represent pre-strains that may be induced in the (RE)BCO layer due to differential thermal contraction of the different tape layers during fabrication and cooldown [27, 29, 165, 116]. For this work, it is assumed that the pre-strain is isotropic and if there is no applied strain along any direction, $T^*_{\mathrm{C,A}} = T^*_{\mathrm{C,B}} = T^*_{\mathrm{C}}(0,0)$, so ε_{xx0} and ε_{yy0} can be set to zero.

A global fit was performed to all $J_{\mathrm{C}}(B,\varepsilon_{xx},\varepsilon_{yy})$ data for Datasets IV-VI, for both $\theta = 90°$ and $\theta = 0°$, using non-linear least squares fitting. The prefactor A in Equation 4.4.2 was allowed to vary between datasets and field orientations so that a good fit could be obtained. The constants p and q were also set to be free (had different values) for different field orientations. The parameters f, g_{A} and g_{B} were set to be independent of the field orientation because they are determined by the microstructure of the tape. The resultant fit parameters are given in Table 4.4, and the lines of best fit are shown in Figure 4.7. The Figure also shows a surface plot for $J_{\mathrm{C}}(\varepsilon_{xx},\varepsilon_{yy})$ generated using the fit parameters in Table 4.4, that is shaped like a ridge. The fit lines for Datasets IV-VI are also shown in the surface plot. The fit line for Dataset IV lies along the top of the ridge, whereas the fit lines for Datasets V and VI pass over the top of the ridge and exhibit parabolic behaviour.

Table 4.4: Fit parameter values from the global fit to the J_C in Datasets IV-VI.

Parameter	Value	
	$\theta = 90°$	$\theta = 0°$
f	0.49 ± 0.03	
g_A ($K\%^{-1}$)	1.8 ± 0.1	
g_B ($K\%^{-1}$)	-1.3 ± 0.1	
p	0.706 ± 0.006	0.674 ± 0.006
q	0.0 ± 0.2	5.8 ± 0.3
A_{IV} ($MAm^{-2}T^{0.5}K^{-2}$)	20.0 ± 0.5	23.2 ± 0.7
A_V ($MAm^{-2}T^{0.5}K^{-2}$)	20.5 ± 0.5	23.2 ± 0.7
A_{VI} ($MAm^{-2}T^{0.5}K^{-2}$)	21.5 ± 0.5	23.6 ± 0.7

4.5 Design of a New Biaxial High Current Strain Probe and Sample Holder

As shown in later chapters, one of the outcomes of the research in this doctoral thesis is the requirement for a high current probe capable of measuring currents up to 2 kA. Figure 4.8 shows the outline of the probe which was designed by the author and built in the Departmental workshop. The probe was partly commissioned together with C. Gurnham, and the commissioning was subsequently completed by him. The design of the probe is briefly summarised here. A new Cu-Be biaxial sample holder (known as a 'Strutted Springboard') has been designed and built that is capable of varying the x-strain of a (RE)BCO tape *in-situ* using a push-pull rod, which pushes the legs of the Strutted Springboard together or apart. The push-pull rod mechanism is similar to that found in Durham's 1D strain probe [27, 148]. The y-strain of the Strutted Springboard is fixed at room temperature using struts made of threaded rods and nuts. The strutted springboard is shown in Figure 4.9. The strain homogeneity of the Strutted Springboard was optimised using FEA. Figure 4.10 shows the results of an FEA simulation for the x-strain and y-strain distributions of the Strutted Springboard. The probe and sample holder are designed to fit in Durham's 15 T horizontal magnet, and the probe is expected to be able to supply currents of at least 1000 A to a tape at 4.2 K.

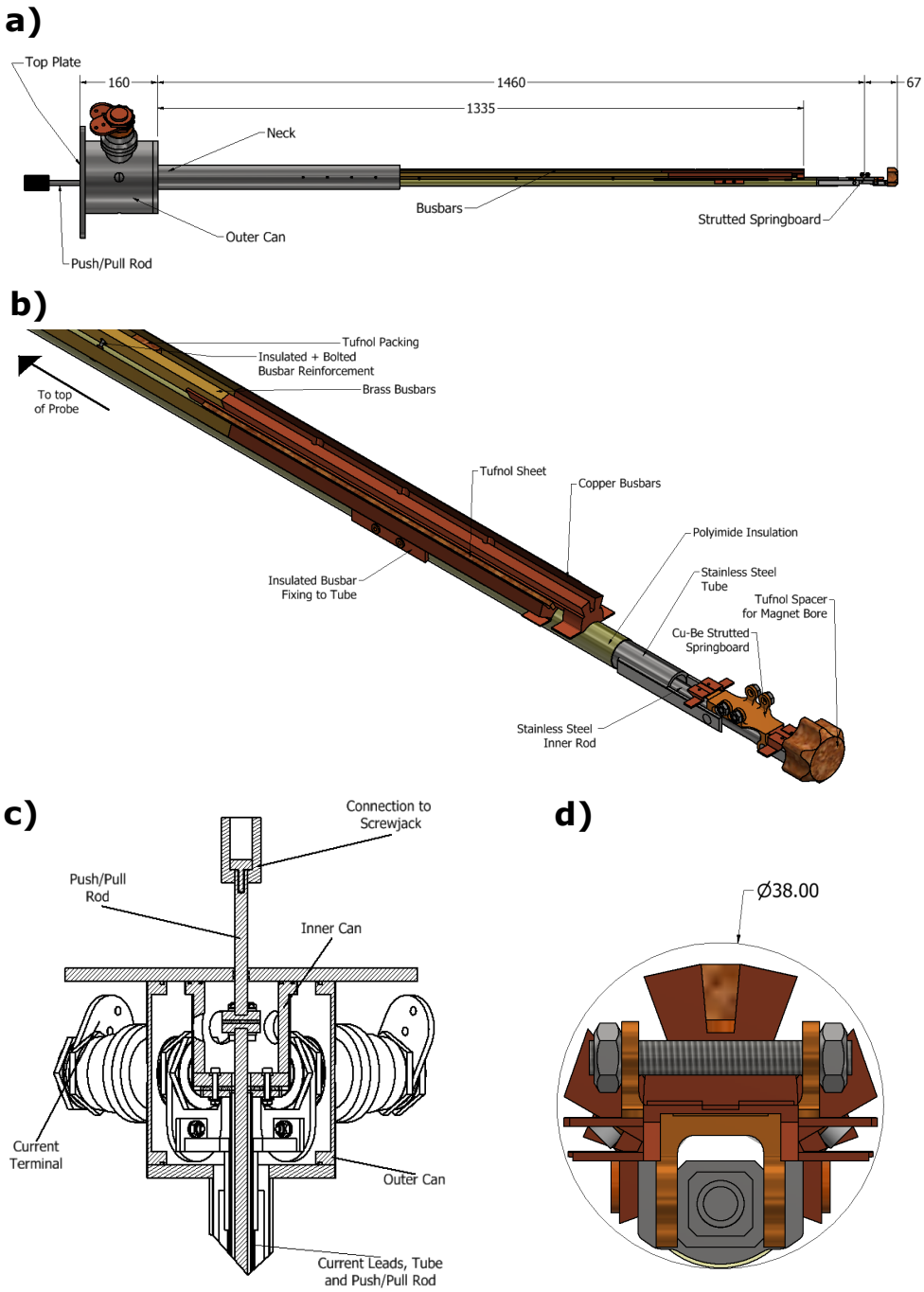

Figure 4.8: a) An overall schematic illustration of the new 2D strain probe. b) A close-up view of the bottom of the probe. Flexible current leads that connect the busbars to the Strutted Springboard are not shown. c) A cross-section through the top of the probe. d) An end view of the bottom part of the probe that must fit within Durham's 15 T magnet. The dimensions shown in a) and d) are in mm.

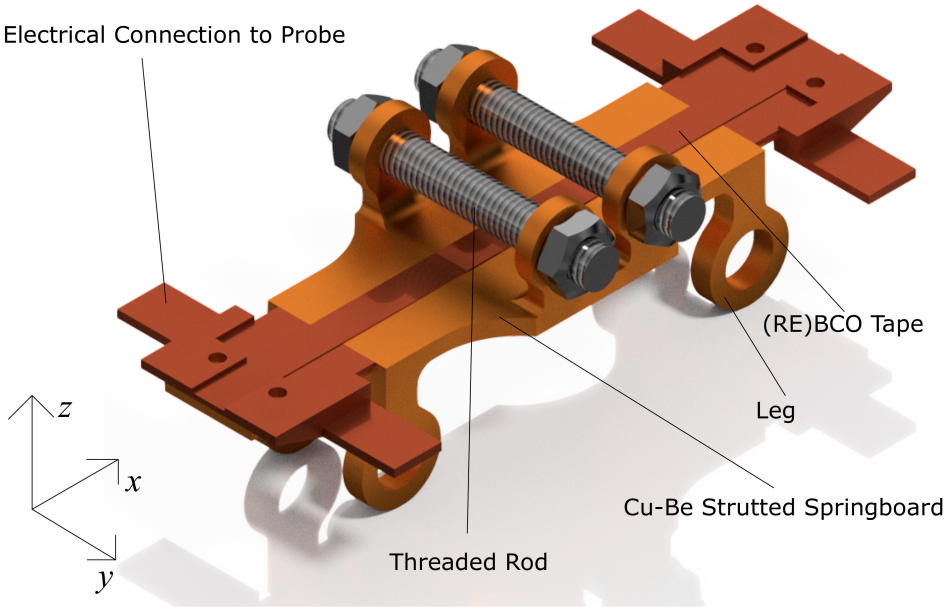

Figure 4.9: A 3D model of a Strutted Springboard and some of its associated equipment.

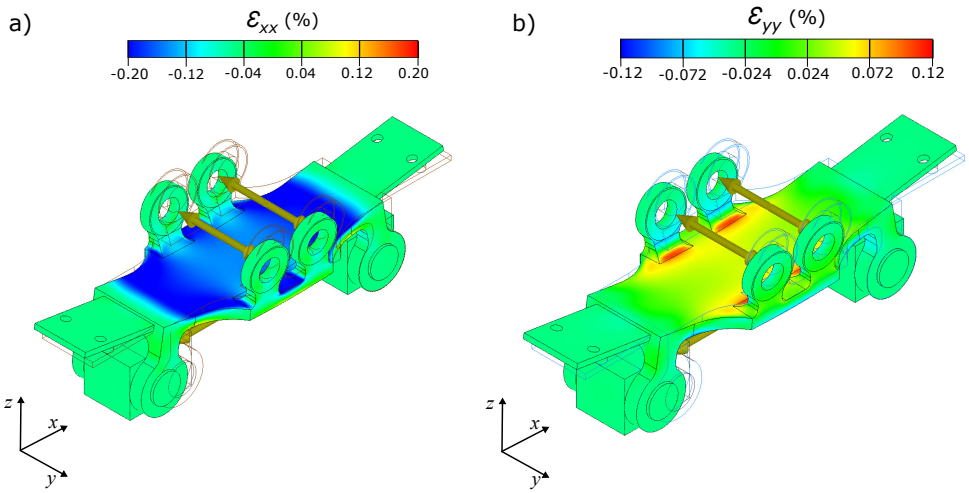

Figure 4.10: a) The x-strain distribution of the Strutted Springboard when forces of 150 N were applied to each of the four hoops on the top of the Strutted Springboard and one of the pairs of legs on the bottom of the Springboard. The cubes attached to the Strutted Springboard's legs are mock probe connections. b) The corresponding y-strain distribution for the same load conditions.

Preliminary J_C data for a THEVA tape are shown in Figure 4.11, when different x-strains were applied to it at 77 K. The value of $\frac{d\varepsilon_{yy}}{d\varepsilon_{xx}}$ was 0.25 for the THEVA tape, and a simple linear fit for the strain dependence of the J_C data using $J_C(\varepsilon_{xx}) =$

$J_C(0,0)\,(1 + c_\varepsilon \varepsilon_{xx})$ yielded a value of $-0.0748\%^{-1}$ for c_ε. The data were collected by C. Gurnham.

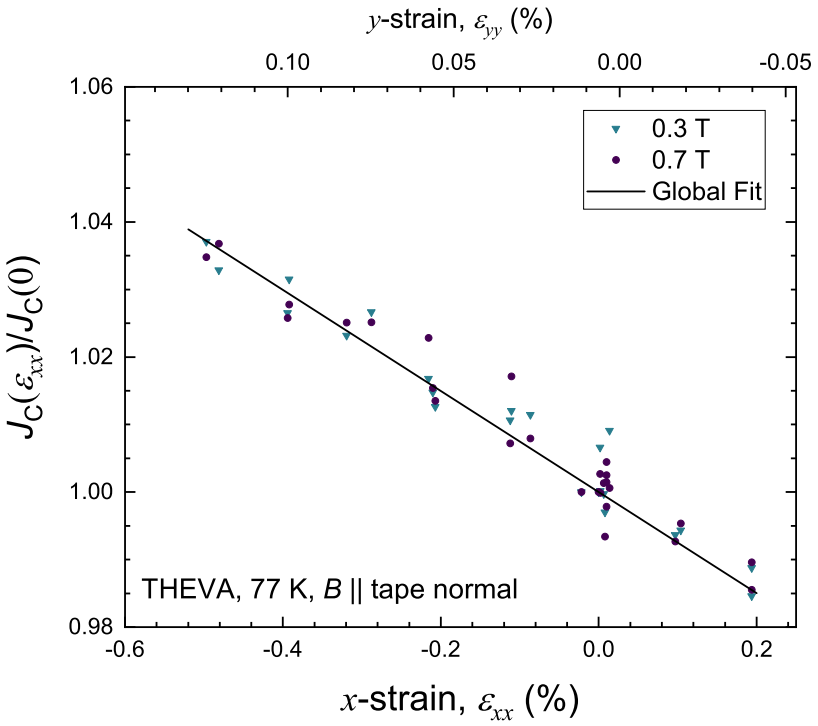

Figure 4.11: $\frac{J_C(\varepsilon_{xx})}{J_C(0)}$ for a THEVA tape.

Future work by Durham University Superconductivity Group will include the use of the probe to perform comprehensive measurements of $J_C(B, \varepsilon_{xx}, \varepsilon_{yy})$ at 4.2 K in both low and high magnetic fields for different field orientations, but this is beyond the scope (more strictly, beyond the time-frame), of the work presented here.

4.6 Discussion

As shown in Figure 4.4 and Table 4.2, when strain is applied purely along the x-axis, the value of $\mathrm{d}\varepsilon_{yy}/\mathrm{d}\varepsilon_{xx}$ is ≈ -0.33 to -0.35, whereas when strain is applied purely along the y-axis, the value of $\mathrm{d}\varepsilon_{yy}/\mathrm{d}\varepsilon_{xx}$ is considerably lower (≈ -0.54 to -0.62) as shown in Table 4.2. In an effort to understand this difference, $\mathrm{d}\varepsilon_{yy}/\mathrm{d}\varepsilon_{xx}$ was measured for a 4 mm x 4 mm piece of tape that was soldered to the centre of

the Crossboard. A value of $d\varepsilon_{yy}/d\varepsilon_{xx}$ of -0.48 was for strains applied along the x-axis and a value of $1/0.48$ was found when strains were applied along the y-axis. Therefore, the difference in the $d\varepsilon_{yy}/d\varepsilon_{xx}$ values for the full 24 mm length tapes can be attributed to the mechanical asymmetry of the tape/Crossboard system.

The main limitation of the Crossboard is that the strain can only be changed at room temperature. This slowed down the rate at which the J_C measurements were taken, and increased the risk of sample or instrumentation failure due to the combination of large applied strains and repeated thermal cycling. For example, measurements on Sample A had to be halted due to the failure of a strain gauge lead, probably because of repeated thermal cycling. The scatter in the J_C data (e.g., $\approx 5\%$ for Datasets IV-VI) was also attributed to the repeated thermal cycling of the tape. Nevertheless, with the setup used, the strain state of the tape at 77 K was reliably predicted from the strain state of the tape at 300 K, as shown by the similarities in the values of $d\varepsilon_{yy}/d\varepsilon_{xx}$ at 300 K and 77 K for the same dataset shown in Table 4.2. Ideally, the apparatus would enable the strain state of the tape to be varied along all three principal strain axes while the tape is held at cryogenic temperatures within a magnet bore - indeed this was part of the motivation.

In order to obtain consistent fits to the data in Sample C, the parameter A in Equation 4.4.2 had to vary between the three sets of strain data as well as between different field angles. More data are required to determine why this has been necessary. It is probably associated with plastic deformation in some components of the tape or the Crossboard and is consistent with the relatively large variation in J_C of up to $\sim 10\%$ at zero applied strain that was found throughout the experiments. For example, during the experiments, the strain states of the tapes did not relax back to zero strain when the stainless steel grippers,nuts and bolts were removed and the Crossboard was allowed to relax.

The data in Figure 4.7 demonstrate a change from linear behaviour to parabolic strain behaviour for the same tape, depending upon the direction of applied strain. Linear behaviour occurs because the T_C's and J_C's of the A- and B- domains both

increase with increasing tensile $\varepsilon_{xx} = \varepsilon_{yy}$ strain. If $|g_A| > |g_B|$, then the tape's J_C increases with increasing tensile $\varepsilon_{xx} = \varepsilon_{yy}$ strain and if $|g_B| > |g_A|$, the tape's J_C decreases with increasing tensile $\varepsilon_{xx} = \varepsilon_{yy}$ strain. Parabolic strain behaviour occurs when the J_C's of one of the domain types increases with increasing tensile ε_{xx} strain and the other domain type's J_C decreases.

The twin boundaries in the (RE)BCO layers of SuperPower's tapes are aligned with the [110] direction. However other manufacturers such as Fujikura, have a different microstructure such that the twin boundaries are aligned with the [100] direction [116]. Indeed THEVA tapes also have twin boundaries that are orientated along the crystallographic [100] direction, but the (RE)BCO layers in those tapes are also at an inclination of 20-30° relative to the tape substrate [30, 166]. The uniaxial strain dependence of J_C for a SuperPower tape is parabolic, whereas Fujikura's and THEVA's tapes have a linear strain dependence [27, 29, 30, 31, 112]. The preliminary data for the THEVA tape taken using the new probe and Strutted Springboard (Figure 4.11) also show linear behaviour that is in agreement with the literature. D. van der Laan *et al.* have shown that the in-plane strain dependence of J_C is anisotropic with respect to the direction of applied strain [30]. For the first time, in this work, both linear and parabolic strain behaviour on a single tape sample has been achieved by applying strain in different directions with respect to the twin boundary orientation. The fit to Sample C (Datasets IV-VI) shows that the Chain Model can reproduce the main features of the data, but more work is needed to provide confidence in the theory described here. For example, single crystal measurements from Welp *et al.* generated values of g_A and g_B that were positive and negative respectively and of roughly equal magnitude [33]. Our g_A and g_B values have opposite signs, however the magnitude of our g_A and g_B values are approximately 30% different. Experiments on annealed, detwinned (RE)BCO tapes have also shown that g_A and g_B can have different magnitudes [113]. Some variability in the magnitude of g_A and g_B is to be expected for the tapes in this work because they contain artificial pinning centres (APC's) to increase J_C. How-

ever, these APC's will also strain the (RE)BCO matrix in which they are located, introducing disorder. We have also assumed that the single crystal variable strain data showing T_C is linear in strain can be extrapolated to tensile strains and over the relatively large range of strains measured in these experiments. This assumption needs independent verification.

4.7 Conclusion

This chapter has introduced a new biaxial sample holder known as a Crossboard, that is capable of applying arbitrary combinations of x-strain and y-strain to a (RE)BCO tape at 77 K. The Crossboard has been used to measure the strain dependence of J_C on 3 different SuperPower APC SCS4050 tapes, for different types of applied strain, in fields up to 0.7 T, for different magnetic field orientations. The Chain Model has been extended to include the effects of biaxial strain on the critical temperatures of the domains in the tape, and it has been used to fit the most comprehensive $J_C(B, \varepsilon_{xx}, \varepsilon_{yy})$ datasets (Sample C). The results show that the fraction of A-domains in the tape is roughly the same as the fraction of B-domains ($f = 0.49$), and that the strain sensitivities of the critical temperatures of both domain types are similar - $1.8\,\mathrm{K}\,\%^{-1}$ for strains along the a-axis and $-1.3\,\mathrm{K}\,\%^{-1}$ for strains along the b-axis. For the first time, a change between linear strain behaviour for J_C and parabolic strain behaviour for J_C in a single tape has been observed and explained. Future work will include the use of the new biaxial strain probe and sample holder to measure $J_C(B, \varepsilon_{xx}, \varepsilon_{yy})$ with *in-situ* x-strain control at 4.2 K in both low and high magnetic fields, for different field orientations. Future work could also involve measuring the biaxial strain dependence of J_C for tapes from other manufacturers, whose (RE)BCO twin boundary orientations are different to those in SuperPower tapes. Some preliminary measurements have already been performed for a THEVA tape using the new probe and sample holder.

Chapter 5

Is J_C in High Fields Determined by the Laws of Transmission and Diffraction, Rather than Pinning?

5.1 Introduction

Flux pinning has long-provided the framework to describe J_C in high magnetic fields. As previous chapters have discussed, the pinning literature is voluminous. However, in this chapter we present new experimental data for a (RE)BCO tape with Artificial Pinning Centres (APC's) that cannot be described using flux pinning scaling without using non-physical fitting parameters. We consider an alternative fitting approach for J_C, based on a model for SNS Josephson Junctions. It is a model based on the work by Blair and Hampshire (BH) [133], who have developed an analytic expression for the J_C's of narrow Josephson Junctions across the entire magnetic field range. It suggests that routes to improve $J_C(B)$ best consider transmission and diffraction rather than pinning. BH have also extended these expressions for wider junctions that can contain fluxons and have shown the model predicts the Kramer-like dependence for $J_C(B)$ in Nb_3Sn [60] and the power law dependence for $J_C(B)$ in (RE)BCO [167].

In the next two sections we briefly describe the experimental equipment that was used to make the measurements and obtain the data. Section 5.4 provides an analysis of the data using the standard scaling/flux pinning approach and shows it leads to non-physical parameters. This provides the motivation for us to proceed to using an SNS model to describe our data. Section 5.5 provides the framework we used to relate microscopic properties in the superconductor and the barrier (of a Josephson junction) to the superconducting parameters in G-L theory. Two different parameterisations of the G-L coefficients that appear in the G-L expression for the free energy of the superconductor and normal barrier (see, for example, Equation 2.4.1 in Chapter 2) are considered. One uses the standard text-book BCS parameterisation that relates the free parameters in G-L theory to microscopic normal state parameters (i.e., $\Upsilon_s = 1$). The second assumes that not all conduction electrons condense into the superconducting state (i.e., $\Upsilon_s < 1$). Section 5.6 provides the formalism used for the SNS model. Then, Section 5.7 provides the fits to the data using the SNS approach including the free parameters derived. We have not only fitted J_C for the APC (RE)BCO sample measured here but also provided fits from the literature (from the Durham group) for a non-APC (RE)BCO sample measured by Branch [28], and a Nb_3Sn sample measured by Tsui and reported by Branch [27, 28, 29]. We complete the chapter with a discussion and conclusions.

5.2 Experimental Setup

The experimental setup used to perform $J_C(B, \theta, T, \varepsilon_{app})$ and $B^{*\rho}_{c2}(\theta, T, \varepsilon_{app})$ measurements depends on the type of superconductor that is measured. The experimental setup used to perform the $J_C(B, T, \varepsilon_{app})$ measurements on the Nb_3Sn strand, whose data are re-analysed in this chapter, has been reported elsewhere [157, 161, 168], and is therefore not discussed further here. The experimental setup used to perform the $J_C(B, \theta, T, \varepsilon_{app})$ and $B^{*\rho}_{c2}(\theta, T, \varepsilon_{app})$ measurements on the Non-APC (RE)BCO sample has been reported by Branch [27, 28, 29]. Here, the same

experimental setup was re-used by the author to collect the $J_C(B, \theta, T, \varepsilon_{app})$ and $B^{*\rho}_{c2}(\theta, T, \varepsilon_{app})$ for the APC (RE)BCO sample. Hence, only a brief overview of the experimental setup used to make the APC (RE)BCO measurements is given here. A 78 mm long SuperPower APC SCS4050 tape was soldered substrate side down onto a Cu-Be springboard using Pb-Sn solder. Voltage taps with a separation of 13 mm were soldered about the centre of the tape. Three Cernox^{TM} thermometers were attached to the top side of the tape using GE varnish. The variation in Cernox^{TM} resistance with magnetic field was corrected for using data from the literature [169]. Three foil strain gauges were glued to the underside of the springboard and acted as sample heaters. The tape and springboard were enclosed in a variable temperature cup, with a vent at the bottom. During the measurements, the temperature of the (RE)BCO tape was controlled using LakeShore 336 temperature controllers and a Proportional-Integral-Derivative (PID) control loop for each Cernox^{TM} thermometer and the heater closest to it. The helium boil-off in the cryostat was vented using water-filled bubblers, as it was previously found that these lead to lower variations in cryostat pressure than mechanical one-way valves [28]. When taken together, the equipment maintained the sample's temperature to better than 100 mK during the measurements.

A strain gauge was glued alongside the centre of the tape on the springboard, to measure the strain of the tape. Tensile and compressive strains were applied to the tape by forcing the legs of the springboard together and apart respectively, using a push-pull rod whose motion was controlled by a screwjack at the top of the probe. After the desired strain was reached, the push/pull-rod was locked off. The strain of the sample was changed *in-situ* at 4.2 K - this avoided issues with thermally cycling the HTS tape as well as the temperature dependence of the strain gauge's resistance. The angle between the magnetic field and the tape surface was set using markings on top of the probe and a laser pen projected onto the walls of the laboratory. Changes in angle as low as 0.5° could be measured and reproducibly re-set using this setup.

Two types of measurements were performed on the tape - J_C measurements and $B^{*\rho}_{c2}$ measurements. The J_C measurements were taken by ramping the sample current over ~60 s. There was no detectable change in the strain gauge resistance during the current ramp. The standard deviation of the $E - J$ trace baseline noise during the J_C measurements was $\leq 3\,\mu V\,m^{-1}$. The $B^{*\rho}_{c2}$ measurements were performed by supplying a current of 100 mA to the tape. The value of 100 mA was chosen to be as low as possible while maintaining a good signal to noise ratio. During each measurement, the magnetic field was fixed and the temperature was lowered from above the resistive transition to below it at a rate of 1 $Kmin^{-1}$.

In terms of the order of the measurements, J_C was first measured as a function of angle for different magnetic fields and temperatures, with $\varepsilon_{app} = 0\%$. The applied strain was then taken to -1% and the angular measurements were repeated. One of the purposes of these measurements was to identify the peaks in $J_C(\theta)$ associated with the APC's and *ab*-planes. Once the peaks were identified, detailed $J_C(B, T, \varepsilon_{app})$ and $B^{*\rho}_{c2}(T, \varepsilon_{app})$ measurements were taken. The applied strain was then changed to -0.75% and the measurements were taken at the same fields and temperatures. This process continued in increments of $\varepsilon_{app} = 0.25\%$ until the measurements at $\varepsilon_{app} = 0.5\%$ had been taken. After this, ε_{app} was taken back to 0% to verify that $J_C(\varepsilon_{app} = 0)$ had not been irreversibly lowered due to the applied strain. It should also be noted that after the initial cooldown of the sample to 4.2 K, the probe and sample were not warmed up above ~100 K at any time during the entire experimental campaign.

5.3 Overview of Results - $J_C(B, \theta, T, \varepsilon_{app})$ and $B^{*\rho}_{c2}(\theta, T, \varepsilon_{app})$

First we consider the role of the springboard that was electrically in parallel with the tape. Our approach is to subtract the current shunted through the springboard from the total sample current I_{Total} to give the current flowing through the

superconductor I_{SC} [28]:

$$I_{SC} = I_{Total} - \frac{V}{R_{shunt}} \tag{5.3.1}$$

where R_{shunt} is the resistance of the springboard. Values of R_{shunt} were taken from the resistivity traces for $B^{*\rho}_{c2}$ just above the superconducting transition. The typical shunt current correction was 0.1 A at $E = 100\,\mu V\,m^{-1}$.

All $E-J$ (or equivalently, $V-I$) traces that were collected during the experiments were analysed using Equation 3.2.3 with $I = I_{SC}$ between $E = 10\,\mu V\,m^{-1}$ and $E = 100\,\mu V\,m^{-1}$ to extract J_C and N. The J_C values presented and fitted in the rest of this chapter correspond to the values extracted at $100\,\mu V\,m^{-1}$. Figure 5.1 shows $J_C(\theta)$ for different fields, temperatures and applied strains. The peak in J_C that is due to the field being aligned with the *ab*-planes is at 87.5° and the less pronounced broader peak due to the APC rods aligning with the fluxons has its maximum at 0°. The peak positions do not change with magnetic field magnitude, temperature or applied strain. The variation of N with angle is shown in Figure 5.2. The variation of N with field, temperature and strain is similar to that found for SuperPower tapes without APC's [29].

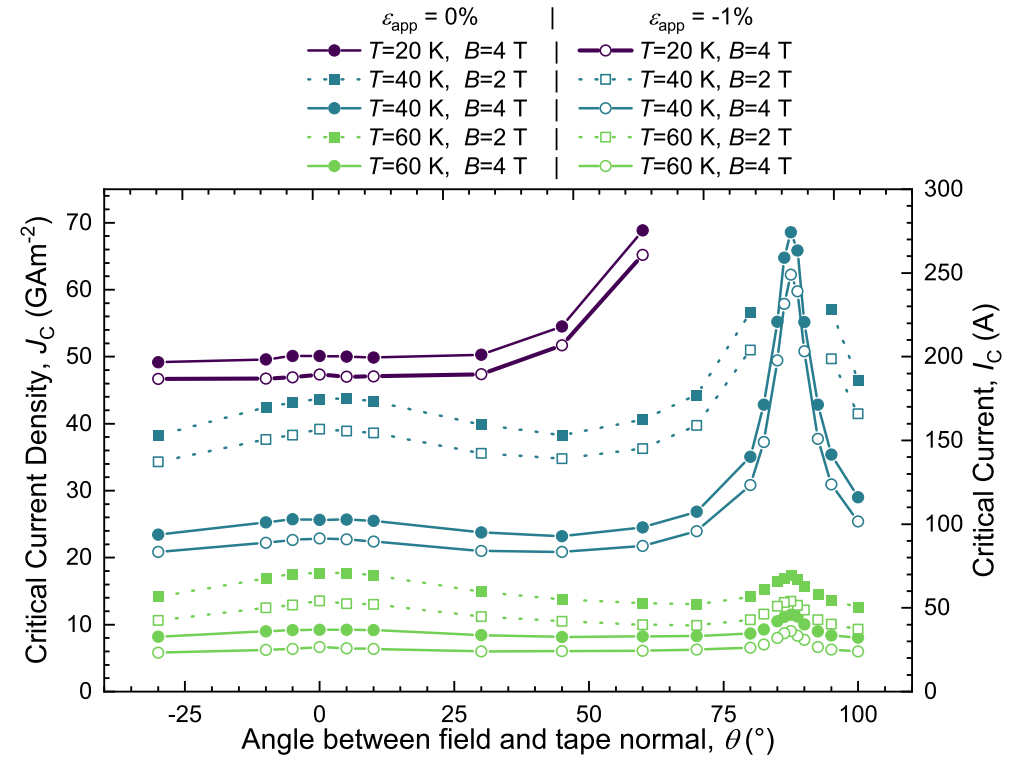

Figure 5.1: The angular dependence of J_C for different magnetic field magnitudes, temperatures and applied strains.

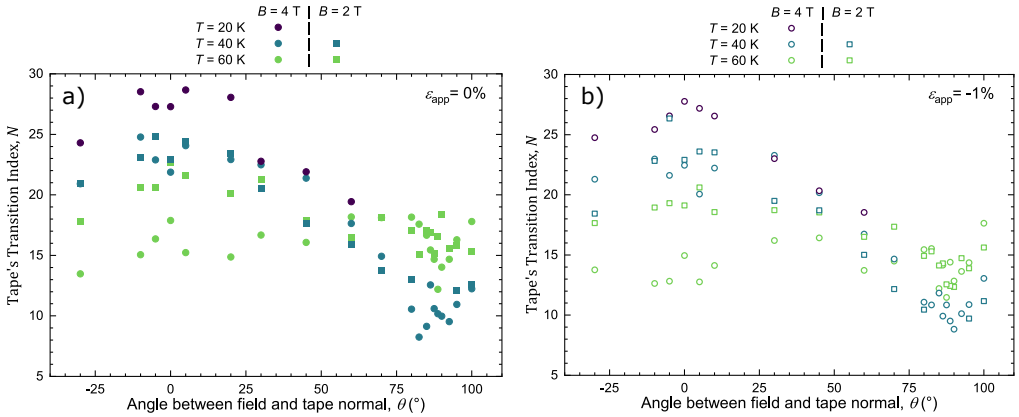

Figure 5.2: a) $N(\theta)$ for different magnetic fields and temperatures and $\varepsilon_{app} = 0\%$. b) The same, but for $\varepsilon_{app} = -1\%$.

Figure 5.3 shows $J_C(\varepsilon_{app})$ for different fields and temperatures. The $J_C(\varepsilon_{app})$ data were fitted using Equation 3.2.1 over the strain range for which $J_C(\varepsilon_{app})$ was parabolic, $-0.75\% \leq \varepsilon_{app} \leq 0.25\%$. The values of ε_{peak} were extracted - it is clear from the parabolic fits that ε_{peak} is magnetic field and temperature dependent.

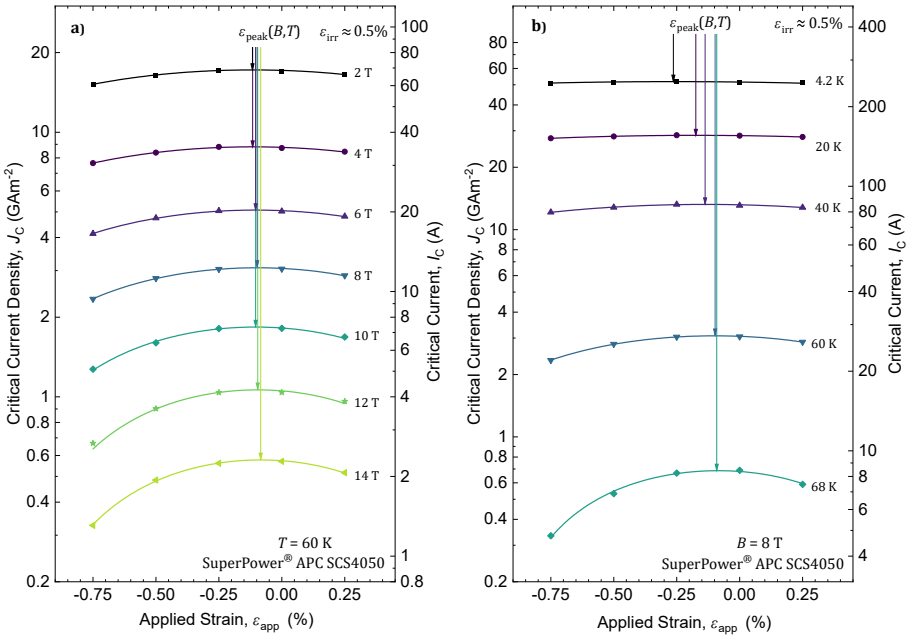

Figure 5.3: a) $J_C(\varepsilon_{app})$ for different magnetic fields, with the field applied normal to the tape surface. b) The strain dependence of J_C for different temperatures, for $\theta = 0°$.The solid lines were found by fitting Equation 3.2.1 at each temperature and field and the value of ε_{peak} noted.

Figure 5.4 shows the variation of N with J_C. The data were fitted using

$$N = 1 + r_N J_C^{S_N}, \tag{5.3.2}$$

where r_N and S_N are constants. This expression was originally developed for LTS [67], although it has found utility for parameterising (RE)BCO tapes too [27, 29]. The data for $\theta = 0°$ fit well, with exception to the data for $T = 4.2$ K, whose N-values were affected by heating during the $E - J$ transition, which was reported previously by Branch for the experimental setup used in this work [28]. However, it is found that r_N and S_N must be allowed to vary with temperature when fitting the data for $\theta = 87.5°$. Table 5.1 gives the values of r_N and S_N for $\theta = 87.5°$.

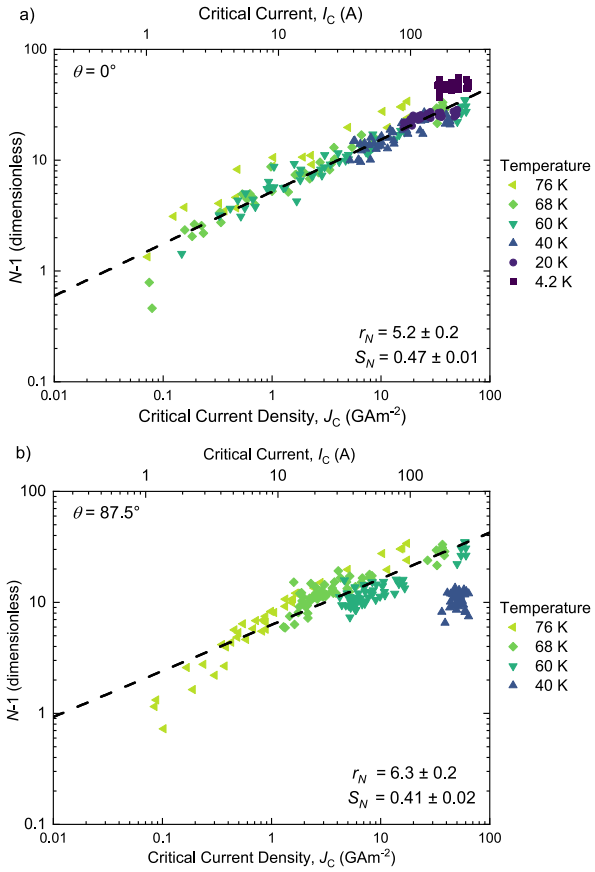

Figure 5.4: a) J_C vs. $N-1$ for $\theta = 0°$. The $T = 4.2$ K data were excluded from the fit. b) The same, but for $\theta = 87.5°$. The dashed black line and r_N and S_N values presented are for a global fit to the 60 K, 68 K and 76 K data.

Table 5.1: Fit parameter values for the fits to $N(J_C)$ for $\theta = 87.5°$ using Equation 5.3.2

Temperature (K)	Parameter	
	r_N	S_N
40 K	6 ± 5	0.2 ± 0.2
60 K	5.0 ± 0.3	0.42 ± 0.03
68 K	7.8 ± 0.3	0.37 ± 0.03
76 K	6.9 ± 0.3	0.52 ± 0.03

Figure 5.5 shows a $\rho(T)$ trace that was measured during the experiments. The (cryogenic) normal state resistivity of the tape ρ_N^{Tape} was assumed to be independent of temperature over the resistive transition. The 'bump' in $\rho(T)$ close to $\rho(T) = \rho_N^{\text{Tape}}$ was also measured previously by Branch for a SuperPower Non-APC tape [28]. The resistivity data that were used to extract $B_{c2}^{*\rho}$ data from each $\rho(T)$ trace

were analysed using two different resistivity criteria - $0.1\rho_N^{Tape}$ and $0.9\rho_N^{Tape}$.

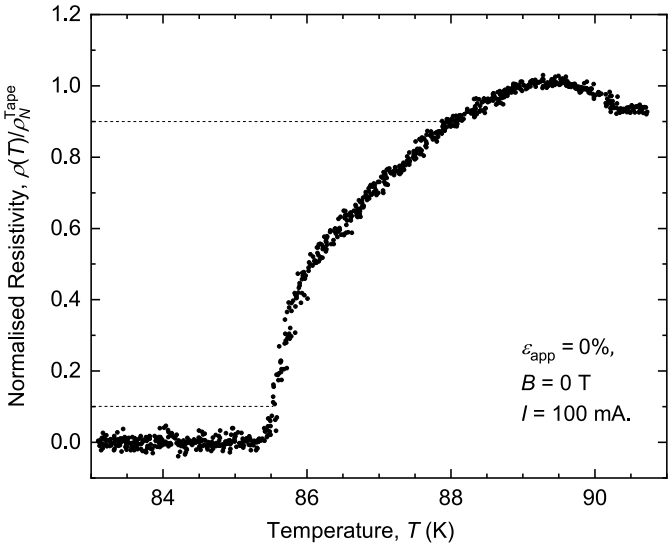

Figure 5.5: Superconducting to normal state resistive transition for the APC (RE)BCO sample with the $0.1\rho_N^{Tape}$ and $0.9\rho_N^{Tape}$ denoted by the dotted lines.

The $B^{*\rho}_{c2}$ data were fitted using

$$B^{*\rho}_{c2}(\theta, T, \varepsilon_{app}) = B^{*\rho}_{c2}(\theta, 0, \varepsilon_{app}) \left[1 - \left(\frac{T}{T^{*\rho}_C(\varepsilon_{app})}\right)^{\nu}\right] \tag{5.3.3}$$

where $B^{*\rho}_{c2}(\theta, 0, \varepsilon_{app}) = B^{*\rho}_{c2}(\theta, 0, 0)(1+b^{\rho}_{\varepsilon 1}\varepsilon_{app}+b^{\rho}_{\varepsilon 2}\varepsilon^2_{app})$ and $T^{*\rho}_C(\varepsilon_{app}) = T^{*\rho}_C(0)(1+c^{\rho}_{\varepsilon 1}\varepsilon_{app}+c^{\rho}_{\varepsilon 2}\varepsilon^2_{app})$. Here, $B^{*\rho}_{c2}(\theta, 0, 0)$, $b^{\rho}_{\varepsilon 1}$, $b^{\rho}_{\varepsilon 2}$, $T^{*\rho}_C(0)$, $c^{\rho}_{\varepsilon 1}$ and $c^{\rho}_{\varepsilon 2}$ and ν are fit parameters. Table 5.2 shows the best fit parameters generated by the fits. In order to get a good fit, the strain parameterisation of both $T^{*\rho}_C(\varepsilon_{app})$ and $B^{*\rho}_{c2}(\theta, 0, \varepsilon_{app})$ had to be allowed to vary as a function of angle. The values of $B^{*\rho}_{c2}(\theta, 0, \varepsilon_{app})$ extracted for both field orientations are in agreement with upper critical field measurements performed on (RE)BCO single crystals using pulsed magnetic fields [164]. Fits were also tried where $B^{*\rho}_{c2}(0, \varepsilon_{app})$ was related to $T^{*\rho}_C(\varepsilon_{app})$ using a form of an expression developed for LTS [91]:

$$B^{*\rho}_{c2}(\theta, 0, \varepsilon_{app}) = B^{*\rho}_{c2}(\theta, 0, 0) \left(\frac{T^{*\rho}_C(\varepsilon_{app})}{T^{*\rho}_C(0)}\right)^{w} \tag{5.3.4}$$

where w is a constant, however these fits had significantly higher RMS errors.

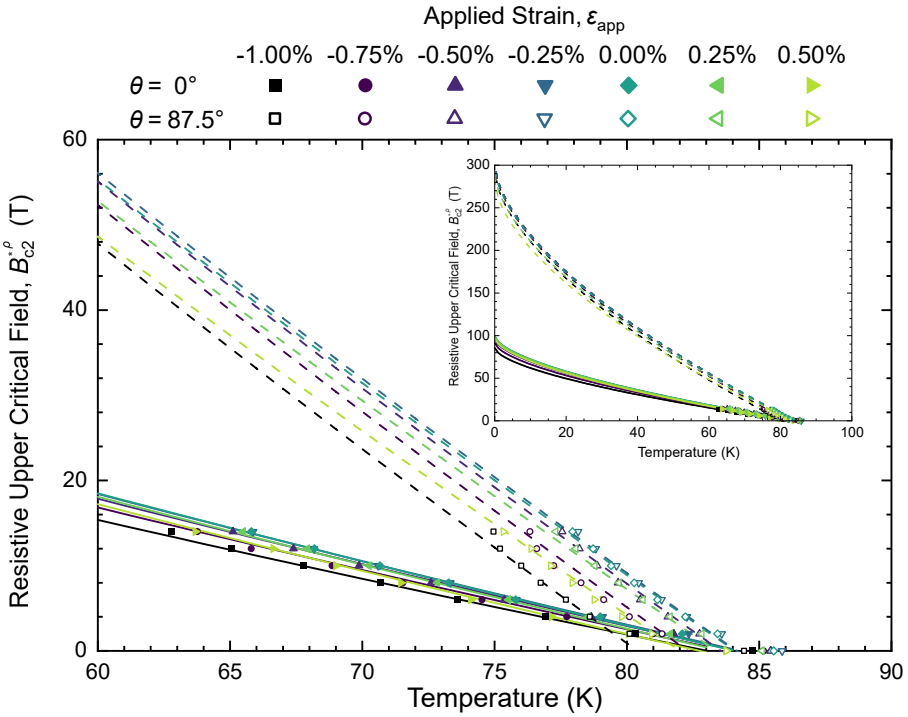

Figure 5.6: $B_{c2}^{*\rho}(\theta, T, \varepsilon_{app})$ for $\theta = 0°$ (solid lines and closed data points) and $\theta = 87.5°$ (dashed lines and open data points). The data were extracted from resistivity traces at the $0.1\rho_N^{Tape}$ criterion. The fit lines were generated using Equation 5.3.3 and the parameters for $0.1\rho_N^{Tape}$ in Table 5.2.

Table 5.2: Fit parameters for the experimental $B_{c2}^{*\rho}$ data, along with the RMS fit error, for 2 different resistivity criteria. The parameter ν was fixed at a value from the literature [99, 164].

Fit Parameter	$0.1\rho_N^{Tape}$		$0.9\rho_N^{Tape}$	
	0°	87.5°	0°	87.5°
ν	**0.61**		**0.61**	
$T_C^{*\rho}(0)$ (K)	84.1		86.8	
$c_{\varepsilon 1}^{\rho}$ $(10^{-3}\%^{-1})$	−17.0	−18.3	−18.4	−16.0
$c_{\varepsilon 2}^{\rho}$ $(10^{-3}\%^{-2})$	−29.4	−62.2	−20.7	−54.8
$B_{c2}^{*\rho}(0,0)$ (T)	99.4	297	110	326
$b_{\varepsilon 1}^{\rho}$ $(10^{-3}\%^{-1})$	10.1	−70.6	77.8	−56.8
$b_{\varepsilon 2}^{\rho}$ $(10^{-3}\%^{-2})$	−130	−87.1	−90.1	−99.7
RMS Error (T)	0.473		0.420	

5.4 Flux Pinning Analysis

The J_C data for the $\theta = 0°$ and $\theta = 87.5°$ orientations were initially fitted using the classic flux pinning theory in two stages, so that a universal curve of the normalised pinning force vs. the reduced field for all J_C data could be generated. In each stage, the data were fitted using [56]

$$F_P = F_{P,max} \left(\frac{B}{B^*_{c2}} \right)^p \left(1 - \frac{B}{B^*_{c2}} \right)^q \tag{5.4.1}$$

where $F_{P,max}$ is the maximum pinning force density, B^*_{c2} is the irreversibility field, and p and q are field, temperature and strain independent constants. $F_{P,max}$ was treated as a free parameter for each combination of temperature, applied strain and field orientation. Figure 5.7 shows the result of the fit.

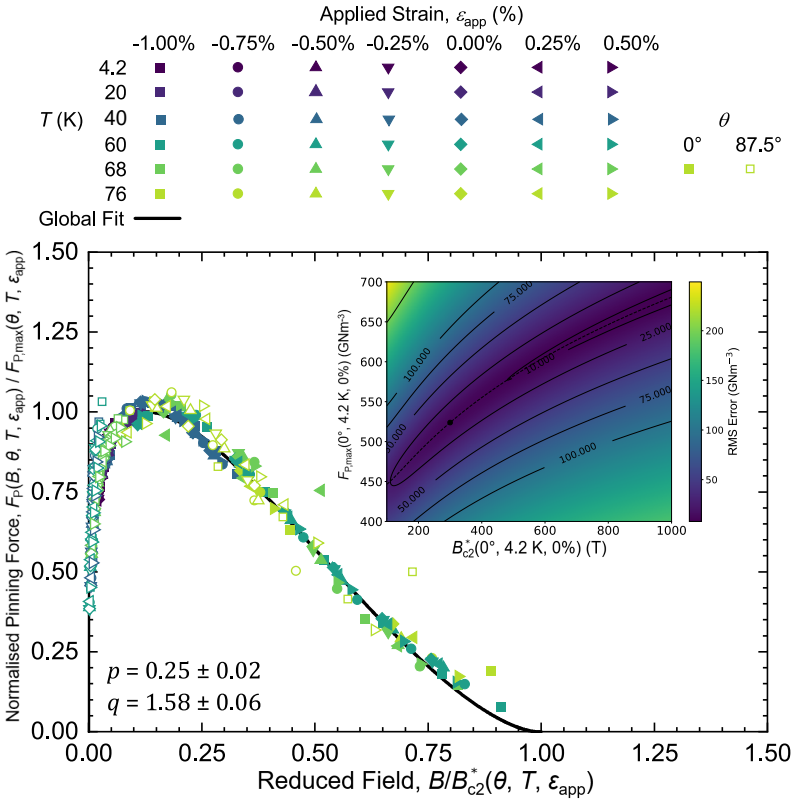

Figure 5.7: $\frac{F_P}{F_{P,max}}$ vs. $b^* = \frac{B}{B^*_{c2}}$. The inset shows an RMS error surface for the two fit parameters $F_{P,max}(0°, 4.2\ K, 0\%)$, along with the value of B^*_{c2} (300 T) and $F_{P,max}$ (520 GNm^{-3}) used to fit the data.

Table 5.3: The strain dependence of the very high B_{c2} values obtained from fits to J_C data after p and q were fixed at 0.25 and 1.58 respectively.

Temperature (K)	Parameter					
	$B^*_{c2}(\theta,T,0)$ (T)		$b_{1\varepsilon}$ ($\%^{-1}$)		$b_{2\varepsilon}$ ($\%^{-2}$)	
	0°	87.5°	0°	87.5°	0°	87.5°
4.2	300	-	0.0669	-	−0.133	-
20	152	-	0.0669	-	−0.133	-
40	52.1	1200	−0.0490	−0.397	−0.232	−0.885
60	-	800	-	−0.397	-	−0.885
68	-	300	-	−0.397	-	−0.885
76	-	27.3	-	−0.397	-	−0.885

Initially, the high temperature data (i.e. $T \geq 60$ K for $\theta = 0°$) were fitted. In this fit the values of B^*_{c2} were fixed using the $0.1\rho_N^{\text{Tape}}$ parameterisation of the $B^{*\rho}_{c2}$ data (Equation 5.3.3 and Table 5.2). Values of p and q of 0.25 and 1.58 respectively were extracted from this first fit. Then, the remaining low temperature data were fitted for both orientations, with p and q fixed at 0.25 and 1.58 respectively. It was found that fixing B^*_{c2} using the parameterisation derived from the experimental $B^{*\rho}_{c2}$ data generally led to poor fits, so B^*_{c2} was parameterised using:

$$B^*_{c2}(\theta,T,\varepsilon_{\text{app}}) = B^*_{c2}(\theta,T,0)\left(1 + b_{1\varepsilon}\varepsilon_{\text{app}} + b_{2\varepsilon}\varepsilon^2_{\text{app}}\right) \tag{5.4.2}$$

and the values of $B^*_{c2}(T,0,\theta)$, $b_{1\varepsilon}$ and $b_{2\varepsilon}$ were left as free parameters for each temperature and field orientation. The values for these parameters are given in Table 5.3.

Although a good fit can be found for the lower temperature data with p and q fixed, the values of B^*_{c2} required at lower temperatures are non-physical - much higher than the values found in measurements of the upper critical magnetic field for single crystals [164]. The global minimum in the error surfaces of $F_{\text{P,max}}$ vs. B^*_{c2} are also very broad. An example of this is shown in the inset of Figure 5.7. The fit consistently forced B^*_{c2} and $F_{\text{P,max}}$ to extremely large values, effectively compressing the experimental data to the very low reduced field range in Figure 5.7. This shows that universal flux pinning scaling breaks down across large temperature ranges and multiple field orientations for this sample unless one introduces non-

physical, very high B^*_{c2} values at low temperatures.

Figure 5.8 shows the values of $F_{P,max}$ and B^*_{c2} that underpin the universal F_P curve in Figure 5.7. The upper panel shows how the angle at which the field is applied to the tape strongly affects the scaling of $F_{P,max}$ vs. B^*_{c2}. This is due to the angular dependence of B^*_{c2}. If one uses an expression for $F_{P,max}$ developed for LTS [23, 24, 25, 91, 163, 170]:

$$F_{P,max}\kappa_1^{*2} \propto B^{*n}_{c2} \tag{5.4.3}$$

with the G-L parameter $\kappa_1^* \propto B^*_{c2}/\left[T^*_C\left(1-(T/T^*_C)^2\right)\right]$, then universal scaling behaviour can be found as shown in Figure 5.8.

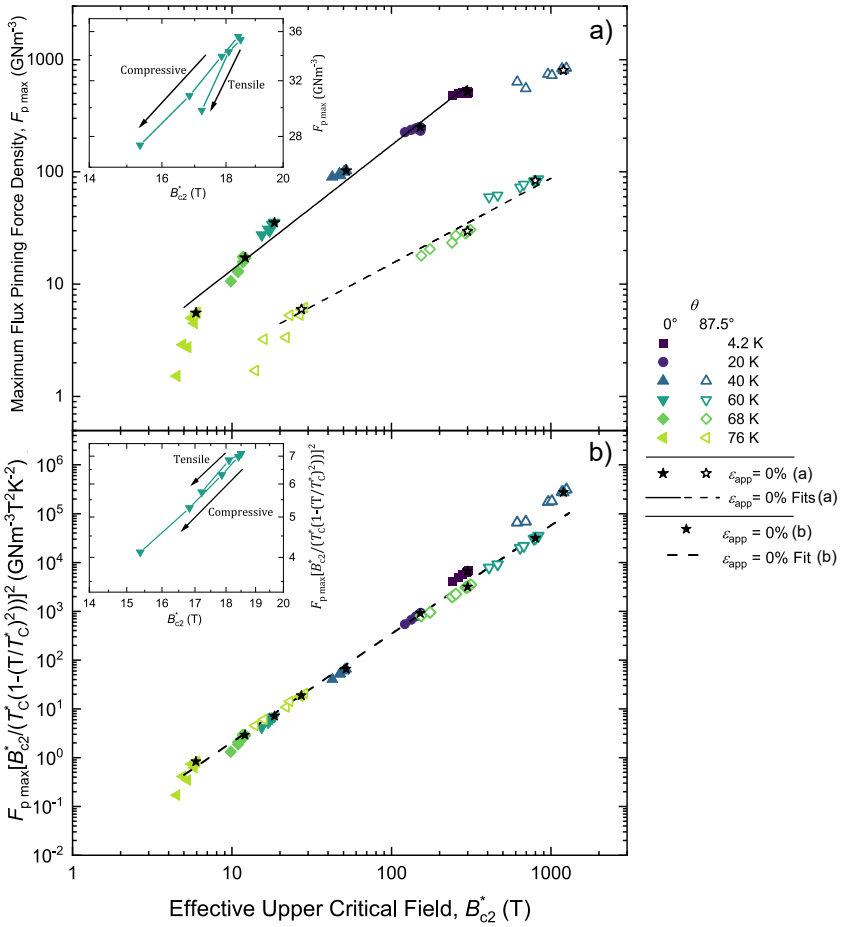

Figure 5.8: a) The scaling of $F_{\mathrm{P,max}}$ with B^*_{c2} for the two field orientations. Power law fits for each orientation are also shown. The $T = 40$ K data for $\theta = 87.5°$ were excluded from the fit for that orientation. b) The scaling of $F_{\mathrm{P,max}}\kappa_1^{*2}$ with B^*_{c2}, along with a single power law fit for both field orientations.

Double-valued behaviour of $F_{\mathrm{P,max}}$ with B^*_{c2} is present for this APC (RE)BCO sample, and similar behaviour has been found for Non-APC (RE)BCO and Nb_3Sn in previous analyses by Branch. However the non-physical very high values of B^*_{c2} required to get a good fit at low temperatures for this APC sample, provided the motivation to abandon the classic flux pinning and scaling approach as a good description of J_{C} and has lead to the SNS analysis presented in this thesis.

5.5 Microscopic Properties of Superconductors and Barriers

In this section, we first consider the standard text-book formalism for the normal state properties of materials and then the equivalent formalism for superconducting properties. We will use these to construct the SNS Josephson junction model for J_C outlined later in the chapter.

5.5.1 Normal State Properties of Superconductors

We note that the normal state properties can be calculated with 3 independent measurements. Thereafter the other normal state properties can be calculated using well-known results from solid state theory [171, 172]. Orlando states that 3 independent material properties are needed to predict all the in-field properties of superconductors in the simple limit considered here, namely that it is weakly coupled and in the dirty limit [173]. Two normal state properties and the critical temperature suffice. Were we to consider superconductors in the clean limit, then the Fermi surface area of the charge carriers normalised to the Fermi surface area of a free electron gas would be required. Were we to further consider strongly coupled superconductors, a 5th parameter (e.g., the gap or the characteristic phonon frequency) would be required to calculate the superconducting properties. Table 5.4 contains calculations and values for the normal state properties of Nb_3Sn and optimally doped YBCO. Three independent parameters were taken from the literature and the other parameters were derived using, for example, the well-known free electron model and Drude model.

Table 5.4: Normal state properties for Nb_3Sn and YBCO, and the equations to calculate them. For Nb_3Sn, experimental values of $\rho_{N,s}$, γ_s and n_s were used to calculate all other parameters. For YBCO, experimental values of $\rho_{N,s}$, γ_s and $\nu_{F,s}$ were used. The density of states $g(E_{F,s})$ is the density of states for one spin direction, and in the calculation for γ_s, there is a factor of 2 to account for spin degeneracy [172]. The Fermi surface area quoted is for a gas of free electrons.

Parameter	Definition	Calculation	Approx. Value at Optimal T_C^*	
			Nb_3Sn	YBCO
$\rho_{N,s}$	Normal State Resistivity	$\rho_{N,s} = \frac{m_s}{n_s e^2 \tau_s}$	3.0×10^{-7} Ωm [174]	2.5×10^{-6} Ωm [175]
T_C^*	Critical Temperature	-	18 K [174]	93 K [43]
$S_{F,s}$	Fermi Surface Area	$S_{F,s} = 4\pi k_{F,s}^2$	5.0×10^{21} m^{-2}	1.0×10^{21} m^{-2}
γ_s	Electronic Specific Heat	$\gamma_s = \frac{2\pi^2}{3} g(E_{F,s}) k_B^2$	1100 $Jm^{-3}K^{-2}$ [173]	200 $Jm^{-3}K^{-2}$ [172]
$g(E_{F,s})$	Density of States	$g(E_{F,s}) = \frac{3\gamma_s}{2\pi^2 k_B^2}$	8.8×10^{47} $J^{-1}m^{-3}$	1.6×10^{47} $J^{-1}m^{-3}$
$k_{F,s}$	Fermi Wavevector	$k_{F,s} = \frac{\hbar^2 \pi^2 g(E_{F,s})}{m_s}$	2.0×10^{10} m^{-1}	9.1×10^{9} m^{-1}
n_s	Charge Carrier Density	$n_s = \frac{k_{F,s}^3}{3\pi^2}$	2.6×10^{29} m^{-3} [173]	2.6×10^{28} m^{-3}
m_s	Effective Mass	$m_s = \frac{3\hbar^2 \gamma_s}{2 k_{F,s} k_B^2}$	$5.4 m_e$	$2.1 m_e$
$\nu_{F,s}$	Fermi Velocity	$\nu_{F,s} = \frac{\hbar k_{F,s}}{m_s}$	4.2×10^{5} ms^{-1}	5.0×10^{5} ms^{-1} [22]
τ_s	Scattering Time	$\tau_s = \frac{m_s}{n_s e^2 \rho_{N,s}}$	2.5×10^{-15} s	1.2×10^{-15} s
l_s	Mean Free Path	$l_s = \nu_{F,s} \tau_s$	1.1×10^{-9} m	5.9×10^{-10} m
D_s	Diffusivity	$D_s = \frac{1}{3} \nu_{F,s}^2 \tau_s$	1.5×10^{-4} $m^2 s^{-1}$	9.8×10^{-5} $m^2 s^{-1}$

5.5.2 Superconducting Properties of Bulk Superconductors

In standard Ginzburg-Landau theory, there are three free parameters α_s, β_s and m_s. Here we also consider an additional free parameter, Υ_s as shown in Equation 2.4.1 in Chapter 2, which is repeated here:

$$g_s = f_n + \alpha_s |\psi|^2 + \frac{\beta_s}{2} |\psi|^4 + \frac{\Upsilon_s}{2m} |(-i\hbar \boldsymbol{\nabla} + 2e\boldsymbol{A})\psi|^2 + \frac{\boldsymbol{B}^2}{2\mu_0} - \boldsymbol{H_0} \cdot \boldsymbol{B} + \frac{\mu_0 \boldsymbol{H_0}^2}{2} \quad (5.5.1)$$

In this section, the free parameters are rewritten in terms of the characteristic fields B_{c2}^* and B_C^* (or $\kappa_s = \frac{B_{c2}^*}{\sqrt{2} B_C^*}$). We also reserve the starred values for the superconductor's critical fields to represent characteristic values of those critical fields that result from the underlying distribution of superconducting parameters in a real superconductor, due to, for example, micro-structural defects or variations in the superconductor's chemical composition. Distributions of critical superconducting parameters are considered comprehensively in Chapter 6.

We now assign the superconductor's temperature and strain dependence. The temperature dependence of B^*_{c2} is the same as that introduced in Equation 5.3.3, but the strain dependence is different. We have developed the following expression to parameterise $T^*_C(\varepsilon_{app})$:

$$T^*_C(\varepsilon_{app}) = T^*_C(0)\exp\left(1 - \left(1 + c_{\varepsilon 1}\varepsilon_{app} + c_{\varepsilon 2}\varepsilon^2_{app} + c_{\varepsilon 3}\varepsilon^3_{app} + c_{\varepsilon 4}\varepsilon^4_{app}\right)^2\right) \quad (5.5.2)$$

where the coefficients in front of the ε_{app}'s are constants. The advantage of this expression compared to a polynomial (often used in the literature) is that $T^*_C(\varepsilon_{app})$ always tends to zero at large compressive and tensile strains, regardless of the values of the 'c_ε' coefficients, which is consistent with experimental data. The strain dependence of B^*_{c2} is parameterised using a form of Equation 4.4.3

$$B^*_{c2}(0, \varepsilon_{app}) = B^*_{c2}(0,0)\left(\frac{T^*_C(\varepsilon_{app})}{T^*_C(0)}\right)^w. \quad (5.5.3)$$

To parameterise the temperature dependence of the thermodynamic critical field B^*_C we use [172]:

$$B^*_C(T, \varepsilon_{app}) = B^*_C(0, \varepsilon_{app})\left(1 - \left(\frac{T}{T^*_C(\varepsilon_{app})}\right)^2\right), \quad (5.5.4)$$

and along with the aforementioned temperature dependence of B^*_{c2}, this completely specifies the temperature dependence of the superconductor's in-field properties. The strain dependence of B^*_C is parameterised using [173, 176, 177]

$$B^*_C(0, \varepsilon_{app}) = B^*_C(0,0)\left(\frac{T^*_C(\varepsilon_{app})}{T^*_C(0)}\right)^1 \quad (5.5.5)$$

which is true regardless of regardless whether the superconductor is in a clean or dirty limit. The exponent here is unity because $B^*_C(0, \varepsilon_{app}) \propto T^*_C(\varepsilon_{app})^1$ and we have assumed that all of the strain dependence in $B^*_C(0, \varepsilon_{app})$ comes from the strain dependence of T^*_C.

To calculate Υ_s (and α_s and β_s) when it is not unity, we use a microscopic argument [178]. The critical aspect of the derivations of $|\alpha_s|$ and β_s is that the reduction in free-energy is only associated with that fraction of the conduction electrons within

Δ_s of the Fermi energy. We start by minimising Equation 2.4.1 in zero-field, which yields

$$f_s = g_s = -\frac{\alpha_s^2}{2\beta_s} \tag{5.5.6}$$

and

$$|\psi_s|^2 = \frac{|\alpha_s|}{\beta_s} = n_s. \tag{5.5.7}$$

Using microscopic theory,

$$g_s = -\frac{1}{2} g(E_{F,s}) \Delta_s^2, \tag{5.5.8}$$

and the empirical relation

$$n_s = g(E_{F,s}) \Delta_s, \tag{5.5.9}$$

we obtain

$$|\alpha_s| = \Delta_s. \tag{5.5.10}$$

We then write down β_s as:

$$\beta_s = g^{-1}(E_{F,s}). \tag{5.5.11}$$

Basic thermodynamic considerations give:

$$f_s = g_s = -\frac{B_{\mathrm{C}}^{*^2}}{2\mu_0}, \tag{5.5.12}$$

therefore,

$$|\alpha_s| = \Delta_s = \frac{B_{\mathrm{C}}^*}{\sqrt{\mu_0 g(E_{F,s})}}. \tag{5.5.13}$$

We can also write Δ_s using the famous BCS result in Equation 2.3.3, which means that $B_{\mathrm{C}}^*(0,0) = 1.76 k_B T_{\mathrm{C}}^*(0) \sqrt{\mu_0 g(E_{F,s})}$. The fit that introduces the factor Υ_s, allows the possibility for not all of the conduction electrons to contribute to the supercurrents that flow, and the value of Υ_s depends on whether the superconductor is in the clean or dirty limit. To calculate Υ_s, we can combine Equation 2.4.5, Equation 2.4.9 and the microscopic expression for α_s to obtain

$$\Upsilon_s = \frac{m_s |\alpha_s|}{e\hbar B_{\mathrm{c2}}^*} = \frac{2 m_s B_{\mathrm{C}}^*}{e\hbar B_{\mathrm{c2}}^* \sqrt{\mu_0 g(E_{F,s})}}. \tag{5.5.14}$$

For a fixed temperature and strain, the value of B^*_{c2} varies depending on whether the superconductor is clean or dirty. In the dirty limit [173, 179]

$$B^*_{c2}(0,0) = \frac{12e}{\pi^3 k_B}\rho_{N,s}\gamma_s T^*_C(0). \tag{5.5.15}$$

Hence we have expressions for α_s, β_s and Υ_s in terms of normal state properties.

5.5.3 The Normal State and Superconducting Properties of Barriers

We now define the normal state and superconducting properties of the normal barrier in the Josephson junction. The normal state properties of the barrier are denoted using the same symbols as those for the superconductor in Table 5.4, except with the 's' subscript replaced by 'n'. For example, the number density of charge carriers in the normal barrier would be n_n. The only exception is the critical temperature of the normal barrier, which is denoted using $T^*_{C,n}$. In a similar way to the superconductor, in the dirty limit, all of the in-field properties of the normal barrier could be calculated if 2 of the normal state properties and the critical temperature were known.

For the temperature dependence of the normal barrier parameters, we assume that both $B^*_{c2,n}$ and $B^*_{C,n}$ have a simple linear temperature dependence, in other words:

$$B^*_{c2,n}(T) = B^*_{c2,n}(0)\left(1 - \frac{T}{T^*_{C,n}}\right) \tag{5.5.16}$$

and

$$B^*_{C,n}(T) = B^*_{C,n}(0)\left(1 - \frac{T}{T^*_{C,n}}\right). \tag{5.5.17}$$

We also assume that $T^*_{C,n}$, $B^*_{c2,n}$ and $B^*_{C,n}$ are independent of strain, the normal barrier thickness d has a simple linear strain dependence for Nb_3Sn:

$$d(\varepsilon_{\text{app}}) = d(0)\left(1 + d_{\varepsilon,1}\right), \tag{5.5.18}$$

where $d_{\varepsilon,1}$ is a constant. For (RE)BCO, we assume that the normal barrier thickness has the following temperature and strain dependence:

$$d(T,\varepsilon_{\mathrm{app}}) = d(0) + \zeta_1\left(\frac{T}{T_{\mathrm{C}}^*(\varepsilon_{\mathrm{app}})}\right) + \zeta_2\left(\frac{T}{T_{\mathrm{C}}^*(\varepsilon_{\mathrm{app}})}\right)^2, \tag{5.5.19}$$

and the normal barrier width w_s has the following temperature and strain dependence:

$$w_s(T,\varepsilon_{\mathrm{app}}) = w_s(0) - \left(\zeta_1\left(\frac{T}{T_{\mathrm{C}}^*(\varepsilon_{\mathrm{app}})}\right) + \zeta_2\left(\frac{T}{T_{\mathrm{C}}^*(\varepsilon_{\mathrm{app}})}\right)^2\right), \tag{5.5.20}$$

where ζ_1 and ζ_2 are constants. The temperature and strain dependent terms represent a correction to the barrier dimensions due to the temperature and strain varying coherence length $\xi_s(T,\varepsilon_{\mathrm{app}})$ [180] and distributions of critical superconducting parameters close to the barrier. Section 5.8 discusses this in more detail. Similar to the calculations for α_s, β_s and Υ_s in Section 5.5.2, we can use microscopic theory to calculate α_n, β_n and Υ_n for the normal barrier. We can also write down expressions for $B_{\mathrm{C},n}^*(0)$ and $B_{\mathrm{c2},n}^*(0)$ using the same approach as before. Table 5.5 shows the final expressions for the α, β and Υ values for the superconducting electrodes and normal barrier of the SNS Josephson junction, as well as the values in the barrier normalised to the values in the superconducting electrodes.

Table 5.5: Expressions for α, β and Υ (and $\tilde{m}_n/\tilde{\Upsilon}_n(0,0)$) in terms of superconducting properties and normal state properties, for the 2 types of fit performed to each dataset.

Parameter	Expression	
	$\Upsilon_s = \Upsilon_n = 1$	Υ_s and Υ_n are free parameters
α_s	$\frac{-\pi\hbar^2 B^*_{\mathrm{c2}}(0,0)}{2\phi_0 m_s}\left(\frac{T^*_{\mathrm{C}}(\varepsilon_{\mathrm{app}})}{T^*_{\mathrm{C}}(0)}\right)^w (1-t^{*^\nu})$	$-1.76k_B T^*_{\mathrm{C}}(0)\frac{T^*_{\mathrm{C}}(\varepsilon_{\mathrm{app}})}{T^*_{\mathrm{C}}(0)}\left(1-t^{*^2}\right)$
α_n	$\frac{\pi\hbar^2 B^*_{\mathrm{c2},n}(0)}{2\phi_0 m_n}\left(\frac{T}{T^*_{\mathrm{C},n}}-1\right)$	$-1.76k_B T^*_{\mathrm{C},n}\left(1-\frac{T}{T^*_{\mathrm{C},n}}\right)$
$\tilde{\alpha}_n$	$-\tilde{B}^*_{\mathrm{c2},n}(0,0)\tilde{m}_n^{-1}\left(\frac{T^*_{\mathrm{C}}(\varepsilon_{\mathrm{app}})}{T^*_{\mathrm{C}}(0)}\right)^{-w}\frac{\frac{T}{T^*_{\mathrm{C},n}}-1}{1-t^{*^\nu}}$	$\tilde{T}^*_{\mathrm{C},n}(0)\left(\frac{T^*_{\mathrm{C}}(\varepsilon_{\mathrm{app}})}{T^*_{\mathrm{C}}(0)}\right)^{-1}\frac{1-\frac{T}{T^*_{\mathrm{C},n}}}{1-t^{*^2}}$
$\tilde{\alpha}_n(0,0)$	$\tilde{\rho}_{N,n}\tilde{g}(E_{F,n})\tilde{T}^*_{\mathrm{C},n}(0)\tilde{m}_n^{-1}$	$\tilde{T}^*_{\mathrm{C},n}(0)$
β_s	$\frac{\mu_0 e^2\hbar^2}{4m_s^2}\left(\frac{B^*_{\mathrm{c2}}(0,0)}{B^*_{\mathrm{C}}(0,0)}\right)^2\left(\frac{T^*_{\mathrm{C}}(\varepsilon_{\mathrm{app}})}{T^*_{\mathrm{C}}(0)}\right)^{2w-2}\left(\frac{1-t^{*^\nu}}{1-t^{*^2}}\right)^2$	$g^{-1}(E_{F,s})$
β_n	$\frac{\mu_0 e^2\hbar^2}{4m_n^2}\left(\frac{B^*_{\mathrm{c2},n}(0)}{B^*_{\mathrm{C},n}(0)}\right)^2$	$g^{-1}(E_{F,n})$
$\tilde{\beta}_n$	$\left(\frac{\tilde{B}^*_{\mathrm{c2},n}(0,0)}{\tilde{B}^*_{\mathrm{C},n}(0,0)\tilde{m}_n}\right)^2\left(\frac{T^*_{\mathrm{C}}(\varepsilon_{\mathrm{app}})}{T^*_{\mathrm{C}}(0)}\right)^{2-2w}\left(\frac{1-t^{*^2}}{1-t^{*^\nu}}\right)^2$	$\tilde{g}^{-1}(E_{F,n})$
$\tilde{\beta}_n(0,0)$	$\tilde{\rho}^2_{N,n}\tilde{g}(E_{F,n})\tilde{m}_n^{-2}$	$\tilde{g}^{-1}(E_{F,n})$
Υ_s	1	$\frac{3.52k_B T^*_{\mathrm{C}}(0)m_s}{e\hbar B^*_{\mathrm{c2}}(0,0)}\left(\frac{T^*_{\mathrm{C}}(\varepsilon_{\mathrm{app}})}{T^*_{\mathrm{C}}(0)}\right)^{1-w}\frac{1-t^{*^2}}{1-t^{*^\nu}}$
Υ_n	1	$\frac{3.52k_B T^*_{\mathrm{C},n}m_n}{e\hbar B^*_{\mathrm{c2},n}(0)}$
$\tilde{\Upsilon}_n$	1	$\tilde{T}_{\mathrm{C},n}(0)\tilde{m}_n\tilde{B}^*_{\mathrm{c2},n}(0,0)^{-1}\left(\frac{T^*_{\mathrm{C}}(\varepsilon_{\mathrm{app}})}{T^*_{\mathrm{C}}(0)}\right)^{w-1}\frac{1-t^{*^\nu}}{1-t^{*^2}}$
$\tilde{m}_n/\tilde{\Upsilon}_n(0,0)$	$\tilde{m}_n$	$\tilde{\rho}_{N,n}\tilde{g}(E_{F,n})$

5.6 SNS Josephson Junction Model Formalism

Although flux pinning theory has provided a useful qualitative description of J_C, and has contributed to providing support for physical principles for increasing J_C values in many technological superconductors (such as through the addition of APC's in (RE)BCO [181, 182] or the refinement of grain size in Nb_3Sn [61]), it struggles to provide a quantitative description of the materials because it is extremely difficult to know how all the individual vortex-pin and vortex-vortex interactions that occur on a mesoscopic scale in a superconductor lead to a macroscopic J_C value. Furthermore, the flux pinning scaling law fit given above for the APC (RE)BCO sample has also highlighted that the pinning framework doesn't even meet the basic requirement of parameterising the data properly, since obtaining a good fit requires non-physical values of B^*_{c2}.

As was shown in Chapter 2, minimising the functional leads to the two famous G-L equations with solutions for the wave function order parameter usually in the form $\psi_s = |\psi_s| e^{i\theta}$ where θ is not gauge invariant. Here we briefly outline the SNS Josephson junction approach of Blair and Hampshire (BH) [133] where the material properties are uniform in the superconducting electrode and the normal barrier. In the barrier, the two normalised gauge-invariant G-L equations are:

$$\left[\frac{\tilde{\Upsilon}_n}{\tilde{m}_n}\left(\tilde{\nabla}^2 - \left(\tilde{\boldsymbol{\nabla}}\gamma\right)^2\right) + \tilde{\alpha}_n - \tilde{\beta}_n\left|\tilde{\psi}^2\right|\right]\tilde{\psi} = 0 \tag{5.6.1}$$

and

$$\tilde{\boldsymbol{J}}_s = \frac{\tilde{\Upsilon}_n}{\tilde{m}_n}\left|\tilde{\psi}^2\right|\tilde{\boldsymbol{\nabla}}\gamma \tag{5.6.2}$$

where the tilde symbols denote standard normalised parameters, the subscripts denote ratios with respect to the superconducting electrodes (for example, $\tilde{\alpha}_n = \alpha_n/\alpha_s$) and the gauge invariant phase γ is given by $\tilde{\boldsymbol{\nabla}}\gamma = \tilde{\boldsymbol{\nabla}}\theta - \tilde{\boldsymbol{A}}$ where $\tilde{\boldsymbol{A}}$ is the normalised magnetic vector potential in the junction. Table 5.6 contains all of the parameter normalisations that are used in this section.

In the limit that the junction system is very narrow (i.e., $w_s < \xi_s$ where w_s is the

junction width), Equation 5.6.1 can be integrated over the y-direction to give

$$\left[\frac{\tilde{\Upsilon}_n}{\tilde{m}_n}\partial_x^2 + \tilde{\alpha}_n - \frac{\tilde{\Upsilon}_n}{\tilde{m}_n}q^2 - \tilde{\beta}_n\left|\tilde{\psi}\right|^2 - \frac{\tilde{m}_n}{\tilde{\Upsilon}_n}\frac{\left\langle \tilde{J}_{s;x}\right\rangle_y^2}{\left|\tilde{\psi}\right|^4}\right]\tilde{\psi} = 0 \tag{5.6.3}$$

where $q^2 = \frac{1}{12}\left(\frac{Bw_s}{B^*_{c2}\xi_s}\right)^2$ is a field dependent pair breaking term and

$$\left\langle \tilde{J}_{s;x}\right\rangle_y = \frac{\tilde{\Upsilon}_n}{\tilde{m}_n}\left(\partial_x\gamma - \tilde{B}\tilde{y}\right) \tag{5.6.4}$$

is the supercurrent density in the x-direction averaged over the y-direction, with $\tilde{B} = B/B^*_{c2}$ with B being the applied field and $\tilde{y} = y/\xi_s$.

Table 5.6: Definition of units used in the normalised TDGL equations (Equations 5.6.1 and 5.6.2).

Symbol	Normalisation	Interpretation
$\tilde{\boldsymbol{r}}$	$\xi_s = \hbar\sqrt{\frac{\Upsilon_s}{-2m\alpha_s}}$	Position Vector
$\tilde{t}$	$\tau_s = \frac{\mu_0\lambda_s^2}{\rho_{N,s}}$	Time
$\tilde{\psi}$	$\lvert\psi_0\rvert = \sqrt{-\frac{\alpha_s}{\beta_s}}$	Order Parameter
$\tilde{\boldsymbol{A}}$	$A_0 = \frac{\phi_0}{2\pi\xi_s}$	Magnetic Vector Potential
φ	$\varphi_0 = \frac{\phi_0}{2\pi\tau_s}$	Electrostatic Potential
$\tilde{\boldsymbol{B}}$	$B^*_{c2} = \frac{\phi_0}{2\pi\xi_s^2}$	Magnetic Induction
$\tilde{\boldsymbol{E}}$	$E = \frac{\phi_0}{2\pi\tau_s\xi_s}$	Electric Field
$\tilde{\boldsymbol{J_s}}$	$J_s = \frac{\phi_0}{2\pi\mu_0\kappa_s^2\xi_s^3}$	Current Density
f_s	$F = \frac{\phi_0^2}{8\pi^2\mu_0\kappa_s^2\xi_s}$	Free Energy
$\tilde{\alpha}_n$	$\frac{\alpha_n}{\alpha_s}$	Relative Condensation Parameter
$\tilde{\beta}_n$	$\frac{\beta_n}{\beta_s}$	Relative Nonlinearity Parameter
$\tilde{m}_n$	$\frac{m_n}{m_s}$	Relative Effective Mass
$\tilde{\Upsilon}_n$	$\frac{\Upsilon_n}{\Upsilon_s}$	Relative 'Upsilon' Parameter

Equation 5.6.3 can be rescaled and solved using Jacobi elliptic functions following the zero-field approach of Fink [183] to find the maximum current density that the junction system can carry without loss (denoted using J_{DJ}), for very narrow, thick junctions in high fields up to B^*_{c2}. The resulting expression is:

$$\lim_{d\gg\xi_s>w_s}\{J_{\mathrm{DJ}}(B)\} = 4J_s\left(1-q^2\right)^{3/2}\frac{1-\sqrt{1-\tilde{s}\tilde{f}_{d/2}^2}}{\tilde{s}\tilde{v}}\exp\left(-\frac{\tilde{d}}{\tilde{\xi}_n}\right) \tag{5.6.5}$$

where $\tilde{d} = d/\xi_s$ and

$$\tilde{f}_{d/2}^2 = \frac{\tilde{v}^2 + 1 - \sqrt{\tilde{v}^2\,(2-\tilde{s}) + 1}}{\tilde{v}^2 + \tilde{s}}, \tag{5.6.6}$$

with

$$\tilde{s} = \frac{\tilde{\beta}_n(1-b^*)}{\tilde{\alpha}_n - \left(\frac{\tilde{m}_n}{\tilde{\Upsilon}_n(T,\varepsilon_{\rm app})}\right)^{-1} b^*}, \tag{5.6.7}$$

and

$$\tilde{v} = \frac{\tilde{m}_n}{\tilde{\Upsilon}_n(T,\varepsilon_{\rm app})}\tilde{\xi}_n\sqrt{1-b^*}, \tag{5.6.8}$$

and

$$\tilde{\xi}_n = \sqrt{\left(\frac{\tilde{m}_n}{\tilde{\Upsilon}_n(T,\varepsilon_{\rm app})}\right)^{-1} \frac{1}{-\tilde{\alpha}_n + \left(\frac{\tilde{m}_n}{\tilde{\Upsilon}_n(T,\varepsilon_{\rm app})}\right)^{-1} b^*}} \tag{5.6.9}$$

and J_s can be written out fully as

$$J_s(T,\varepsilon_{\rm app}) = \frac{\sqrt{2}B_{\rm C}^*(0,0)}{\mu_0\lambda_L(0,0)}\left(\frac{T_{\rm C}^*(\varepsilon_{\rm app})}{T_{\rm C}^*(0)}\right)^{2-\frac{w}{2}}\left(1-t^{*^\nu}\right)^{-\frac{1}{2}}\left(1-t^{*^2}\right)^2 \tag{5.6.10}$$

where BH used the London penetration depth in order to recover the standard expression for the depairing current density at zero strain and zero temperature. We note that for anisotropic superconductors such as (RE)BCO, the J_s for the transport current flow direction should be used. Using Clem's high field results [131], BH assume that the junction width w_s is replaced by the fluxon-fluxon spacing a_0, so that

$$J_{\rm C} = c_0\left(\frac{\phi_0}{B_{\rm app}w_s^2}\right)^{c_1} J_{\rm DJ}(w_s \to a_0). \tag{5.6.11}$$

Clem's work shows that $c_0 \approx 0.3/c_1$ for junctions with a wide range of aspect ratios [133, 184] and by combining this with Equation 5.6.5 and Equation 5.6.11 we ultimately arrive at

$$J_{\rm C} = \frac{1.2}{c_1}\left(\frac{\phi_0}{B_{\rm app}w_s^2}\right)^{c_1} J_s(1-b^*)^{\frac{3}{2}}\frac{1-\sqrt{1-\tilde{s}\tilde{f}_{d/2}^2}}{\tilde{s}\tilde{v}}\exp\left(-\frac{\tilde{d}}{\tilde{\xi}_n}\right). \tag{5.6.12}$$

In all fits, the constraint $J_{\rm C}(B_{\rm cr}) < J_{\rm DJ}$ for $B = B_{cr}$ where B_{cr} is the crossover field [184] must be included. For the (RE)BCO samples considered here, w_s had to be larger than 2×10^2 nm, as the value of c_0 was close to 0.5. We will find that the final fit values of $\approx 230-240$ nm suggest that $J_{\rm C}$ is close to $J_{\rm DJ}$ in these samples.

The fit parameters $\tilde{\alpha}_n(0,0)$, $\tilde{\beta}_n(0,0)$ and $\tilde{m}_n/\tilde{\Upsilon}_n(0,0)$ can be rewritten in terms of normal state properties of the barrier relative to the superconductor, as shown in Table 5.5. This therefore allows us to extract some of these properties, and the normal state properties of the barrier, when taken in conjunction with the values for the superconductor in Table 5.4. For the parameter fits where Υ_n and Υ_s are not fixed at 1, $\alpha_n(0,0)$ is a combination of two other free parameters, $T_C^*(0)$ and $T_{C,n}^*$, so $\alpha_n(0,0)$ is not a free parameter in those fits. Hence it is not possible to calculate all of the normal state properties because knowledge of $\tilde{\rho}_{N,n}$ and $\tilde{g}(E_{F,n})$ alone is not enough to calculate all of the other normal state properties.

5.7 Using the SNS Josephson Model to Fit J_C Data

The fits to the J_C data using Equation 5.6.12 for the SuperPower APC (RE)BCO sample, the SuperPower Non-APC sample, and Nb_3Sn sample are now presented. The fits to the J_C data for APC (RE)BCO are shown in Figures 5.9, 5.10, 5.11, and 5.12 and the fits to the J_C data for Non-APC (RE)BCO are shown in Figures 5.9, 5.13, 5.14, and 5.15. The fits to the J_C data for Nb_3Sn are shown in Figures 5.16 and 5.17. At large compressive strains, $J_C(\varepsilon_{app})$ tends to zero. The fit is similar in quality to the flux pinning fit reported by Branch [28] (indeed, the flux pinning fit for Nb_3Sn by Branch and the SNS Josephson junction fits here have RMS errors of around 0.02 GAm^{-2}).

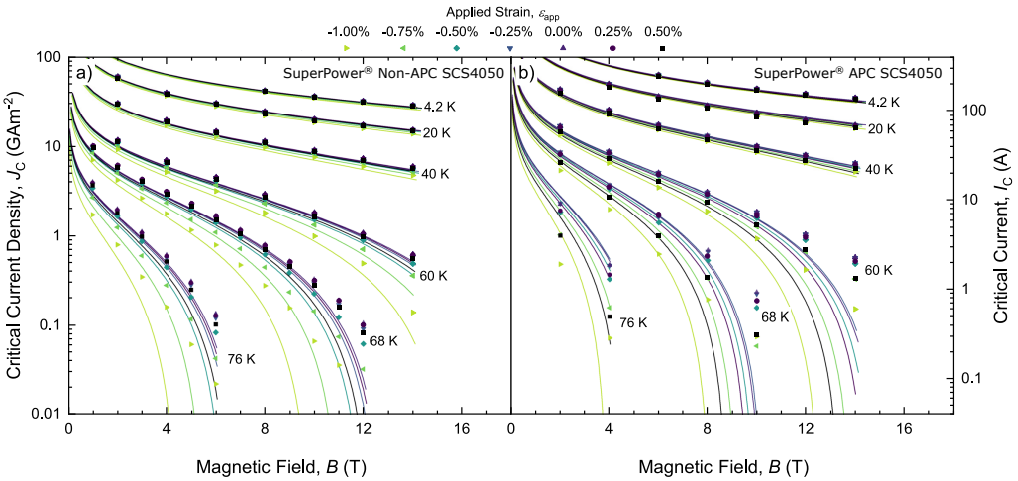

Figure 5.9: $J_C(B)$ for both (RE)BCO samples, for $\theta = 0°$. The fit lines correspond to the $\tilde{\Upsilon}_n$ free fits.

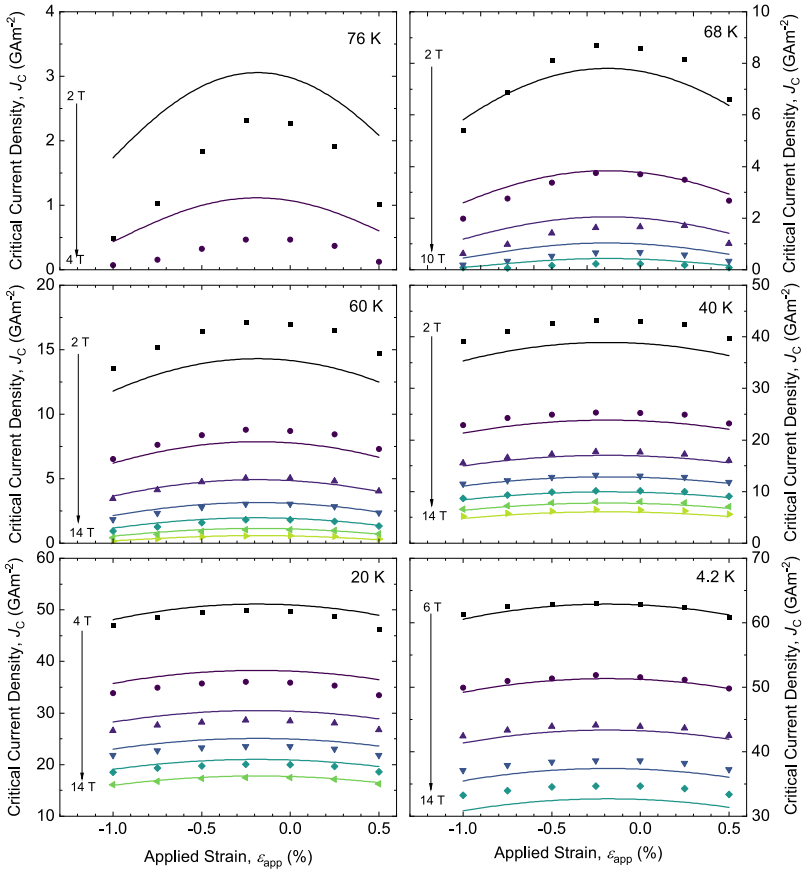

Figure 5.10: $J_C(\varepsilon_{app})$ for the SuperPower APC sample, for $\theta = 0°$. The fit lines correspond to the $\Upsilon_s = \Upsilon_n = 1$ fit.

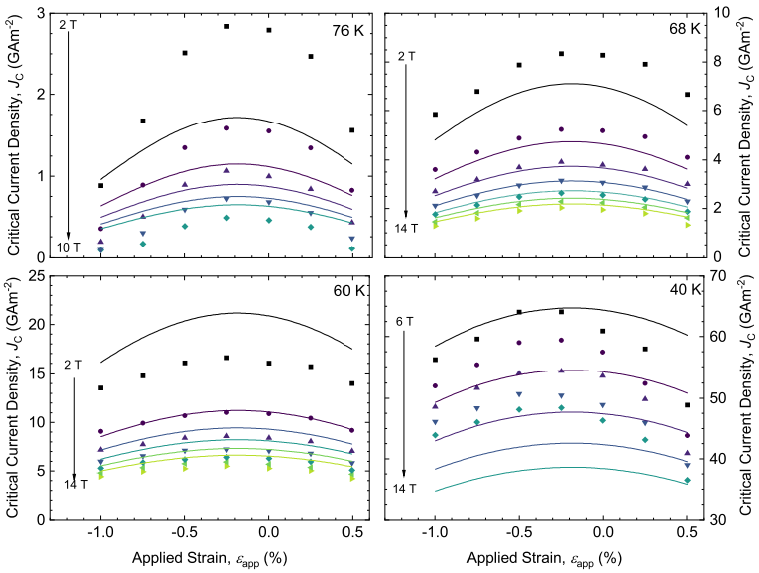

Figure 5.11: $J_C(\varepsilon_{app})$ for the SuperPower APC sample, for $\theta = 87.5°$. The fit lines correspond to the $\Upsilon_s = \Upsilon_n = 1$ fit.

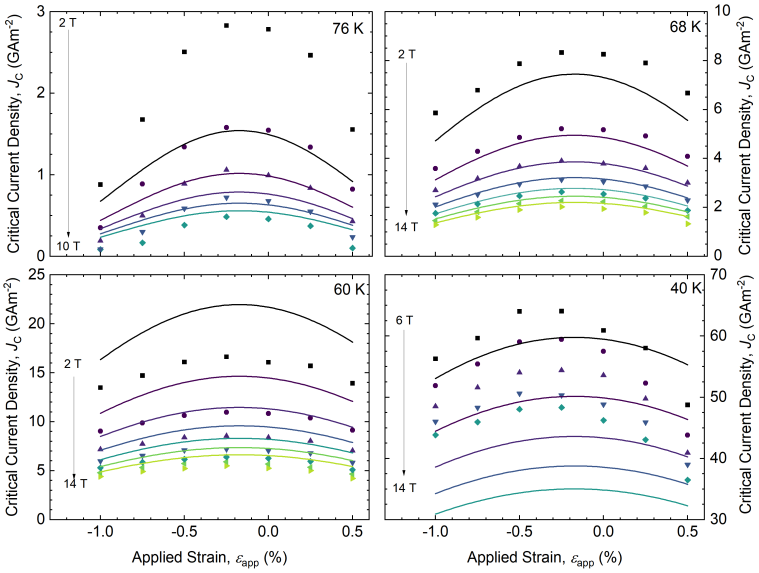

Figure 5.12: $J_C(\varepsilon_{app})$ for the SuperPower APC sample, for $\theta = 87.5°$. The fit lines correspond to the $\tilde{\Upsilon}_n$ free fit.

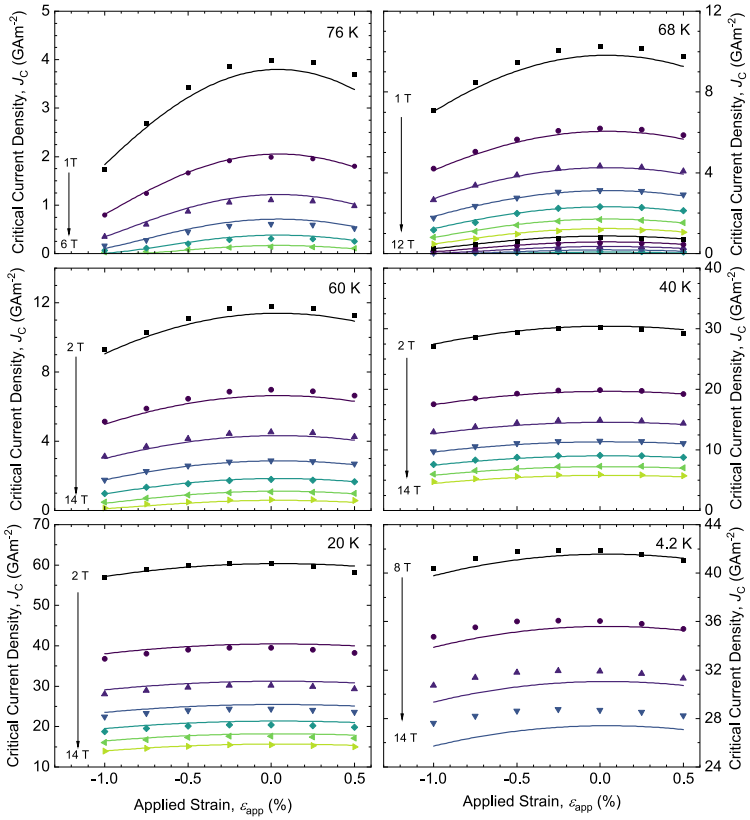

Figure 5.13: $J_C(\varepsilon_{app})$ for the SuperPower Non-APC sample, for $\theta = 0°$. The fit lines correspond to the $\Upsilon_s = \Upsilon_n = 1$ fit.

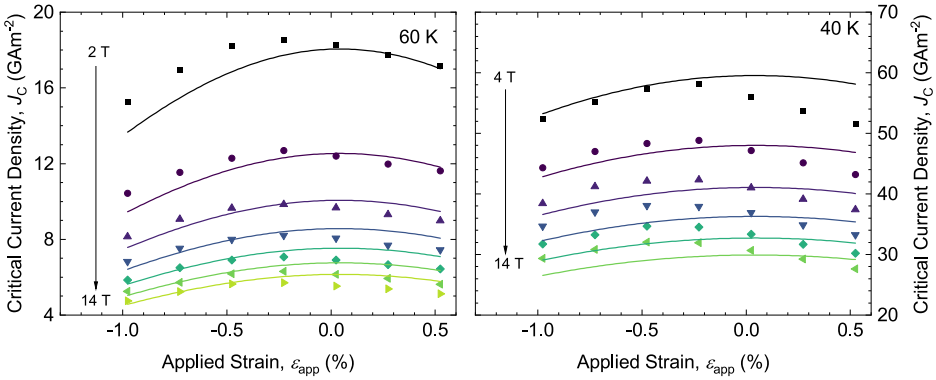

Figure 5.14: $J_C(\varepsilon_{app})$ for the SuperPower Non-APC sample, for $\theta = 87.5°$. The fit lines correspond to the $\Upsilon_s = \Upsilon_n = 1$ fit.

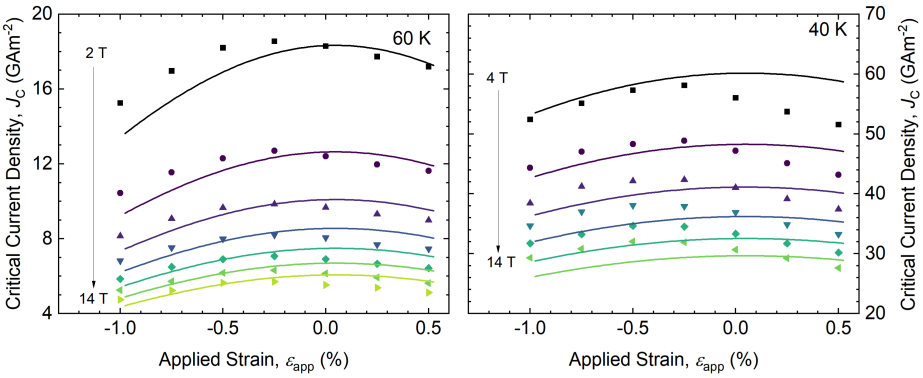

Figure 5.15: $J_C(\varepsilon_{app})$ for the SuperPower Non-APC sample, for $\theta = 87.5°$. The fit lines correspond to the $\tilde{\Upsilon}_n$ free fit.

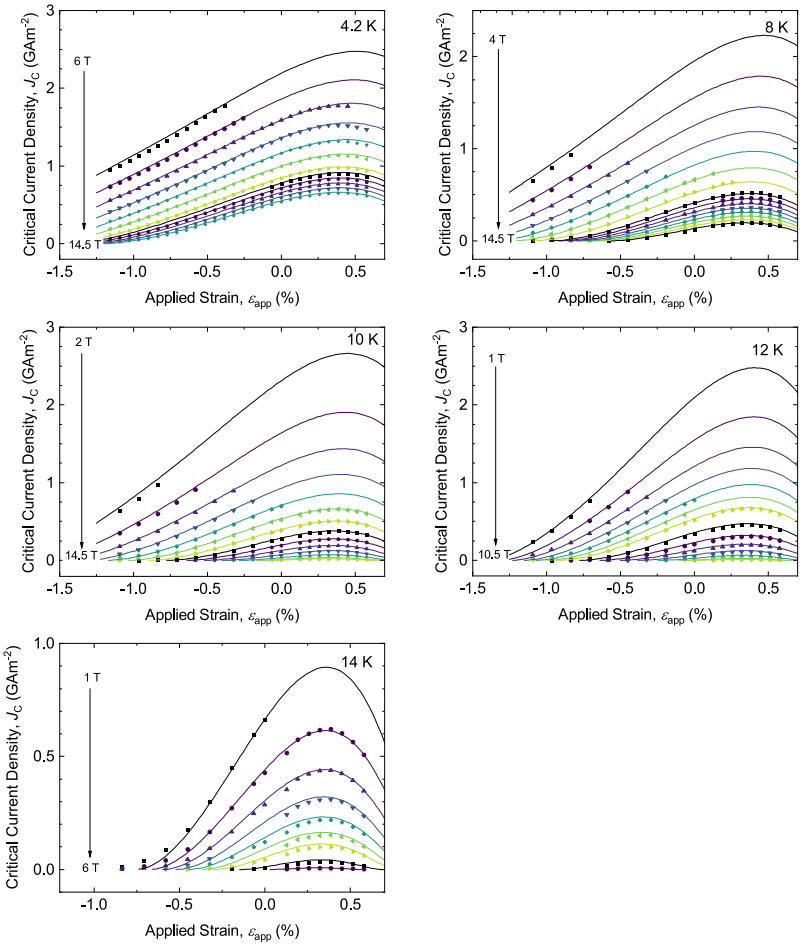

Figure 5.16: $J_C(\varepsilon_{app})$ for Nb_3Sn for different temperatures and applied magnetic fields.The fit lines correspond to the fit where $\tilde{\Upsilon}_n$ free fit.

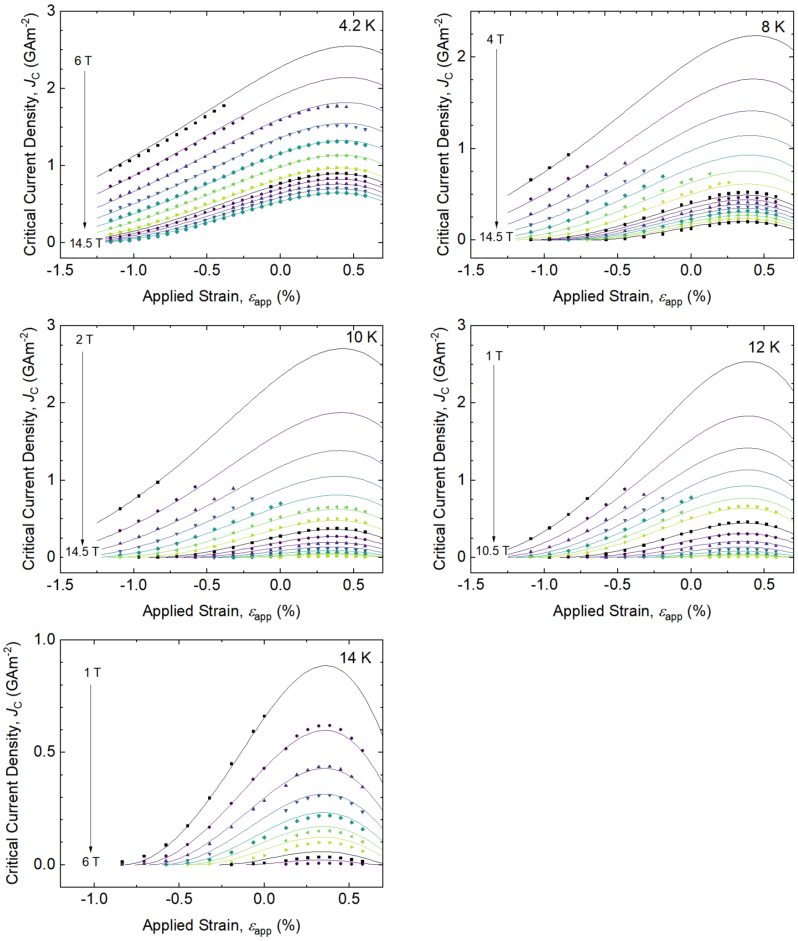

Figure 5.17: $J_C(\varepsilon_{app})$ for Nb_3Sn for different temperatures and applied magnetic fields.The fit lines correspond to the $\Upsilon_s = \Upsilon_n = 1$ fit.

We note that for both (RE)BCO samples, fits were performed for 0° and 87.5° separately. The 0° fits were performed first and many of the fit parameters for the 87.5° orientation were fixed using the values from 0°. In the Nb_3Sn fits, any J_C data below 0.02 GAm^{-2} were excluded from the fit, because these low J_C datapoints caused the non-linear least squares fitting algorithm to tend towards poor local minima in the error surface. Low J_C data were also excluded from the APC (RE)BCO and Non-APC (RE)BCO fits too, in this case all J_C data below 0.5 GAm^{-2}. As J_C data for the (RE)BCO samples were only measured at 7 different applied strains, it wasn't necessary to include 3rd and 4th order terms in Equation 5.5.2 for those samples.

Having a non-zero value of $d_{\varepsilon,1}$ leads to ε_{peak} having some field and temperature

dependence. Figure 5.18 shows the fit to $\varepsilon_{\text{peak}}$ for the Nb_3Sn sample. No analytic expression could be found for $\varepsilon_{\text{peak}}$ by taking the derivative of Equation 5.6.12 with respect to strain, so the fit lines were produced by finding the values of $\varepsilon_{\text{peak}}$ numerically. The strain dependencies in Equations 5.5.19 and 5.5.20 do not lead to significant varying $\varepsilon_{\text{peak}}$ values.

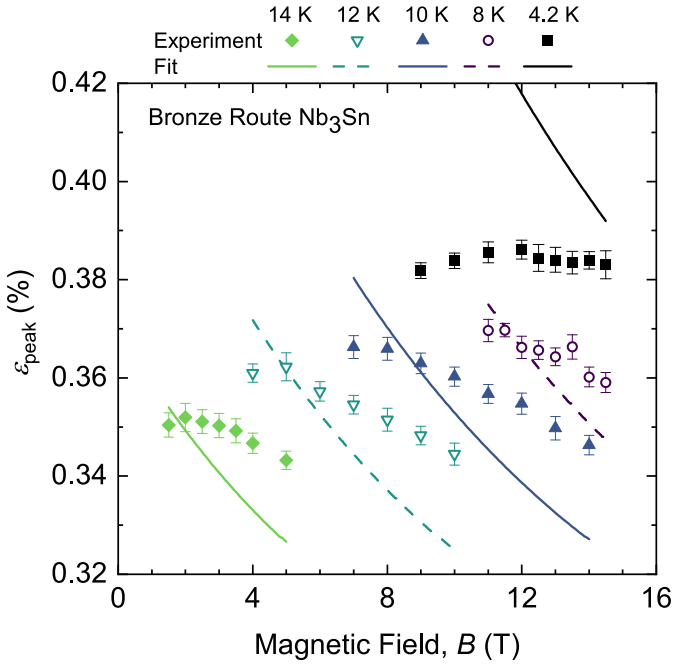

Figure 5.18: $\varepsilon_{\text{peak}}$ for the Nb_3Sn sample. The fit lines were generated using the fit where $\tilde{\Upsilon}_n$ was not fixed at 1. The $\varepsilon_{\text{peak}}$ values were taken from parabolic fits performed by Branch [28].

Table 5.7 shows the resultant fit parameters for all 3 samples. We note that some of the fit parameters are highly correlated. We found that the correlation matrices for the fits did not always provide a good measure of the strength of the correlations as a whole, due to the complex shapes of the error surfaces. Nevertheless, inspection of Table 5.7 shows that reasonable values for the physical parameters are obtained as discussed in the next section. It was found that a large range of $\tilde{\beta}_n$ values led to equally good fits for the $\tilde{\Upsilon}_n$ free fits, as highlighted by examples of the fit error surfaces in Figure 5.19. For this reason, the density of states ratio $\tilde{g}(E_{F,n})$ was fixed at 1 in all fits, which meant that $\tilde{\beta}_n$ was fixed at 1 for the $\tilde{\Upsilon}_n$ free fits and $\tilde{\beta}_n(0,0)$ could be written as $\tilde{\beta}_n(0,0) = \tilde{\alpha}_n^2(0,0)\tilde{T}_{C,n}^{*-2}(0)$ for the $\Upsilon_s = \Upsilon_n = 1$ fits.

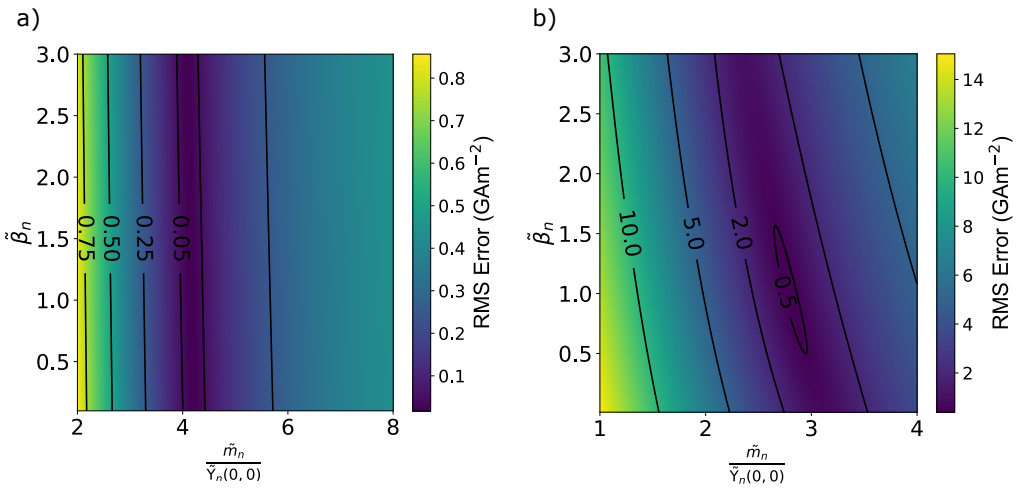

Figure 5.19: a) Error surface for Nb_3Sn for the fit with $\tilde{\Upsilon}_n$ as a free parameter. b) Error surface for Non-APC (RE)BCO, for $\theta = 0°$ and $\tilde{\Upsilon}_n$ as a free parameter.

Table 5.7: Fit parameters for the SNS model fits. Bold parameters were fixed from the literature or set at zero to reduce the number of free parameters. For both (RE)BCO samples, for 87.5°, the italicised values were fixed at the 0° values. The starred value (*) of $w_s = 450$ nm was fixed from microscopy (see the references in [90]) and a factor of π to account for sphericity of grains. The dagger values (†) of $\tilde{\alpha}_n(0,0)$ were not free parameters as $\tilde{\alpha}_n(0,0) = \tilde{T}^*_{C,n}(0)$ when $\tilde{\Upsilon}_n$ is free (see Table 5.5).

		Nb_3Sn $\tilde{\Upsilon}_n$ free, $\Upsilon_s = \Upsilon_n = 1$	(RE)BCO (Non-APC) $\tilde{\Upsilon}_n$ free, $\Upsilon_s = \Upsilon_n = 1$		(RE)BCO (APC) $\tilde{\Upsilon}_n$ free, $\Upsilon_s = \Upsilon_n = 1$	
Constraint Type	Parameter		0°	87.5°	0°	87.5°
Fit parameters	$w_s(0)$ (nm)	**450***, **450*** [90]	334, 244	242, 245	234, 237	234, 237
	$d(0)$ (nm)	2.79, 3.14	0.584, 0.540	0.219, 0.0621	0.400, 0.400	0.0401, 0.0418
	c_1	0.524, 0.605	0.510, 0.504	*0.510*, *0.504*	0.559, 0.559	*0.559*, *0.559*
	$\lambda_L(0,0)$ (nm)	**93.5**, **93.5** [22]	**135**, **135** [22]	***135***,***135***	**135**, **135** [22]	***135***,***135***
	$T^*_C(0)$ (K)	16.3, 16.5	86.3, 88.1	*86.3*, *88.1*	87.0, 91.0	*87.0*, *91.0*
	$B^*_{c2}(0,0)$ (T)	30.6, 31.5	94.2, 73.5	**240**, **240** [164]	112, 83.8	**240**, **240** [164]
	ν	1.40, 1.49	0.616, 0.795	4.50, 3.67	0.387, 0.629	7.68, 6.05
	$c_{\varepsilon 1}$ ($10^{-3}\%^{-1}$)	−51.7, −51.0	−1.81, −1.63	*-1.81*, *-1.63*	9.44, 9.52	*9.44*, *9.52*
	$c_{\varepsilon 2}$ ($10^{-3}\%^{-2}$)	58.2, 55.8	18.6, 19.0	*18.6*, *19.0*	27.3, 25.5	*27.3*, *25.5*
	$c_{\varepsilon 3}$ ($10^{-3}\%^{-3}$)	43.3, 41.3	**0**	***0***	**0**	***0***
	$c_{\varepsilon 4}$ ($10^{-3}\%^{-4}$)	39.9, 12.3	**0**	***0***	**0**	***0***
	w	2.45, 2.52	**2.2**, **2.2** [67]	***2.2***, ***2.2***	**2.2**, **2.2** [67]	***2.2***, ***2.2***
	$d_{\varepsilon 1}$ ($10^{-3}\%^{-1}$)	−60.5, −63.8	**0**, **0**	***0***, ***0***	**0**, **0**	***0***, ***0***
	ζ_1 (nm)	**0**, **0**	2.64, 1.97	**0**, **0**	1.85, 3.19	0.246, −1.20
	ζ_2 (nm)	**0**, **0**	−1.50, −0.985	1.35, 1.85	−0.923, 1.60	1.53, 3.75
	$\tilde{\alpha}_n(0,0)$	$-3.23^\dagger$, −2.34	$-1.51^\dagger$, −1.35	$-1.51^\dagger$, −0.893	$-1.90^\dagger$, −1.14	$-1.90^\dagger$, −0.876
	$\tilde{\beta}_n(0,0)$	**1**, $1.49^\dagger$	**1**, $0.410^\dagger$	***1***, $0.179^\dagger$	**1**, $0.193^\dagger$	***1***, $0.114^\dagger$
	$\frac{\tilde{m}_n}{\tilde{\Upsilon}_n(0,0)}$	4.35, 2.70	2.80, 7.32	4.01, 5.95	3.92, 3.64	2.15, 5.52
	$T^*_{C,n}$ (K)	−52.5, −31.6	−130, −186	*-130*, *-186*	−165, −236	*-165*, *-236*
Calculated parameters	$J_s(0,0)$ (GAm^{-2})	9130, 9280	7690, 6790	7690, 6790	8380, 7250	8380, 7250
	$\tilde{g}(E_{F,n})$	1, 1	1, 1	1, 1	1, 1	1, 1
	$\tilde{\rho}_{N,n}$	7.83, 3.29	2.80, 4.69	4.01, 2.51	3.92, 1.63	2.15, 1.86
	$\tilde{n}_n$	n/a, 0.0506	n/a, 2.55×10^{-3}	n/a, 4.76×10^{-3}	n/a, 0.0207	n/a, 5.94×10^{-3}
	$\tilde{\tau}_n$	n/a, 16.2	n/a, 614	n/a, 497	n/a, 108	n/a, 187
	$\tilde{l}_n$	n/a, 2.22	n/a, 11.4	n/a, 14.1	n/a, 8.14	n/a, 6.11
RMS J_c Error (GAm^{-2})		0.0208, 0.0259	0.396, 0.543	1.82, 1.69	1.22, 1.38	4.51, 3.22

5.8 Discussion

5.8.1 $B_{c2}^{*\rho}$ and T_C^*

The $B_{c2}^{*\rho}$ measurements in this work indicate that there may be quite a broad range of T_C within the (RE)BCO layer, as the resistive transition spans several kelvin (in both zero field and in-field), and the value of $T_C^{*\rho}$ itself is quite low, at ≈ 84 - 87 K compared to ideal single crystal values. This low value of $T_C^{*\rho}$ is probably due to the strain fields in the (RE)BCO matrix that are caused by the APC's [185]. Conversely, the values of $B_{c2}^{*\rho}(0,0)$ for $\theta = 0°$ are higher by about 20 T in our tape that contains APC's compared to the sample that do not contain APC's. This could be, for example, due to enhanced superconductivity in the vicinity of the nanorods, that locally causes $B_{c2}^{*\rho}$ to increase towards the surface critical field B_{c3}. At temperatures close to T_C^* where the resistive measurements are performed, the coherence length is much larger than the diameters of the nanorods, so it is unlikely that the enhanced $B_{c2}^{*\rho}$ values are an artefact of enhanced pinning. There is a difference between the $T_C^{*\rho}$ values that were measured directly at 0 T and the $T_C^{*\rho}$ values extracted from the $B_{c2}^{*\rho}$ fits when they are extrapolated to 0 T. This may be because the directly measured $T_C^{*\rho}$ values in zero field are associated with the underlying distribution of T_C within the (RE)BCO layer, while the extrapolated values give an indication of the temperature at which J_C effectively drops to zero and the current shunts through the copper and silver layer(s) of the tape. To gain a full understanding of the $B_{c2}^{*\rho}$ behaviour of the (RE)BCO tape measured in this work, or indeed any (RE)BCO tape, one must consider the effects of current percolation and distributions of critical superconducting parameters and current shunting through other tape layers. This issue is the central theme for Chapter 6. For (RE)BCO, the temperature dependence of B_{c2}^* is often parameterised using $(1 - t^{*\nu})^s$ [186, 187, 188, 29], often with $\nu = 1$, rather than the $(1 - t^{*\nu})$ that has been used in this work. When the $B_{c2}^{*\rho}$ data were fitted, there was no notice-

able difference in fit quality between either expression, and it was decided that the $(1 - t^{*\nu})$ parameterisation should be used as it describes the behaviour for $B_{c2}(T)$ in (RE)BCO single crystals well [99, 164] and also prevents any coherence lengths derived from $B_{c2}^{*\rho}$ using Equation 2.4.9 from blowing up to infinity as the temperature approaches the critical temperature. As an additional check, a full flux pinning parameterisation of the J_C data for the (RE)BCO APC data was performed using the $(1 - t^{*\nu})^s$ expression and the conclusions of that analysis were broadly the same, with regards to the extremely high values of B_{c2}^* and $F_{P,max}$ needed at lower temperatures to get a universal fit with a single value of p and q.

5.8.2 Pinning in (RE)BCO and Nb_3Sn

Pinning within (RE)BCO tapes is complex but can broadly be split into two categories - 'intrinsic' and 'extrinsic'. Intrinsic pinning sites include random point defects resulting from the manufacturing process [189, 190, 191], stacking faults in the *ab*-plane [192], and the periodic variation of the order parameter along the *c*-direction [193, 194]. Extrinsic pinning sites include APC's such as nanoparticles and nanorods. The SuperPower APC (RE)BCO tape measured in this work is loaded with nanorods, whose diameters are typically a few nm [182, 195], which is larger than the *ab*-plane coherence length at all fields and temperatures except very close to B_{c2}, which is why there is a strong peak in J_C around 90° in this sample. Given that each type of pinning site present in a tape contributes its own field and temperature dependence to J_C, it is not particularly surprising that a simple flux pinning parameterisation with a single value of p and q failed to fit the J_C data at all fields and temperatures with physically justifiable fit parameters, since it makes no assumptions about the temperature, angular or strain dependence of the pre-factor $F_{P,max}$. The peak in $J_C(\theta)$ associated with the *ab*-planes has a similar shape and field and temperature dependence as that for a (RE)BCO tape without APC's [29], suggesting that intrinsic pinning may dominate for this field orienta-

tion. Given the long-standing use of scaling laws for Nb_3Sn, it is clear that pinning can provide a good parameterisation of J_C. However, it has long been known that the motion of flux through a polycrystalline superconductor is predominantly along the grain boundaries, which naturally leads to an SNS Josephson junction description and has not been described using a flux pinning approach that gives the establish Kramer parameterisation parameters of $p = 1/2$ and $q = 2$ [60]. In contrast to a pinning description which for any given values of p and q gives little information about how to improve or increase J_C, we turn to the SNS Josephson junction description which provides detailed microscopic parameters that can be tested with complementary measurements and provides optimisation strategies that may help the community achieve values of J_C in technological materials closer to the theoretical limits.

5.8.3 Junction behaviour in (RE)BCO and Nb_3Sn

The SNS Josephson junction model in this work considered the superconducting electrodes and normal barrier of the junction to be gapless, s-wave superconductors in the dirty limit. This is a reasonable assumption for Nb_3Sn, however, there is no overall consensus within the community on the pairing mechanism responsible for superconductivity in the cuprates such as (RE)BCO although d-wave pairing is one strong possibility [172]. While the G-L equations for a superconductor with a different pairing mechanism such as d-wave are available, we leave it as a subject for future work as to whether the complexity of introducing d-wave pairing warrants the changes to the final expression for J_C. In this context, the fit parameters and normal state properties for the (RE)BCO samples where Υ_s and Υ_n are free should be interpreted with some caution, as these fits used the weak-coupling, s-wave expression for the energy gaps Δ_s and Δ_n.

For transport J_C measurements on (RE)BCO tapes taken in very low magnetic fields, the self-field generated by a tape is greater than the background magnetic

field, and J_C tends to a constant value as $B \to 0$. Gurnham has modelled the effects of self-field on J_C for a (RE)BCO tape by treating it as a collection of SNS Josephson junctions in parallel, and investigated the characteristic crossover field B_{cr} at which the applied magnetic field becomes larger than the self-field [184] and the source of dissipation changes from fluxon-antifluxon annihilation to flux flow along the normal barriers. For a (RE)BCO tape with a (RE)BCO layer that is 1 µm, using J_C data taken at 77 K and 0.01 T by Higgins [196], the crossover field is 12.6 mT.

The SNS junction model provides a straightforward building block for polycrystalline superconductors such as Nb_3Sn. Simulations show that there is a large energy penalty for the fluxons to leave the grain boundaries [179]. In this context, the model assumes fluxons shear along low angle grain boundaries or twin boundaries. Table 5.5 shows the normal barriers (cf $d(0)$) in the (RE)BCO samples appear to be quite thin - as low as the approximate (RE)BCO unit cell size in the *a*- or *b*-directions [32] or smaller. This is in broad agreement with the grain boundary thicknesses resulting from grain boundary channel models, in which a low-angle grain boundary is treated as a 1D chain of dislocation loops (see Chapter 3, or Gurevich [121]). As the temperature increases, the barrier becomes considerably thicker which indicates that there may be distributions of critical superconducting parameters in the vicinities of the barriers, which is not surprising as strain fields and poor oxygen content are often found at (RE)BCO grain boundaries, and these can suppress T_C. Alternatively, the increasing thickness could be thought of as a correction to the chemical thickness of the barrier associated with the finite coherence length [180]. The temperature and strain dependence of the barrier width was included to complement the expression for $d(T, \varepsilon_{app})$, it had little effect on the value of w_s.

The G-L depairing current density of the superconducting electrodes J_D can be related to J_0 using $J_D = \frac{2}{3\sqrt{3}} J_0$. If the superconducting electrodes had $B^*_{c2}(0,0)$ values that were equal to optimally doped single crystal values of $\sim$ 128 T for

$\theta = 0°$ [164], then the depairing current density (and J_0, and J_C of the tape) would be $\sim 7\% - 20\%$ higher for the APC (RE)BCO tape depending upon the chosen fit from Table 5.7, and $\sim 20\% - 30\%$ higher for the non-APC tape. Improvements in J_D, J_0 and J_C of similar magnitudes could be achieved if the electrodes had $T_C^*(0)$ values that were equal to the optimally doped single crystal value of 93 K for YBCO [43]. This shows that to get substantial further improvements in J_C (through increasing J_{DJ}), then the properties of the barriers need to be improved (i.e., dimensions reduced and normal state properties being made more conducive to supercurrent flow). This will probably require grain boundary engineering on the coherence length scale, which will be a very challenging undertaking.

In the context of the SNS model, the two main reasons why J_C appears to be lower in the non-APC sample compared to the APC sample is because its normal barrier dimensions are higher and the superconducting properties of the electrodes ($B_{c2}^*(0,0)$ and $T_C^*(0)$) are lower. This is not unexpected when one considers that the non-APC sample was procured a few years before the APC sample, meaning that the tape manufacturing process may have been refined in that time to improve the quality of both the grain boundaries and the grains. The SNS model fit to the Nb_3Sn sample provide excellent parameterisation of the J_C data and indicate that the grain boundaries are quite resistive as concluded by Wang *et al.* [22]. The fit is slightly poorer at 14 K and high fields, which is likely due to a combination of a distribution in T_C in the Nb_3Sn filaments and current sharing between those filaments and the copper matrix and is the subject of the next chapter.

5.9 Conclusions

In this chapter comprehensive J_C data have been fitted to three high field superconductors. We argue that for the (RE)BCO tapes, the SNS description fits the data better than a flux pinning model because the SNS model gives physically reasonable B_{c2} values whereas flux pinning does not. For Nb_3Sn, the SNS model fits the

J_C data as well as flux pinning, but we suggest that because the free parameters can be related to microscopic parameters, the SNS approach is far superior. In the next chapter, we will include inhomogeneity and percolation in the description of these materials. In this thesis, we have chosen to leave a detailed discussion of the microscopic parameters (provided here in Table 5.7) and the quality of the fits to the data, until they are finalised in Chapter 6.

Chapter 6

The Effects of Current Percolation and Distributions on the Critical Surfaces of Technological Superconductors

6.1 Introduction

Since the advent of the flux pinning framework to characterise $J_C(B,T,\varepsilon)$, the material under analysis has generally been assumed to have single characteristic or averaged values of the critical superconducting parameters T_C, B_{c2} and B_C. This assumption has a tendency to lead to relatively poor fits for the strain dependence of J_C for (RE)BCO as it cannot explain the strong field and temperature dependence of the strain at which J_C is at its maximum (i.e., ε_{peak}). It also cannot fit J_C data close to B^*_{c2} well. In this chapter, we first present the first global fits for $J_C(B,T,\varepsilon)$ using the chain model, and show that while the chain model can fit ε_{peak} well, it cannot fit J_C well at larger strains such as -1%. We then consider an alternative model for $J_C(B,T,\varepsilon)$ that is based upon a rule of mixtures for current percolation in a network that consists of a mixture of insulating bonds and SNS Josephson

junction bonds, where the electrodes of the different junctions in the network are allowed to take different critical superconducting parameter values T_C, B_{c2} and B_C. We show that in the limit that the distribution of T_C is a delta function, and that the percolation threshold $p_c \to 1$ (see Chapter 3), we recover the 1D chain model, but the 1D chain model limit does not best describe the dimensionality of the current flow and T_C distribution characteristics of the (RE)BCO layers within tapes, nor the Nb_3Sn filaments within Nb_3Sn strands. In the following section we outline the 1D chain model that uses the BH SNS Josephson junction formalism for J_C in high fields, and we use it to analyse the experimental J_C datasets that were analysed in Chapter 5. We then outline the percolation model for $J_C(B,T,\varepsilon)$ in Section 6.3, starting with a review of percolation in resistor-insulator networks, then moving onto percolation in SNS Josephson junction-insulator networks that contain distributions of critical superconducting parameters, and then percolation model fits to experimental data. We complete the chapter with a discussion and conclusions.

6.2 $J_C(B,T,\varepsilon)$ for a 1D Chain of Josephson Junctions

The 1D chain model in the literature treats a superconducting material as a bimodal set of superconductors that are in series with each other and whose individual critical superconducting parameters either increase with increasing tensile strain (A-domains) or decrease (B-domains) [27, 28, 29, 30, 31]. There is a fraction f of A-domains and a fraction $1-f$ of B-domains. Until now, a high-field chain model has only been developed using flux pinning scaling laws to relate the T_C's of the domains to their J_C's [27, 28, 29]. Here, we consider a 1D chain of SNS Josephson junctions instead, as shown in Figure 6.1.

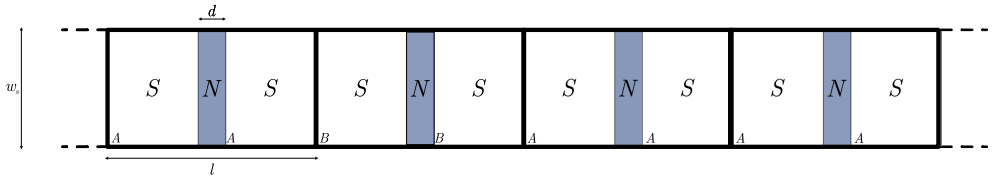

Figure 6.1: A 1D chain of SNS Josephson junctions that are either type A or B. Each junction is treat using the BH framework [133, 132] outlined in Chapter 5.

The two superconducting electrodes within a single junction have the same critical superconducting parameters (i.e., type A or B), but different junctions are allowed to be type A or type B. We assume that the T_C^*'s of the electrodes of a junction of type k have a simple linear strain dependence:

$$T_{Ck}^*(\varepsilon_{JJ}) = \begin{cases} T_{Ck}^*(0) + \left|\frac{dT_C}{d\varepsilon_{JJ}}\right|_{\varepsilon_{JJ}=0\%} \varepsilon_{JJ}, & k = \text{A}, \\ T_{Ck}^*(0) - \left|\frac{dT_C}{d\varepsilon_{JJ}}\right|_{\varepsilon_{JJ}=0\%} \varepsilon_{JJ}, & k = \text{B}. \end{cases} \tag{6.2.1}$$

Here, ε_{JJ} is the strain in the Josephson junction, which is assumed to be uniform throughout the junction and given by

$$\varepsilon_{JJ} = \varepsilon_{app} - \varepsilon_{J_{CA}=J_{CB}} \tag{6.2.2}$$

where $\varepsilon_{J_{CA}=J_{CB}}$ is the applied strain at which $\varepsilon_{JJ} = 0\%$. $T_{Ck}^*(0)$ is assumed to be the same for both type A and B junctions and $\left|\frac{dT_C}{d\varepsilon_{JJ}}\right|_{\varepsilon_{JJ}=0\%}$ is the magnitude of the strain dependence of the T_C^*'s of the junctions and could, for example, be taken from literature data for single crystals [33, 34, 197]. To relate the J_C of a junction to its T_C^* value, we use the equations in Chapter 5 Section 5.6. We assume that we can relate the J_C of a junction of type k (J_{Ck}) to its $E-J$ transition index N_k using the empirical expression

$$N_k = 1 + r_N J_{Ck}^{S_N}, \tag{6.2.3}$$

where r_N and S_N are constants. This expression was originally developed by Taylor for Nb_3Sn [91], although it has also been used successfully by Branch for the 1D chain model based upon a flux pinning expression for J_C [27, 28, 29].

To calculate the J_C of the 1D chain, J_C^{Chain}, we assume that the $E-J$ power

law in Equation 3.2.3 can be used to calculate the electric field generated by each junction. This leads to

$$\left(\frac{J}{J_C^{Chain}}\right)^{N^{Chain}} = f\left(\frac{J}{J_{CA}}\right)^{N_A} + (1-f)\left(\frac{J}{J_{CB}}\right)^{N_B}. \tag{6.2.4}$$

Here, N^{Chain} is the $E-J$ transition index of the chain as a whole. At $J = J_C^{Chain}$, we obtain

$$1 = f\left(\frac{J_C^{Chain}}{J_{CA}}\right)^{N_A} + (1-f)\left(\frac{J_C^{Chain}}{J_{CB}}\right)^{N_B}. \tag{6.2.5}$$

There is no analytical solution for J_C^{Chain}, so it must be found using a numerical technique such as a root-finding algorithm. This motivated Branch to instead derive an approximate expression for ε_{peak} and fit ε_{peak} data that were obtained from parabolic fits to $J_C(\varepsilon)$. In this work, we choose to fit experimental $J_C(B,T,\varepsilon)$ data across the entire experimental strain range using Equation 6.2.5 instead. These fits are now presented.

We have performed fits to the experimental datasets that were analysed in Section 5.6, for both the $\Upsilon_n = \Upsilon_s = 1$ case and the case where not all conduction electrons condense ($\tilde{\Upsilon}_n$ free). Figure 6.2 shows a fit to $J_C(B,T,\varepsilon)$ for Nb_3Sn, Figure 6.3 shows a fit for the Non-APC (RE)BCO sample for $\theta = 0°$ and Figure 6.4 shows a fit for the APC (RE)BCO sample for $\theta = 0°$. Table 6.1 contains the fit parameter values. For the (RE)BCO samples, fits for $\theta = 0°$ were performed first, then fits for $\theta = 87.5°$.

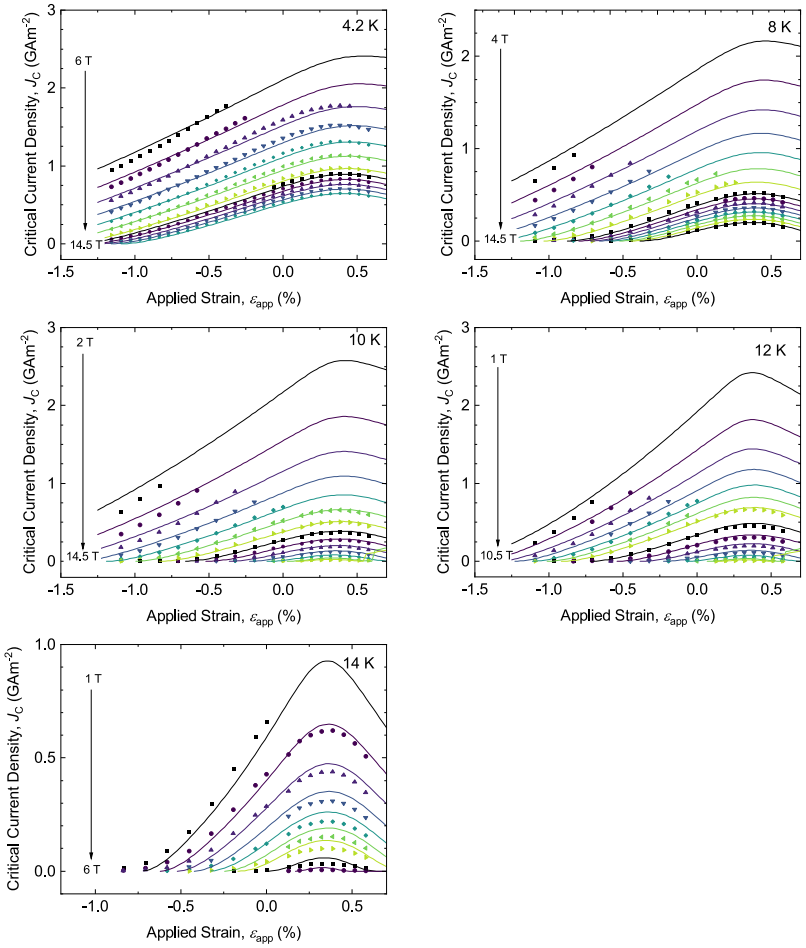

Figure 6.2: Chain model fit for $J_C(\varepsilon_{app})$ for Nb_3Sn, for the fit where not all the conduction electrons condense ($\tilde{\Upsilon}_n$ free).

While the fits identify the position of $\varepsilon_{peak}(B,T)$ well, they do not fit $J_C(\varepsilon_{app})$ at larger strains as well as the empirical exponential function for $T_C^*(\varepsilon_{app})$ introduced in Chapter 5. In addition, the N-values that are needed to fit the data well using the chain model are significantly lower than those extracted from experimental $E-J$ data (compare, for example, the r_N-values in Table 6.1 for the APC sample with those in Figure 5.4 and Table 5.1 in Chapter 4). In an attempt to improve the fits, nonlinear expressions for the T_C^*'s of the A- and B-junctions were implemented, and the constraint that the strain dependencies for the T_C^*'s of the two junction types are equal and opposite was also removed. This did not substantially improve the fit quality. As with the fit in Chapter 5, the fits also do not capture the field, temperature and strain dependence of J_C close to $B = B_{c2}^*$. This motivated the

development of the percolation model for J_C.

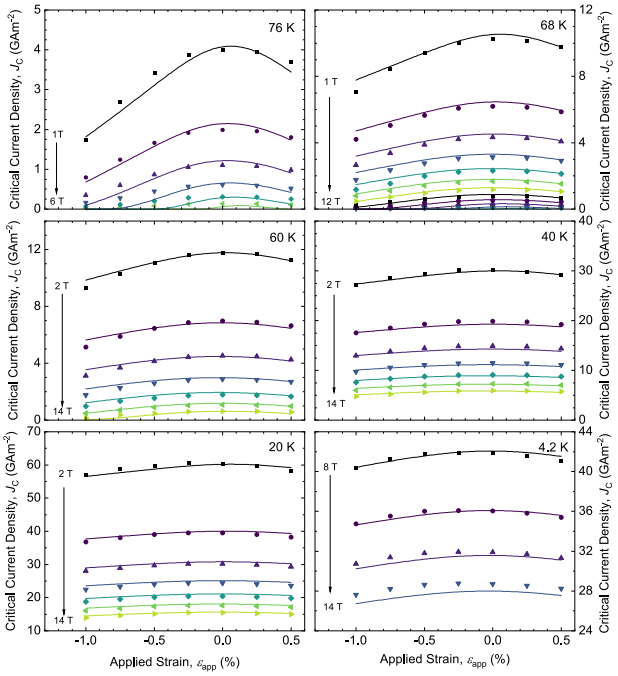

Figure 6.3: Chain model fit for $J_C(\varepsilon_{app})$ for Non-APC (RE)BCO ($\theta = 0°$), for the fit where not all the conduction electrons condense ($\tilde{\Upsilon}_n$ was not fixed at 1).

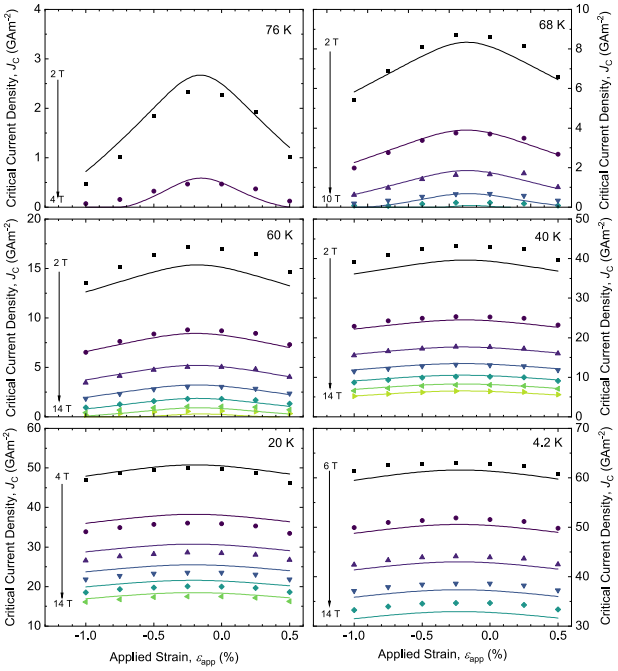

Figure 6.4: Chain model fit for $J_C(\varepsilon_{app})$ for APC (RE)BCO ($\theta = 0°$), for the fit where not all the conduction electrons condense ($\tilde{\Upsilon}_n$ was not fixed at 1).

Table 6.1: Fit parameters for the chain model fits. Bold parameters were fixed from the literature or set at zero to reduce the number of free parameters. For both (RE)BCO samples, for 87.5°, the italicised values were fixed at the 0° values. The starred value (*) of $w_s = 450$ nm was fixed from microscopy (see the references in [90]) and a factor of π to account for sphericity of grains. The dagger values (†) of $\tilde{\alpha}_n(0,0)$ were not free parameters as $\tilde{\alpha}_n(0,0) = \tilde{T}^*_{C,n}(0)$ when $\tilde{\Upsilon}_n$ is free (see Table 5.5).

		Nb_3Sn $\tilde{\Upsilon}_n$ free, $\Upsilon_s = \Upsilon_n = 1$	(RE)BCO (Non-APC) $\tilde{\Upsilon}_n$ free, $\Upsilon_s = \Upsilon_n = 1$		(RE)BCO (APC) $\tilde{\Upsilon}_n$ free, $\Upsilon_s = \Upsilon_n = 1$	
Constraint Type	Parameter		0°	87.5°	0°	87.5°
Fit parameters	$w_s(0)$ (nm)	**450***, **450*** [90]	336, 235	242, 244	234, 235	233, 235
	$d(0)$ (nm)	2.87, 3.16	0.579, 0.440	0.126, 0.0400	0.400, 0.430	0.0400, 0.0400
	c_1	0.519, 0.604	0.515, 0.513	*0.515*, *0.513*	0.561, 0.555	*0.561*, *0.555*
	$\lambda_L(0,0)$ (nm)	**93.5**, **93.5** [22]	**135**, **135** [22]	***135***,***135***	**135**, **135** [22]	***135***,***135***
	$T^*_C(0)$ (K)	16.7, 16.8	86.4, 87.5	*86.4*, *87.5*	86.5, 88.4	*86.5*, *88.4*
	$B^*_{c2}(0,0)$ (T)	31.4, 34.6	101, 73.5	**240**, **240** [164]	113, 76.1	**240**, **240** [164]
	ν	1.45, 1.40	0.577, 0.774	2.83, 2.84	0.427, 0.743	5.10, 8.04
	$c_{\varepsilon 1}$ ($10^{-3}\%^{-1}$)	12.7, 12.8	48.1, 51.8	*48.1*, *51.8*	56.3, 60.7	*56.3*, *60.7*
	$\varepsilon_{J_{C,A}=J_{C,B}}$ (%)	0.320, 0.320	0.170, 0.160	*0.170*, *0.160*	−0.110, −0.120	*-0.110*, *-0.120*
	f	0.551, 0.550	0.340, 0.380	*0.340*, *0.380*	0.370, 0.370	*0.370*, *0.370*
	r_N ($(\mathrm{GAm}^{-2})^{-S_N}$)	6.11, 2.98	1.24, 0.741	0.996, 0.646	2.39, 4.34	1.28, 1.21
	S_N	1.09, 1.59	0.843, 1.01	0.415, 0.423	0.656, 0.322	0.666, 0.665
	w	2.88, 3.30	**2.2**, **2.2** [67]	***2.2***, ***2.2***	**2.2**, **2.2** [67]	***2.2***, ***2.2***
	$d_{\varepsilon 1}$ ($10^{-3}\%^{-1}$)	−59.0, −43.0	**0**, **0**	***0***, ***0***	**0**, **0**	***0***, ***0***
	ζ_1 (nm)	**0**, **0**	2.61, 2.27	0, 0	1.81, 3.22	−0.0879, −1.30
	ζ_2 (nm)	**0**, **0**	−1.49, −1.14	1.08, 0.895	−0.923, −1.61	1.79, 3.71
	$\tilde{\alpha}_n(0,0)$	$-2.98^\dagger$, −2.86	$-1.59^\dagger$, −0.969	$-1.59^\dagger$, −2.51	$-1.90^\dagger$, −1.03	$-1.90^\dagger$, −1.01
	$\tilde{\beta}_n(0,0)$	**1**, $1.16^\dagger$	**1**, $0.183^\dagger$	***1***, $1.23^\dagger$	**1**, $0.133^\dagger$	***1***, $0.129^\dagger$
	$\frac{\tilde{m}_n}{\tilde{\Upsilon}_n(0,0)}$	4.32, 1.88	2.63, 9.67	8.00, 8.74	3.84, 3.51	2.77, 4.57
	$T^*_{C,n}$ (K)	−49.9, −44.5	−137, −198	*-137*, *-198*	−165, −249	*-165*, *-249*
Calculated parameters	$J_s(0,0)$ (GAm^{-2})	9260, 9710	7960, 6790	7960, 6790	8420, 6910	8420, 6910
	$\tilde{g}(E_{F,n})$	1, 1	1, 1	1, 1	1, 1	1, 1
	$\tilde{\rho}_{N,n}$	4.32, 2.03	2.63, 4.14	8.00, 9.70	3.84, 1.28	2.77, 1.65
	$\tilde{n}_n$	n/a, 0.150	n/a, 1.11×10^{-3}	n/a, 1.50×10^{-3}	n/a, 0.0231	n/a, 0.0104
	$\tilde{\tau}_n$	n/a, 6.19	n/a, 2110	n/a, 602	n/a, 119	n/a, 266
	$\tilde{l}_n$	n/a, 1.75	n/a, 22.6	n/a, 7.88	n/a, 9.62	n/a, 12.7
RMS J_c Error (GAm^{-2})		0.0350, 0.0245	0.403, 0.456	1.47, 1.48	1.26, 1.36	3.54, 2.84

6.3 Percolation Model for $J_{\mathrm{C}}(B, T, \varepsilon)$

6.3.1 Percolation in Resistor-Insulator Networks

We start by considering an infinite network that has an occupation fraction p_r of resistive bonds and $1 - p_r$ of insulating bonds. As the fraction of resistive bonds increases from 0, isolated clusters of resistive bonds begin to appear. At a critical fraction of resistive bonds, p_c, an infinitely spanning cluster of resistive bonds appears for the first time. This critical fraction is known as the percolation threshold, as outlined in Chapter 2. As p_r increases from p_c up to 1, the sizes of the isolated resistive clusters increase and the sizes of the infinite spanning resistive clusters increase as more and more isolated resistive clusters and individual resistive bonds become attached to them. Therefore, the active (current carrying) conducting area of the network increases. We assume that the conductivity of the network σ^{Net} can be related to the fraction of resistive bonds p_r using Equation 3.4.2, with $t_p = 1$. We further assume that the conductivity of the network can be equated to an active conducting area A_{act} using:

$$\sigma^{Net}(p_r) \approx \frac{A_{\mathrm{act}}\,(p_r)}{A_{\mathrm{tot}}}\sigma^{Net}(p_r = 1), \tag{6.3.1}$$

where $A_{\mathrm{tot}} = A_{\mathrm{act}}(p_r = 1)$. Therefore,

$$\frac{A_{\mathrm{act}}\,(p_r)}{A_{\mathrm{tot}}} = \begin{cases} 0, & p_r \leq p_c, \\ \frac{p_r - p_c}{1 - p_c}, & p_r > p_c. \end{cases} \tag{6.3.2}$$

We now consider a system where the bonds switch from being insulating to resistive at a certain temperature, T_{s}, and there is a top hat distribution of such temperatures within the network, where the jth bond switches from being resistive to insulating at $T_{\mathrm{s},j}$. The Probability Density Function (PDF) for $T_{\mathrm{s},j}$ is given by:

$$g(T_{\mathrm{s},j}) = \begin{cases} \frac{1}{\delta T_{\mathrm{s}}}, & T_{\mathrm{s}}^{Min} \leq T_{\mathrm{s},j} \leq T_{\mathrm{s}}^{Max} \\ 0, & \text{elsewhere.} \end{cases} \tag{6.3.3}$$

where $\delta T_{\rm s}$ is the width of the PDF, $T_{\rm s}^{Max}$ is the maximum $T_{{\rm s},j}$ in the distribution and $T_{\rm s}^{Min} = T_{\rm s}^{Max} - \delta T_{\rm s}$. The integral of the PDF from $-\infty$ to ∞ has a value of 1. As the operating temperature decreases below $T_{\rm s}^{Max}$, some of the bonds become resistive and they form isolated resistive clusters. The conductivity of the network remains zero. At $T_{\rm s,act}^{Max}$, the first infinite spanning resistive cluster appears, and the conductivity of the network begins to increase from zero. At this temperature, $p_r(T) = p_c$. As the operating temperature decreases further, the conductivity of the network continues to increase and when the temperature reaches $T_{\rm s}^{Min}$, all bonds are resistive. This is summarised in Figure 6.5.

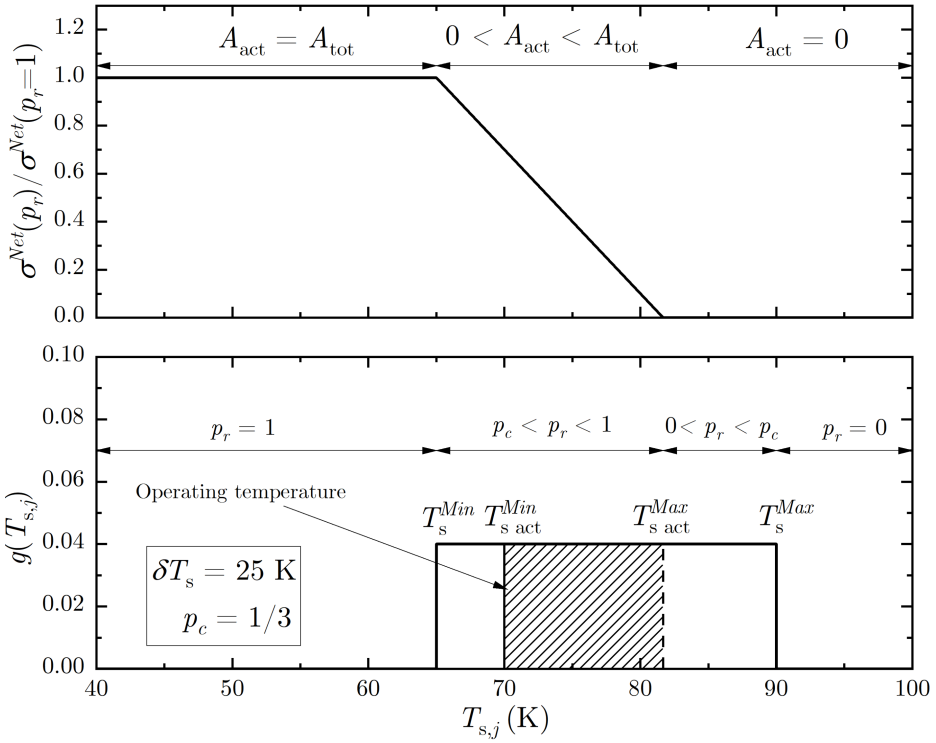

Figure 6.5: Top panel- the conductivity of the network as a function of temperature. Bottom panel- the top hat distribution of $T_{{\rm s},j}$'s.

We have effectively created a rule of mixtures for percolation, where we have divided the network into an insulating part and a conducting part, as shown in Figure 6.6.

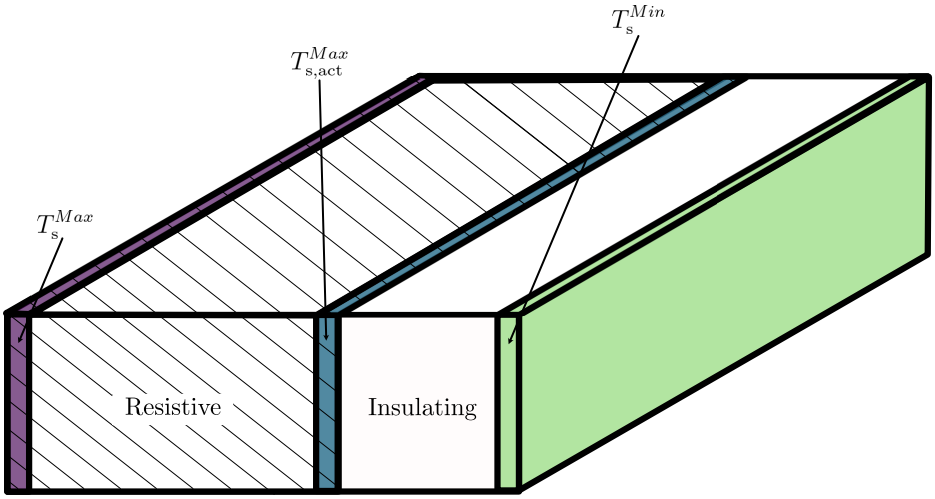

Figure 6.6: The rule of mixtures for percolation for an insulator-resistor network, where the lattice is split up into a conducting and an insulating part.

The insulating and conducting parts contain slices which correspond to the different $T_{\mathrm{s},j}$'s in the distribution. There are a range of $T_{\mathrm{s},j}$ values in each slice, that represent the isolated bonds and clusters and the critical bond that connects these bonds to an infinite spanning cluster when it switches from being insulating to resistive. A slice does not switch from being insulating to resistive until the network's operating temperature reaches the minimum switching temperature in that slice. As we lower the operating temperature from just above $T_{\mathrm{s},act}^{Max}$ to just below $T_{\mathrm{s},act}^{Max}$, the active conducting area becomes greater than zero and the first slice of the material (which is highlighted as the leftmost (purple) slice in Figure 4) becomes resistive. The minimum $T_{\mathrm{s},j}$ in that slice is $T_{\mathrm{s,act}}^{Max}$. The weakest link in the resistive material varies from $T_{\mathrm{s},act}^{Max}$ for the first (leftmost) slice at $p_r = p_c$ to $T_{\mathrm{s,act}}^{Min}$ in the last part of the active conducting area (the middle highlighted slice). $T_{\mathrm{s,act}}^{Min}$ is equal to the operating temperature if the operating temperature is above T_{s}^{Min}, otherwise it is equal to T_{s}^{Min}.

6.3.2 Percolation in Josephson Junction-Insulator Networks

We begin by replacing the resistive bonds from the previous section with Josephson junction bonds that have the characteristics of those described in Chapter 5. A junction switches from insulating to superconducting when the operating temperature is lowered and reaches the critical temperature of the superconducting electrodes that are on both sides of the junction. Within the network, there is a distribution of these critical temperatures. Like the Chain Model analysis, within a single junction, the electrodes have the same superconducting (and normal state) properties. We also assume that the properties for all of the barriers within all of the junctions in the network are the same. We start by providing the expressions for the distribution in T_{C} and the resultant distributions in B_{c2} and J_{C}, building upon the work in Chapter 5. Section 6.3.2.2 provides a method for calculating the J_{C} of the whole network, J_{C}^{Net} using a rule of mixtures for percolation, along with fits to J_{C} data.

6.3.2.1 Distributions of T_{C}, B_{c2} and J_{C}

We start by considering a bimodal, top hat distribution for the critical temperatures of the electrodes of the Josephson junctions $g(T_{\mathrm{C},j})$. Mathematically, $g(T_{\mathrm{C},j})$ can be expressed as

$$g(T_{\mathrm{C},j}) = f \times g(T_{\mathrm{CA},j}) + (1-f)\, g(T_{\mathrm{CB},j}) \tag{6.3.4}$$

and

$$g(T_{\mathrm{C}k,j}) = \begin{cases} \frac{1}{\delta T_{\mathrm{C}}}, & T_{\mathrm{C}k}^{Min} \leq T_{\mathrm{C}k,j} \leq T_{\mathrm{C}k}^{Max} \\ 0, & \text{elsewhere.} \end{cases} \tag{6.3.5}$$

where k =A or B, $0 \leq f \leq 1$, and δT_{C} is the width of each mode of the distribution such that $\int_{-\infty}^{\infty} g\left(T_{\mathrm{C},j}\right) dT_{\mathrm{C},j} = 1$. Similar to the Chain Model analysis, we consider the strain dependence for the T_{C}'s in each mode of the distribution to be equal and

opposite:

$$T_{Ck}^{Max}(\varepsilon_{JJ}) = \begin{cases} T_{Ck}^{Max}(0) + \left|\frac{dT_C}{d\varepsilon_{JJ}}\right| \varepsilon_{JJ}, & k = \text{A}, \\ T_{Ck}^{Max}(0) - \left|\frac{dT_C}{d\varepsilon_{JJ}}\right| \varepsilon_{JJ}, & k = \text{B}. \end{cases} \tag{6.3.6}$$

$\varepsilon_{JJ} = \varepsilon_{app} - \varepsilon_{J_{C,A}=J_{C,B}}$ is the strain on the junction such that at $\varepsilon_{JJ} = 0\%$, $T_{CA}^{Max} = T_{CB}^{Max}$. Figure 6.7 shows an example of such a distribution. In the figure, the strain is sufficiently large to make the modes of the distribution fully separate.

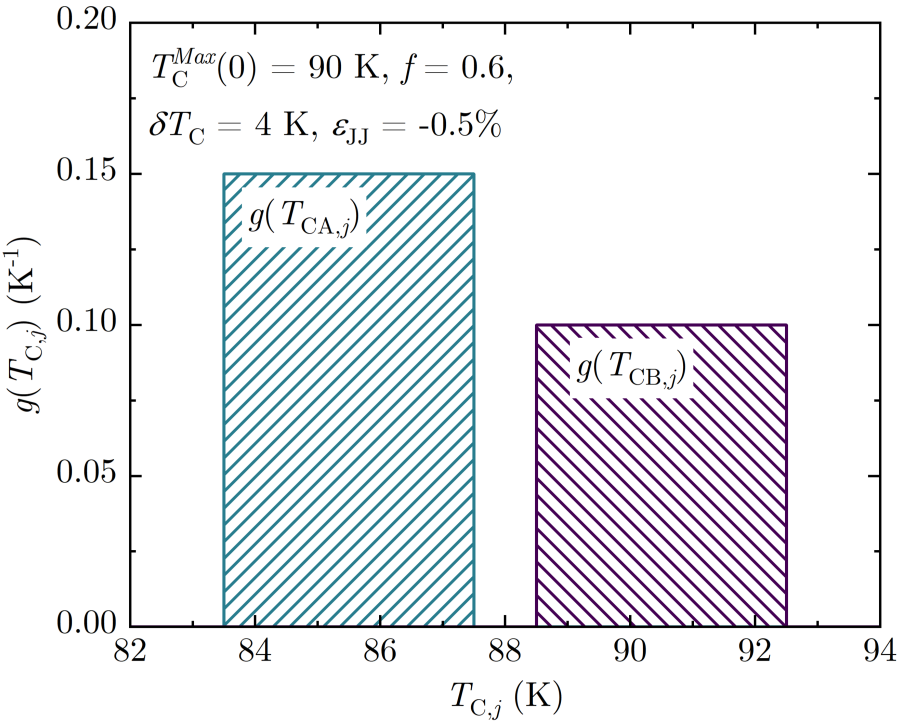

Figure 6.7: An example of $g(T_{C,j})$ after applying a strain of -0.5 % to a system with an average T_C of 87.5 K.

We can map each mode of the T_C distribution to a distribution in B_{c2}, that we denote $g(B_{c2k,j})$, using

$$g(T_{Ck,j}) = \left|\frac{dB_{c2k,j}}{dT_{Ck,j}}\right| g(B_{c2k,j}). \tag{6.3.7}$$

To calculate the values of B_{c2} within the modes of the distribution, we start by relating $B_{c2k,j}(0,0)$ to the maximum B_{c2} in the distribution at zero strain and temperature, $B_{c2}^{Max}(0,0)$, using:

$$B_{c2A,j}(0,0) = B_{c2B,j}(0,0) = B_{c2}^{Max}(0,0) \left[\frac{T_{C,j}(0)}{T_C^{Max}(0)}\right]^{w_d} \tag{6.3.8}$$

where w_d is a dimensionless constant. This expression is similar to the empirical expression developed by Taylor to relate the strain dependence of B_{c2} at zero temperature to the strain dependence of T_C [91]. Similarly, we parameterise the strain dependence of the B_{c2}'s in the distribution at 0 K using:

$$\frac{B_{c2k,j}\left(0,\varepsilon_{JJ}\right)}{B_{c2k,j}\left(0,0\right)}=\frac{B_{c2k}^{Max}\left(0,\varepsilon_{JJ}\right)}{B_{c2k}^{Max}\left(0,0\right)}=\left(\frac{T_{Ck}^{Max}\left(\varepsilon_{JJ}\right)}{T_{C}^{Max}\left(0\right)}\right)^{w_\varepsilon}=\left(\frac{T_{Ck,j}\left(\varepsilon_{JJ}\right)}{T_{Ck,j}\left(0\right)}\right)^{w_\varepsilon} \tag{6.3.9}$$

where w_ϵ is a dimensionless constant. By parameterising the B_{c2}'s in this way, we allow the possibility of strain affecting a junction's B_{c2} at 0 K differently to how the junction's position in the zero-strain $T_{C,j}$ distribution affects B_{c2} at 0 K. This reflects the reality that (RE)BCO material properties such as oxygen doping may affect T_C and $B_{c2}(0)$, as well as strain [198]. We parameterise the temperature dependence of $B_{c2k,j}$ using $(1-t^\nu)$ as in Chapter 5 and Section 6.2 of this chapter. Therefore, the full temperature and strain dependencies of the B_{c2}'s are

$$B_{c2A,j}(T,\varepsilon_{JJ})=B_{c2}^{Max}(0,0)\left(\frac{T_{CA,j}(\varepsilon_{JJ})}{T_{C}^{Max}(0)}\right)^{w_d}\times \left(1+\frac{1}{T_{C}^{Max}(0)}\left|\frac{dT_C}{d\varepsilon_{JJ}}\right|_{\varepsilon_{JJ}=0\%}\varepsilon_{JJ}\right)^{w_e-w_d}\left(1-\left(\frac{T}{T_{CA,j}(\varepsilon_{JJ})}\right)^{\nu}\right) \tag{6.3.10}$$

for the A-mode and

$$B_{c2B,j}(T,\varepsilon_{JJ})=B_{c2}^{Max}(0,0)\left(\frac{T_{CB,j}(\varepsilon_{JJ})}{T_{C}^{Max}(0)}\right)^{w_d}\times \left(1-\frac{1}{T_{C}^{Max}(0)}\left|\frac{dT_C}{d\varepsilon_{JJ}}\right|_{\varepsilon_{JJ}=0\%}\varepsilon_{JJ}\right)^{w_e-w_d}\left(1-\left(\frac{T}{T_{CB,j}(\varepsilon_{JJ})}\right)^{\nu}\right) \tag{6.3.11}$$

for the B-mode.

As the magnetic field is gradually lowered through the $g(B_{c2,j})$ distribution from the maximum B_{c2} value, the electrodes in the Josephson junctions will switch from being insulating to superconducting. When $B = B_{c2,act}^{Max}$ is reached, an infinite spanning cluster of junctions with superconducting electrodes appears for the first time and the active superconducting area of the network begins to increase from zero. $B_{c2,act}^{Max}$ is the maximum value of B_{c2} in the active superconducting area. Figure 6.8 shows an example of the temperature dependence of $B_{c2,act}^{Max}$ at $\varepsilon_{JJ} = 0\%$.

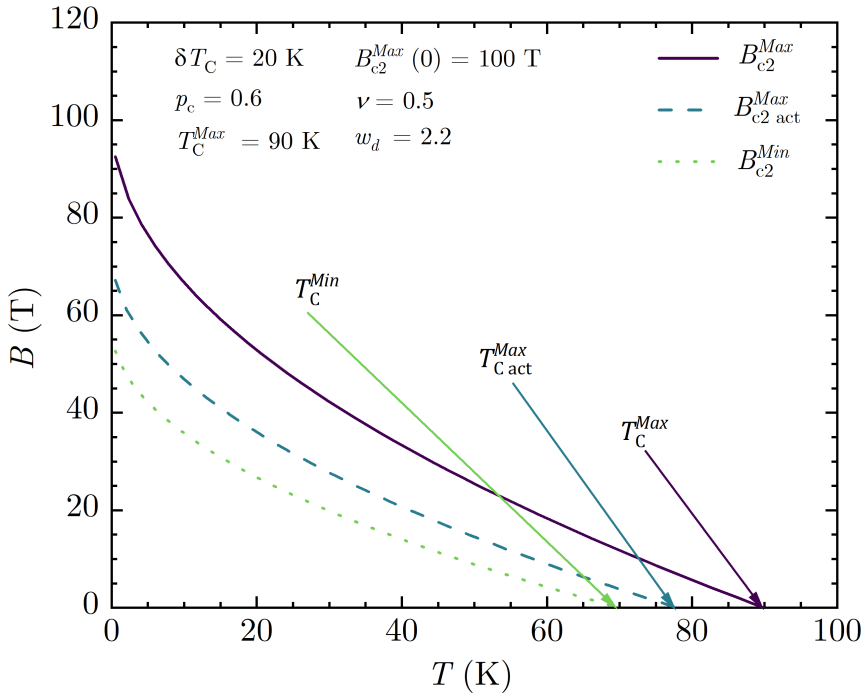

Figure 6.8: Example of the temperature dependencies of $B_{c2,act}^{Max}(T)$, the minimum B_{c2} in the distribution (B_{c2}^{Min}) and the maximum B_{c2} in the distribution (B_{c2}^{Max}).

Examples of the strain dependence of $B_{c2,act}^{Max}$ for different f and p_c values are shown in Figure 6.9. To ensure that $B_{c2,act}^{Max}$ always decreases at large tensile strains, we require $f < p_c$ and to ensure that $B_{c2,act}^{Max}$ always decreases at large compressive strains, we require $1 - f < p_c$. Incorporating these constraints ensures that p_c is always associated with the distribution mode whose B_{c2}'s are decreasing as the strain increases at large compressive or tensile strains. The discontinuities in the gradient of $B_{c2,act}^{Max}(\varepsilon_{JJ})$ are due to our choice of using a simple top hat distribution to describe each mode of the $T_{C,j}$ distribution. If we were to plot $T_{C,act}^{Max}(\varepsilon_{JJ})$, we would find similar behaviour. PDF's that are continuous between 0 K and $T_C^{Max}(0)$ such as a Beta or Weibull distribution would fix this issue, although it would also require mathematical constraints to ensure junction electrodes never have negative values of T_C under strain.

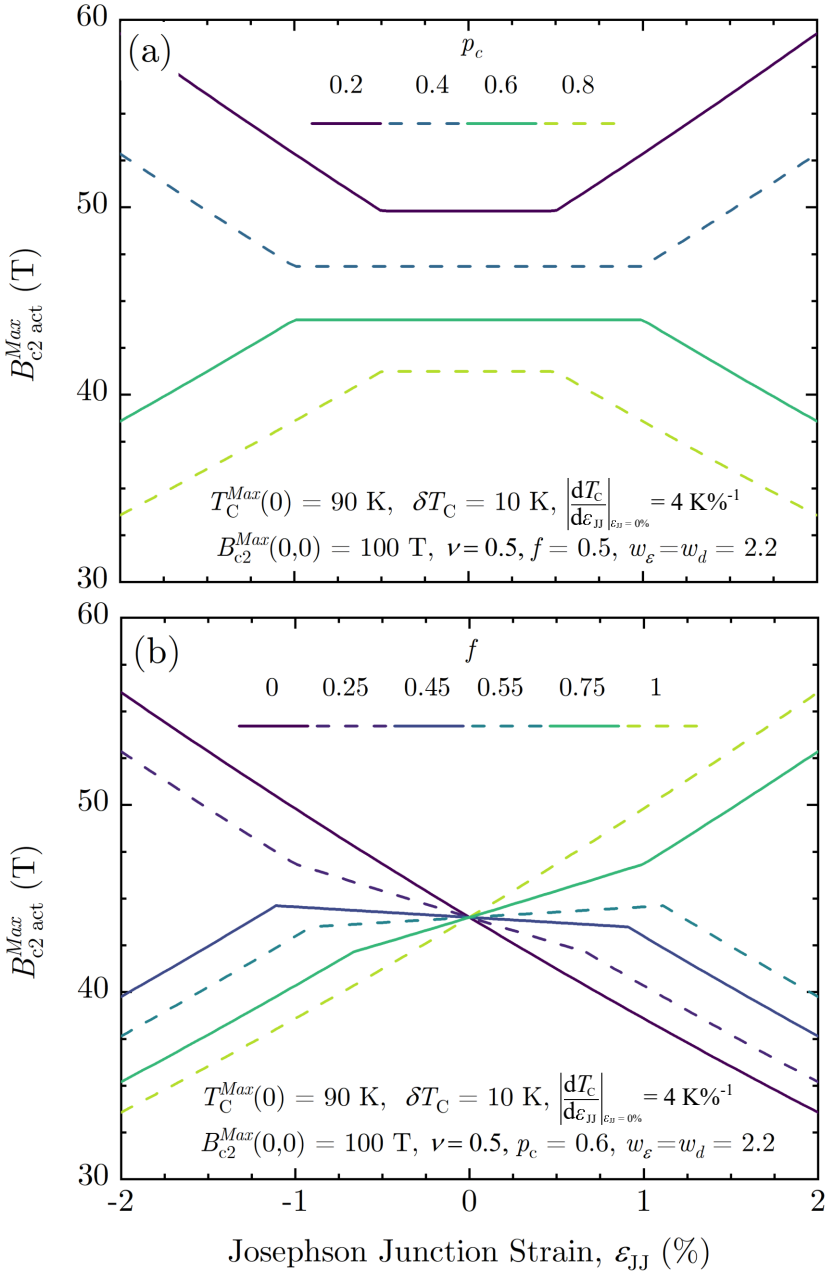

Figure 6.9: (a) The strain dependence of $B_{c2,act}^{Max}$ for different p_c values. (b) The strain dependence, but for different f values. The temperature was 20 K.

We can relate each mode of the distribution in T_C to a mode of a distribution in J_C for the junctions, which we denote $g(J_{Ck,j})$, using

$$g(J_{Ck,j}) = \left|\frac{dT_{Ck,j}}{dJ_{Ck,j}}\right| g(T_{Ck,j}), \tag{6.3.12}$$

where $J_{Ck,j}$ is the J_C of the jth junction in the kth mode in the distribution.

Similar to the Chain Model analysis, we use the Josephson junction framework in Chapter 6 to relate $J_{Ck,j}$ to $T_{Ck,j}$:

$$J_{Ck,j}\left(B,T,\varepsilon_{JJ}\right)=\frac{1.2}{c_1}\left(\frac{\phi_0}{Bw_s^2}\right)^{c_1}J_{sk,j}\left(T,\varepsilon_{JJ}\right)\left(1-\frac{B}{B_{c2k,j}\left(T,\varepsilon_{JJ}\right)}\right)^{\frac{3}{2}}\times \frac{1-\sqrt{1-\tilde{s}_{k,j}\tilde{f}^2_{d/2,k,j}\left(T,\varepsilon_{JJ}\right)}}{\tilde{s}_{k,j}\tilde{v}_{k,j}}\exp\left(-\frac{\tilde{d}_{sk,j}}{\tilde{\xi}_{nk,j}}\right). \quad (6.3.13)$$

The $J_{sk,j}$'s are given by

$$J_{sA,j}(T,\varepsilon_{JJ})=\sqrt{\frac{\phi_0}{2\pi}}\frac{B_{c2}^{Max}\left(0,0\right)}{\mu_0\lambda^{Max^2}\left(0,0\right)}\left[\frac{T_{CA,j}\left(\varepsilon_{JJ}\right)}{T_C^{Max}\left(0\right)}\right]^{2-\frac{w_d}{2}}\times \left[1+\frac{1}{T_C^{Max}\left(0\right)}\left|\frac{dT_C}{d\varepsilon_{JJ}}\right|_{\varepsilon_{JJ}=0\%}\right]^{\frac{w_d-w_\varepsilon}{2}}\times \left[1-\left(\frac{T}{T_{CA,j}(\varepsilon_{JJ})}\right)^{\nu}\right]^{-\frac{1}{2}}\left[1-\left(\frac{T}{T_{CA,j}(\varepsilon_{JJ})}\right)^{2}\right]^{2} \quad (6.3.14)$$

and

$$J_{sB,j}(T,\varepsilon_{JJ})=\sqrt{\frac{\phi_0}{2\pi}}\frac{B_{c2}^{Max}\left(0,0\right)}{\mu_0\lambda^{Max^2}\left(0,0\right)}\left[\frac{T_{CB,j}\left(\varepsilon_{JJ}\right)}{T_C^{Max}\left(0\right)}\right]^{2-\frac{w_d}{2}}\times \left[1-\frac{1}{T_C^{Max}\left(0\right)}\left|\frac{dT_C}{d\varepsilon_{JJ}}\right|_{\varepsilon_{JJ}=0\%}\right]^{\frac{w_d-w_\varepsilon}{2}}\times \left[1-\left(\frac{T}{T_{CB,j}(\varepsilon_{JJ})}\right)^{\nu}\right]^{-\frac{1}{2}}\left[1-\left(\frac{T}{T_{CB,j}(\varepsilon_{JJ})}\right)^{2}\right]^{2}. \quad (6.3.15)$$

Here, we have used microscopic theory [176] to derive

$$\frac{B_{Ck,j}(0,\varepsilon_{JJ})}{B_{Ck,j}(0,0)}=\frac{T_{Ck,j}(\varepsilon_{JJ})}{T_{Ck,j}(0)}=\begin{cases}1+\frac{1}{T_C^{Max}(0)}\left|\frac{dT_C}{d\varepsilon_{JJ}}\right|_{\varepsilon_{JJ}=0\%}, & k=\mathrm{A},\\ 1-\frac{1}{T_C^{Max}(0)}\left|\frac{dT_C}{d\varepsilon_{JJ}}\right|_{\varepsilon_{JJ}=0\%}, & k=\mathrm{B},\end{cases} \quad (6.3.16)$$

and

$$\frac{B_{Ck,j}(0,0)}{B_C^{Max}(0,0)}=\frac{T_{Ck,j}(0)}{T_C^{Max}(0)} \quad (6.3.17)$$

where $B_C^{Max}(0,0)=\frac{1}{\lambda^{Max}(0,0)}\left(\frac{\phi_0 B_{c2}^{Max}(0,0)}{4\pi}\right)^{\frac{1}{2}}$ [53] is the maximum thermodynamic critical field within the distribution at zero temperature and strain and $\lambda^{Max}(0,0)$ is the maximum penetration depth within the distribution at zero temperature and strain.

Similar to Chapter 5, we can write down expressions for the normalised α's, β's and Υ's within the barrier of each junction in the distribution ($\tilde{\alpha}_{nk,j}$'s, $\tilde{\beta}_{nk,j}$'s and $\tilde{\Upsilon}_{nk,j}$'s respectively). For a given temperature and strain, the normalised α's, β's and Υ's will have different values for each of the barriers within the distribution, as the superconducting electrodes all have different values of T_{C}, B_{c2} and B_{C}. However, we can relate the zero temperature, zero strain values of $\tilde{\alpha}_{nk,j}$, $\tilde{\beta}_{nk,j}$ and $\tilde{\Upsilon}_{nk,j}$ to their maximum values in the distribution at zero temperature and strain ($\tilde{\alpha}^{Max}_{nk,j}(0,0)$, $\tilde{\beta}^{Max}_{nk,j}(0,0)$ and $\tilde{\Upsilon}^{Max}_{n}(0,0)$ respectively). In addition, like Chapter 5, we can once again either assume that all of the conduction electrons condense upon the transition from the normal state to the superconducting state ($\Upsilon_{s,j} = \Upsilon_n = 1$), or not ($\tilde{\Upsilon}_{n,j}$ is a free parameter). By parameterising the α's, β's and Υ's in this way, we are able to extract the normal state properties of the barriers in the distribution that are normalised to the normal state properties of the junction in the distribution whose electrodes have the maximal values of T_{C}, B_{c2} and B_{C} at zero temperature and strain. Once again, we use a dirty limit expression for $B^{Max}_{\mathrm{c2}}(0,0)$:

$$B^{Max}_{\mathrm{c2}}(0,0) = \frac{12e}{\pi^3 k_B}\rho^{Max}_{N,s}\gamma^{Max}_{s}T^{Max}_{\mathrm{C}}(0). \tag{6.3.18}$$

We denote the normal state properties for the junction with $T_{\mathrm{C},j}(0) = T^{Max}_{\mathrm{C}}(0)$ and $T_{\mathrm{C},j}(0) = B^{Max}_{\mathrm{c2}}(0,0)$ using the superscript 'Max' (for example its electrodes would have a normal state resistivity of $\rho^{Max}_{N,s}$ and an electronic specific heat of γ^{Max}_{s}). Table 6.2 summarises this information.

Table 6.2: Expressions for α, β and Υ (and $\tilde{m}_n/\tilde{\Upsilon}_n^{Max}$) in terms of superconducting properties and normal state properties. m_s is the same in each junction.

Parameter	Expression	
	$\Upsilon_{sk,j} = \Upsilon_n = 1$	$\tilde{\Upsilon}_{nk,j}$ free
$\alpha_{sk,j}$	$\frac{-\pi\hbar^2 B_{c2k,j}(0,0)}{2\phi_0 m_s}\left(\frac{T_{Ck,j}(\varepsilon_{JJ})}{T_{Ck,j}(0)}\right)^{w_\varepsilon}\left(1-t^{*^\nu}\right)$	$-1.76k_B T_{Ck,j}(0)\frac{T_{Ck,j}(\varepsilon_{app})}{T_{Ck,j}(0)}\left(1-\left(\frac{T}{T_{Ck,j}(\varepsilon_{JJ})}\right)^2\right)$
α_n	$\frac{\pi\hbar^2 B^*_{c2,n}(0)}{2\phi_0 m_n}\left(\frac{T}{T^*_{C,n}}-1\right)$	$-1.76k_B T^*_{C,n}\left(1-\frac{T}{T^*_{C,n}}\right)$
$\tilde{\alpha}_{nk,j}$	$\tilde{\alpha}_n^{Max}(0,0)\left(\frac{T_C^{Max}(0)}{T_{Ck,j}(\varepsilon_{JJ})}\right)^{w_d}\left(\frac{T_{Ck,j}(\varepsilon_{JJ})}{T_{Ck,j}(0)}\right)^{w_d-w_\varepsilon}\frac{\frac{T}{T^*_{C,n}}-1}{1-\left(\frac{T}{T_{Ck,j}(\varepsilon_{JJ})}\right)^\nu}$	$\tilde{\alpha}_n^{Max}(0,0)\frac{T_C^{Max}(0)}{T_{Ck,j}(\varepsilon_{JJ})}\frac{1-\frac{T}{T^*_{Cn}}}{1-\left(\frac{T}{T_{Ck,j}(\varepsilon_{JJ})}\right)^2}$
$\tilde{\alpha_n}^{Max}(0,0)$	$\tilde{\rho}_{N,n}^{Max}\tilde{g}^{Max}(E_{F,n})\tilde{T}_{C,n}^{Max}(0)\tilde{m}_n^{-1}$	$\tilde{T}_{C,n}^{Max}(0)$
$\beta_{sk,j}$	$\frac{\mu_0 e^2\hbar^2}{4m_s^2}\left(\frac{B_{c2k,j}(0,0)}{B_{Ck,j}(0,0)}\right)^2\left(\frac{T_{Ck,j}(\varepsilon_{app})}{T_{Ck,j}(0)}\right)^{2w_\varepsilon-2}\left(\frac{1-\left(\frac{T}{T_{Ck,j}(\varepsilon_{JJ})}\right)^\nu}{1-\left(\frac{T}{T_{Ck,j}(\varepsilon_{JJ})}\right)^2}\right)^2$	$g^{-1}(E_{F,s})$
β_n	$\frac{\mu_0 e^2\hbar^2}{4m_n^2}\left(\frac{B^*_{c2,n}(0)}{B^*_{C,n}(0)}\right)^2$	$g^{-1}(E_{F,n})$
$\tilde{\beta}_{nk,j}$	$\tilde{\beta}_n^{Max}(0,0)\left(\frac{T_C^{Max}(0)}{T_{Ck,j}(\varepsilon_{JJ})}\right)^{2w_d-2}\left(\frac{T_{Ck,j}(\varepsilon_{JJ})}{T_{Ck,j}(0)}\right)^{2w_d-2w_\varepsilon}\left(\frac{1-\left(\frac{T}{T_{Ck,j}(\varepsilon_{JJ})}\right)^2}{1-\left(\frac{T}{T_{Ck,j}(\varepsilon_{JJ})}\right)^\nu}\right)^2$	$\tilde{g}^{-1}(E_{F,n})$
$\tilde{\beta}_n^{Max}(0,0)$	$\tilde{\rho}_{N,n}^{Max^2}\tilde{g}^{Max}(E_{F,n})\tilde{m}_n^{-2}$	$\tilde{g}^{Max^{-1}}(E_{F,n})$
$\Upsilon_{sk,j}$	1	$\frac{3.52k_B T_{Ck,j}(0)m_s}{e\hbar B_{c2k,j}(0,0)}\left(\frac{T_{Ck,j}(\varepsilon_{JJ})}{T_{Ck,j}(0)}\right)^{1-w_\varepsilon}\frac{1-(\frac{T}{T_{Ck,j}(\varepsilon_{JJ})})^2}{1-(\frac{T}{T_{Ck,j}(\varepsilon_{JJ})})^\nu}$
Υ_n	1	$\frac{3.52k_B T^*_{C,n}m_n}{e\hbar B^*_{c2,n}(0)}$
$\tilde{\Upsilon}_{nk,j}$	1	$\tilde{\Upsilon}_n^{Max}(0,0)\left(\frac{T_{Ck,j}(\varepsilon_{JJ})}{T_C^{Max}(0)}\right)^{w_d-1}\left(\frac{T_{Ck,j}(\varepsilon_{JJ})}{T_{Ck,j}(0)}\right)^{w_\varepsilon-w_d}\frac{1-\left(\frac{T}{T_{Ck,j}(\varepsilon_{JJ})}\right)^\nu}{1-\left(\frac{T}{T_{Ck,j}(\varepsilon_{JJ})}\right)^2}$
$\tilde{m}_n/\tilde{\Upsilon}_n^{Max}(0,0)$	$\tilde{m}_n$	$\tilde{\rho}_{N,n}^{Max}\tilde{g}^{Max}(E_{F,n})$

6.3.2.2 J_C for a Percolative Superconducting Network

Now that we have expressions for the J_C's of the junctions in the network, we can calculate the J_C of the network as a whole, J_C^{Net}. We start by reconsidering the rule of mixtures for percolation that we introduced in Section 6.3.1 for resistor-insulator networks. We assume that the same rule of mixtures can be used to describe Josephson junction-insulator network. We split the network up into an insulating and superconducting part, with the superconducting part containing Josephson junctions whose electrodes are in the superconducting state. The insulating and superconducting parts are further split into slices, as shown in Figure 6.10.

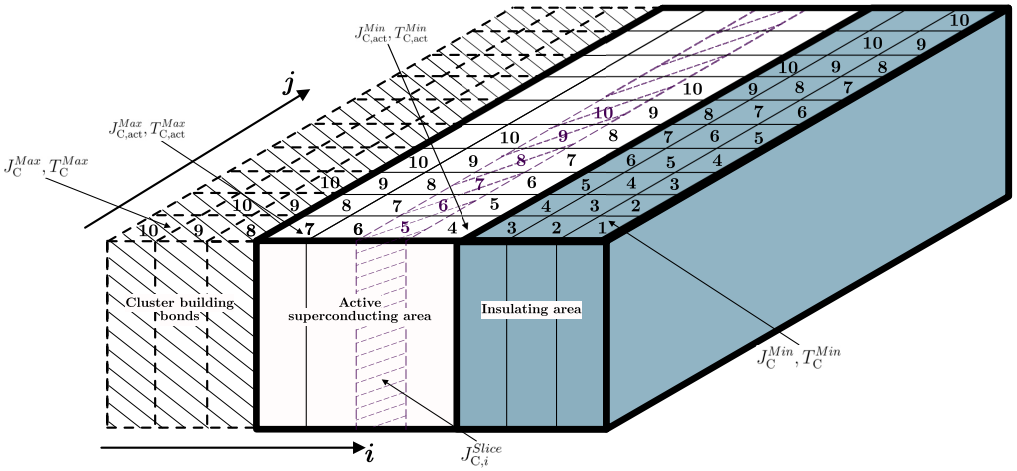

Figure 6.10: Rule of mixtures for percolation for a Josephson junction/insulator mixture.

There is a distribution of J_C's in each slice that spans from J_C^{Max} - the maximum J_C in the material, to $J_{C,i}$ - the minimum J_C in that slice. We denote the J_C distribution function for a slice by $g_i(J_{C,j})$, where the i subscript denotes the slice and the j subscript denotes the bond in that slice. $J_{C,i}$ is found at the front of each slice and J_C^{Max} is found at the back of each slice. Each slice has a different $J_{C,i}$ and the slices are arranged in order of their $J_{C,i}$'s. For example, in Figure 6.10, we have a $J_{C,i}$ distribution ranging from 10 to 1 with 10 being the highest $J_{C,i}$ and 1 being the lowest $J_{C,i}$.

There is also a distribution of T_C's which corresponds to the distribution of J_C's.

The ith slice has bonds with T_C's spanning from $T_{C,i}$ to T_C^{Max} and the T_C distribution for a slice is given by $g_i(T_{C,j})$. There is also a distribution of B_{c2}'s which can be found by mapping $g_i(T_{C,j})$ to B_{c2} space. The ith slice switches from insulating to superconducting when the junction with the minimum T_C and/or B_{c2} in that slice switches from insulating to superconducting as the temperature and/or field are lowered.

There are some Josephson junction bonds with high T_C's which help to build system spanning superconducting clusters, but they cannot complete them. These bonds are labelled in Figure 6.10 as cluster building bonds and they form 'virtual' slices that cannot carry any current because the bonds in these slices are isolated from each other. When the temperature is ramped down from above T_C^{Max}, the active superconducting area doesn't begin to increase from zero until $T = T_{C,act}^{Max}$. For example, in Figure 6.10, the bond labelled 7 has $T_{C,i} = T_{C,act}^{Max}$ and this is the first slice that can carry current when the temperature is ramped down. All the slices are superconducting for the first time when $T = T_C^{Min}$.

To calculate the critical current of the network, we start by deriving an expression for the critical current density of the ith slice, $J_{C,i}^{Slice}$. The $J_{C,j}$ PDF in the ith slice, $g_i(J_{C,j})$, is given by:

$$g_i(J_{C,j}) = \frac{g(J_{C,j})}{\int_{J_{C,i}}^{J_C^{Max}} g(J_{C,j})\mathrm{d}J_{C,j}}. \tag{6.3.19}$$

The denominator ensures that the integral of $g_i(J_{C,j})$ over all values of $J_{C,j}$ within the ith slice is equal to 1. By considering the ith slice as a 1D chain of bonds, where each bond in the chain carries the same current density J, we use the continuous form of the 1D Chain Model to derive:

$$\begin{aligned}\left(\frac{1}{J_{C,i}^{Slice}}\right)^{N_i} &= \int_{J_{C,i}}^{J_C^{Max}} g_i(J_{C,j}) \left(\frac{1}{J_{C,j}}\right)^{N_i} dJ_{C,j} \\ &= \int_{T_{C,i}}^{T_C^{Max}} g_i(T_{C,j}) \left(\frac{1}{J_{C,j}(T_{C,j})}\right)^{N_i} dT_{C,j}. \end{aligned} \tag{6.3.20}$$

Here, we have related the J_C values to their N-values using [67]:

$$N_i = 1 + r_N J_{C,i}^{S_N} \tag{6.3.21}$$

and

$$N_j = 1 + r_N J_{C,j}^{S_N} \tag{6.3.22}$$

where r_N and S_N are constants. We have also assumed that $N_i \approx N_j$. The rationale is that the bonds that will generate the highest electric field (and therefore most determine $J_{C,i}^{Slice}$) are found at the front of the slice (i.e., they have $J_{C,j}$ values close to $J_{C,i}$).

Now that we have an expression for $J_{C,i}^{Slice}$, we can calculate the critical current density of the whole network, J_C^{Net}. To do this, we add the critical currents of all the superconducting slices together, and then divide by the total area of the network. Mathematically,

$$I_C^{Net} = \sum_i I_{C,i}^{Slice} = \sum_i J_{C,i}^{Slice} A_i^{Slice} \approx A_{act} \overline{J_{C,act}}, \tag{6.3.23}$$

where $I_{C,i}^{Slice}$ is the critical current in the ith slice, $J_{C,i}^{Slice}$ is the critical current density of the ith slice, A_i^{Slice} is the area of the ith slice, A_{act} is the active superconducting area and $\overline{J_{C,act}}$ is the average critical current density in the average superconducting area. To calculate the critical current density of the network J_C^{Net}, we use:

$$J_C^{Net} = \frac{A_{act}\overline{J_{C,act}}}{A_{tot}} \tag{6.3.24}$$

where A_{tot} is the total area for supercurrent flow when all the bonds are superconducting Josephson junctions. Calculating $\overline{J_{C,act}}$ requires averaging over all the $J_{C,i}^{Slice}$'s in the active superconducting area:

$$\overline{J_{C,act}} = \frac{\int_{J_{C,act}^{Min}}^{J_{C,act}^{Max}} g(J_{C,i}) J_{C,i}^{Slice}(J_{C,i}) dJ_{C,i}}{\int_{J_{C,act}^{Min}}^{J_{C,act}^{Max}} g(J_{C,i}) dJ_{C,i}}$$
$$= \frac{\int_{T_{C,act}^{Min}}^{T_{C,act}^{Max}} g(T_{C,i}) J_{C,i}^{Slice}(T_{C,i}) dT_{C,i}}{\int_{T_{C,act}^{Min}}^{T_{C,act}^{Max}} g(T_{C,i}) dT_{C,i}}. \tag{6.3.25}$$

In the limit that $p_c \to 1$ and $\delta T_C \to 0$ K (i.e., a delta function), we recover the 1D Chain Model. In general, the integral in Equation 6.3.20 and the numerator in 6.3.25 have no analytic solution. Therefore, numerical integration is required. To

make the expression for J_C^{Net} practical for analysing experimental J_C datasets, it is recommended that:

- The numerical integrals are calculated using an implementation of QUADPACK [199, 200]. In the development of the percolation model, multiple techniques were tried, such as Simpson's rule and Romberg's method, but it was found that QUADPACK gave the most consistent results in the shortest amount of time.
- The integrals are calculated with the T_C's being the variable to be integrated over, rather than J_C's.
- Integrating over discontinuities in $g(T_{C,j})$ is avoided. Discontinuities arise when the two modes of the $T_{C,j}$ distribution partially overlap. The integral should be split into multiple parts to avoid this.
- As a minimum, the integrands are written in a compiled language such as C, rather than an interpreted language such as Python, to reduce computation time. For example, the Cython package in Python [201] can be used to generate C code for the integrands that can be interpreted and integrated in Python.
- When calculating large numbers of J_C^{Net} values, multiple Central Processing Unit (CPU) cores are utilised to parallelise the calculations.

6.3.2.3 The functional behaviour of J_C in a Percolative Superconducting Network

Some examples of the functional behaviour for the strain dependence of J_C^{Net} are now presented. Figure 6.11 shows an example of $J_C^{Net}(\varepsilon_{JJ})$. For small strains where the two modes of the distribution overlap and $T_{C,act}^{Max}$ can be found within both, the $J_C^{Net}(\varepsilon_{JJ})$ behaviour is approximately parabolic. At larger strains, the modes separate, $T_{C,act}^{Max}$ can only be found in one mode and $J_C(\varepsilon_{JJ})$ is linear until

very large strains where the active superconducting area begins to decrease due to some junctions becoming insulating. At this point, $J_C^{Net}(\varepsilon_{JJ})$ has a convex shape and it tends to zero.

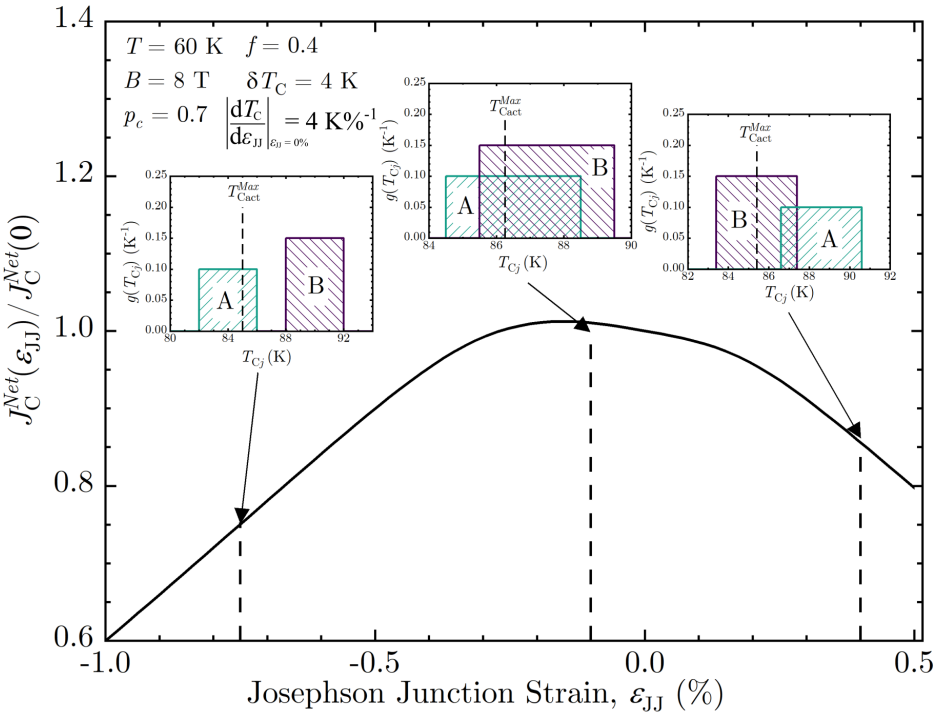

Figure 6.11: An example of J_C^{Net} for a fixed field and temperature. Beyond those parameters given in the top left of the figure, the other parameters used to generate this curve are taken from the fit to J_C for Non-APC (RE)BCO, $\theta = 0°$ ($\tilde{\Upsilon}_n$ free).

Figure 6.12 shows the variation of $J_C^{Net}(\varepsilon_{JJ})$ with f. Unlike $B_{c2,act}^{Max}(\varepsilon_{JJ})$, we do not require $f < p_c$ and $1 - f < p_c$ to ensure that J_C^{Net} always decreases at large tensile and compressive strains respectively. However, as $f \to 0$ and $f \to 1$, we still obtain linear behaviour for $J_C^{Net}(\varepsilon_{JJ})$. Figure 6.13 shows the variation of $J_C^{Net}(\varepsilon_{JJ})$ with p_c. For low values of p_c, we observe double peak behaviour for J_C^{Net}. The relative heights of the peaks vary depending on the value of f. As the N-values of the bonds get lower for a given J_C value (i.e., r_N decreases), the relative heights of the peaks compared to the value of $J_C^{Net}(0)$ increases. Double-peak behaviour has been observed experimentally on some samples [112, 152] and recently, Okada

has provided a possible explanation for the double-peak behaviour based upon multiple pinning mechanisms [202]. Further work is needed to understand whether the behaviour observed on the samples in the literature can be described using the percolation model.

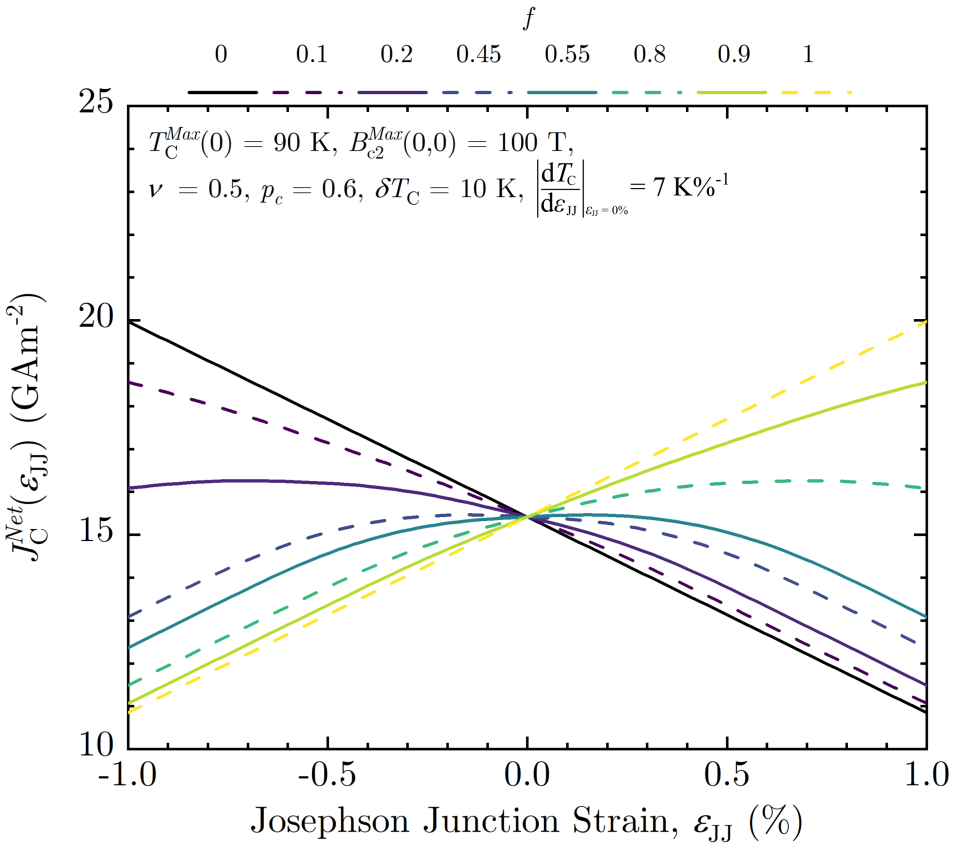

Figure 6.12: An example of J_C^{Net} for a fixed field (6 T) and temperature (40 K), but different f-values. Beyond those parameters given in the top left of the figure, the other parameters used to generate this curve are taken from the fit to J_C for Non-APC (RE)BCO, $\theta = 0°$ ($\tilde{\Upsilon}_n$ free).

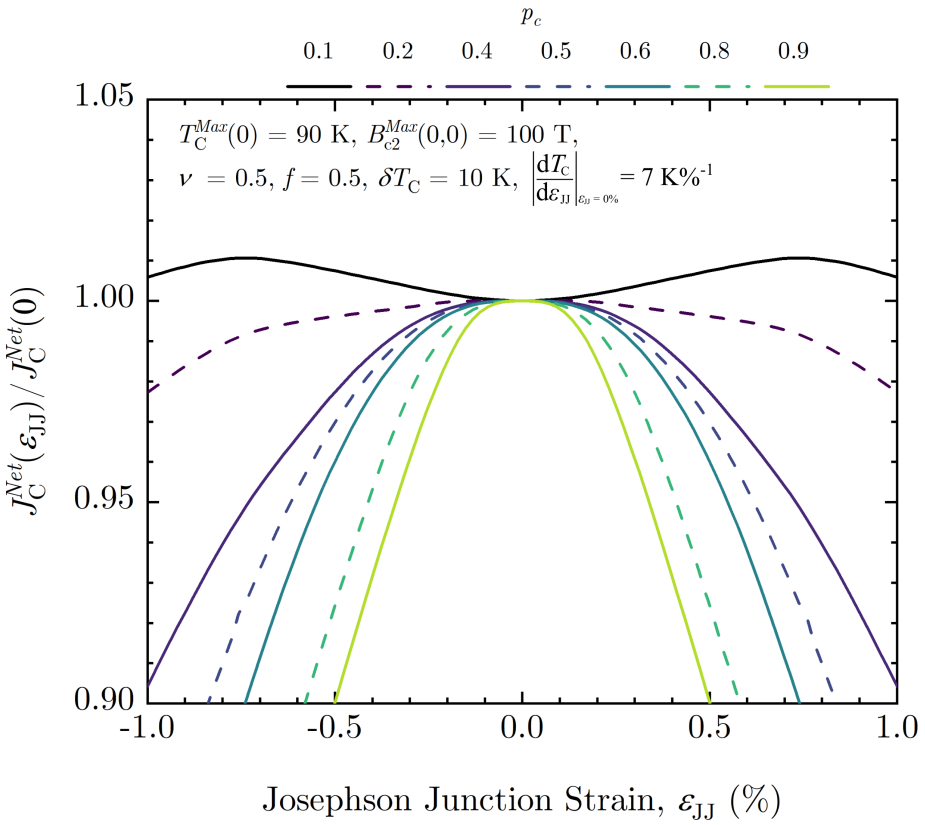

Figure 6.13: J_C^{Net} for a fixed field (6 T) and temperature (40 K), but different p_c-values. Beyond those parameters given in the top left of the figure, the other parameters used to generate this curve are taken from the fit to J_C for Non-APC (RE)BCO, $\theta = 0°$ ($\tilde{\Upsilon}_n$ free).

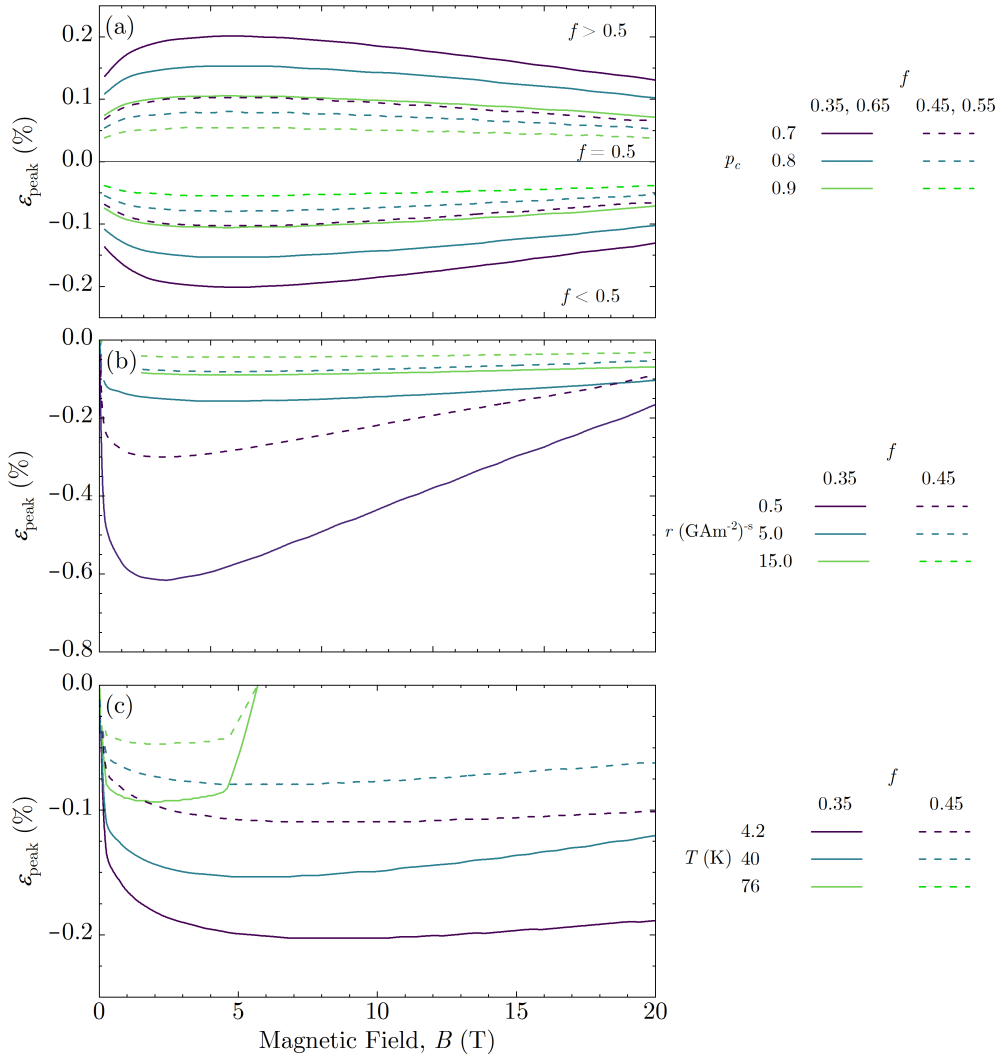

Figure 6.14: (a) $\varepsilon_{\text{peak}}(B)$ for different f and p_c values (at 40 K). (b) $\varepsilon_{\text{peak}}(B)$ for different f and r_N values (at 40 K). (c) $\varepsilon_{\text{peak}}(B)$ for different f's and temperatures. The other parameters used to generate this curve are taken from the fit to J_C for Non-APC (RE)BCO, $\theta = 0°$ ($\tilde{\Upsilon}_n$ free).

Figure 6.14 shows the variation of $\varepsilon_{\text{peak}}$ with field for different f's, p_c's, N-values and temperatures. Qualitatively, the behaviour is similar to that of the Chain Model [27]. Figure 6.15 shows $F_P^{Net}(B)$ (i.e., $J_C^{Net}(B) \times B$) for different p_c and δT_C values. As δT_C increases, the lower the value of reduced field at which A_{act} begins to decrease from 1. If we were to fit these curves using Equation 2.5.3, we would find different p and q values. When we use the percolation model in combination

with the BH expression for J_C, we find that the values of p and q required to fit the $F_P^{Net}(B)$ curves at each temperature and strain vary significantly. Figure 6.16 shows an example of how the shapes of F_P curves may vary with T and demonstrates that the percolative superconducting network model offers a completely different explanation for the temperature dependence of J_C (and F_P) associated with the distribution in T_C rather than the pinning literature usually attributes to different pinning mechanisms.

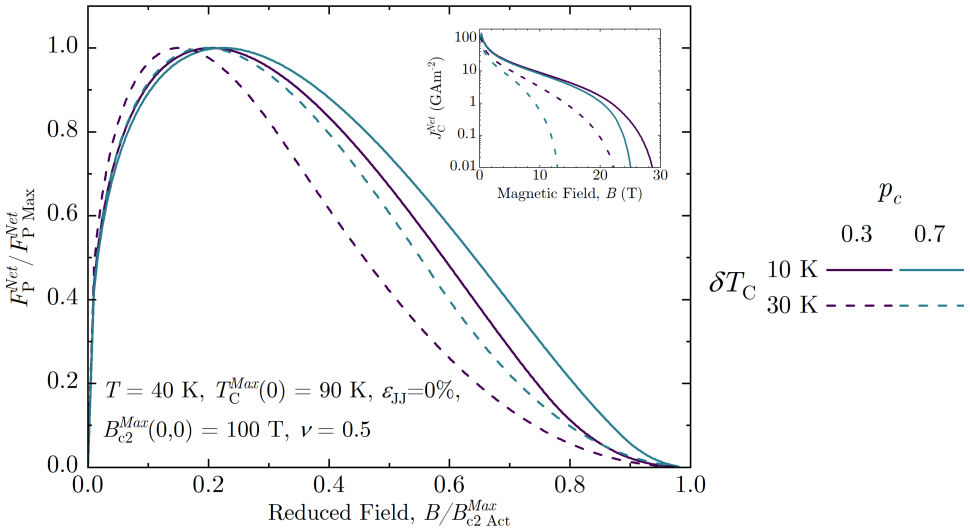

Figure 6.15: $F_P^{Net}/F_{P,max}^{Net}$ vs. $B/B_{c2,act}^{Max}$ for different p_c and δT_C values. Beyond those parameters given in the figure, the other parameters used to generate these curves are taken from the fit to J_C for Non-APC (RE)BCO, $\theta = 0°$ ($\tilde{\Upsilon}_n$ free) - See Table 6.3.

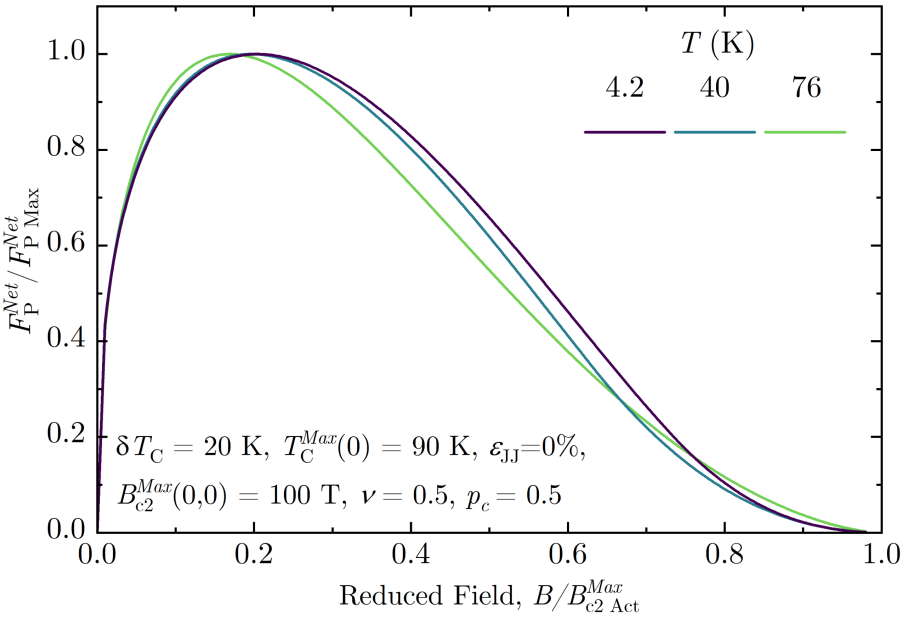

Figure 6.16: $F_P^{Net}/F_{P,max}^{Net}$ vs. $B/B_{c2,act}^{Max}$ for different T values. Beyond those parameters given in the figure, the other parameters used to generate these curves are taken from the fit to J_C for Non-APC (RE)BCO, $\theta = 0°$ ($\tilde{\Upsilon}_n$ free) - See Table 6.3.

6.3.2.4 Fitting the Experimental J_C Data using the Percolative Superconducting Network Model

We now present the fits to experimental J_C data. Figures 6.17 and 6.18 show the fits to the J_C data for Nb_3Sn, Figures 6.19 to 6.22 show fits to the J_C data for the APC (RE)BCO sample and Figures 6.23 to 6.26 show fits to the J_C data for the Non-APC (RE)BCO sample.

Similar to Chapter 5, we fixed the density of states ratio $\tilde{g}(E_{F,n})$ in all junctions to be 1. We also imposed the constraints that $w_d = w_\varepsilon$ for all samples and restricted the possible values of f to ensure that $B_{c2,act}^{Max}$ always decreased at large strains (see Figure 6.9 and its accompanying text in Section 6.3.2.1). For the Nb_3Sn sample, it was still necessary to allow $d_{\varepsilon 1}$ to be a free parameter to ensure a good fit to the data in high compression, especially at the lower temperatures. For the APC (RE)BCO fits with $\theta = 87.5°$, fits with significantly lower RMS J_C fit errors for $T \geq 60$ K

could be found by not including the 40 K data in the fits. For example, an RMS fit error of 0.470 GAm^{-2} was found for $\tilde{\Upsilon}_n = 1$ for $T \geq 60$ K but when the 40 K data were included, RMS fit errors on the order of those found for the Chain Model fit in Table 6.1 for $T \geq 40$ K were found. In a further attempt to assess and improve the fit quality for $\theta = 87.5°$ for both (RE)BCO samples, the values of r_N and S_N were allowed to have different values at each temperature. Branch found that universal scaling of N with J_C for the Non-APC sample for $\theta = 87.5°$ does not occur [28], and we have found that this is also true for the APC sample, as shown in Chapter 5.

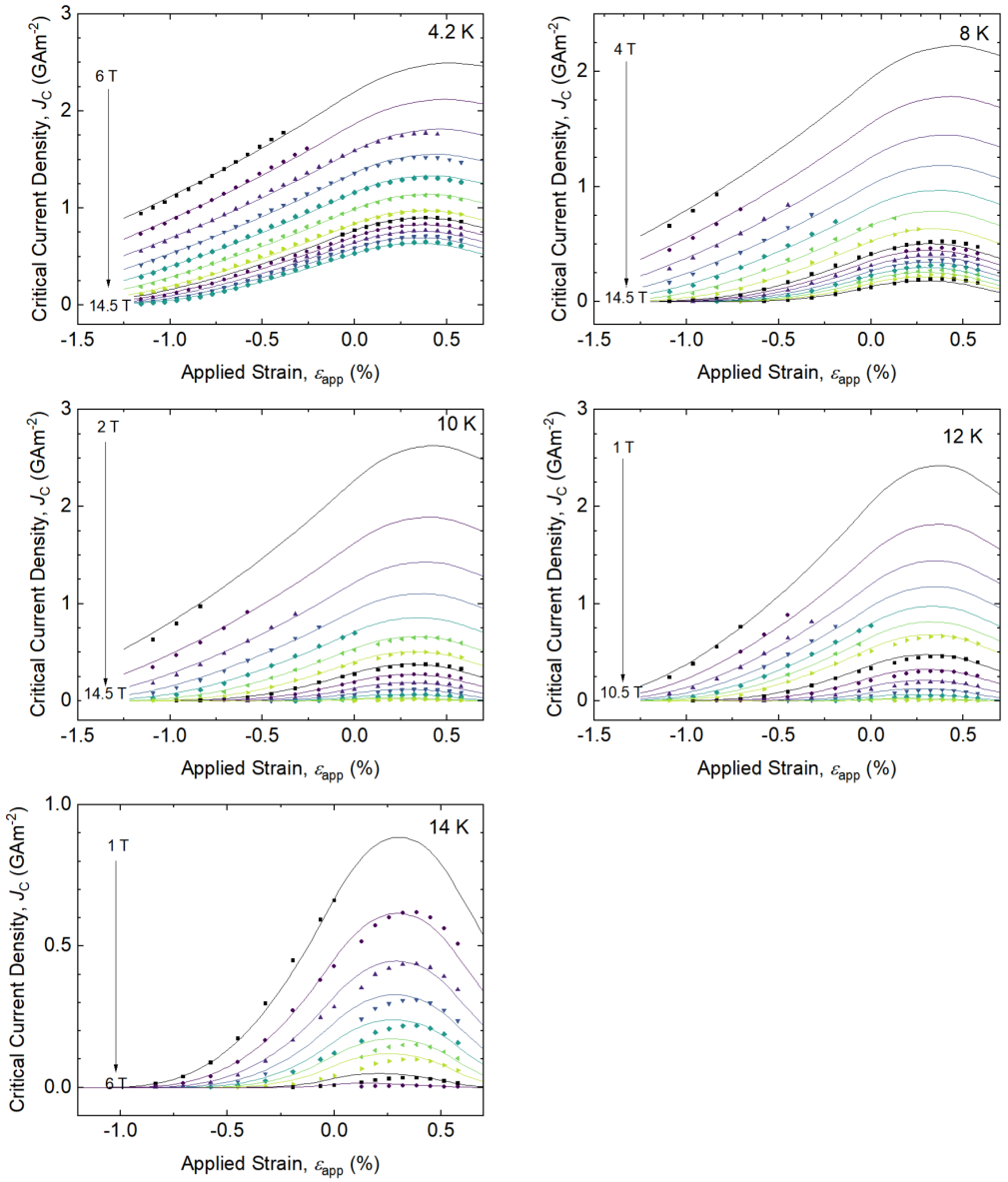

Figure 6.17: $J_C(\varepsilon_{app})$ for Nb_3Sn for the fit where not all conduction electrons condense ($\tilde{\Upsilon}_{n,j}$ free).

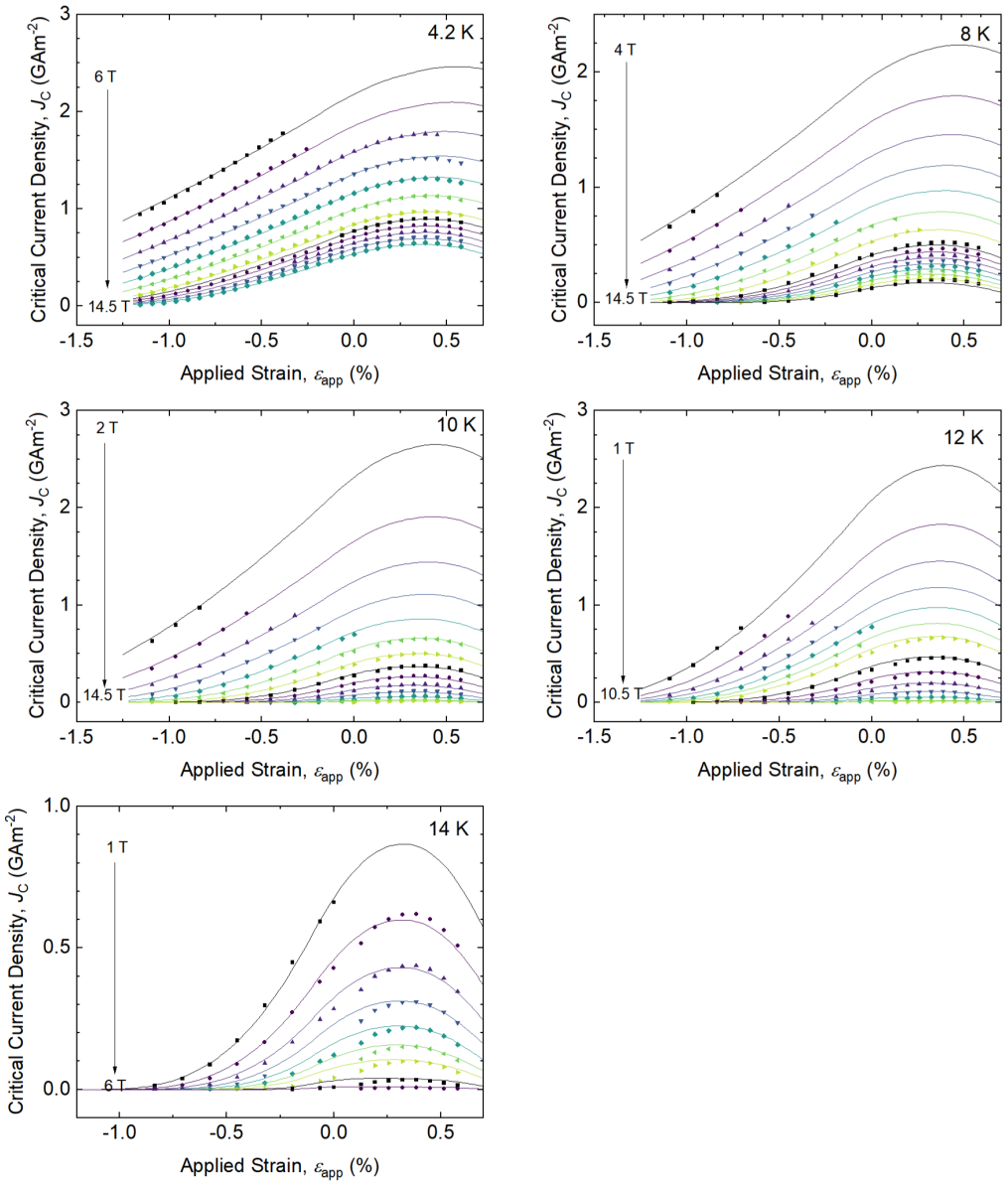

Figure 6.18: $J_C(\varepsilon_{app})$ for Nb_3Sn for the fit where $\Upsilon_{s,j} = \Upsilon_n = 1$.

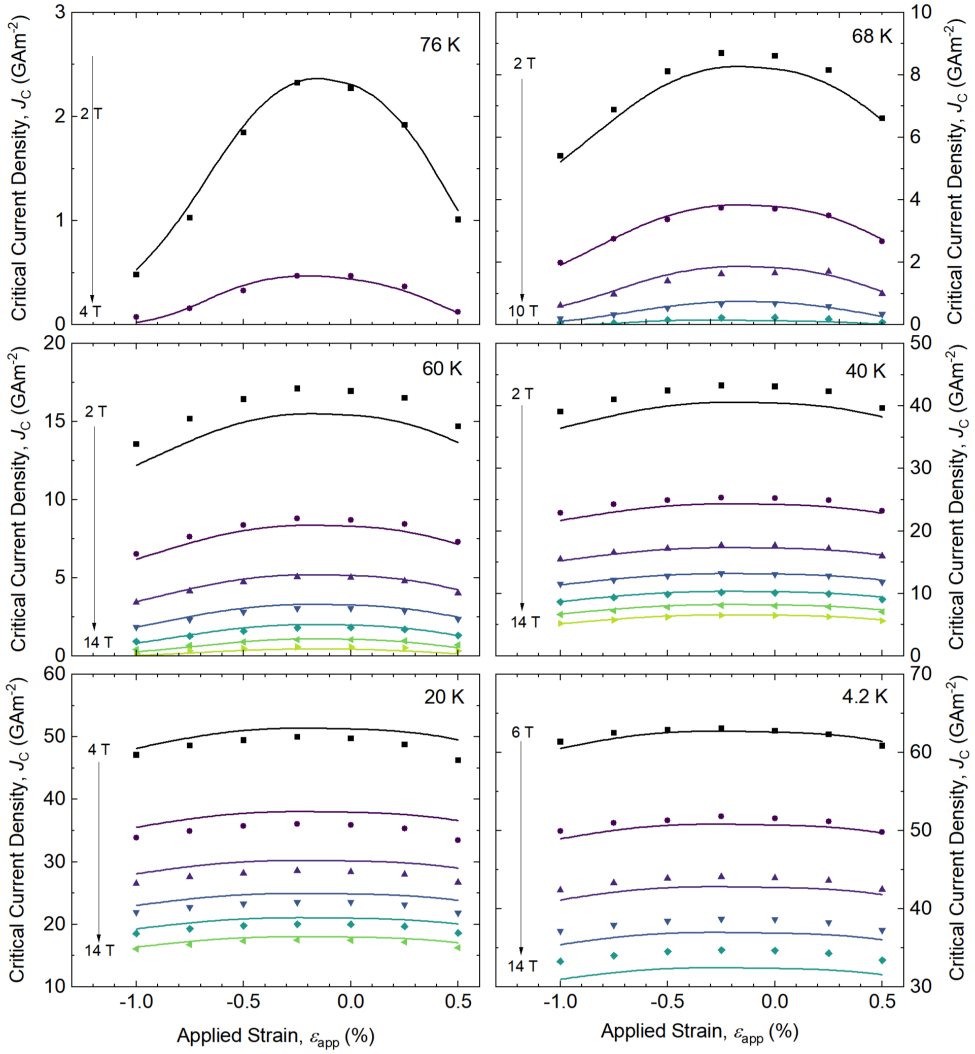

Figure 6.19: $J_C(\varepsilon_{app})$ for APC (RE)BCO for $\theta = 0°$ for the fit where not all conduction electrons condense ($\tilde{\Upsilon}_{n,j}$ free).

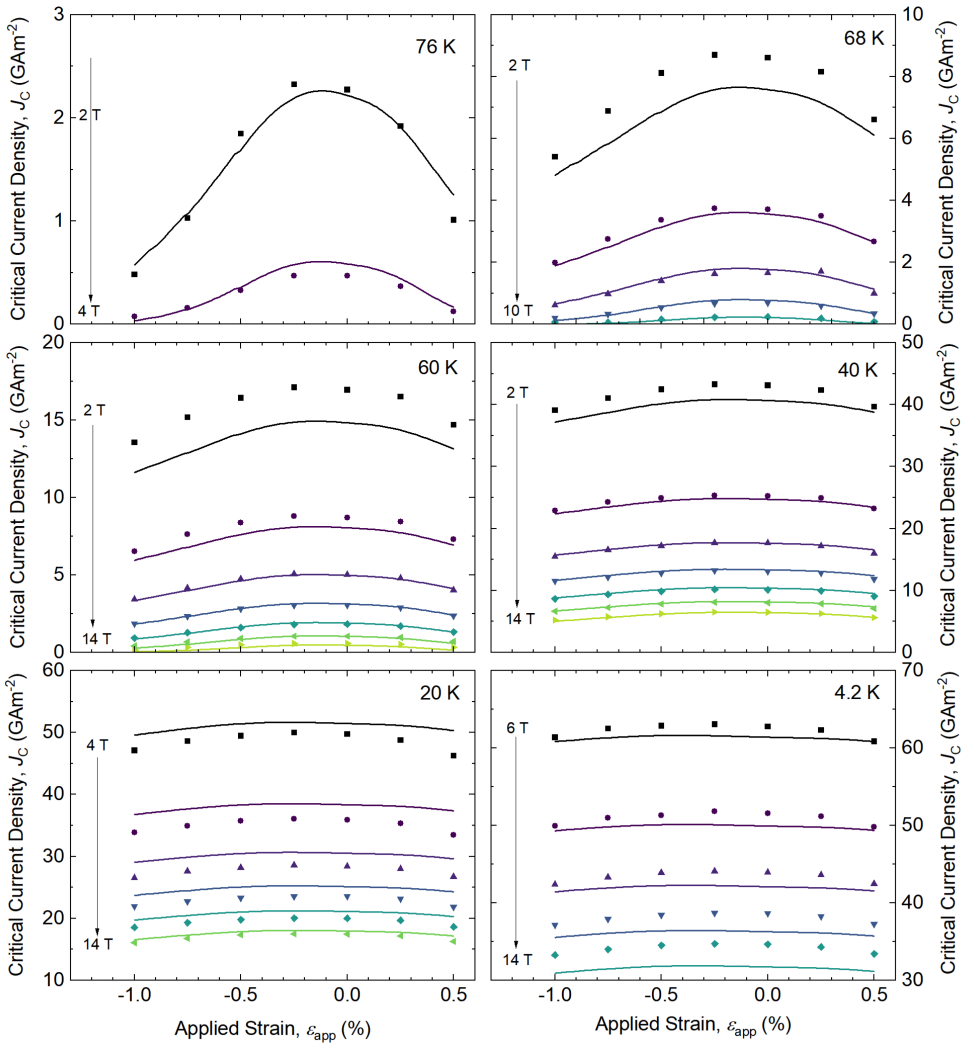

Figure 6.20: $J_C(\varepsilon_{app})$ for APC (RE)BCO for $\theta = 0°$ for the fit where $\Upsilon_{s,j} = \Upsilon_n = 1$.

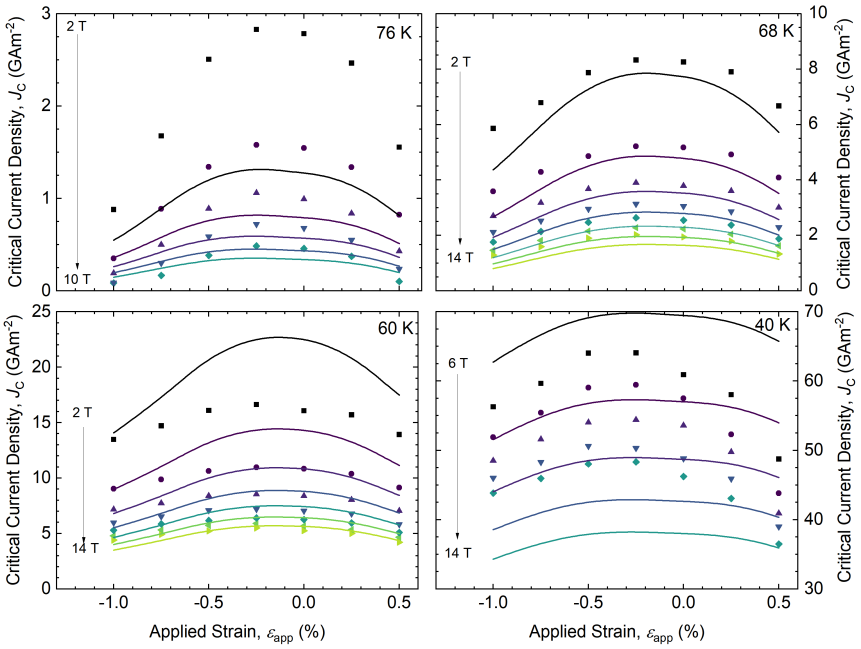

Figure 6.21: $J_C(\varepsilon_{app})$ for APC (RE)BCO for $\theta = 87.5°$ for the fit where not all conduction electrons condense ($\tilde{\Upsilon}_{n,j}$ free). The 40 K data were included in the fit.

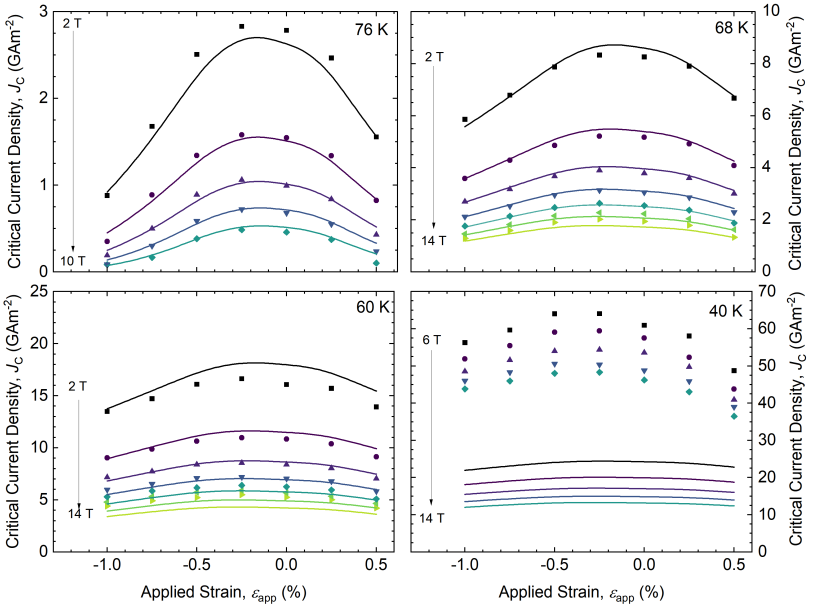

Figure 6.22: $J_C(\varepsilon_{app})$ for APC (RE)BCO for $\theta = 87.5°$ for the fit where $\Upsilon_{s,j} = \Upsilon_n = 1$. The 40 K data were not included in the fit. The r_N and S_N values for 40 K were assumed to be the same as the values at 60 K.

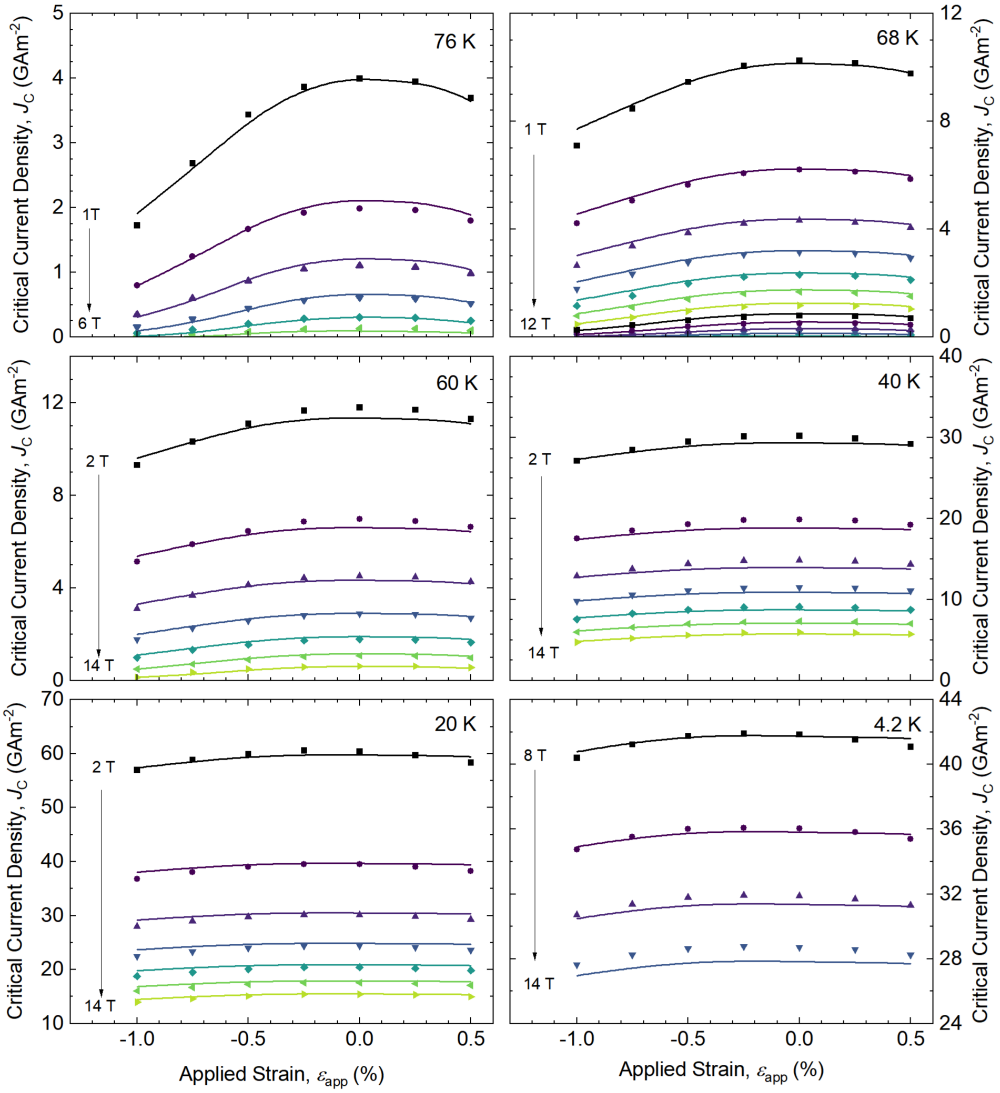

Figure 6.23: $J_C(\varepsilon_{app})$ for Non-APC (RE)BCO for $\theta = 0°$ for the fit where not all conduction electrons condense ($\tilde{\Upsilon}_{n,j}$ free).

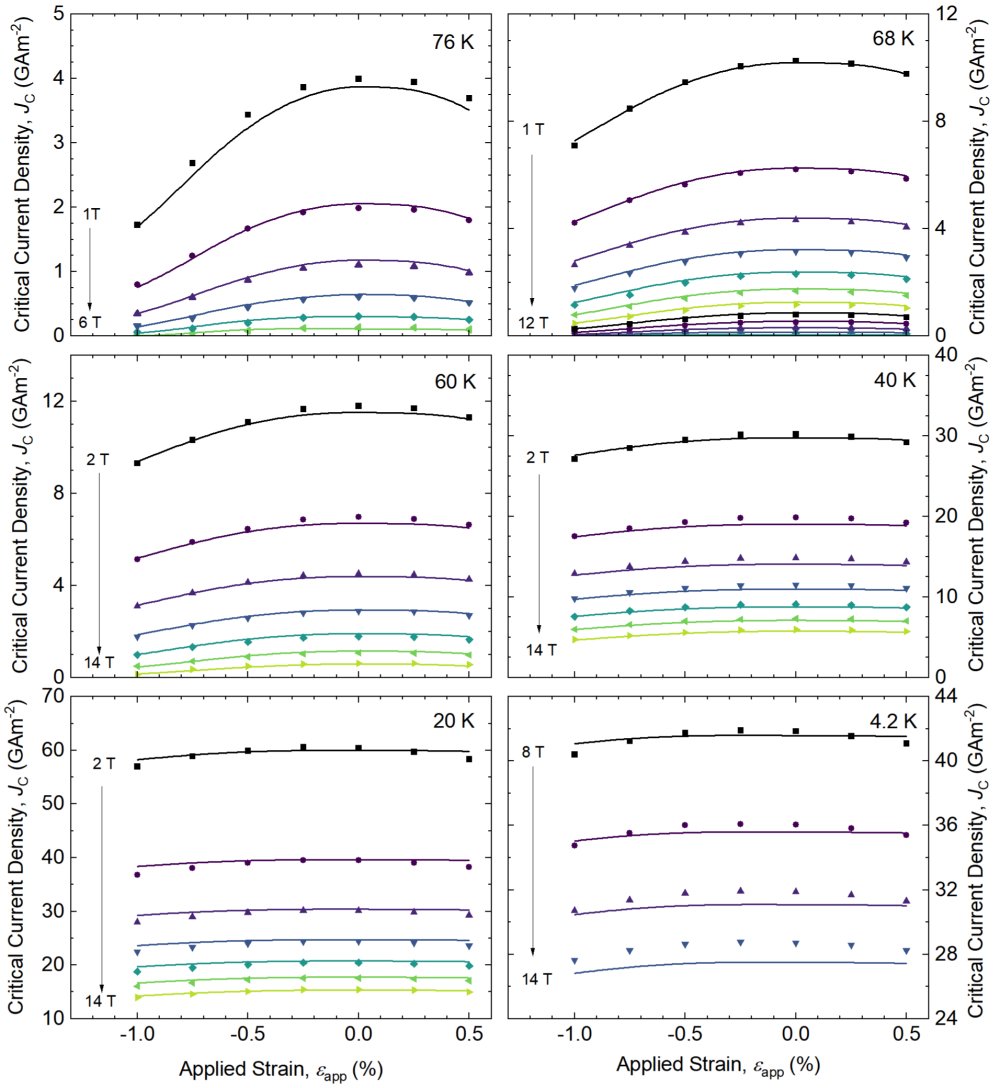

Figure 6.24: $J_C(\varepsilon_{app})$ for Non-APC (RE)BCO for $\theta = 0°$ for the fit where $\Upsilon_{s,j} = \Upsilon_n = 1$.

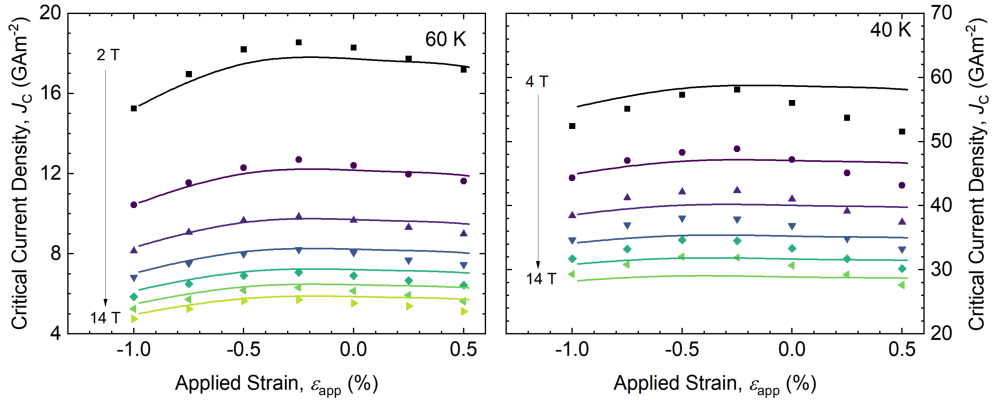

Figure 6.25: $J_C(\varepsilon_{app})$ for Non-APC (RE)BCO for $\theta = 87.5°$ for the fit where not all conduction electrons condense ($\tilde{\Upsilon}_{n,j}$ free).

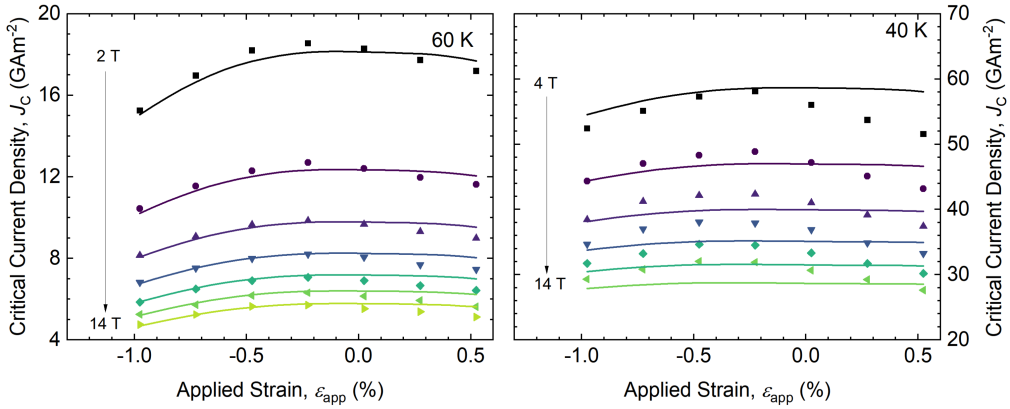

Figure 6.26: $J_C(\varepsilon_{app})$ for Non-APC (RE)BCO for $\theta = 87.5°$ for the fit where $\Upsilon_{s,j} = \Upsilon_n = 1$.

Table 6.3: Fit parameters for the percolation model fits. Bold parameters were fixed from the literature or set at zero to reduce the number of free parameters. For both (RE)BCO samples, for 87.5°, the italicised values were fixed at the 0° values. The starred value (*) of $w_s = 450$ nm was fixed from microscopy (see the references in [90]) and a factor of π to account for sphericity of grains. The dagger values (†) of $\tilde{\alpha}_n(0,0)$ were not free parameters as $\tilde{\alpha}_n^{Max}(0,0) = \tilde{T}_{C,n}^{Max}(0)$ when $\tilde{\Upsilon}_{nk,j}$ is free (see Table 6.2). For the APC sample, for $\Upsilon_n = \Upsilon_{sk,j} = 1$ for 87.5°, the 40 K data were excluded from the fit and the calculation of the RMS J_C error.

		Nb_3Sn	(RE)BCO (Non-APC)		(RE)BCO (APC)	
		$\tilde{\Upsilon}_{nk,j}$ free, $\Upsilon_{sk,j} = \Upsilon_n = 1$	$\tilde{\Upsilon}_{nk,j}$ free, $\Upsilon_{sk,j} = \Upsilon_n = 1$		$\tilde{\Upsilon}_{nk,j}$ free, $\Upsilon_{sk,j} = \Upsilon_n = 1$	
Constraint Type	Parameter		0°	87.5°	0°	87.5°
Fit parameters	$w_s(0)$ (nm)	**450***, **450*** [90]	339, 334	245, 241	235, 234	234, 245
	$d(0)$ (nm)	2.84, 2.95	0.587, 0.156	0.0122, 0.0377	0.119, 0.126	0.0840, 0.269
	c_1	0.514, 0.505	0.520, 0.527	*0.520, 0.527*	0.625, 0.584	*0.625, 0.584*
	$\lambda_L^{Max}(0,0)$ (nm)	**93.5**, **93.5** [22]	**135**, **135** [22]	***135***,***135***	**135**, **135** [22]	***135***,***135***
	$T_C^{Max}(0)$ (K)	17.9, 17.9	90.3, 93.0	*90.3, 93.0*	90.1, 89.7	*90.1, 89.7*
	$B_{c2}^{Max}(0,0)$ (T)	35.0, 35.0	115, 89.4	240, 240	134, 85.1	240, 240
	δT_C (K)	1.72, 1.95	5.64, 9.63	*5.64, 9.63*	7.65, 4.84	*7.65, 4.84*
	p_c	0.65, 0.55	0.55, 0.55	*0.55, 0.55*	0.55, 0.60	*0.55, 0.6*
	ν	1.51, 1.49	0.538, 0.755	7.08, 3.79	0.445, 0.700	1.50, 1.10
	$\left\lvert\frac{dT_C}{d\varepsilon_{JJ}}\right\rvert_{\varepsilon_{JJ}=0\%}$ (K%$^{-1}$)	2.43, 2.46	4.77, 5.95	*4.77, 5.95*	7.09, 6.04	*7.09, 6.04*
	$\varepsilon_{J_{CA}=J_{CB}}$ (%)	0.350, 0.300	0.137, 0.101	*0.137, 0.101*	−0.0648, −0.0218	*-0.0648, -0.0218*
	f	0.352, 0.461	0.460, 0.481	*0.460, 0.481*	0.452, 0.402	*0.452, 0.402*
	r_N ((GAm^{-2})$^{-s}$)	45.3, 45.3	5.59, 5.59	Table 6.4	5.20, 5.20	Table 6.4
	S_N	0.461, 0.461	0.440, 0.440	Table 6.4	0.470, 0.470	Table 6.4
	w_ε	2.27, 2.24	**2.2**, **2.2** [67]	***2.2***, ***2.2***	**2.2**, **2.2** [67]	***2.2***, ***2.2***
	$d_{\varepsilon 1}$ (10^{-3}%$^{-1}$)	−76.4, −66.5	**0**, **0**	***0***, ***0***	**0**, **0**	***0***, ***0***
	ζ_1 (nm)	**0**, **0**	2.64, 3.19	0, 0	1.75, 3.21	−0.916, −0.176
	ζ_2 (nm)	**0**, **0**	−1.43, −1.59	1.10, 0.884	−0.875, 1.61	1.96, 3.96
	$\tilde{\alpha}_n^{Max}(0,0)$	−2.64†, −1.84	−1.58†, −0.582	−1.58†, −2.69	−1.86†, −0.750	−1.86†, −4.88
	$\tilde{\beta}_n^{Max}(0,0)$	**1**, 0.164†	**1**, 0.0594†	***1***, 1.27†	**1**, 0.127†	***1***, 5.36†
	$\frac{\tilde{m}_n}{\tilde{\Upsilon}_n^{Max}(0,0)}$	4.40, 6.37	2.39, 8.10	8.68, 8.83	4.18, 5.23	8.18, 2.45
	$T_{C,n}^*$ (K)	−47.2, −60.0	−143, −222	*-143, -222*	−168, −189	*-168, -189*
Calculated parameters	$J_s^{Max}(0,0)$ (GAm^{-2})	9770, 9770	8490, 7490	8490, 7490	9170, 7310	9170, 7310
	$\tilde{g}^{Max}(E_{F,n})$	1, 1	1, 1	1, 1	1, 1	1, 1
	$\tilde{\rho}_{N,n}^{Max}$	4.40, 3.51	2.39, 1.97	8.68, 9.95	4.18, 1.86	8.18, 5.67
	$\tilde{n}_n^{Max}$	n/a, 3.86×10^{-3}	n/a, 1.88×10^{-3}	n/a, 1.45×10^{-3}	n/a, 6.98×10^{-3}	n/a, 0.0680
	$\tilde{\tau}_n^{Max}$	n/a, 471	n/a, 2180	n/a, 610	n/a, 402	n/a, 6.35
	$\tilde{l}_n^{Max}$	n/a, 11.6	n/a, 33.2	n/a, 7.83	n/a, 14.7	n/a, 1.06
RMS J_c Error (GAm^{-2})		0.0209, 0.0168	0.375, 0.373	1.50, 1.56	1.01, 1.27	3.38, 0.470

Table 6.4: N-value parameterisation for the (RE)BCO fits for $\theta = 87.5°$

Parameter	Temperature (K)	(RE)BCO (Non-APC) $\tilde{\Upsilon}_n$ free	(RE)BCO (Non-APC) $\Upsilon_s = \Upsilon_n = 1$	(RE)BCO (APC) $\tilde{\Upsilon}_n$ free	(RE)BCO (APC) $\Upsilon_s = \Upsilon_n = 1$
r_N $(\mathrm{GAm}^{-2})^{-S_N}$	76	-	-	4.27	5.86
	68	-	-	4.54	3.23
	60	4.16	4.05	5.98	2.61
	40	0.359	0.126	4.22	-
S_N	76	-	-	0.773	~ 0
	68	-	-	0.122	0.719
	60	~ 0	~ 0	0.798	0.698
	40	0.900	1.17	0.285	-

6.4 Discussion

In this section, we begin by discussing the characteristics of the distributions of critical superconducting parameters in the grains of the (RE)BCO and Nb_3Sn samples, the current flow characteristics, and the strain dependencies of J_C^{Net} and the distributions. We then discuss the consistency of our fit parameters with experimental $B_{c2}^{*\rho}$ data and the $\rho(T)$ transition (Section 6.4.3). We then offer possible ways to improve the fits to the $\theta = 87.5°$ data for both (RE)BCO samples, after which we make some general comments about the quality of the analysis that our percolation model is able to generate and how it may be particularly useful for modelling irradiated superconducting materials.

6.4.1 Current Percolation and Distribution Characteristics of (RE)BCO and Nb_3Sn

The percolation threshold values for Nb_3Sn and the (RE)BCO samples are consistent with those found for resistor-insulator networks that have coordination numbers of $\sim$ 3 - 4 [140]. These coordination numbers are often, but not exclusively, associated with 2D networks. It is not particularly surprising that such p_c values have been found for the SuperPower (RE)BCO tapes because the *ab*-planes of the (RE)BCO are parallel with the macroscopic tape plane and the depairing currents (and indeed critical currents) of (RE)BCO single crystals are substantially weaker

along the c-axis [22]. The (RE)BCO layer is also thin ($\sim$ 1 μm) compared to its width ($\sim$ 4 mm) and the distance between the voltage taps ($\sim$ 13 mm) used to measure I_{C}. As p_c decreases, J_{C}^{Net} increases. It will be extremely challenging to substantially lower p_c for (RE)BCO tapes due to the anisotropy of (RE)BCO's material properties and the dimensions of (RE)BCO tapes themselves.

For Nb_3Sn, one may have expected lower percolation threshold values that are often associated with 3D networks (e.g., 1/3) due to the polycrystalline, isotropic nature of the Nb_3Sn grains within the filaments. However, our model has shown that low percolation threshold values can not produce the correct behaviour for the strain dependence of J_{C} for reasonable values of $\left|\frac{\mathrm{d}T_{\mathrm{C}}}{\mathrm{d}\varepsilon_{\mathrm{JJ}}}\right|_{\varepsilon_{\mathrm{JJ}}=0\%}$. The fact that the filaments within the Nb_3Sn strand are much longer than their diameter may be partially responsible for the relatively high percolation thresholds. Equally, the preferential transport current flow along the length of the wire rather than orthogonal to it may also explain the high percolation threshold values (i.e. ~ 0.6). Directed percolation models can be used to describe such current flows and they tend to have higher percolation thresholds than equivalent isotropic percolation models, for the same network coordination number [140, 203].

In this work, we have restricted the T_{C} distribution to be a bimodal top hat distribution. Because of this, we get discontinuities in the gradients of $A_{\mathrm{act}}(B, T, \varepsilon_{\mathrm{JJ}})$, $T_{\mathrm{C}}^{Max}(\varepsilon_{\mathrm{JJ}})$, and $B_{\mathrm{c2,act}}^{Max}(T, \varepsilon_{\mathrm{JJ}})$. Using an alternative distribution such as a Weibull distribution will overcome this issue, at the cost of introducing additional free parameters into the global fits for J_{C}. As far as we are aware, there are currently no other experimental techniques that can be used to extract relevant T_{C} distribution characteristics, other than by inferring them from J_{C} data, as we have here. New techniques need to be developed so that the results of this analysis can be independently verified for example with local measurements of T_{C} throughout the sample.

6.4.2 The Strain Dependence of J_C^{Net} and the Distributions

The values of $\left|\frac{dT_C}{d\varepsilon_{JJ}}\right|_{\varepsilon_{JJ}=0\%}$ for all 3 samples are physically reasonable [197, 33, 34, 113, 28]. The quite high values of $T_C^{Max}(0)$ mean that for large strains, the T_C's of some of the Josephson junctions are as high as 93 K and therefore exceed a little the values found in optimally doped single crystals. We don't consider this to be a serious problem since it may simply be an artefact of the top-hat distribution we have used and the Josephson junctions with these high T_C's only contribute to cluster building bonds (c.f. Figure 6.10). These bonds would play a larger role in determining J_C^{Net} for samples with lower percolation thresholds. A more complex percolation model for (RE)BCO would implement the dome-like behaviour for $T_C(\varepsilon)$ that has been seen, for example, in detwinned tapes [113], but is not as yet required.

6.4.3 The $\rho(T)$ Resistive Transition and $B_{c2}^{*\rho}$

For low currents, our percolation model predicts that the resistive transition width for a superconductor in self field is equal to $(1-p_c)\times\delta T_C$. The products of the $1-p_c$ and δT_C values for the (RE)BCO samples in Table 6.3 are in good agreement with the measured transition widths in self-field at $\varepsilon_{JJ}=0\%$ (see Section 5.3 and [28]). While the resistive transition was not measured for the Nb_3Sn sample, the p_c and δT_C values are also consistent with the transition widths of other similar Nb_3Sn strands in the literature [204].

For higher currents, in-field, we may expect the resistive transition width to broaden because of flux flow. Flux flow will lead to the material having a non-zero voltage before it transitions to the normal state. In our model, we are able to extract approximate values of $B_{c2}^{*\rho}$ for (RE)BCO by identifying the field at which $J_C^{Net}\times A_{Tot}=100$ mA, as this was the current used to find $B_{c2}^{*\rho}$ for both samples [27]. We denote this field $B_{c2}^{*J_C}$. Figure 6.27 shows an example for the APC (RE)BCO

sample and demonstrates that the calculated values of $B^{*J_C}_{c2}$ are best associated with experimental $B^{*\rho}_{c2}$ data at the $0.1\rho_N$ criterion. By comparing the $B^{Max}_{c2,act}$ (the maximum field at which an infinitely spanning superconducting cluster can exist in the material) and $B^{*J_C}_{c2}$ data, we see that flux flow has a limited impact on the measured voltages during the in-field $\rho(T)$ transition as the magnitude and strain dependence of the $B^{Max}_{c2,act}$ data are in very good agreement (slightly higher) than the $B^{*J_C}_{c2}$ data. Also shown in Figure 6.27 is a comparison of the experimental $B^{*\rho}_{c2}$ data with the parameterisation of B^{*}_{c2} in Section 5.6, in which a single value of B^{*}_{c2} (i.e., a delta function) was assumed for the entire material (which we refer to in this discussion as $B^{*\delta}_{c2}$). While the temperature dependence is in broad agreement with the other data in the figure, the strain dependence has a negative curvature. Therefore, while reasonable fits can be achieved for J_C across the entire field, temperature and strain range for (RE)BCO by using the literature approach of considering single values of the critical superconducting parameters, the only way to get self-consistent fits for J_C and $B^{*\rho}_{c2}$ is to consider the material as a percolative network that has a bimodal distribution of superconducting properties.

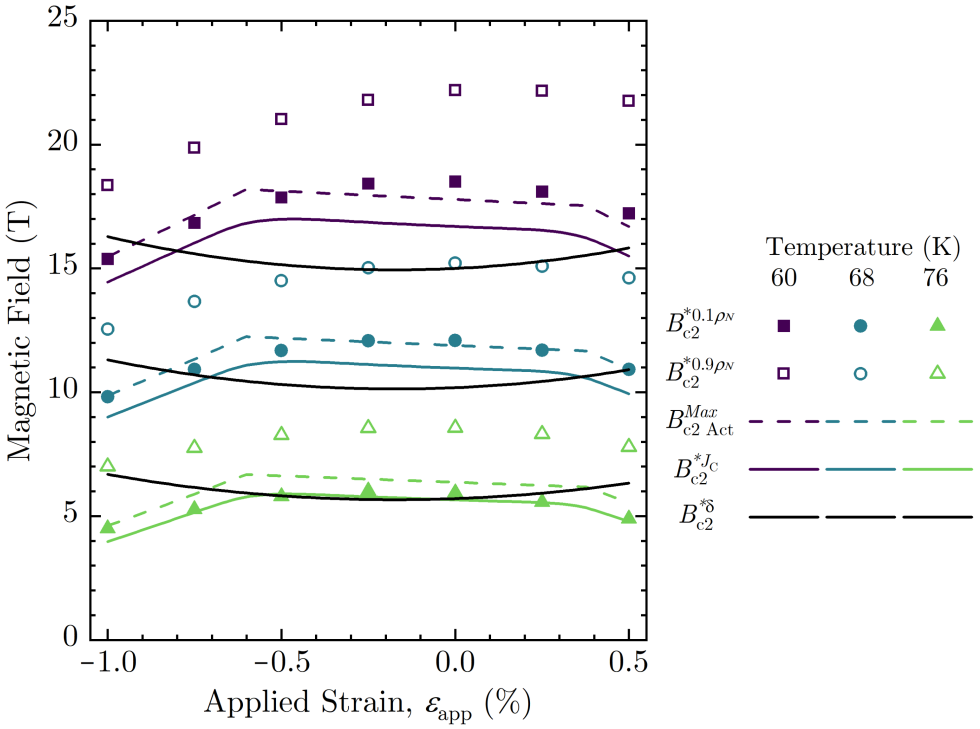

Figure 6.27: Different values of B_{c2}^{*} for the APC (RE)BCO sample with $\theta = 0°$, extracted from experimental $\rho(T)$ data or global fits to J_C in this thesis. The $B_{c2}^{*0.1\rho_N}$ and $B_{c2}^{*0.9\rho_N}$ data were calculated from Table 5.2, the $B_{c2,act}^{Max}$ and $B_{c2}^{*J_C}$ data were calculated from Table 6.3 (for free $\tilde{\Upsilon}_n$), and the $B_{c2}^{*\delta}$ values were taken from the fit in Table 5.7 for free $\tilde{\Upsilon}_n$, that used a single value for T_C for the entire material (i.e., a delta function).

These results will need verification for the Nb_3Sn strands by comparing detailed $B_{c2}^{*\rho}$ and J_C data on a single strand. We also suggest that the discrepancy between the $B_{c2}^{*J_C}$ values and the experimental $B_{c2}^{*\rho}$ data will decrease as the choice of resistivity criterion slowly decreases towards zero resistivity. This will require an improvement to the experimental setup to improve the signal to noise ratio.

It is more challenging to associate the $B_{c2}^{*\rho}$ data at the $0.9\rho_N$ criterion with a distribution or network characteristic within our percolation model. This is because in the experiments, even when there is no infinite spanning superconducting cluster in the (RE)BCO layer, some of the current may flow in/out of the isolated superconducting clusters from/to the Cu and Ag layers of the tape. Current shunting will also affect the measured J_C values at higher temperatures and fields and larger

strains as the N-values get closer to 1. Future extensions to this work could include $B_{c2}^{*\rho}$ measurements on tapes with the Cu and Ag layers removed, and possibly even J_C measurements if the thermal stability of the sample can be controlled. Alternatively, a normal conducting layer in parallel to the slices in our rule of mixtures for percolation (Figure 6.10) could be introduced.

The measured $B_{c2}^{*\rho}$ data for the Non-APC and APC data on these samples are best associated with the irreversibility field B_{irr} in the literature, due to the convex temperature dependence [205, 206], rather than single crystal B_{c2} data that display concave WHH-like behaviour [164, 207] that is also observed in LTS (see e.g., [90]). The same is true for the temperature dependencies for the B_{c2}'s of each of the Josephson junctions, and $B_{c2,act}^{Max}$. In our percolation model, we tried incorporating a concave temperature dependence for the B_{c2}'s of the junctions, and modelled $B_{c2}^{*J_C}$ for very large δT_C and low p_c values, however, we were unable to obtain convex behaviour. Branch made the reasonable suggestion that current shunting may be responsible for the discrepancy between the single crystal B_{c2} and B_{irr} data [28] which is worthy of future work.

6.4.4 J_C^{Net} for $B_{||ab}$ for (RE)BCO

For both (RE)BCO samples, for $\theta = 87.5°$, the fields at which J_C was measured for $T = 40$ K are very low compared to the values of $B_{c2,act}^{Max}$ (and $B_{c2,act}^{*\rho}$). We have demonstrated that significantly better fits can be achieved for $\theta = 87.5°$ by excluding the 40 K data or equivalently that mapping the limited J_C data we have for $\theta = 87.5°$ onto the $\theta = 0°$ data is progressively less successful (or useful) at low temperatures. This naturally points to a changing pinning mechanism or regime at low temperatures. We suggest that the 2D-3D dimensionality cross-over [208] provides a natural explanation. At this cross-over, which calculations suggest occur between 20 and 50 K [208], the fluxons become smaller than the unit cell size, so we can expect the pinning to change and perhaps as the data suggest, a marked change to the strain dependence at 40 K. Necessarily this avenue is best pursued with more

detailed J_C data for $\theta = 87.5°$ at the highest fields available. There are some less data driven solutions that we could in principle also look at - Incorporating the effects of self-field [184] may provide a better fit to the 40 K data, and therefore a better fit overall, however, we don't expect it to improve the agreement with the strain dependence. In Section 5.3, we saw the breakdown in the universal N vs J_C scaling for $\theta = 87.5°$, which is why the r_N and S_N values were allowed to vary for the percolation model fits (see Table 6.4). We suggest that an alternative scaling could be used for this field orientation. Preferably, the new scaling should lead to the J_C's of the bonds at the front of the slices being weighted far more than those towards the back in Figure 6.10 when the modes are separated, which would drive down J_C for larger strains.

6.5 Fitting J_C Data Using the Percolative Superconducting Network Model

The central issue in the analysis of the J_C data presented in the last two chapters of this thesis has followed from the break-down of the scaling law in (RE)BCO. The very clear universality shown in Figure 5.7 clearly demonstrates why the scaling law approach has been so useful for decades. However the non-physical values of B^*_{c2}, namely ~ 1000 T at 4.2 K, show the scaling law simply doesn't describe the J_C data of (RE)BCO at all, at low temperatures. In this thesis we have first used the SNS junction approach (Chapter 5) and then added percolative current flow through an inhomogeneous superconducting network (Chapter 6) that naturally incorporates the required break-down of scaling. It is clear from the figures in Chapters 5 and 6, that the approach adopted gives physically reasonable parameters across the entire field-temperature-strain phase space and hence provides a route forward for parameterising J_C data for (RE)BCO. This approach also provides (for the first time) the microscopic properties of the important pinning components as well as a natural explanation for the prevalence amongst many different superconductors for

J_C to be at a maximum when the intrinsic strain is zero. It is important to note in comparing the fits in Chapters 5 and 6, that in Chapter 5 we have used polynomials to characterise the strain dependence of the critical superconducting parameters. In Chapter 6, although we have introduced an additional free-parameter associated with the inhomogeneity of the samples, we have reduced the number of free parameters by requiring competing strain dependencies. Here we consider some brief final observations about the different fits made to the data in Chapters 5 and 6 in turn:

Nb_3Sn: The Nb_3Sn data are the most comprehensive data known to the author. Most fits to these types of data are limited to temperatures below 12 K because the accuracies of the fits reduce when extended to the highest temperatures. The quality of the SNS fits with polynomial strain dependencies (cf Figures 5.16 and 5.17 and Table 5.7) is simply state-of-the-art and also provides physically reasonable values for the grain boundary thickness [209] and grain size (see the references in [90]). In the context of G-L theory, all materials are eventually superconducting. The fits suggest that the grain boundaries themselves are pair-breaking for the superelectrons ($T^*_{C,n}$ is negative), which is not unreasonable, but clearly needs more work to be independently confirmed. Adding percolative current flow with bimodal grains and competing strain dependencies also gives good fits (cf Figures 6.17 and 6.18 and Table 6.3) to the data as well as physically reasonable and self-consistent range of T_C of ~ 0.6 K [204].

(RE)BCO: The (RE)BCO fits (both APC and non-APC) are also good for both $\Upsilon_n = \Upsilon_s = 1$ and $\tilde{\Upsilon}_n$ free (cf Figures 5.9 to 5.15 and Table 5.7) at low temperatures, although less good at high temperatures. The fits have been improved at high temperatures by explicitly adding in the distribution in T_C (cf Figures 6.19 to 6.26 and Table 6.3). Again the widths of the junctions are reasonable and the thicknesses very small. These small thickness values are consistent with strong pinning sites separated by superconducting matrix material that is hardly degraded at all - analogous to strong pinning sites in a matrix. Again we interpret the barriers as

pair breaking.

Finally, we include several routes to improve this analysis further. The percolation model presented in this Chapter could be used with other expressions for the J_C's of the bonds. The model originally used the flux pinning expression for J_C in Section 5.6, however, it was found that unphysically high values of B_{c2} for the bonds were still required at lower temperatures. Therefore we chose to use the BH SNS Josephson junction expression for J_C.

We suggest that our percolation model will be useful for predicting the degradation in the superconducting properties of irradiated tapes and strands. While the δT_C values of these technological superconductors appear to be only a small fraction of $T_C^{Max}(0)$, in fusion reactors, radiation damage from neutrons and gamma rays will lead to a broadening of the T_C distribution due to, for example, dislocation loops or transmutation. For example, Iliffe has performed measurements on the effects of cryogenic neutron irradiation on T_C (via the resistive $\rho(T)$ transition) and J_C [210]. The transition broadened and J_C was lowered with increasing dose, which is consistent with the predictions of our percolation model. Accurately predicting the evolution of the superconducting critical surface with neutron damage will be critical for future fusion power plants that are based on compact, spherical tokamaks with superconducting magnets, such as UKAEA's STEP reactor [9] and Tokamak Energy's ST-E1 reactor [211]. Compact, spherical tokamaks have limited room for radiation shielding between the plasma and the magnets, especially in the centre column.

6.6 Conclusions

In this chapterfits have been made to the $J_C(B, T, \varepsilon)$ data for Nb_3Sn and 2 (RE)BCO tapes using the chain model in the literature across the entire experimental strain range, for the first time. We have shown that chain model cannot fit J_C data at

large strains or J_C data measured at fields close to B_{c2}. In order to get good fits to the J_C data across the entire strain range, the material must be considered as a percolative network of Josephson junctions with distributions of critical superconducting parameters that has $p_c < 1$ and $\delta T_C > 0$ K. Using the percolation model is also the only way to ensure that the J_C fits are self-consistent with $B_{c2}^{*\rho}$ data extracted from $\rho(T)$ data. For all 3 samples, the extracted p_c values are consistent with network coordination numbers of 3-4. The δT_C values are typically no more than $\sim 10\%$ of $T_C^{Max}(0)$.

More fundamentally, when taken in combination with the BH formalism for J_C in SNS Josephson junctions, our percolation model offers an alternative explanation for the strong temperature dependence of the p and q values that are found when fitting J_C data for (RE)BCO using a flux pinning formalism. Distributions in T_C (and B_{c2}) lead to a suppression in J_C at high fields and temperatures, near $b = 1$. This effect cannot be understood by any existing model in the literature. Understanding how factors such as δT_C and p_c limit J_C will be crucial for further optimising the J_C's of technological superconductors for all applications. For fusion reactors, understanding how δT_C evolves with radiation damage will be extremely important, as it may prove to be the lifetime limiting factor for commercial fusion power plants.

Chapter 7

Conclusion and Future Work

This thesis has shown that flux pinning scaling laws for isotropic superconductors do not adequately describe the field, temperature and strain dependence of J_C for (RE)BCO tapes. The 1D chain model is also unable to provide a full description of J_C across the entire reversible strain range. J_C is better described by a new type of scaling law in which the material is treat as a percolative network that contains a mixture of insulating bonds and SNS Josephson junction bonds. This scaling law has allowed us to extract the dimensions and normal state properties of the normal barriers/grain boundaries within superconducting materials that limit or prohibit supercurrent flow. It has also allowed us to extract information about the distribution of T_C within the material and the dimensionality of the supercurrent flow via the percolation threshold p_c. We have also presented the first measurements for the 2D, in-plane strain dependence of J_C.

In terms of future experimental work, the most obvious place to start would be to commission the 2D strain probe outlined in Chapter 4 at 4 K for high field $J_C(B, \theta, \varepsilon_{xx}, \varepsilon_{yy})$ measurements. This will enable a better understanding of the biaxial strain dependence in an environment that fusion magnets are more likely to be operated in. Special consideration will need to be given to the flexible superconducting current leads at the bottom of the probe to ensure that they can carry 1 kA without causing the probe to twist [148]. The probe could be modified to include a variable temperature cup, to enable variable temperature measurements

of J_C to be made, and also $B^{*\rho}_{c2}(T, \theta, \varepsilon_{xx}, \varepsilon_{yy})$ measurements. The 15 T horizontal magnet in Durham has a bore diameter of < 40 mm. Designing a temperature cup would inevitably involve reducing the size of the 2D springboard so that it fits inside the cup. Given that a lot of the hardware used to apply the strain is already at the smaller end of what manufacturers are able to supply (see, e.g., [212]), this will be a very challenging undertaking. Nevertheless, we ultimately envisage an experimental setup with full in-situ strain control where one would be able to measure $J_C(B, \theta, T, \varepsilon_{xx}, \varepsilon_{yy})$ and $B^{*\rho}_{c2}(\theta, T, \varepsilon_{xx}, \varepsilon_{yy})$ to the same level of detail as the measurements outlined in Chapter 4 for the uniaxial strain dependence of J_C. In parallel to the biaxial strain measurements of J_C, the biaxial strain measured by the 2D T-rosette strain gauge on the sample will need to be calibrated against the intrinsic strain within the (RE)BCO layer. This could be achieved using neutron diffraction experiments that are similar to those that have been used to compare the strain measured by strain gauges and the intrinsic strain within the (RE)BCO layer for the 1D springboard [31, 32].

The model for J_C in Chapter 4 was restricted to a simple linear strain dependence for T_C, taking into account the Poisson ratio. The biaxial strain response of the T_C's of (RE)BCO's A- and B-domains will need to be investigated, for all quadrants of the ε_{yy} vs. ε_{xx} plot. Given the challenging nature of uniaxial pressure dependent measurements of T_C for (RE)BCO single crystals [33, 34], an easier method may be to perform measurements on detwinned tapes that can be produced by bending and annealing tapes [113, 213], if the f-value can be brought sufficiently close to 0 or 1.

The biaxial strain dependence of J_C, could, of course, be measured for other technological superconductors such as Bi-2223 tapes or MgB_2 tapes. However, it will be very challenging to perform measurements like these on Nb_3Sn strands, that have already been shown to possibly exhibit competing behaviour. Some of the earliest technological Nb_3Sn superconductors were grown in a flexible tape form using chemical vapour deposition so that they could be wound into magnets [214].

$J_C(\varepsilon_{xx}, \varepsilon_{yy})$ measurements on Nb_3Sn tapes may shed further light on the competing behaviour within Nb_3Sn. However, if the grain boundaries in Nb_3Sn are responsible for the competing behaviour, rather than the grains, then the differences in grain boundary structures between the tapes and filaments in strands may significantly complicate the analysis.

The analyses in this thesis have shown that it is possible to extract rich information about the mechanisms suppressing J_C in technological LTS and HTS from $J_C(B, T, \varepsilon)$ data alone. Many of the parameter values extracted from our fits will require verification using other experimental or simulation techniques. For example, methods for measuring δT_C and $T_C^{Max}(0)$ within (RE)BCO tapes will need to be developed. Devising a method of measuring the percolation threshold experimentally without relying on transport measurements will be a formidable challenge. Perhaps instead, 2D or 3D FE or TDGL simulations could be performed on representative (RE)BCO or Nb_3Sn grain structures, in which each grain is assigned a different T_C value (or even a T_C distribution within each grain/superconducting electrode). If one were to then extract J_C for different temperatures and applied fields from the simulations, it may be possible to extract information about the percolation threshold, if the system size is sufficiently large.

If the dimensions of the normal barriers within the (RE)BCO layers of tapes are indeed accurate, then it will be extremely challenging to experimentally determine their normal state properties such as their resistivity. In fact, there is even a legitimate question to be asked as to whether the Sommerfeld model expressions used to relate the normal state properties to each other in Chapters 5 and 6 are valid on length scales on the order of, or smaller than, a unit cell. The normal state properties and dimensions for the barriers extracted for (RE)BCO in this thesis can only be used to quantify the amount that the grain boundaries are still suppressing J_C in tapes (if indeed the barriers are the grain boundaries, perhaps the twin boundaries are responsible). This is also exemplified by the strong correlations between the $d(0)$ values and the phenomenological parameters $\tilde{\alpha}_n$, $\tilde{\beta}_n$, and $\tilde{\Upsilon}_n$ at

zero temperature and strain. Another factor to consider is our choice of assuming that the superconductors under analysis can be treated as weakly coupled, with s-wave pairing, in the dirty limit. This was chosen to keep the analysis as simple as possible, however, strong coupling corrections [91, 215], d-wave pairing [216], or clean limit expressions [173] may lead to different values for the phenomenological parameters α, β and Υ in the electrodes and boundaries (and therefore, the normal state properties of these regions).

One of the original aims of the percolation model was to try to explain the discrepancy between single crystal $B_{c2}(T)$ data obtained by RF measurements that display WHH-like behaviour [164] and the experimentally observed B_{irr} data. Current percolation and distributions in T_C with bonds exhibiting WHH-like behaviour are not sufficient to reproduce the convex $B_{irr}(T)$ or $B_{c2}^{*\rho}$ behaviour seen in the samples in the literature in fields up to 35 T [208]. The rule of mixtures for percolation in resistor-insulator networks breaks down when there are only just enough resistive bonds to form an infinitely spanning cluster [139]. The same will be true for our mixed network of insulating bonds and Josephson junction bonds. Just above p_c, where the path for supercurrent flow is particularly tortuous, the active conducting area A_{act} will vary with the fraction of Josephson junction bonds as a power law, rather than linearly [139]. As $B_{c2}^{*\rho}$ will likely be measured at A_{act} values just above 0 in experiments, especially for low resistivity criteria such as $0.1\rho_N$, it may be that a power law dependence for A_{act} on the fraction of Josephson junctions may reproduce the convex behaviour for B_{irr} and $B_{c2}^{*\rho}$. Alternatively, including the effects of current shunting from the (RE)BCO layer to the Cu and Ag layers due to the low N-values may explain the discrepancy between the concave WHH behaviour and the convex behaviour observed.

It would be interesting to use our percolation model to analyse J_C data for other superconducting materials. For example, the J_C's of Bi-2212 strands have often been reported to be limited by the connectivities of the grains due to the presence of voids [217, 218, 219]. Efforts by the community have led to improved J_C values

via densification processes [220, 221]. In our percolation model, low connectivities would correlate to low coordination numbers in the percolative network, making the percolation threshold close to 1. Another interesting material to investigate would be polycrystalline MgB_2 wires, in which the effects of distributions of grain orientations on J_C have already been quantified by Eisterer [94]. The temperature dependent percolation threshold found by Eisterer may well be explained by a distribution in T_C. It may also be possible to extend our percolation model to include distributions in T_C and grain orientation.

In the coming years, a huge amount of work will need to be done to qualify (RE)BCO tapes for prototype and commercial fusion magnet systems. This will involve a thorough understanding of the superconducting critical surface for multiaxial strains, as already discussed. Equally importantly, the evolution of the critical surface with neutron and gamma irradiation will need to be understood. Some experiments for neutron irradiation are already underway [210, 222, 223]. We suggest that many of the defects caused by radiation damage, such as transmutations, damage cascades and point defects will fundamentally affect the T_C of the underlying material due to changes in oxygen doping and the lattice parameters. Experiments to measure the effects of radiation damage of (RE)BCO will be complex and expensive. One of the reasons for this is that the oxygen in (RE)BCO is quite mobile at room temperature, sufficiently so that simply bending a tape for several hours is enough to cause the twinning to change substantially [213]. Therefore, (RE)BCO tapes will have to be irradiated and then have their J_C values measured at cryogenic temperatures without any thermal cycles to room temperature. Predicting the evolution of J_C using a percolation model like ours may prove to be a very useful tool to model how J_C evolves under irradiation due to changes in the distributions of T_C and B_{c2}. It will also be interesting to see whether radiation damage affects the values of $\left|\frac{dT_C}{d\varepsilon_{JJ}}\right|_{\varepsilon_{JJ}=0\%}$ or even the nature of the competing behaviour itself. For large doses of irradiation, where the microstructure of the (RE)BCO could be substantially different, it is not clear if the twinning will still

play an important role in the strain dependence of J_C.

The future of global energy production and our climate look uncertain. Recent events have only increased the urgency with which human civilisation must move away from fossil fuels. Could HTS magnet technology be the key that finally unlocks affordable energy for all, from fusion energy?

Bibliography

[1] W. Penney, B. F. J. Schonland, J. M. Kay, J. Diamond, and D. E. H. Peirson, "Report on the accident at Windscale No. 1 Pile on 10 October 1957," *Journal of Radiological Protection*, vol. 37, no. 3, p. 780, 2017.

[2] NRC, "Investigation into the March 28, 1979 Three Mile Island Accident by the Office of Inspection and Enforcement," Tech. Rep., 1979.

[3] NRC, "Report on the Accident at the Chernobyl Nuclear Power Station," Tech. Rep., 1987.

[4] IAEA, "The Fukushima Daiichi Incident," Report, 2015.

[5] Nuclear Waste Services, "GDF Annual Report 2020-21," Tech. Rep., 2021. [Online]. Available: https://assets.publishing.service.gov.uk/government/uploads/system/uploads/attachment_data/file/1057186/GDF_Annual_Report_2020_21.pdf

[6] V. P. Smirnov, "Tokamak foundation in USSR/Russia 1950–1990," *Nuclear Fusion*, vol. 50, no. 1, p. 014003, 2010.

[7] The ITER Organisation, "The ITER Tokamak," 2021. [Online]. Available: https://www.iter.org/mach

[8] K. Tobita, R. Hiwatari, Y. Sakamoto, Y. Someya *et al.*, "Japan's Efforts to Develop the Concept of JA DEMO During the Past Decade," *Fusion Science and Technology*, vol. 75, no. 5, 2019.

[9] UKAEA, "Spherical Tokamak for Energy Production," 2021. [Online]. Available: https://step.ukaea.uk/

[10] G. Zhuang, G. Q. Li, J. Li, Y. X. Wan *et al.*, "Progress of the CFETR design," *Nuclear Fusion*, vol. 59, no. 11, p. 112010, 2019.

[11] G. Federici, R. Kemp, D. Ward, C. Bachmann *et al.*, "Overview of EU DEMO design and RD activities," *Fusion Engineering and Design*, vol. 89, pp. 882–889, 2014.

[12] Tokamak Energy Ltd, "Tokamak Energy," Oxfordshire, UK, 2021. [Online]. Available: https://www.tokamakenergy.co.uk/

[13] A. J. Creely, M. J. Greenwald, S. B. Ballinger, D. Brunner *et al.*, "Overview of the SPARC tokamak," *Journal of Plasma Physics*, vol. 86, no. 5, p. 865860502, 2020.

[14] Y. Lvovsky and J. Jarvis, "Superconducting Systems for MRI- Present Solutions and New Trends," *IEEE Transactions on Applied Superconductivity*, vol. 15, no. 2, 2005.

[15] L. Rossi, "Superconductivity: its role, its success and its setbacks in the Large Hadron Collider of CERN," *Superconductor Science and Technology*, vol. 23, p. 034001, 2010.

[16] S. Hahn, K. Kwanglok, K. Kim, X. Hu *et al.*, "45.5-tesla direct-current magnetic field generated with a high-temperature superconducting magnet," *Nature*, vol. 570, pp. 496–499, 2019.

[17] M. Ono, S. Koga, and H. Ohtsuki, "Japan's superconducting Maglev train," *IEEE Instrumentation Measurement Magazine*, vol. 5, no. 1, 2002.

[18] C. A. Luongo, P. J. Masson, T. Nam, D. Mavris *et al.*, "Next Generation More-Electric Aircraft: A Potential Application for HTS Superconductors," *IEEE Transactions on Applied Superconductivity*, vol. 19, no. 3, pp. 1055–1068, 2009.

[19] D. Dimos, P. Chaudhari, J. Mannhart, and F. K. LeGoues, "Orientation Dependence of Grain-Boundary Critical Currents in $YBa_2Cu_3O_{7-\delta}$ Bicrystals," *Physical Review Letters*, vol. 61, no. 2, pp. 219–222, 1988.

[20] H. Hilgenkamp and J. Mannhart, "Grain boundaries in high-T_C superconductors," *Reviews of Modern Physics*, vol. 74, no. 2, pp. 485–549, 2002.

[21] J. G. Bednorz and K. A. Muller, "Possible High-T_C Superconductivity in the Ba-La-Cu-O System," *Zeitschrift Fur Physik B-Condensed Matter*, vol. 64, no. 2, pp. 189–193, 1986.

[22] G. Wang, M. J. Raine, and D. P. Hampshire, "How resistive must grain boundaries in polycrystalline superconductors be, to limit J_C?" *Superconductor Science and Technology*, vol. 30, no. 10, p. 104001, 2017.

[23] J. W. Ekin, "Unified scaling law for flux pinning in practical superconductors: I. Separability postulate, raw scaling data and parameterization at moderate strains," *Superconductor Science and Technology*, vol. 23, p. 083001, 2010.

[24] J. W. Ekin, N. Cheggour, L. Goodrich, J. Splett *et al.*, "Unified Scaling Law for flux pinning in practical superconductors: II. Parameter testing, scaling constants, and the Extrapolative Scaling Expression," *Superconductor Science and Technology*, vol. 29, no. 12, p. 38, 2016.

[25] J. W. Ekin, N. Cheggour, L. Goodrich, J. Splett *et al.*, "Unified Scaling Law for flux pinning in practical superconductors: III. Minimum datasets, core parameters, and application of the Extrapolative Scaling Expression," *Superconductor Science and Technology*, vol. 30, p. 033005, 2017.

[26] M. Greenwald, D. Whyte, P. Bonoli, Z. Hartwig *et al.*, "The High-Field Path to Practical Fusion Energy," Massachusetts Institute of Technology, Tech. Rep., 2018. [Online]. Available: https://library.psfc.mit.edu/catalog/reports/2010/18rr/18rr002/18rr002_full.pdf

[27] P. O. Branch, Y. Tsui, K. Osamura, and D. P. Hampshire, "Weakly-Emergent Strain-Dependent Properties of High Field Superconductors," *Nature Scientific Reports*, vol. 9, p. 13998, 2019.

[28] P. O. Branch, "The strain dependent critical current of high field superconductors for fusion energy applications," Ph.D. dissertation, 2019. [Online]. Available: http://etheses.dur.ac.uk/13186/

[29] P. Branch, K. Osamura, and D. Hampshire, "Weak emergence in the angular dependence of the critical current density of the high temperature superconductor coated conductor REBCO," *Superconductor Science and Technology*, vol. 33, no. 10, p. 104006, 2020.

[30] D. C. van der Laan, D. Abraimov, A. A. Polyanskii, D. C. Larbalestier *et al.*, "Anisotropic in-plane reversible strain effect in $Y_0 \cdot 5\,Dd_0 \cdot 5\,Ba_2Cu_3O_{7-d}$ coated conductors," *Superconductor Science and Technology*, vol. 24, no. 11, p. 8, 2011.

[31] K. Osamura, S. Machiya, and D. P. Hampshire, "Mechanism for the uniaxial strain dependence of the critical current in practical REBCO tapes," *Superconductor Science and Technology*, vol. 29, no. 6, p. 065019, 2016.

[32] K. Osamura, S. Machiya, K. Kajiwara, T. Kawasaki *et al.*, "Inverted-parabolic and weak strain dependencies on the critical current in practical <110>and <100>oriented REBCO tapes," *AIP Advances*, vol. 9, no. 7, p. 075216, 2019.

[33] U. Welp, M. Grimsditch, S. Fleshler, W. Nessler *et al.*, "Effect of Uniaxial Stress on the Superconducting Transition in $YBa_2Cu_3O_7$," *Physical Review Letters*, vol. 69, no. 14, p. 2130, 1992.

[34] W. H. Fietz, K. P. Weiss, and S. I. Schlachter, "Influence of intrinsic strain on T_C and critical current of high-T_C superconductors," *Superconductor Science and Technology*, vol. 18, no. 12, pp. S332–S337, 2005.

[35] K. Ilin, K. A. Yagotintsev, C. Zhou, P. Gao *et al.*, "Experiments and FE modeling of stress-strain state in ReBCO tape under tensile, torsional and transverse load," *Superconductor Science and Technology*, vol. 28, no. 5, p. 17, 2015.

[36] J. S. Murtomaki, R. Kouhia, A. Stenvall, L. Bottura *et al.*, "Investigation of REBCO Roebel Cable Irreversible Critical Current Degradation Under Transverse Pressure," *IEEE Transactions on Applied Superconductivity*, vol. 28, no. 4, 2018.

[37] M. Takayasu, J. Minervini, and L. Bromberg, "Torsion Strain Effects on Critical Currents of HTS Superconducting Tapes," *AIP Conference Proceedings*, vol. 1219, no. 337, 2010.

[38] D. C. van der Laan, D. C. McRae, and J. D. Weiss, "Effect of transverse compressive monotonic and cyclic loading on the performance of superconducting CORC® cables and wires," *Superconductor Science and Technology*, vol. 32, 2019.

[39] H. K. Onnes, "The resistance of pure mercury at helium temperatures," *Communications from the Physical Laboratory of the University of Leiden*, vol. 12, p. 120, 1911.

[40] T. G. Berlincourt and R. R. Hake, "Superconductivity at High Magnetic Fields," *Physical Review*, vol. 131, no. 1, pp. 140–157, 1963.

[41] B. T. Matthias, T. H. Geballe, S. Geller, and E. Corenzwit, "Superconductivity of Nb_3Sn," *Physical Review*, vol. 95, no. 6, p. 1435, 1954.

[42] N. Mitchell, J. Zheng, C. Vorpahl, V. Corato *et al.*, "Superconductors for Fusion: a Roadmap," *Superconductor Science and Technology*, 2021.

[43] M. K. Wu, J. R. Ashburn, C. J. Torng, P. H. Hor *et al.*, "Superconductivity at 93 K in a new mixed-phase Y–Ba–Cu–O compound system at ambient pressure," *Physical Review Letters*, vol. 58, no. 9, pp. 908–910, 1987.

[44] E. Snider, N. Dasenbrock-Gammon, R. McBride, M. Debessai *et al.*, "Room-temperature superconductivity in a carbonaceous sulfur hydride," *Nature*, vol. 586, no. 7829, pp. 373–377, 2020.

[45] J. E. Hirsch and M. F, "Clear evidence against superconductivity in hydrides under high pressure," *Matter and Radiation at Extremes*, vol. 7, no. 5, 2022.

[46] W. Meissner and R. Ochsenfeld, "Ein neuer Effekt bei Eintritt der Supraleitfähigkeit," *Naturwissenschaften*, vol. 21, pp. 787–788, 1933.

[47] F. London and H. London, "The electromagnetic equations of the supraconductor," *Proceedings of the Royal Society of London. Series A*, vol. A149, pp. 71–88, 1935.

[48] H. Fröhlich, "Theory of the Superconducting State. I. The Ground State at the Absolute Zero of Temperature," *Physical Review*, vol. 79, no. 5, pp. 845–856, 1950.

[49] J. Bardeen, L. N. Cooper, and J. R. Schrieffer, "Theory of Superconductivity," *Physical Review*, vol. 108, no. 5, pp. 1175–1204, 1957.

[50] E. Maxwell, "Isotope effect in the superconductivity of mercury," *Physical Review*, vol. 78, no. 4, p. 477, 1950.

[51] C. A. Reynolds, B. Serin, W. H. Wright, and L. B. Nesbitt, "Superconductivity of isotopes of mercury," *Physical Review*, vol. 78, no. 4, p. 487, 1950.

[52] V. L. Ginzburg and L. D. Landau, "On the Theory of Superconductivity," *Zhurnal Eksperimental'noi i Teoreticheskoi Fiziki*, vol. 20, pp. 1064–1082, 1950.

[53] D. R. Tilley and J. Tilley, *Ginzburg-Landau Theory*, 3rd ed. Bristol: IOP publishing Ltd., 1990, pp. 296–302.

[54] A. A. Abrikosov, "On the magnetic properties of superconductors of the second group," *Zhurnal Eksperimental'noi i Teoreticheskoi Fiziki*, vol. 5, no. 6, pp. 1174–1182, 1957.

[55] M. Tinkham, *Magnetic Properties of Classic Type II Superconductors*, 2nd ed. New York: Dover Publications, 1996, pp. 149–154.

[56] D. Dew-Hughes, "Flux pinning mechanisms in type II superconductors," *Philosophical Magazine*, vol. 30, no. 2, pp. 293–305, 1974.

[57] W. A. Fietz and W. W. Webb, "Hysteresis in superconducting alloys—Temperature and field dependence of dislocation pinning in niobium alloys," *Physical Review*, vol. 178, no. 2, pp. 657–667, 1969.

[58] A. M. Campbell and J. E. Evetts, "Flux vortices and transport currents in Type II superconductors," *Advances in Physics*, vol. 21, no. 90, pp. 395–399, 1972.

[59] R. G. Hampshire and M. T. Taylor, "Critical supercurrents and pinning of vortices in commercial Nb-60 at% Ti," *Journal of Physics F: Metal Physics*, vol. 2, pp. 89–106, 1972.

[60] E. J. Kramer, "Scaling Laws for Flux Pinning in Hard Superconductors," *Journal of Applied Physics*, vol. 44, no. 3, pp. 1360–1370, 1973.

[61] R. M. Scanlan, W. A. Fietz, and E. F. Koch, "Flux pinning centers in superconducting Nb_3Sn," *Journal of Applied Physics*, vol. 46, no. 5, pp. 2244–2249, 1975.

[62] D. M. Kroeger, D. S. Easton, A. DasGupta, C. C. Koch, and J. O. Scarbrough, "The effect of strain upon the scaling law for flux pinning in bronze process Nb_3Sn," *Journal of Applied Physics*, vol. 51, no. 4, pp. 2184–2192, 1980.

[63] D. P. Hampshire, J. Seuntjens, L. D. Cooley, and D. C. Larbalestier, "Anomalous suppression of transport critical current below $B_{c2}(T)$ in oriented sintered samples of $DyBa_2Cu_3O_7$," *Applied Physics Letters*, vol. 53, no. 9, pp. 814–815, 1988.

[64] A. Matsumoto, H. Kumakura, H. Kitaguchi, B. J. Senkowicz *et al.*, "Evaluation of connectivity, flux pinning, and upper critical field contributions to the critical current density of bulk pure and SiC-alloyed MgB_2," *Applied Physics Letters*, vol. 89, no. 13, p. 132508, 2006.

[65] N. Cheggour and D. P. Hampshire, "The unified strain and temperature scaling law for the pinning force density of bronze-route Nb_3Sn wires in high magnetic fields," *Cryogenics*, vol. 42, pp. 299 – 309, 2002.

[66] S. A. Keys and D. P. Hampshire, "A scaling law for the critical current density of weakly and strongly-coupled superconductors, used to parameterise data from a technological Nb_3Sn strand," *Superconductor Science and Technology*, vol. 16, pp. 1097–1108, 2003.

[67] D. M. J. Taylor and D. P. Hampshire, "Relationship between the n-value and critical current in Nb_3Sn superconducting wires exhibiting intrinsic and extrinsic behaviour," *Superconductor Science and Technology*, vol. 18, pp. S297–S302, 2005.

[68] X. F. Lu and D. P. Hampshire, "The field, temperature and strain dependence of the critical current density of a powder-in-tube (PIT) Nb_3Sn superconducting strand," *Superconductor Science and Technology*, vol. 23, p. 025002, 2010.

[69] IEA, "World Energy Outlook 2018," IEA, Tech. Rep., 2018. [Online]. Available: https://www.iea.org/reports/world-energy-outlook-2018

[70] E. G. R. Davies, P. Kyle, and J. A. Edmonds, "An integrated assessment of global and regional water demands for electricity generation to 2095," *Advances in Water Resources*, vol. 52, pp. 296–313, 2013.

[71] A. M. Thomson, K. V. Calvin, S. J. Smith, G. P. Kyle *et al.*, "RCP4.5: a pathway for stabilization of radiative forcing by 2100," *Climatic Change*, vol. 109, no. 1, p. 77, 2011.

[72] D. P. van Vuuren, E. Stehfest, M. G. J. den Elzen, T. Kram *et al.*, "RCP2.6: exploring the possibility to keep global mean temperature increase below 2°C," *Climatic Change*, vol. 109, no. 1, p. 95, 2011.

[73] K. Riahi, S. Rao, V. Krey, C. Cho *et al.*, "RCP 8.5—A scenario of comparatively high greenhouse gas emissions," *Climatic Change*, vol. 109, no. 1, p. 33, 2011.

[74] M. Nocente, G. Gorini, J. Kallne, and M. Tardocchi, "Cross section of the d + 3He → + p reaction of relevance for fusion plasma applications," *Nuclear Fusion*, vol. 50, no. 5, 2010.

[75] W. M. Haynes, *CRC Handbook of Chemistry and Physics*, 93rd ed. CRC Press, 2012.

[76] S. Yang, F. Zhang, H. Ding, P. He, and H. Zhou, "Lithium Metal Extraction from Seawater," *Joule*, vol. 2, no. 9, pp. 1648–1651, 2018.

[77] The ITER Organisation, "Fuelling the Fusion Reaction," 2021. [Online]. Available: https://www.iter.org/sci/FusionFuels

[78] F. F. Chen, *Introduction to Plasma Physics and Controlled Fusion*, 3rd ed. Springer International Publishing, 2016.

[79] A. Prša, P. Harmanec, G. Torres, E. Mamajek *et al.*, "Nominal Values for Selected Solar and Planetary Quantities: IAU 2015 Resolution B3," *The Astronomical Journal*, vol. 152, no. 2, p. 41, 2016.

[80] G. de Tommasi, "Plasma Magnetic Control in Tokamak Devices," *Journal of Fusion Energy*, vol. 38, no. 3, pp. 406–436, 2019.

[81] R. Aymar, P. Barabaschi, and Y. Shimomura, "The ITER design," *Plasma Physics and Controlled Fusion*, vol. 44, no. 5, pp. 519–565, 2002.

[82] D. R. Cohn and L. Bromberg, "Advantages of High Field Tokamaks for Fusion Reactor Development," *Journal of Fusion Energy*, vol. 5, no. 3, pp. 161–170, 1986.

[83] H. Zohm, "On the Minimum Size of DEMO," *Fusion Science and Technology*, vol. 58, no. 2, pp. 613–624, 2010.

[84] Euratom, "The JET Joint Undertaking," ECSC/EEC/EURATOM, Tech. Rep., 1982, eUR8306 EN (EUR-JET-RI I). [Online]. Available: http://aei.pitt.edu/88591/1/1982.pdf

[85] F. R. Fickett, "Magnetoresistivity of Copper and Aluminum at Cryogenic Temperatures," in *4th International Conference on Magnet Technology (MT-4)*, Y. Winterbottom, Ed., vol. C720919, 1972, Conference Proceedings, p. 539.

[86] R. M. Scanlan, A. P. Malozemoff, and D. C. Larbalestier, "Superconducting materials for large scale applications," *Proceedings of the IEEE*, vol. 92, no. 10, pp. 1639–1654, 2004.

[87] S. B. L. Chislett-McDonald, Y. Tsui, E. Surrey, M. Kovari, and D. P. Hampshire, "The magnetic field, temperature, strain and angular dependence of the critical current density for Nb-Ti," *Journal of Physics: Conference Series*, vol. 1559, p. 012063, 2020.

[88] "Transverse and longitudinal critical current densities in Nb46wt%Ti multifilamentary wire from 2 K up to T_C in magnetic fields up to 15 Tesla," in *Applied Superconductivity.* DGM Informationsgesellschaft mbH, 1993, pp. 23 –26.

[89] T. Boutboul, S. Le Naour, D. Leroy, L. Oberli, and V. Previtali, "Critical Current Density in Superconducting Nb-Ti Strands in the 100 mT to 11 T Applied Field Range," *IEEE Transactions on Applied Superconductivity*, vol. 16, no. 2, pp. 1184–1187, 2006.

[90] A. Godeke, "A review of the properties of Nb_3Sn and their variation with A15 composition, morphology and strain state," *Superconductor Science and Technology*, vol. 19, pp. R68–R80, 2006.

[91] D. M. J. Taylor and D. P. Hampshire, "The scaling law for the strain dependence of the critical current density in Nb_3Sn superconducting wires," *Superconductor Science and Technology*, vol. 18, pp. S241–S252, 2005.

[92] C. Buzea and T. Yamashita, "Review of the superconducting properties of MgB_2," *Superconductor Science and Technology*, vol. 14, no. 11, pp. R115–R146, 2001.

[93] G. Z. Li, M. D. Sumption, M. A. Susner, Y. Yang *et al.*, "The critical current density of advanced internal-Mg-diffusion-processed MgB_2 wires," *Superconductor Science and Technology*, vol. 25, no. 11, p. 115023, 2012.

[94] M. Eisterer, M. Zehetmayer, and H. W. Weber, "Current Percolation and Anisotropy in Polycrystalline MgB_2," *Physical Review Letters*, vol. 90, no. 24, p. 247002, 2003.

[95] M. Rübhausen, P. Guptasarma, D. G. Hinks, and M. V. Klein, "Spin and charge excitations in optimally doped $Bi_2Sr_2CaCu_2O_{8-\delta}$," *Physical Review B*, vol. 58, no. 6, pp. 3462–3467, 1998.

[96] M. Mittag, M. Rosenberg, D. Peligrad, R. Wernhardt *et al.*, "A study of the reversible and irreversible magnetic properties of a Bi-2212 single crystal in high magnetic fields," *Superconductor Science and Technology*, vol. 7, no. 4, pp. 214–221, 1994.

[97] D. C. Larbalestier, J. Jiang, U. P. Trociewitz, F. Kametani *et al.*, "Isotropic round-wire multifilament cuprate superconductor for generation of magnetic fields above 30 T," *Nature Materials*, vol. 13, no. 4, pp. 375–381, 2014.

[98] N. Clayton, N. Musolino, E. Giannini, V. Garnier, and R. Flükiger, "Growth and superconducting properties of $Bi_2Sr_2Ca_2Cu_3O_{10}$ single crystals," *Superconductor Science and Technology*, vol. 17, no. 9, pp. S563–S567, 2004.

[99] P. Sunwong, J. S. Higgins, Y. Tsui, M. J. Raine, and D. P. Hampshire, "The critical current density of grain boundary channels in polycrystalline HTS and LTS superconductors in magnetic fields," *Superconductor Science and Technology*, vol. 26, p. 095006, 2013.

[100] N. Ayai, S. Kobayashi, M. Kikuchi, T. Ishida *et al.*, "Progress in performance of DI-BSCCO family," *Physica C: Superconductivity*, vol. 468, no. 15, pp. 1747–1752, 2008.

[101] G. Grissonnanche, O. Cyr-Choiniere, F. Laliberte, S. R. de Cotret *et al.*, "Direct measurement of the upper critical field in cuprate superconductors," *Nat. Commun.*, vol. 5, p. 8, 2014.

[102] J. D. Lawson, "Some Criteria for a Power Producing Thermonuclear Reactor," *Proceedings of the Physical Society of London Section B*, vol. 70, no. 1, pp. 6–10, 1957.

[103] C. C. Koch and D. S. Easton, "A review of mechanical behaviour and stress effects in hard superconductors," *Cryogenics*, vol. 17, pp. 391–413, 1977.

[104] G. de Marzi, B. Bordini, and D. Baffari, "On the mechanisms governing the critical current reduction in Nb3Sn Rutherford cables under transverse stress," *Scientific Reports*, vol. 11, no. 1, p. 7369, 2021.

[105] S. Takahashi, Y. Suetomi, T. Takao, Y. Yanagisawa *et al.*, "Hoop Stress Modification, Stress Hysteresis and Degradation of a REBCO Coil Due to the Screening Current Under External Magnetic Field Cycling," *IEEE Transactions on Applied Superconductivity*, vol. 30, no. 4, pp. 1–7, 2020.

[106] S. Rogers, W. K. Chan, and J. Schwartz, "Effects of room-temperature tensile fatigue on critical current and n-value of IBAD–MOCVD $YBa_2Cu_3O_{7x}$/Hastelloy coated conductor," *Superconductor Science and Technology*, vol. 29, no. 8, p. 085013, 2016.

[107] N. Cheggour, P. J. Lee, L. F. Goodrich, Z. H. Sung *et al.*, "Influence of the heat-treatment conditions, microchemistry, and microstructure on the irreversible strain limit of a selection of Ti-doped internal-tin Nb_3Sn ITER wires," *Superconductor Science and Technology*, vol. 27, no. 10, p. 21, 2014.

[108] K. Osamura, S. Machiya, and G. Nishijima, "Reversible stress and strain limits of the critical current of practical REBCO and BSCCO wires," *Superconductor Science and Technology*, vol. 29, no. 9, p. 094003, 2016.

[109] H. S. Shin and Z. M. Bautista, "Evaluation of Irreversible Strain/Stress Limits for Ic Degradation in Practical REBCO CC Tapes Under Uniaxial Tension," *IEEE Transactions on Applied Superconductivity*, vol. 28, no. 4, pp. 1–5, 2018.

[110] M. Sugano, S. Machiya, H. Oguro, M. Sato *et al.*, "The effect of the 2D internal strain state on the critical current in GdBCO coated conductors," *Superconductor Science and Technology*, vol. 25, no. 5, p. 054014, 2012.

[111] B. Bordini, P. Alknes, L. Bottura, L. Rossi, and D. Valentinis, "An exponential scaling law for the strain dependence of the Nb_3Sn critical current

density," *Superconductor Science and Technology*, vol. 26, no. 7, p. 075014, 2013.

[112] M. Sugano, K. Shikimachi, N. Hirano, and S. Nagaya, "The reversible strain effect on critical current over a wide range of temperatures and magnetic fields for YBCO coated conductors," *Superconductor Science and Technology*, vol. 23, p. 085013, 2010.

[113] S. Awaji, T. Suzuki, H. Oguro, K. Watanabe, and K. Matsumoto, "Strain-controlled critical temperature in $REBa_2Cu_3O_y$-coated conductors," *Scientific Reports*, vol. 5, p. 11156, 2015.

[114] T. Suzuki, S. Awaji, H. Oguro, and K. Watanabe, "Applied Strain Effect on Superconducting Properties for Detwinned $(Y, Gd)BCO$ Coated Conductors," *IEEE Transactions on Applied Superconductivity*, vol. 25, no. 3, pp. 1–4, 2015.

[115] O. Kraut, C. Meingast, G. Bräuchle, H. Claus *et al.*, "Uniaxial pressure dependence of T_C of untwinned $YBa_2Cu_3O_x$single crystals for x=6.5–7," *Physica C: Superconductivity*, vol. 205, no. 1, pp. 139–146, 1993.

[116] K. Osamura, S. Machiya, Y. Tsuchiya, H. Suzuki *et al.*, "Microtwin Structure and Its Influence on the Mechanical Properties of REBCO Coated Conductors," *IEEE Transactions on Applied Superconductivity*, vol. 22, no. 1, 2012.

[117] J. W. Ekin, *Experimental Techniques for Low-Temperature Measurements*. New York: Oxford University Press, 2007.

[118] A. T. van Kessel, H. W. Myron, and F. M. Mueller, "Electronic Structure of Nb_3Sn," *Physical Review Letters*, vol. 41, no. 3, pp. 181–184, 1978.

[119] D. O. Welch, "Alteration of the superconducting properties of A15 compounds and elementary composite superconductors by nonhydrostatic elastic strain," *Advances in Cryogenic Engineering*, vol. 26, pp. 48–65, 1980.

[120] M. F. Chisholm and D. A. Smith, "Low-angle tilt grain boundaries in $YBa_2Cu_3O_7$ superconductors," *Philosophical Magazine A*, vol. 59, no. 2, pp. 181–197, 1989.

[121] A. Gurevich and E. A. Pashitskii, "Current transport through low-angle grain boundaries in high-temperature superconductors," *Physical Review B*, vol. 57, no. 21, pp. 13 878–13 893, 1998.

[122] D. Dimos, P. Chaudhari, and J. Mannhart, "Superconducting transport properties of grain boundaries in YBa2Cu3O7 bicrystals," *Physical Review B*, vol. 41, no. 7, pp. 4038–4049, 1990.

[123] M. F. Chisholm and S. J. Pennycook, "Structural origin of reduced critical currents at $YBa_2Cu_3O_{7-\delta}$ grain boundaries," *Nature*, vol. 351, no. 6321, pp. 47–49, 1991.

[124] B. H. Moeckly, D. K. Lathrop, and R. A. Buhrman, "Electromigration study of oxygen disorder and grain-boundary effects in $YBa_2Cu_3O_{7-\delta}$ thin films," *Physical Review B*, vol. 47, no. 1, pp. 400–417, 1993.

[125] B. H. Moeckly and R. A. Buhrman, "Electromagnetic properties of YBa/sub 2/Cu/sub 3/O/sub 7-/spl delta// thin-film grain-boundary weak links," *IEEE Transactions on Applied Superconductivity*, vol. 5, no. 2, pp. 3414–3417, 1995.

[126] H. Hilgenkamp, J. Mannhart, and B. Mayer, "Implications of $d_{x^2-y^2}$ symmetry and faceting for the transport properties of grain boundaries in high-T_c superconductors," *Physical Review B*, vol. 53, no. 21, pp. 14 586–14 593, 1996.

[127] B. D. Joesphson, "Possible new effects in superconductive tunnelling," *Physics Letters*, vol. 1, no. 7, pp. 251–253, 1962.

[128] D. R. Tilley and J. Tilley, *Josephson Effects*, 3rd ed. Bristol: IOP publishing Ltd., 1990, ch. 7, pp. 260–293.

[129] L. Dobrosavljevi̧-Gruji̧ and Z. Radovi̧, "Magnetic Field Dependence of the Critical Currents in High T_C Superconductors," *Physica C*, vol. 185-189, pp. 2313–2314, 1991.

[130] L. Dobrosavljevi̧-Gruji̧ and Z. Radovi̧, "Critical currents in superconductor-normal metal-superconductor junctions," *Superconductor Science and Technology*, vol. 6, no. 7, pp. 537–541, 1993.

[131] J. R. Clem, "Josephson junctions in thin and narrow rectangular superconducting strips," *Physical Review B*, vol. 81, no. 14, 2010.

[132] A. I. Blair, "Simulations of Critical Currents in Polycrystalline Superconductors Using Time-Dependent Ginzburg–Landau Theory," Ph.D. dissertation, 2021.

[133] A. I. Blair and D. P. Hampshire, "Critical current density of superconducting-normal-superconducting Josephson junctions and polycrystalline superconductors in high magnetic fields," *Physical Review Research*, vol. 4, no. 2, p. 023123, 2022.

[134] P. Grassberger, "On the critical behavior of the general epidemic process and dynamical percolation," *Mathematical Biosciences*, vol. 63, no. 2, pp. 157–172, 1983.

[135] J. Shao, S. Havlin, and H. E. Stanley, "Dynamic Opinion Model and Invasion Percolation," *Physical Review Letters*, vol. 103, no. 1, p. 018701, 2009.

[136] T. Beer and I. G. Enting, "Fire spread and percolation modelling," *Mathematical and Computer Modelling*, vol. 13, no. 11, pp. 77–96, 1990.

[137] A. Aleksiejuk and J. A. Hołyst, "A simple model of bank bankruptcies," *Physica A: Statistical Mechanics and its Applications*, vol. 299, no. 1, pp. 198–204, 2001.

[138] Y. Gueguen and J. Dienes, "Transport properties of rocks from statistics and percolation," *Mathematical Geology*, vol. 21, no. 1, pp. 1–13, 1989.

[139] S. Kirkpatrick, "Percolation and Conduction," *Reviews of Modern Physics*, vol. 45, no. 4, 1973.

[140] M. F. Sykes and J. W. Essam, "Some Exact Critical Percolation Probabilities for Bond and Site Problems in Two Dimensions," *Physical Review Letters*, vol. 10, no. 1, pp. 3–4, 1963.

[141] M. F. Sykes and J. W. Essam, "Critical Percolation Probabilities by Series Methods," *Physical Review*, vol. 133, no. 1A, pp. A310–A315, 1964.

[142] M. E. Fisher and J. W. Essam, "Some Cluster Size and Percolation Problems," *Journal of Mathematical Physics*, vol. 2, no. 4, pp. 609–619, 1961.

[143] R. B. Stinchcombe, "Conductivity and spin-wave stiffness in disordered systems - an exactly soluble model," *J. Phys. C - Solid State*, vol. 7, pp. 179–203, 1974.

[144] D. A. G. Bruggeman, "Berechnung verschiedener physikalischer Konstanten von heterogenen Substanzen. I. Dielektrizitätskonstanten und Leitfähigkeiten der Mischkörper aus isotropen Substanzen," *Annalen der Physik*, vol. 416, no. 7, pp. 636–664, 1935.

[145] W. D. Markiewicz and J. Toth, "Percolation and the resistive transition of the critical temperature T_C of Nb_3Sn," *Cryogenics*, vol. 46, no. 6, pp. 468–476, 2006.

[146] M. Eisterer, "Magnetic properties and critical currents of MgB_2," *Superconductor Science and Technology*, vol. 20, no. 12, pp. R47–R73, 2007.

[147] D. C. van der Laan and J. W. Ekin, "Dependence of the critical current of $YBa_2Cu_3O_{7-\delta}$ coated conductors on in-plane bending," *Superconductor Science and Technology*, vol. 21, no. 11, p. 115002, 2008.

[148] P. Sunwong, J. S. Higgins, and D. P. Hampshire, "Probes for investigating the effect of magnetic field, field orientation, temperature and strain on the critical current density of anisotropic high-temperature superconducting tapes in a split-pair 15 T horizontal magnet," *Review of Scientific Instruments*, vol. 85, no. 6, p. 065111, 2014.

[149] D. C. van der Laan, P. D. Noyes, G. E. Miller, H. W. Weijers, and G. P. Willering, "Characterization of a high-temperature superconducting conductor on round core cables in magnetic fields up to 20 T," *Superconductor Science and Technology*, vol. 26, no. 4, p. 045005, 2013.

[150] J. D. Weiss, T. Mulder, H. J. ten Kate, and D. C. Van der Laan, "Introduction of CORC® wires: highly flexible, round high-temperature superconducting wires for magnet and power transmission applications," *Superconductor Science and Technology*, vol. 30, 2017.

[151] P. Bruzzone, W. H. Fietz, J. Minervini, M. Novikov *et al.*, "High temperature superconductors for fusion magnets," *Nuclear Fusion*, vol. 58, no. 10, p. 103001, 2018.

[152] D. C. van der Laan, J. W. Ekin, J. F. Douglas, C. C. Clickner *et al.*, "Effect of strain, magnetic field and field angle on the critical current density of $YBa_2Cu_3O_{7-\delta}$ coated conductors," *Superconductor Science and Technology*, vol. 23, p. 072001, 2010.

[153] C. Barth, G. Mondonico, and C. Senatore, "Electro-mechanical properties of REBCO coated conductors from various industrial manufacturers at 77 K, self-field and 4.2 K, 19 T," *Superconductor Science and Technologu*, vol. 28, 2015.

[154] H. S. Shin, M. J. Dedicatoria, A. Gorospe, H. Oguro, and S. Awaji, "Ic Response With High Magnetic Field, Low Temperature, and Uniaxial Strain

in REBCO Coated Conductor Tapes," *IEEE Transactions on Applied Superconductivity*, vol. 26, no. 4, pp. 1–4, 2016.

[155] J. R. Greenwood, E. Surrey, and D. P. Hampshire, "Biaxial Strain Measurements of J_C on a (RE)BCO Coated Conductor," *IEEE Transactions on Applied Superconductivity*, vol. 28, no. 4, 2018.

[156] J. R. Greenwood, E. Surrey, and D. P. Hampshire, "The Biaxial Strain Dependence of J_C of a (RE)BCO Coated Conductor at 77 K in Low Fields," *IEEE Transactions on Applied Superconductivity*, vol. 29, no. 5, 2019.

[157] *Characterisation of the Transport Critical Current Density for Conductor Applications*. Accepted by Taylor and Francis, 2017.

[158] Autodesk, "Autodesk Inventor," 2022. [Online]. Available: https://www.autodesk.com/

[159] SuperPower-Furukawa, "SuperPower 2G HTS Coated Conductors," 2022. [Online]. Available: http://www.superpower-inc.com/content/2g-hts-wire

[160] HBM, "XY T Rosettes with 2 Measuring Grids for Analyzing Biaxial Stress States with Known Principal Directions," 2018. [Online]. Available: https://www.hbm.com/en/3443/xy-t-rosettes-with-measuring-grids-for-analyzing-biaxial-stress/

[161] Y. Tsui and D. P. Hampshire, "Critical current scaling and the pivot-point in Nb_3Sn strands," *Superconductor Science and Technology*, vol. 25, no. 5, p. 054008, 2012.

[162] X. F. Lu and D. P. Hampshire, "The Magnetic Field, Temperature and Strain Dependence of the Critical Current of a Nb_3Sn Strand Using a Six Free-Parameter Scaling Law," *IEEE Transactions on Applied Superconductivity*, vol. 19, no. 3, pp. 2619–2623, 2009.

[163] S. A. Keys, N. Koizumi, and D. P. Hampshire, "The strain and temperature scaling law for the critical current density of a jelly-roll Nb_3Al strand in high magnetic fields," *Superconductor Science and Technology*, vol. 15, pp. 991–1010, 2002.

[164] T. Sekitani, N. Miura, S. Ikeda, Y. H. Matsuda, and Y. Shiohara, "Upper critical field for optimally-doped $YBa_2Cu_3O_{7-\delta}$," *Physica B: Condensed Matter*, vol. 346–347, pp. 319–324, 2004.

[165] K. Osamura, S. Machiya, Y. Tsuchiya, and H. Suzuki, "Force free strain exerted on a YBCO layer at 77 K in surround Cu stabilized YBCO coated conductors," *Superconductor Science and Technology*, vol. 23, no. 4, p. 045020, 2010.

[166] M. Lao, J. Bernardi, M. Bauer, and M. Eisterer, "Critical current anisotropy of GdBCO tapes grown on ISD-MgO buffered substrate," *Superconductor Science and Technology*, vol. 28, no. 12, p. 124002, 2015.

[167] C. Senatore, C. Barth, M. Bonura, M. Kulich, and G. Mondonico, "Field and temperature scaling of the critical current density in commercial REBCO coated conductors," *Superconductor Science and Technology*, vol. 29, no. 1, p. 8, 2016.

[168] N. Cheggour and D. P. Hampshire, "A probe for investigating the effect of magnetic field, temperature and strain on transport critical currents in superconducting tapes and wires," *Review of Scientific Instruments*, vol. 71, no. 12, p. 4521, 2000.

[169] B. L. Brandt and L. G. Rubin, "Low temperature thermometry in high magnetic fields. VII Cernox^{TM} sensors to 32 T," *Review of Scientific Instruments*, vol. 70, no. 1, pp. 104–110, 1999.

[170] D. Hampshire, H. Jones, and E. Mitchell, "An in-depth characterisation of $(NbTa)_3Sn$ filamentary superconductor," *IEEE Transactions on Magnetics*, vol. 21, pp. 289–292, 1985.

[171] C. Kittel, *Introduction to Solid State Physics*, 8th ed. John Wiley Sons, 2004.

[172] C. P. Poole, H. A. Farach, R. J. Creswick, and R. Prozorov, *Superconductivity*. London: Elsevier, 2014.

[173] T. P. Orlando, E. J. McNiff, S. Foner, and M. R. Beasley, "Critical fields, Pauli paramagnetic limiting, and material parameters of Nb_3Sn and V_3Si," *Physical Review B*, vol. 19, no. 9, pp. 4545–4561, 1979.

[174] M. G. T. Mentink, M. M. J. Dhalle, D. R. Dietderich, A. Godeke *et al.*, "The effects of disorder on the normal state and superconducting properties of Nb_3Sn," *Superconductor Science and Technology*, vol. 30, no. 2, p. 025006, 2016.

[175] M. Tinkham, "Resistive Transition of High-Temperature Superconductors," *Physical Review Letters*, vol. 61, pp. 1658–1661, 1988.

[176] M. Wilson, *Superconducting Magnets*. Oxford, UK: Oxford University Press, 1986.

[177] R. R. Hake, "Paramagnetic superconductivity in extreme Type-II superconductors," *Physical Review*, vol. 158, no. 2, pp. 356–376, 1967.

[178] V. B. Eltsov, "Theory of Superconductivity," Aalto University, Tech. Rep., 2021. [Online]. Available: https://mycourses.aalto.fi/pluginfile.php/1414652/mod_resource/content/13/theory_sc.pdf

[179] G. J. Carty, "Studies of coated and polycrystalline superconductors using the time-dependent Ginzburg-Landau equations," Ph.D. dissertation, 2006.

[180] B. P. Din, A. I. Blair, F. Schoofs, and D. P. Hampshire, "Critical Current Densities through Josephson Junctions in Low Magnetic Fields," *IEEE Transactions on Applied Superconductivity*, vol. 34, no. 4, 2022.

[181] J. L. MacManus-Driscoll, S. R. Foltyn, Q. X. Jia, H. Wang *et al.*, "Strongly enhanced current densities in superconducting coated conductors of $YBa_2Cu_3O_{7-x}$+$BaZrO_3$," *Nature Materials*, vol. 3, pp. 439–443, 2004.

[182] V. Braccini, A. Xu, J. Jaroszynski, Y. Xin *et al.*, "Properties of recent IBAD-MOCVD coated conductors relevant to their high field, low temperature magnet use," *Superconductor Science and Technology*, vol. 24, no. 3, p. 9, 2011.

[183] H. J. Fink, "Supercurrents through superconducting-normal-superconducting proximity layers. I. Analytic solution," *Physical Review B*, vol. 14, no. 3, pp. 1028–1038, 1976.

[184] C. W. A. Gurnham and D. P. Hampshire, "Self-Field Effects in a Josephson Junction Model for J_c in REBCO Tapes," *IEEE Transactions on Applied Superconductivity*, vol. 32, no. 4, 2022.

[185] G. Majkic, J. S. Jeong, H. Yun, F. C. R. Hernandez *et al.*, "New insight into strain and composition of $BaZrO_3$ nanorods in REBCO superconductor," *Superconductor Science and Technology*, vol. 34, no. 11, p. 115002, 2021.

[186] L. T. Sagdahl, S. Gjo/lmesli, T. Laegreid, K. Fossheim, and W. Assmus, "Flux pinning and irreversibility in $YBa_2Cu_3O_7$ superconducting crystal," *Physical Review B*, vol. 42, no. 10, pp. 6797–6800, 1990.

[187] Y. Xu and M. Suenaga, "Irreversibility temperatures in superconducting oxides: The flux-line-lattice melting, the glass-liquid transition, or the depinning temperatures," *Physical Review B*, vol. 43, no. 7, pp. 5516–5525, 1991.

[188] L. W. Lombardo, D. B. Mitzi, A. Kapitulnik, and A. Leone, "Defect dependence of the irreversibility line in $Bi_2Sr_2CaCu_2O_8$ single crystals," *Physical Review B*, vol. 46, no. 9, pp. 5615–5620, 1992.

[189] L. Civale, B. Maiorov, A. Serquis, J. O. Willis *et al.*, "Angular-dependent vortex pinning mechanisms in $YBa_2Cu_3O_7$ coated conductors and thin films," *Applied Physics Letters*, vol. 84, p. 2121, 2004.

[190] T. L. Hylton and M. R. Beasley, "Flux-pinning mechanisms in thin films of $YBa_2Cu_3O_x$," *Physical Review B*, vol. 41, no. 16, pp. 11 669–11 672, 1990.

[191] P. Lu, Y. Q. Li, J. Zhao, C. S. Chern *et al.*, "High density, ultrafine precipitates in YBa2Cu3O7x thin films prepared by plasma-enhanced metalorganic chemical vapor deposition," *Applied Physics Letters*, vol. 60, no. 10, pp. 1265–1267, 1992.

[192] H. Yamasaki, K. Ohki, I. Yamaguchi, M. Sohma *et al.*, "Strong flux pinning due to dislocations associated with stacking faults in $YBa_2Cu_3O_{7-\delta}$ thin films prepared by fluorine-free metal organic deposition," *Superconductor Science and Technology*, vol. 23, no. 10, p. 105004, 2010.

[193] M. Tachiki and S. Takahashi, "Anisotropy of critical current in layered oxide superconductors," *Solid State Communications*, vol. 72, no. 11, pp. 1083–1086, 1989.

[194] M. Tachiki and S. Takahashi, "Strong vortex pinning intrinsic in high-T_C oxide superconductors," *Solid State Communications*, vol. 70, no. 3, pp. 291–295, 1989.

[195] A. Francis, D. Abraimov, Y. Viouchkov, Y. Su *et al.*, "Development of general expressions for the temperature and magnetic field dependence of the critical current density in coated conductors with variable properties," *Superconductor Science and Technology*, vol. 33, no. 4, p. 044011, 2020.

[196] J. S. Higgins and D. P. Hampshire, "Critical Current Density of $YBa_2Cu_3O_{7-\delta}$ Coated Conductors Under High Compression in High Fields," *IEEE Transactions on Applied Superconductivity*, vol. 21, no. 3, pp. 3234–3237, 2011.

[197] J. P. McEvoy, "Effect of uniaxial stress on the superconducting transition temperature of monocrystalline Nb_3Sn," *Physica*, vol. 55, pp. 540–544, 1971.

[198] J. G. Ossandon, J. R. Thompson, D. K. Christen, B. C. Sales *et al.*, "Influence of oxygen deficiency on the superconductive properties of grain-aligned $YBa_2Cu_3O_{7-\delta}$," *Physical Review B*, vol. 45, no. 21, pp. 12 534–12 547, 1992.

[199] R. Piessens, E. de Doncker-Kapenga, C. W. Überhuber, and D. K. Kahaner, *Quadpack: A Subroutine Package for Automatic Integration*, 1st ed. Springer-Verlag Berlin Heidelberg, 1983, vol. 1.

[200] SciPy, "scipy.integrate.quad," 2022. [Online]. Available: https://docs.scipy.org/doc/scipy/reference/generated/scipy.integrate.quad.html

[201] Cython, "Cython: C-Extensions for Python," 2022. [Online]. Available: https://cython.org/

[202] T. Okada, H. Misaizu, and S. Awaji, "A possible explanation for double-peak structure in strain dependence of critical current density in REBa2Cu3O7-d coated conductors," *Superconductor Science and Technology*, vol. 33, no. 9, 2020.

[203] J. W. Essam, K. De'Bell, J. Adler, and F. M. Bhatti, "Analysis of extended series for bond percolation on the directed square lattice," *Physical Review B*, vol. 33, no. 3, pp. 1982–1986, 1986.

[204] A. Godeke, M. C. Jewell, C. M. Fischer, A. A. Squitieri *et al.*, "The upper critical field of filamentary Nb_3Sn conductors," *Journal of Applied Physics*, vol. 97, 2005.

[205] D. E. Farrell, J. P. Rice, and D. M. Ginsberg, "Experimental evidence for flux-lattice melting," *Physical Review Letters*, vol. 67, no. 9, pp. 1165–1168, 1991.

[206] D. S. Fisher, M. P. A. Fisher, and D. A. Huse, "Thermal fluctuations, quenched disorder, phase transitions, and transport in type-II superconductors," *Physical Review B*, vol. 43, no. 1, pp. 130–159, 1991.

[207] N. R. Werthamer, E. Helfand, and P. C. Hohenberg, "Temperature and Purity Dependence of the Superconducting Critical Field, H_{c2}. III. Electron Spin and Spin-Orbit Effects." *Physical Review*, vol. 147, no. 1, pp. 295–302, 1966.

[208] A. P. Smith, M. J. Raine, E. Surrey, S. Awaji *et al.*, "3-D Properties in (RE)BCO Tapes Measured in Fields up to 35T," *IEEE Transactions on Applied Superconductivity*, vol. 29, no. 5, 2019.

[209] M. Suenaga and W. Jansen, "Chemical compositions at and near the grain boundaries in bronze-processed superconducting Nb_3Sn," *Applied Physics Letters*, vol. 43, pp. 791–793, 1983.

[210] W. Iliffe, N. Peng, G. Brittles, R. Bateman *et al.*, "In-situ measurements of the effect of radiation damage on the superconducting properties of coated conductors," *Superconductor Science and Technology*, vol. 34, no. 9, p. 09LT01, 2021.

[211] T. E. Ltd, "Tokamak Energy Future Roadmap," 2022. [Online]. Available: https://www.tokamakenergy.co.uk/technology/#future

[212] Accu Engineering, "Accu Engineering," 2022. [Online]. Available: https://www.accu.co.uk/

[213] T. Okada, H. Misaizu, and S. Awaji, "In-Plane Domain Control of REBCO Coated Conductors by Annealing Under Bending Strain," *IEEE Transactions on Applied Superconductivity*, vol. 31, no. 5, 2021.

[214] J. J. Hanak, K. Strater, and G. W. Cullen, "Preparation and Properties of Vapor-Deposited Niobium Stannide," *RCA Review*, vol. 25, pp. 342–65, 1964.

[215] F. Marsiglio and J. P. Carbotte, "Strong-coupling corrections to Bardeen-Cooper-Schrieffer ratios," *Physical Review B*, vol. 33, no. 9, pp. 6141–6146, 1986.

[216] A. J. Berlinsky, A. L. Fetter, M. Franz, C. Kallin, and P. I. Soininen, "Ginzburg-Landau theory of vortices in d-wave superconductors," *Physical Review Letters*, vol. 75, no. 11, pp. 2200–2203, 1995.

[217] C. Scheuerlein, M. Di Michiel, M. Scheel, J. Jiang *et al.*, "Void and phase evolution during the processing of Bi-2212 superconducting wires monitored by combined fast synchrotron micro-tomography and x-ray diffraction," *Superconductor Science and Technology*, vol. 24, no. 11, p. 115004, 2011.

[218] A. Malagoli, F. Kametani, J. Jiang, U. P. Trociewitz *et al.*, "Evidence for long range movement of Bi-2212 within the filament bundle on melting and its significant effect on Jc," *Superconductor Science and Technology*, vol. 24, no. 7, p. 075016, 2011.

[219] F. Kametani, T. Shen, J. Jiang, C. Scheuerlein *et al.*, "Bubble formation within filaments of melt-processed Bi2212 wires and its strongly negative effect on the critical current density," *Superconductor Science and Technology*, vol. 24, no. 7, p. 7, 2011.

[220] J. Jiang, W. L. Starch, M. Hannion, F. Kametani *et al.*, "Doubled critical current density in Bi-2212 round wires by reduction of the residual bubble density," *Superconductor Science and Technology*, vol. 24, no. 8, 2011.

[221] J. Jiang, G. Bradford, S. I. Hossain, M. Brown *et al.*, "High-Performance Bi-2212 Round Wires Made With Recent Powders," *IEEE Transactions on Applied Superconductivity*, vol. 29, no. 5, 2019.

[222] D. X. Fischer, R. Prokopec, J. Emhofer, and M. Eisterer, "The effect of fast neutron irradiation on the superconducting properties of REBCO coated con-

ductors with and without artificial pinning centers," *Superconductor Science and Technology*, vol. 31, no. 4, 2018.

[223] R. J. Nicholls, S. Diaz-Moreno, W. Iliffe, Y. Linden *et al.*, "Understanding irradiation damage in high-temperature superconductors for fusion reactors using high resolution X-ray absorption spectroscopy," *Communications Materials*, vol. 3, no. 1, p. 52, 2022.

Colophon

This thesis is based on a template developed by Matthew Townson and Andrew Reeves. It was typeset with LaTeX 2_ε. It was created using the *memoir* package, maintained by Lars Madsen, with the *madsen* chapter style. The font used is Latin Modern, derived from fonts designed by Donald E. Knuth.